Development of Stable, High Optoelectronic Quality Perovskites Using Photoluminescence, Photoconductivity, and Machine Learning

Ryan J. Stoddard

A dissertation

submitted in partial fulfillment of the

requirements for the degree of

Doctor of Philosophy

University of Washington

2020

Reading Committee:

Hugh Hillhouse, Chair

Qiuming Yu

Dan Schwartz

Program Authorized to Offer Degree:

Chemical Engineering

University of Washington

Abstract

Development of Stable, High Optoelectronic Quality Perovskites Using Photoluminescence, Photoconductivity, and Machine Learning

Ryan J. Stoddard

Chair of the Supervisory Committee:
Rehnberg Chair Professor Hugh W. Hillhouse
Chemical Engineering

Improving the economics of solar cells is a key component to enable rapid adoption of clean electricity. Reducing the cost of photovoltaics can be attained by improving power conversion efficiency, increasing module lifetime, and reducing processing and CAPEX costs. However, mature technologies such as silicon are presently approaching fundamental efficiency limits, and cost reductions have plateaued. Hybrid Perovskites (HPs) are an emerging material class that show promise since they are inexpensive to fabricate via solution processing, and they have broadly tunable material properties. The HP bandgap can be precisely tuned to pair with silicon in a tandem solar cell, increasing the theoretical power conversion efficiency limit with minimal additional processing costs. The work presented in this dissertation is broadly focused on improving the performance and reliability of perovskite materials for photovoltaic applications.

First, I demonstrate a photoluminescence-photoconductivity (PL-PC) technique that directly measures HP quasi-Fermi level splitting (ΔE_F) and carrier diffusion length (L_D), which are predictors of device open-circuit voltage and short-circuit current respectively. I use this PC-PL technique to highlight several cases where ΔE_F and L_D are anti-correlated and show the importance of quantifying L_D in determining overall absorber optoelectronic quality.

Next, I focus on development of high-bandgap HPs for tandem applications. Although halide mixing can increase the bandgap to make an ideal bandgap pairing with silicon in tandem applications, the mixed-halide HPs suffer from lower relative voltages and phase instabilities under illumination. Using high-throughput combinatorial exploration, I identified a new compositional motif using larger guanidinium and smaller cesium to form a stable HP structure with enhanced lattice strain. This class of mixed-halide HPs with enhanced strain show modified band structure, higher film ΔE_F, and device open-circuit voltage. I expanded the combinatorial exploration of HP compositions and collect a dataset of 13,000 photoluminescence (PL) spectra indexed by composition. Additionally, I show a proof of concept of using a machine learning approach to predict material bandgap and optoelectronic quality fraction. I also study the origin and impact of phase segregation in mixed-halide HPs and discover phase segregation occurs due to excess charge carriers, which can be generated either by photoexcitation or by current injection.

Finally, I study degradation of HP films and devices in various combinations of light, atmosphere, humidity, and thermal stresses and use a machine learning model to link early time behavior to the time it takes the material or device to degrade. This effort reveals simple optical measurements such as transmittance and dark field microscopy have considerable utility in identifying early signs of HP degradation.

Collectively, the work included in this dissertation demonstrates considerable progress toward understanding optoelectronic performance and reliability of a wide class of HP materials, with focus on high-bandgap HPs useful for tandem applications.

TABLE OF CONTENTS

LIST OF FIGURES

LIST OF TABLES

ACKNOWLEDGEMENTS

I have been fortunate to have an incredible support network, both professionally and personally, that has enabled the completion of this work. I would like to acknowledge some notable individuals who have supported me through my PhD.

First, I would like to acknowledge my advisor, Dr. Hugh Hillhouse. Thank you for challenging me and holding my work to a high standard, your guidance has enabled me to become a thoughtful scientist. Thank you for giving me freedom in my PhD and for always encouraging healthy scientific debate. I especially appreciate your natural curiosity and interest in your students' work, and your contagious optimism that contends science can truly lead to positive societal change.

I also would like to acknowledge my other committee members. Dr. Qiuming Yu, thank you for your kindness and encouragement through the years as we crossed paths at conferences and in my exams. Dr. Daniel Schwartz, thank you for your support through the Clean Energy Institute and Torrance Tech Due Diligence Fellowship; I have always appreciated your "big picture" perspective on my work. Dr. Marjorie Olmstead, thank you for your patience as I was first learning solid state physics concepts in Physics 423 office hours, and thank you for serving as GSR on my committee.

I would also like to thank my colleagues and collaborators from University of Washington. Dr. Ian Braly, thank you for all the office chats, I learned so much from you during these conversations and appreciated how you fueled my curiosity, which led to very informative experiments. Dr. Adharsh Rajagopal, thank you for your hard work and insight in all our collaborative work. Working with you was truly an exciting time for me, and I always looked forward to discussing results with you to hear your thoughtful perspective. Dr. Felix Eickemeyer, thank you for all your

hard work keeping the lab running and helping me with the theory and experimental set up for the first photoconductivity paper. Dr. Alex Uhl, thank you for all your wisdom you shared with me during my early PhD years, especially on how to design good experiments and conduct research with excellence. Dr. Wiley Dunlap-Shohl, thank you for your hard work and for taking initiative as I transferred leadership of the perovskite subgroup to you and throughout collection of the dataset for our transmittance/dark field paper. Ray Palmer, thank you for your intellectual engagement in the perovskite work and for your support collecting data for the GA manuscript. Jason Moore, thank you for building competence in the spray coating methodology and generating reliable spray coated samples for the hpdb dataset. Yuhuan Meng, thank you for taking initiative in the lab to keep everything running as several of the senior lab members moved on, and thank you for your help with device fabrication for my final paper. Hongbo Qiao, thank you for all your hard work in sample generation and data collection that contributed to the dataset for my final paper. Jac Clark, thank you for your camaraderie through the years; your perspective and thoughtful comments in my research presentations were always extremely relevant and useful. I also want the thank John Katahara, Kyle Harrigan, Wylie Kau, Dr. David Beck, Dr. Marina Meila, Yu-Chia Chen, Soumya Phadke, and Yuhang Yang. I also want the thank Dr. Kim Woodrow for her encouragement and support prior to starting my PhD and helping me with my application to the UW ChemE program.

I would like to acknowledge funding from the Department of Energy Sunshot initiative, University of Washington Chemical Engineering Department, and the Clean Energy Institute (via the Washington Research Foundation).

I would also like to thank my personal friends for their support through my PhD. Thank you to Chris Szynal, Honorio Valdes, Alexey Gilman, Jerry Chen, Kelly Carpenter, Evan Barbre,

Damon Ormberg, Grant Shaver, Bora Banjanin, Philp Bunge, Rebecca Leong, Dave Swoish, Kristin Thomas, Kaitlin Tripi, Richard Kresser, Maudie Jordan, Jess Kubat, Zuzana Svitek, Josh Noble, Laurie Terry, Josh Epstein, Kenton Popovich, John Kalmar, David Scott, Rikki Hinz, and Andre Gougisha for all the good times during my PhD.

I would also like to thank my family for all their support. Thank you Mom for always supporting me. Thank you Cara for staying close and for all of the experiences we shared together in the PNW during these years. And most of all, thank you to my wife Kristin for always supporting and encouraging me and for the numerous sacrifices you made to enable me to complete my PhD.

DEDICATION

This dissertation is dedicated to my father, Rick L. Stoddard. Thank you for inspiring in me a curiosity and wonder for the world around me. Thank you for being a role model and for giving me the tools to succeed. Love always, Ryan.

Chapter 1. INTRODUCTION

Rapid reduction in CO_2 emissions to meet Paris climate targets and curtail the effects of climate change requires development of cheap renewable energy generation capable of meeting global demand. Remarkably, the system costs of c-Si, the incumbent photovoltaic (PV) technology, have decreased dramatically in recent years to 2.70 $/W (residential) and 1.06 $/W (utility-scale)[1], achieving "grid parity" (i.e. where the cost of electricity from PV is less than or equal to the cost of electricity from the grid) in many states. However, solar energy still only accounts for 1.3% of U.S. utility electricity generation[2]. Part of the reason for the slow adoption of solar is the prohibitively high cost of building new photovoltaic (PV) production facilities to increase the production rate of PV modules. This up-front capitol expense, or CAPEX, is typically about $1 for every peak-watt of PV modules the factory produces per year for c-Si[3]. Typical PV factories manufacture at least 200 MWp/yr, and thus the upfront investment is typically in excess of $200M. Since the profit margin for PV manufacturing is low, this upfront investment carries substantial financial risk[3-5]. Another factor prohibiting further cost reductions in current PV is the high proportion of soft costs (all costs except module and hardware) in the final price, which accounted for 1.90 $/W for residential c-Si in 2017 (63% of the price)[1]. These soft costs include installation and permitting and are unlikely to see dramatic cost reductions in coming years. Increasing module efficiency is one viable approach to reduce these soft costs on a per watt basis and reduce the overall levelized cost of electricity (LCOE). One method to increase module efficiency is to combine absorbers with different bandgap to more efficiently manage the solar spectrum (called a "tandem" solar cell when two absorbers and two junctions are used). Indeed, Sofia e*t al.* recently compared the economics of state-of-the-art II-VI and CIGS cells in single junction, two-terminal

and four-terminal tandem configurations[6]. They found the four-terminal configuration has *the lowest LCOE* for residential installations in all climate zones considered (dry, temperate, and humid) despite having the *highest module cost per Watt*. This work demonstrates the added complexity of multijunction solar cells has economic benefit.

Beyond power conversion efficiency, another factor intimately tied to the economics of PV is reliability. First, any new PV technology must first demonstrate it is reliable in order to secure investment in production and growth (it must have "bankability"). Further, the LCOE of a particular technology can be reduced by decreasing degradation rates and extending lifetime electricity production. For example, the DOE Solar Energy Technology Office 2030 goal of 3 cents / kWhr LCOE can be met by an 25% efficient device with 0.2% year-over-year, 50 year lifetime, and $0.25 module price, yet a 25% device with 1% year-over-year degradation and 20 year lifetime cannot meet the 3 cents / kWhr LCOE even if the module is free. Thus, the practicality and economics of any PV technology is intimately tied to its reliability.

In summary, a PV technology capable of meeting the global energy demand at a competitive cost to fossil fuel alternatives should (i) be processed on equipment that doesn't require exorbitant CAPEX, (ii) have high efficiency (to offset installation and other soft costs), (iii) be composed materials with earth-abundance capable of meeting global demand, and (iv) have a reliably long module lifetime.

The hybrid perovskites (HPs) are a recently discovered material class with potential to meet the above requirements. Power conversion efficiencies (PCEs) of HP solar cells have increased faster than any other PV material in history, and HP devices do not require use of any rare or expensive elements.[7-9] Cells can be fabricated from low temperature (< 150 ˚C) solution processing, indicating that CAPEX up to an order of magnitude lower than c-Si is possible[3]. Open-

circuit voltages (V_{OC}) from completed devices of the 1.6 eV HPs have reached 92% of their detailed-balance maximum ($V_{OC,SQ}$)[9]. The limited effect of non-radiative recombination in HPs despite fabrication via solution processing have shown that energetically favored intrinsic defects do not create effective Shockley-Read-Hall recombination centers[10-12]. Either their populations are low, they have small capture cross-sections due to the large dielectric constant of HPs, or their energy levels lie close to the band edges or within the bands themselves. This "defect tolerance" in HPs has been attributed to the orbital character of the band extrema (CB minimum consisting of bonding orbitals with the VB maximum consisting of antibonding orbitals – opposite of typical semiconductors), the low charge carrier effective masses, and the high static dielectric constant[13-16].

An intriguing and exceptionally useful quality of the HP material class is its compositional variation leading to tunability of material properties. HPs have stoichiometry ABX_3, where A may be an organic or inorganic monovalent cation such as methylammonium (MA^+), formamidinium (FA^+), or cesium (Cs^+), the B site is a divalent metal cation (usually Pb^{+2} or Sn^{+2}), and X is a monovalent anion, typically I or Br. Since each lattice site can be continuously alloyed between different ions, the HP material class has an endless composition space contributing to the material versatility. For example, as the X site is alloyed from pure I^- to pure Br^- in $MAPbX_3$, the material bandgap (E_g) changes continuously from 1.6eV to 2.3eV[17]. Further, for $(FA,Cs)BI_3$, as B is changed from pure Pb^{+2} the pure Sn^{+2}, the bandgap goes through a minimum at about B = $Sn_{0.75}Pb_{0.25}$ with E_g = ~1.2 eV[18-21]. This bandgap tunability enables the realization of two-terminal tandem solar cells which have potential to better utilize the solar spectrum without adding significant additional module costs. HPs can be implemented into a tandem with a mature PV technology with ~1.1eV bandgap (such as c-Si[22] or CIGS[23]) as a runway to commercialization, or

HPs with different bandgaps can be utilized together in tandem configuration for a completely solution-processed technology with practically attainable PCE of 32%[24].

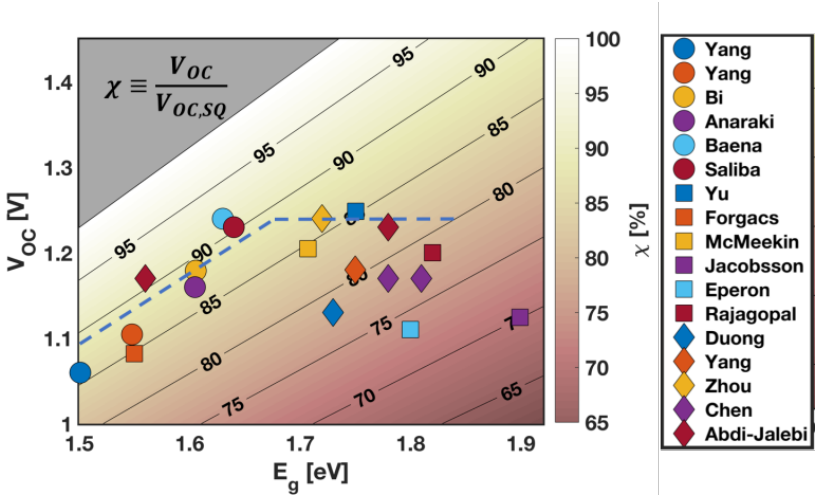

Figure 1.1. **Select literature data showing device VOC vs. Eg for many different HP devices** from Yang[25], Yang[26], Bi[27], Anaraki[4], Baena[5], Saliba[9], Yu[12], Forgacs[15], McMeekin[16], Jacobsson[21], Eperon[18], Rajagopal[19, 28], Duong[29], Yang[30], Zhou[31], Chen[32], and Abdi-Jalebi[33]. The χ value represents photovoltage as a percent of theoretical ("Shockley-Queisser") maximum. The dashed lines are to guide the reader, highlighting the VOC does not increase as expected for Eg > 1.70 eV.

Although two-terminal tandem configurations have the greatest possible economic benefit[34], the current matching constraint requires precise bandgap pairings to optimally utilize the solar spectrum, with 1.75eV and 1.82eV having ideal top-cell bandgaps for 1.10eV (c-Si) and 1.22eV (Pb-Sn HP) bottom cells respectively[19]. However, the highest $V_{OC}/V_{OC,SQ}$ reported for a HP in the 1.70-1.85eV bandgap range is ~85%[12, 28], compared to 92% for the lower bandgap HPs[9]. In other words, as the HP bandgap increases from 1.6 to 1.8 eV, the maximum reported V_{OC} remains constant at ~1.24V, suggesting there is no benefit in using a 1.75eV top cell over a thinner 1.6eV top cell. Figure 1.1 shows many reported V_{OC}'s as a function of bandgap and confirms the voltage deficit is greater for HPs above ~1.7eV[29, 35]. High-bandgap perovskites also suffer from shorter

carrier diffusion lengths than the lower E_g alternatives, which is due to shorter carrier lifetimes (faster non-radiative recombination) as well as lower carrier mobilities[36, 37].

Another concern with the high bandgap HPs is their phase instabilities upon illumination or current injection[30, 31, 38-40]. Hoke *et al.* demonstrated the I and Br ions redistribute under illumination and form a secondary phase. The photo-excited carriers transfer into the lower bandgap I-rich phase before recombining radiatively as shown by a photoluminescence (PL) peak red-shift upon continuous illumination. This phase segregation is reversible as evidenced by the PL peak position reverting to its original position after the perovskite is left in the dark. Phase segregation has been shown to have adverse effects on device performance[40], which has been associated with carrier confinement in the low bandgap phase, reducing current collection and attainable ΔE_F[40, 41]. Several groups have reported high bandgap $(FA,Cs)Pb(I,Br)_3$ HPs are phase stable and have shown stable PL emission and device power output under 1 Sun illumination for modest time periods[16, 29, 36, 37], yet the phase stability of this composition is debated and seems to depend on fabrication route[42, 43]. In addition to phase segregation exhibited by the mixed-halides, HPs have exhibited other forms of instability issues. HPs degrade upon exposure to water or in the simultaneous presence of oxygen and photoexcited or current injected carriers[32, 44-47]. HP devices have further instabilities due to reactions with metal electrodes and some carrier transport layers[22, 33, 48, 49]. Understanding the operational stability of perovskites is essential for the technology to mature, yet forecasting performance is particularly difficult since degradation modes are quite different from more mature PV technologies so industry standard tests are not sufficient to prove reliability of HP modules. To achieve the DOE SunShot goal of \$0.03 \$/kWh levelized cost of electricity by 2030, year-over-year degradation rates in operational deployment must be reduced to less than 1%[50].

This dissertation contributes to development of perovskite photovoltaics through three different thrusts: i) development of tools for rapid perovskite optoelectronic quality evaluation, ii) discovering factors limiting the optoelectronic quality of high bandgap perovskites and leveraging this insight to develop high quality high bandgap perovskite materials, and iii) identifying early signs of degradation of hybrid perovskites in order to forecast perovskite solar cell lifetime. The chapters of this dissertation are organized as follows:

Chapter 2 outlines theory and practical considerations for performing photoluminescence and photoconductivity measurements on neat perovskite films. This chapter does not present any data, but rather reads like a tutorial and is included as a reference for future researchers (particularly future Hillhouse lab students and post-docs).

Chapter 3 presents work examining the correlation between photoluminescence and carrier transport in perovskite thin films, which was published in Journal of Physical Chemistry Letters[37]. In this work, we demonstrate a simultaneous method to determine perovskite quasi-Fermi level splitting and carrier diffusion length and compare these properties to device V_{OC} and J_{SC}. This work provides a framework for much of the subsequent work involving study of perovskite quasi-Fermi level splitting and carrier diffusion length.

Chapter 4 studies the stability of high bandgap, mixed-halide perovskites and demonstrates halide phase segregation occurs under current injection. This work was published in ACS Energy Letters[51]. This work progresses the understanding of the phase segregation phenomenon and directly demonstrates the impact of phase segregation in two terminal tandem solar cell operation.

Chapter 5 addresses the voltage deficit in high bandgap perovskites and demonstrates non-radiative recombination can be suppressed by inducing lattice strain on the A-site with guanidinium alloying. This work was also published in ACS Energy Letters[52]. We demonstrate

record high bandgap device V_{OC}'s in this paper, and section 5.5 includes some unpublished work that shares a method to improve V_{OC}'s even further.

Chapter 6 shares high throughput perovskite compositional exploration and subsequent machine learning modelling of perovskite bandgap and optoelectronic quality. This work provides a proof of concept that machine learning can be used to predict perovskite properties, and it reveals some unique machine learning challenges that arise from our combinatorial library dataset.

Chapter 7 focuses on understanding the degradation trajectory in perovskite films and devices and leverages this insight to predict material lifetime using machine learning. We show that simple optical measurements of transmittance and dark field microscopy at early times in the degradation trajectory can accurately forecast a material or device lifetime. This work was published in ACS Energy Letters[53].

Collectively, the body of this work contributes to operational realization of efficient and stable perovskite devices, with a particular emphasis on high bandgap perovskites for tandem applications and understanding perovskite reliability. The work is summarized in Chapter 8 which also gives a future outlook.

Chapter 2. OPTOELECTRONIC CHARACTERIZATION OF NEAT HYBRID PEROVSKITE FILMS

Solar cell research naturally must include regular device fabrication to test hypotheses in a real power production scenario. However, device fabrication can be complex and time-consuming, and device results do not lend toward complete understanding of the underlying material level properties. In much of the following work, we employ measurements on perovskite neat absorbers outside of a device to understand the perovskite material properties and how these properties may influence device performance. Studies on neat semiconductor material properties have many benefits: i) simple measurements are amenable to high-throughput collection allowing for broad exploration, ii) direct measure of optoelectronic properties clearly shows the capabilities of a particular material without confounding information from devices, and iii) evaluation of material optoelectronic properties in coordination with device measurements can be used as a diagnostic tool to understand what is the limiting factor in devices.

Here, I discuss use of photoluminescence (PL) and photoconductivity (PC) for measurement of neat perovskite optoelectronic properties. These two measurements are informative for the device application of these semiconductors because the PL is related to the device $V_{OC,}$ and the PC is related to the carrier transport contribution to J_{SC}. This chapter is included to give relevant theory as well as practical considerations for performing these measurements of neat perovskite thin films. Some of the information is redundant with work included in certain publications[37, 52] but is organized here in a single chapter for use by future researchers who are interested in performing these measurements.

2.1 PHOTOLUMINESCENCE

Excellent PV materials will also function as excellent emitters, since the balance between unavoidable radiative recombination and undesirable non-radiative recombination will be favorable. The photoluminescence quantum yield (PLQY) encodes information about the relative rates of radiative and non-radiative recombination. The steady-state quasi-Fermi level splitting (ΔE_F), which is the difference between the steady-state non-equilibrium Fermi energy of the conduction band and of the valence band, sets the intensity of the PL and can be determined by fitting the spectral emission profile[54, 55]. A material with 100% PLQY would have precisely the radiative limit quasi-Fermi level splitting ($\Delta E_{F,rad}$), which is typically slightly reduced from the Shockley-Queisser quasi-Fermi level splitting ($\Delta E_{F,SQ}$) due to the presence of a non-abrupt absorption onset because of sub-bandgap absorption. Measuring ΔE_F on a neat film gives the maximum attainable V_{OC} for a device with that film as its active layer ($V_{OC,max} = \Delta E_F/q$). Further, comparing the measured ΔE_F to $\Delta E_{F,SQ}$ gives an easily calculated and fair metric to reveal if increases in ΔE_F are keeping up with increases in bandgap. By studying the quality of the HP layer outside of a completed device stack, we directly assess the limitations of the material itself without complicating factors such as defective interfaces or band alignment. In the following work, various methods of calculating ΔE_F from AIPL spectra are employed, the "full-peak fit", the "high energy tail", and the "PLQY" methods. These three methods are discussed below.

2.1.1 *PLQY Method*

The simplest method uses an expression proposed by Ross:[56]

$$\Delta E_F = \Delta E_{F,max} + kT \ln PLQY_{Ext} \quad (2.1)$$

where $PLQY_{Ext}$ is the external photoluminescence quantum yield. This method, which we will call the "PLQY" method, is simple and can be used to estimate quasi-Fermi level splitting if little is known about the material. One limitation is ambiguity about what is the most appropriate value for $\Delta E_{F,max}$. If little is known about the material, we can do a Shockley-Queisser calculation assuming the bandgap equals the PL peak position and replace $\Delta E_{F,max}$ with $\Delta E_{F,SQ}$. However, this can overestimate the quasi-Fermi level splitting if there is a significant portion of sub-bandgap absorption and emission. More appropriately, if $\Delta E_{F,rad}$ is determined, it can be used as the $\Delta E_{F,max}$ in eq. 2.1.

Some limitations of the PLQY method are i) the temperature is typically arbitrarily chosen (usually we use T = 320K), ii) if $\Delta E_{F,SQ}$ is used for $\Delta E_{F,max}$, then this method will overestimate the ΔE_F since losses from sub-bandgap absorptivity are not taken into account, and iii) calculation of $\Delta E_{F,SQ}$ requires accurate knowledge of bandgap, which is not always available, and use of PL peak position as the bandgap can give additional error.

2.1.2 *High Energy Tail Fit Method*

Alternatively, the "high energy tail fit" method fits the high energy tail of the PL peak to the generalized plank law. Rearranging the plank law and employing the Wein approximation yields

$$\ln\left[\frac{I_{PL}(E)h^3c^2}{2\pi E^2}\right] = -\frac{1}{kT}E + \frac{\Delta E_F}{kT} \tag{2.2}$$

which can be fit with a line when the photoluminescence is plot on a log-scale. This method improves upon the simple PLQY method since it does not rely upon an assumed value for T or for $\Delta E_{F,max}$. Although this is a relatively simple method, the fit temperature (and thus ΔE_F) is dependent on precisely which energy window is used for the linear fit suggesting there is not

necessarily a unique T-ΔE_F combination that gives the best fit. Thus, in practice I find myself using the PLQY method and/or the full peak fit method but rarely the high energy tail method.

2.1.3 *Full Peak Fit Method*

The third method used to calculate ΔE_F is the "full peak fit" method which follows the procedure of Katahara and Hillhouse[54]. We use a modified Lasher-Stern-Würfel equation[57, 58] given by

$$I_{PL}(E) = \frac{2\pi E^2}{h^3 c^2} \cdot \frac{a(E, \Delta E_F, T)}{\exp\left(\frac{E - \Delta E_F}{kT}\right) - 1} \tag{2.3}$$

where the absorption coefficient is modeled by

$$\alpha(E) = \frac{\alpha_0}{\gamma 2\Gamma(1 + 1/\theta)} \int_{-\infty}^{E_g} \left(\exp\left(-\left|\frac{u}{\gamma}\right|^{\theta} \right) \sqrt{(E - E_g) - u} \right) du \tag{2.4}$$

where Γ is the gamma function, γ is an energy broadening parameter for sub-bandgap absorption, θ is an exponent to describe the form of the sub-bandgap tail, and E_g is the direct transition energy[54]. The full form of eq. 2.3 used in this study is given as equation 22 in Katahara and Hillhouse[54], which accounts for non-zero band occupation in the absorption model. The modified absorption coefficient, which incorporates occupation effects (assuming symmetric splitting of quasi-Fermi levels from mid gap) is given by

$$\alpha(E, \Delta E_F) = \alpha_{0K}(E) \left(1 - \frac{2}{e^{\frac{E - \Delta E_F}{2kT}} + 1} \right) \tag{2.5}$$

where $\alpha_{0K}(E)$ is the absorption coefficient model at zero band occupation (given by eq. 2.4). Note that the full peak fit requires a single photoluminescence peak.

The full peak fit gives us a model for sub-bandgap absorption that describes measured data. Thus, we can use this absorption model to determine the radiative limit quasi-Fermi level splitting,

$\Delta E_{F,rad}$, which is typically lower than the Shockley-Queisser limit due to the presence of sub-bandgap absorption and emission. $\Delta E_{F,rad}$ is calculated numerically with an internal balance equation (Generation = Recombination) where the only recombination considered is radiative. This balance can be expressed as

$$G(E_g, \theta, \gamma, \Delta E_F) = \int_0^\infty I_{PL}(E)dE \tag{2.6}$$

where $I_{PL}(E)dE$ is given by equations 2.3-2.5 and the generation flux G is given by

$$G(E_g\theta, \gamma, \Delta E_F) = \int_0^\infty b_{AM1.5GT}(E)\left(1 - \exp\left(-d\alpha(E, E_g, \theta, \gamma, \Delta E_F)\right)\right)dE \tag{2.7}$$

where d is film thickness and $b_{AM1.5GT}(E)$ is the AM1.5GT spectral photon flux. We use the sub-bandgap absorption model described in eq. 2.4-2.5 in the expression for absorptivity, accounting for occupation effects.

The full peak fit method is the most accurate and justifiable method for determining the ΔE_F since it determines the temperature through fit to experimental data and accounts for losses due to sub bandgap absorption. Additionally, the full peak fit gives quantitative information about the nature of sub-bandgap states and provides a method to determine $\Delta E_{F,rad}$. However, the full peak fit is also the most complex method so some care needs to be employed in fitting spectra (typically it is poor practice to fit a large number of spectra without manually observing the quality of the fit). Additionally, the PL data needs to have good signal to noise for a meaningful full peak fit. Some practical considerations for the full peak fit are listed below.

2.1.4 *Practical Consideration for Full Peak Fit*

A few practical considerations should be followed for most accurate and reproducible full peak fit results. First, the $\alpha_0 d$ parameter should be set rather than fit, fitting the $\alpha_0 d$ can lead to unstable fit results (fitted parameter values that depend strongly on the initial guesses). The $\alpha_0 d$ can be fit

from literature or by using measuring UVvis absorption and profilometry on your film to determine an appropriate value. Second, the fitting range should be chosen carefully. Typically, the fitting range should be the entire range of the spectra where there is signal above some noise threshold (typically I use 10 cts/sec). That means I cut off the edges of the spectra that fall below 10 cts/sec. However, a subset of this range should be used to exclude low-energy tail data if it is clear there are deviations from the LSWK model at low energies. See Figure 5.8 for an example of a perovskite film that has a sub-bandgap absorption behavior that follows $\theta = 1.5$ near the bandedge and $\theta = 1.0$ far below the bandgap. If this behavior is observed, excluding this region will give better estimates of the fit parameters (although the fit will then slightly underestimate ΔE_F). Finally, I recommend fitting the log-transform of the PL spectra rather than the PL spectra in normal units. Without a log-transform, the high energy and low energy tail regions will have minimal impact on the total fit which can lead to large errors fitting these regions. Python code for performing the full peak fitting is in my "PVtools" Github repository.

2.1.5 *Absolute Intensity Wide-field PL*

The confocal PL instrument is calibrated to absolute emitted photon flux units using a blackbody calibration (see Ian Braly's dissertation[59] for the most detailed account). However, the wide-field instrument does not provide spectral information, so such a calibration is not possible. Our strategy is to use an indirect calibration by comparison to the confocal PL emitted flux. First, take several samples (with various PLQY) and measure with both wide-field PL and confocal PL (ensure the region of interest is the same and there are many spectra collected across the region of interest to ensure good statistics). Then prepare a "calibration curve" (should be a straight line) comparing the counts/sec from the wide-field camera to the PLQY from the confocal instrument. Some important considerations: i) ensure the spectral emission is similar for the test samples and

the calibration samples, since the responsivity of wide-field optical path depends strongly on emission energy, and ii) ensure that the background counts are subtracted from wide-field data. The camera defines as 100 counts for 1x1 binning and 1600 counts for 4x4 binning, the curve will have significant error in 4x4 binning case if this is not considered.

2.2 PHOTOCONDUCTIVITY

PL allows for quantification of ΔE_F, which is the maximum V_{OC} that can be attained with a device made with the same material. However, as I discuss in detail in Chapter 3, high ΔE_F is necessary but not sufficient for a good PV material – a perfect PV material will also have excellent transport. The J_{SC} of a solar cell will depend on i) the total absorbed photon flux, ii) presence or lack of energy barriers to carrier extraction in electron or hole selective contacts, and iii) ability for charge carriers to move through the absorber through a combination of drift and diffusion. Clearly, even with an absorber with excellent properties, some device engineering is essential to deal with factors i) and ii) and enable high J_{SC}. However, an absorber with poor carrier transport through the film will have limiting J_{SC} due to iii), which is particularly important in HP devices where built in fields are largely screened out due to ion migration[60]. Thus, we developed a simple photoconductivity measurement as a method to assess diffusion in perovskite films.

The PC measurement provides a relative measure of carrier transport in semiconductor thin films. Through the theory below, we show photoconductivity can be transformed to quantify a "mean carrier diffusion length" in perovskites, which can be used to rapidly assess transport in perovskite films.

2.2.1 *Theory*

To assess the carrier transport properties we measure the lateral DC photoconductivity:

$$\sigma_{ph} = \sigma_l - \sigma_d \quad (2.8)$$

in a four-point probe geometry. Here, σ_l is the conductivity under illumination and σ_d is the conductivity in the dark. At steady state under constant illumination with a known photon flux from a calibrated LED source, the average volumetric photogeneration rate G (cm^{-3} s^{-1}) in an optically thick film is approximated by dividing the incident photon flux by the film thickness. For cases where the carrier diffusion length is close to or greater than the film's thickness (such as the case here), the effective non-equilibrium excess carrier concentration is approximated by $p_{eff} = G\tau_h$ for holes and $n_{eff} = G\tau_e$ for electrons, where τ_h is the free hole and τ_e is the free electron lifetime. Here, the free carrier lifetime is the average time a photoexcited charge carrier is free to move spatially before it recombines[61]. The relation between photoconductivity and mobility-lifetime product of the charge carriers is given by[61]:

$$\sigma_{ph} = q(\mu_h p_{eff} + \mu_e n_{eff}) = qG(\mu_h \tau_h + \mu_e \tau_e). \quad (2.9)$$

Here, q is the elementary charge, μ_h is the hole mobility, and μ_e the electron mobility. Noting that the diffusion coefficients and diffusion lengths for holes and electrons are $D_h = kT\mu_h/q$, $D_e = kT\mu_e/q$, $L_h = \sqrt{D_h\tau_h}$, and $L_e = \sqrt{D_e\tau_e}$, respectively, where k is the Boltzmann constant and T is the absolute temperature. We multiply both sides of eq. 2.9 by $kT/2q^2G$ and then take the square root:

$$\sqrt{\frac{\sigma_{ph}kT}{2q^2G}} = \sqrt{\frac{1}{2}({L_h}^2 + {L_e}^2)}. \quad (2.10)$$

We note that the right-hand side is simply the root mean square of the electron and hole diffusion lengths. Importantly though, the left-hand side is easily calculated from a known photogeneration rate and measured photoconductivity. We define this mean diffusion length as $L_D \equiv \sqrt{\sigma_{ph}kT/2q^2G}$.

This photoconductivity measurement may be carried out concurrently with time-dependent measurement of absolute-intensity PL using a calibrated wide-field PL microscope with low magnification lens to provide illumination over the entire device and collect the PL. Hence, one gets information about photoexcited carrier transport and the steady-state radiative efficiency (and thus the quasi-Fermi level splitting, ΔE_F), simultaneously. We note, however, the information contained in L_D does not reveal the individual diffusion lengths of electrons and holes. In the most general case individual diffusion lengths of electrons and holes may differ significantly since each may have different free lifetimes due to defects with different capture cross-sections for the two carrier types. Here, L_D measurements provide a simple method to detect relative changes in diffusive transport properties in an HP film. Several examples showing comparison between film L_D and device J_{SC} are presented in Chapter 3.

2.2.2 *PC Measurements using Lock-in Technique*

In early work, we used a 4-point probe geometry to assess photoconductivity and measure L_D[37]. Eventually, we moved to a 2-point geometry since we found good agreement between the 4-point and 2-point geometry indicating that there was ohmic contact between Au contacts and HP film, and the 2-point geometry is able to detect weaker photoconductivity signals[62]. More recently, we have needed to detect very small photoconductivity signals with high background signal for measuring a small region of interest along a composition gradient, which motivated development of a modified photoconductivity method that includes lock-in amplification of the photoconductivity signal. This method allows for accurate quantification down to very low signals. A schematic of the updated method is shown in Figure 2.1.

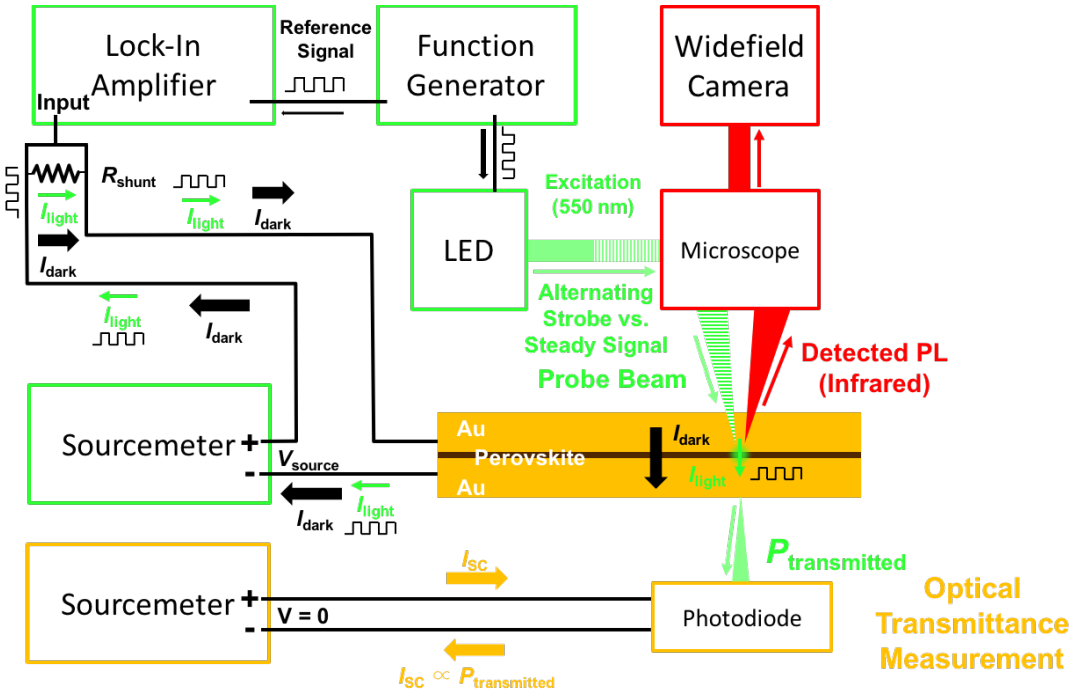

Figure 2.1. **Schematic of photoconductivity measurement including lock-in amplification and simultaneous wide-field photoluminescence and transmissivity**

The basic principle behind the lock-in measurement is that the excitation light source is modulated at a high frequency which creates an AC photoconductivity signal. This AC signal is detected by a lock-in amplifier which rejects all DC background. This is extraordinarily useful – we have successfully used this method to detect smaller photoconductivity signals as well as photoconductivity signals with long channel geometries (for gradients) with a high background noise. The pulsed excitation source is attained using a waveform generator connected to Lumencor LED (no mechanical chopper is needed). All the instrument control for Keithley 2400 source measurement unit, SRS810 lock-in amplifier, Agilent waveform generator, and Lumencor LED is performed with Python's pymeasure; all codes can be found in my "hpdb" Github repository.

2.2.3 *Practical Considerations for PC Measurements*

Best practices for accurate and reproducible PC measurements should adhere to these practical considerations. First, note the temperature effects will influence the photoconductivity; care should be taken to control temperature, minimize radiative heating, or at the very least, ensure all samples have the same measurement protocol and heating profile. When moving to a new material system, start with a 4-point measurement voltage–current sweep and compare results to a 2-point measurement before adopting the 2-point measurement. Note the channel width and film thickness will impact the absolute values of the photoconductivity. For channel width, a channel width larger than the quenching length should be used. As the channel width decreases to within a length where PL is noticeably quenched by the proximity of the contacts then the measured L_D will be lower than the true L_D. Understanding the thickness dependence is more difficult – the assumptions in the above L_D definition require that the film thickness is less than or equal to L_D. If this is not true, relative trends will hold, yet the measured L_D will again be an underestimation of the true L_D (since carrier density diminishes through the depth of the film). Interpretation of L_D vs. film thickness is not necessarily straightforward since altering thickness is usually accomplished by modulating solution concentration, which can have other effects on crystallization and defect density (not to mention thinner films will have less absorption and higher steady-state carrier density). Note for lock-in measurements, care must be taken to choose the shunt resistor resistance – higher resistance will give better signal to noise, yet resistance must remain less than 10% of the total resistance in the circuit (including the sample). The sensitivity and time constant values for lock-in should also be chosen appropriately.

Chapter 3. CORRELATION BETWEEN PHOTOLUMINESCENCE AND CARRIER TRANSPORT IN PEROVSKITES

This chapter describes a photoconductivity technique to extract carrier diffusion length and shows the importance of quantifying transport in HPs in three important example cases (degradation, phase segregation, and passivation). This chapter was published in Journal of Physical Chemistry Letters[37] and awarded ACS Editors' Choice. Reproduced with permission[37];

3.1 ABSTRACT

High bandgap mixed-halide hybrid perovskites have higher open-circuit voltage deficits and lower carrier diffusion lengths than their lower-bandgap counterparts. We have developed a Ligand-Assisted Crystallization (LAC) technique that introduces additives in-situ during the solvent wash and developed a new method to dynamically measure the absolute-intensity steady-state photoluminescence and the mean carrier diffusion length simultaneously. The measurements reveal four distinct regimes of material changes and show that photoluminescence brightening often coincides with losses in carrier transport, such as in degradation or phase segregation. Further, the measurements enabled optimization of LAC on 1.75 eV bandgap $FA_{0.83}Cs_{0.17}Pb(I_{0.66}Br_{0.34})$, resulting in an enhancement of photoluminescence quantum yield (PLQY) of over an order-of-magnitude, an increase of 80 meV in the quasi-Fermi Level splitting (to 1.29 eV), an increase in diffusion length by a factor of 3.5 (to over 1 μm), and enhanced open-circuit voltage and short-circuit current from photovoltaics fabricated from the LAC treated films.

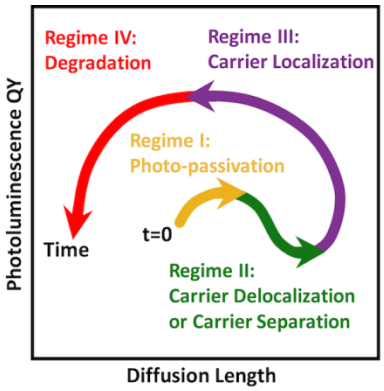

Figure 3.1. **Correlation Between Photoluminescence and Carrier Transport in Perovskites**

3.2 INTRODUCTION

Hybrid Perovskites (HPs) with composition ABX_3 have emerged as a candidate to increase solar energy market penetration due to their low cost, earth abundance, and unprecedented power conversion efficiency (PCE) improvement to over 22% in just 6 years[9]. HPs can be solution processed at low temperature and exhibit defect tolerance, which allows remarkable optoelectronic properties; open-circuit voltage (V_{OC}) has reached 92% of the theoretical limit[9], and photoluminescence quantum yield has surpassed 30%[63]. Another attractive feature of HPs is the easily tunable bandgap with composition, making them ideal candidates for tandem solar cells and LEDs[17]. The high-bandgap perovskites best suited for the top cell of a two-terminal tandem with CIGS, c-Si, or a 1.2 eV Pb-Sn HP[18] typically contain about 40% Br and have a bandgap of 1.75-1.80 eV. However, high-bandgap mixed-halide perovskites do not have as high of defect tolerance as their 1.6 eV-bandgap predecessors; they have a greater voltage deficit[16, 17, 41, 64], exhibit carrier diffusion lengths too low for optically thick, current-matched devices[16, 18], and can undergo phase segregation into I-rich and Br-rich domains under illumination[35, 38, 41, 42, 65-67]. Indeed, the best two-terminal Si-HP tandems to date have employed a 1.6 eV top cell[22, 68, 69], which is not optimally current-matched and has lower theoretical maximum efficiency than a tandem with a 1.75-1.8eV

HP top cell[70-72]. Recently, phase segregation has been reduced by manipulating composition[16, 29, 36, 40, 73-76] and morphology[77, 78]. One strategy uses a double-cation FA/Cs composition (FA = formamidinium) with about 15% Cs, which stabilizes the mixed-halide perovskite while avoiding the photo-inactive delta-phase that appears in pure $FAPb(I,Br)_3$[16]. Nonetheless, the best V_{OC} attained with a 1.75 eV perovskite is 1.24 V, precisely the same as the highest V_{OC} of a lower-bandgap perovskite[9], implying there is no voltage benefit when increasing the bandgap from 1.63 to 1.75 eV.

Here, we report the development and use of a new and simple treatment in which Lewis bases are incorporated into a solvent and applied to the nascent hybrid perovskite film during spin-coating (after spinning the hybrid perovskite ink) to induce rapid crystallization and simultaneously passivate grain-boundaries. This ligand-assisted crystallization (LAC) reduces the voltage deficit and improves carrier diffusion length in the high bandgap $FACsPb(I,Br)_3$ perovskite. The LAC method has several advantages over existing passivation strategies, which typically either add the passivation agent in a post-deposition step[63, 79] or in the perovskite ink itself[80, 81]. By using the solvent wash solution as a carrier for passivating ligands, we uniquely incorporate passivation agent at the precise instant crystallization occurs, allowing for ligand coordination at grain boundaries through the depth of the film. Further, adding ligands into the solvent wash solution (rather than the perovskite ink itself) is a versatile technique, as it allows for utilization of materials that would significantly alter perovskite ink chemistry, perhaps even crashing out perovskite precursors. To understand the overall impact of LAC, we develop a measurement technique to quantify both photoluminescence quantum yield (PLQY) and photoexcited mean carrier diffusion length. The experiments reveal several scenarios where the

PLQY and mean carrier diffusion length are anticorrelated, which should be considered when characterizing film quality with PL.

Understanding non-radiative recombination in mixed-halide HPs is essential for reducing the voltage deficit (i.e. increasing the open circuit voltage) and improving performance of HP-based tandems. Radiative band-band recombination of photoexcited carriers is unavoidable when carriers are co-located in the material, and efforts are generally made to maximize it during PV material development since increased radiative recombination (and thus PLQY) signify increased non-equilibrium carrier concentrations and a decrease in other avoidable non-recombination mechanism. Non-radiative recombination can be reduced by decreasing the concentration of deep-level defects or reducing their efficacy in a Shockley-Read-Hall mechanism (by either reducing their carrier capture cross-section, shifting the defect's energy level closer to the band edges, or creating internal electric fields that push electrons or holes away from the region of the defect, such as the field at a material junction). While shallow-level defects do not play a significant direct role in recombination since, once trapped, the electron (hole) is thermally emitted back into the conduction band (valence band) much faster than it recombines with a hole (electron), they may play an indirect role via their effect on mobility. Absolute intensity photoluminescence (AIPL) may be used to determine the quasi-Fermi level splitting (ΔE_F)[41, 54] and thus quantify the relative rates of radiative and non-radiative recombination at steady-state under 1 Sun equivalent illumination (the conditions identical to those in which solar cells operate). Under steady-state illumination, ΔE_F is the free energy per electron-hole pair delivered to a load[82]. The ΔE_F calculated from PL is the maximum attainable V_{OC} (V_{OC}^{max}) for a device with that absorber (see Supporting Information for calculation details). Further, the ratio $\chi \equiv V_{OC}^{max}/V_{OC,SQ}$, where $V_{OC,SQ}$ is the detailed balance limit V_{OC}, represents one component of material optoelectronic quality which can

be compared for materials of different bandgap. Thus, one advantage of AIPL is the ability to probe the inherent absorber material quality χ without the additional processing steps needed for completed devices, which introduce variability and defects. In HPs, photoluminescence has been used to study the effects of composition[41], defect passivation[63, 79], and atmospheric exposure[83, 84] on optoelectronic quality.

However, studying photoluminescence alone to characterize overall optoelectronic quality has some potential pitfalls as alone it does not provide information on carrier transport, which may affect the recombination process by localizing carriers. Imagine the limiting case of a film of nanocrystals with passive surfaces but that are spaced apart such that there is no overlap between the carrier wavefunctions in adjacent nanocrystals[85, 86]. The film may emit with high PLQY but have no ability to transport charge carriers to the contacts. While photobrightening has been observed in perovskites under several situations including low-light exposure (trap filling)[87], treatment with Lewis bases (defect passivation)[63, 79] or during aging in air[83, 84], it is unclear if the PL enhancement is due to a reduction or passivation of non-radiative recombination centers in the bulk or due to spatial confinement of carriers. Quantifying carrier transport by measuring the *effective* diffusion length simultaneously with photoluminescence would reveal the coupling (or lack thereof) between transport and recombination and provide a clearer understanding of the optoelectronic properties of hybrid perovskites along with a means to assess material stability and defect passivation efforts. Several methods have been employed to measure the diffusion lengths in nearly-intrinsic semiconductors like HPs including the steady-state photocarrier grating technique[88-91], terahertz spectroscopy[36, 88, 91-93]. Here, we choose a photoconductivity based method since it can be easily coupled with absolute-intensity PL measurements.

To assess the carrier transport properties in this work we measure the lateral DC photoconductivity:

$$\sigma_{ph} = \sigma_l - \sigma_d \tag{3.1}$$

in a four-point probe geometry as shown in Figure 3.2.

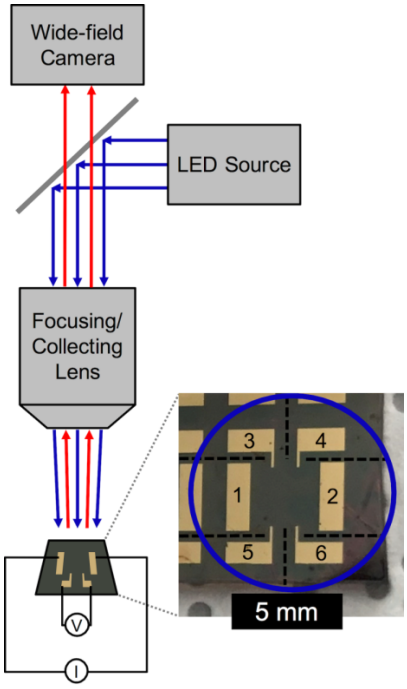

Figure 3.2. **Experimental setup to simultaneously measure PLQY and mean carrier diffusion length** using calibrated LED excitation, quantitative wide-field photoluminescence, and 4-point photoconductivity. Blue circle indicates illuminated area (excitation with blue LED). Dashed lines indicate scribe lines to avoid parasitic current pathways. Current is sourced along Au contact pads 1 and 2, and voltage is measured with inner probes (between 3 and 4 or 5 and 6).

Here, σ_l is the conductivity under illumination and σ_d is the conductivity in the dark. At steady state under constant illumination with a known photon flux from a calibrated LED source, the average volumetric photogeneration rate G (cm^{-3} s^{-1}) in an optically thick film is approximated by dividing the incident photon flux by the film thickness. For cases where the carrier diffusion length is close to or greater than the film's thickness (such as the case here), the effective non-equilibrium excess carrier concentration is approximated by $p_{eff} = G\tau_h$ for holes and $n_{eff} = G\tau_e$ for

electrons, where τ_h is the free hole and τ_e is the free electron lifetime. Here, the free carrier lifetime is the average time a photoexcited charge carrier is free to move spatially before it recombines[61]. The relation between photoconductivity and mobility-lifetime product of the charge carriers is given by[61]:

$$\sigma_{ph} = q(\mu_h p_{eff} + \mu_e n_{eff}) = qG(\mu_h \tau_h + \mu_e \tau_e). \quad (3.2)$$

Here, q is the elementary charge, μ_h is the hole mobility, and μ_e is the electron mobility. Noting that the diffusion coefficients and diffusion lengths for holes and electrons are $D_h = kT\mu_h/q$, $D_e = kT\mu_e/q$, $L_h = \sqrt{D_h\tau_h}$, and $L_e = \sqrt{D_e\tau_e}$, respectively, where k is the Boltzmann constant and T the absolute temperature. We multiply both sides of eq. 3.2 by $kT/2q^2G$ then take the square root:

$$\sqrt{\frac{\sigma_{ph}kT}{2q^2G}} = \sqrt{\frac{1}{2}({L_h}^2 + {L_e}^2)}. \quad (3.3)$$

We note that the right-hand side simply is the root mean square of the electron and hole diffusion lengths. Importantly though, the left-hand side is easily calculated from a known photogeneration rate and measured photoconductivity. We define this mean diffusion length as $L_D \equiv \sqrt{\sigma_{ph}kT/2q^2G}$.

This photoconductivity measurement may be carried out concurrently with time-dependent measurement of absolute-intensity PL using a calibrated wide-field PL microscope with low magnification lens to provide illumination over the entire device and collect the PL. Hence, one gets information about photoexcited carrier transport and the steady-state radiative efficiency (and thus the quasi-Fermi level splitting, ΔE_F), simultaneously. We note, however, the information contained in L_D does not reveal the individual diffusion lengths of electrons and

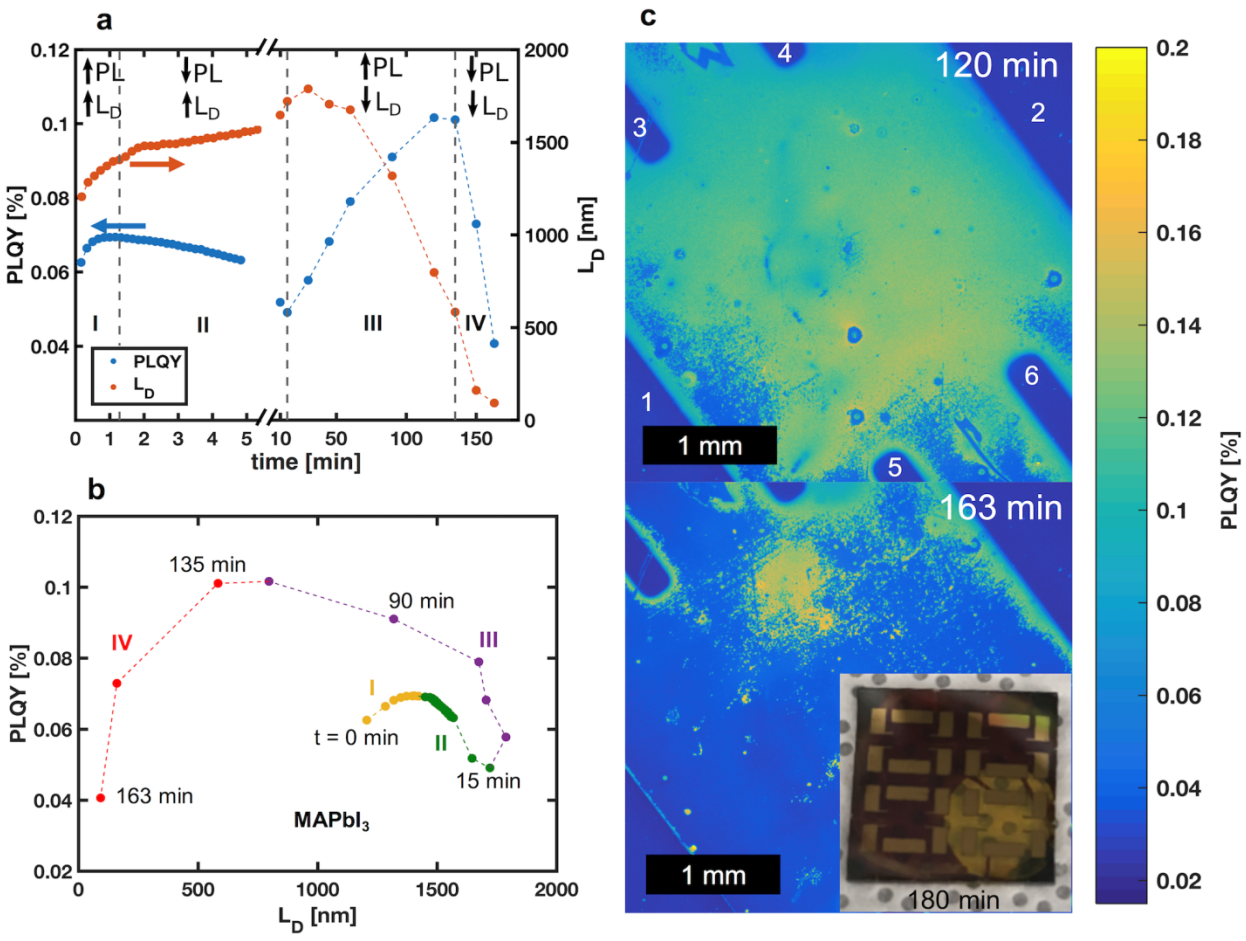

Figure 3.3. **Correlation between photoluminescence quantum yield and mean carrier diffusion length** as a function of time for $MAPbI_3$ degradation in air (35% RH) under steady 1 Sun illumination. (a) The PLQY and L_D plotted each with time for 1.61 eV bandgap $MAPbI_3$ at effective 1 Sun illumination with a calibrated blue LED. Ideal stable behavior would appear as straight horizontal lines. However, several distinct regimes of change and correlation are observed (I, II, III, and IV). Note region III where significant photobrightening is observed simultaneously with loss of diffusion length. (b) Same data as in part (a) but plotted together (PLQY vs. L_D) parametrically with time. Ideal stable behavior would be a stationary point. (c) Wide-field PL images at 120 min and 163 min during the $MAPbI_3$ degradation. Au contacts are labeled in 120 min PL image (compare with Figure 3.2). (c, inset) Photo of $MAPbI_3$ film after exposure to air and 1 Sun excitation for three hours.

holes. In the most general case individual diffusion lengths of electrons and holes may differ significantly since each may have different free lifetimes due to defects with different capture cross-sections for the two carrier types. Here, L_D measurements provide a simple method to detect

relative changes in diffusive transport properties in an HP film. Further, we compare changes in L_D with changes in J_{SC} (measured on solar cells fabricated from the films) to reveal the relevance of detected L_D changes to device performance.

3.3 Results and Discussion

To understand the connection between carrier transport and PLQY in HPs, we investigated two scenarios using our technique: degradation of $MAPbI_3$ in air and light-induced phase segregation in the mixed-halide $MAPb(I_{0.66}Br_{0.34})_3$ (in dry N_2). Figure 3.3 shows PLQY and L_D measurements of a $MAPbI_3$ film during exposure to air (~35% RH) and 1 Sun illumination. PLQY is calculated as the emitted PL photon flux from a 2.1 mm^2 area divided by the incident excitation photon flux, where PL photon flux is measured in a calibrated wide-field PL instrument (as described in methods). This film undergoes irreversible degradation to methyl amine and HI vapor, which is accelerated by the presence of light and humidity, ultimately leaving behind a Pb/PbI_2 mixture[44, 45]. During this degradation, we see distinct regimes of changing PLQY and L_D trends with time as highlighted in Figure 3.3a-b. Two example wide-field PL images showing spatial distribution of PLQY are presented in Figure 3.3c, with a photo of the film after three hours of light exposure shown as an inset (yellow PbI_2 degradation product is observed where the film was illuminated).

To understand the changes in PLQY and L_D that occur, we consider the radiative recombination rate[94] $U_{rad} = B_{rad}(np - n_i^2)$, where B_{rad} is the carrier concentration independent bimolecular radiative recombination coefficient, n and p are total electron and hole densities, and n_i is the intrinsic carrier density. Under constant excitation and temperature, an increase in radiative recombination rate indicates higher *np at the same material location* (and thus higher local quasi-Fermi level splitting and higher PLQY), which can be observed in at least two cases: (1) a decrease

in the Shockley-Read-Hall recombination rate with higher effective carrier lifetimes or (2) carrier localization into small domains resulting in higher *np*. For case 1, PLQY and L_D will increase (as shown in Figure 3.3 during regime I). Case 2 may result when regions of the film degrade to PbI_2. PbI_2, which has a bandgap of 2.3 eV, will still absorb photons with energy >2.3eV (including the 2.83 eV blue light used in this study), and the photoexcited excited carriers may transfer (without an energy barrier) into small persistent perovskite domains with locally lower bandgap, resulting in much higher local *np* than in a homogenous perovskite film. The film inhomogeneity and carrier localization in smaller perovskite domains with passive surfaces/grain boundaries could result in a decrease in L_D and a simultaneous increase in PLQY, as observed in regime III (Figure 3.3a-b). Macroscopic inhomogeneity is particularly obvious in wide-field PL images at 120 and 163 minutes (see Figure 3.3c), which shows regions of weak PL, where complete conversion to PbI_2 has likely occurred, mixed with regions of bright PL where small, separated $MAPbI_3$ domains exist within PbI_2 regions. We note photobrightening in HPs has been attributed elsewhere to photopassivation of defects[83, 84]. However, without accompanying measurement of the diffusion length, such photobrightening could be regime I or regime III. In regime IV, the overall or average PLQY begins to decrease as the remaining small perovskite domains ultimately degrade to PbI_2. Regime II (decreasing PLQY with increasing L_D) is intriguing. It could be due to continued photopassivation (or trap-filing) of shallow defects (increasing the mobility) coinciding with formation of deep defects from onset of degradation (decreasing the PLQY). Alternatively, the decrease in PLQY could signify the appearance of passive grain boundaries that have an associated electric field. The electric field would serve to enhance carrier separation. So long as the grain boundaries are passive and have not yet percolated to isolate perovskite domains, they may not negatively affect the diffusion length which may be continuing to increase.

Having established the utility of combined transport and PL measurements on the standard $MAPbI_3$ films, we investigate the PL-L_D interdependence during phase segregation in mixed-halide perovskites. This phenomenon inhibits realization of stable perovskites with bandgap 1.7-1.85eV, and thus has been widely studied[38, 42, 65] given its relevance to tandem solar cells with Si or CIGS. In some compositions with Br content between 20% and 80% of total halide composition, the mixed-halide phase is not stable under 1 Sun illumination[38]. Under illumination, the halide ions migrate and reorder in two separate phases, an I-rich phase and Br-rich phase[65]. The I-rich phase dominates PL spectrum due to its lower bandgap, which results in an observed PL peak red-shift[38]. We investigate PL and L_D during phase segregation of the mixed-halide $MAPb(I_{0.66}Br_{0.34})_3$ (denoted subsequently $MAPb(I,Br)_3$) as shown in Figure 3.4. This experiment was conducted in N_2 to isolate phase segregation from known degradation processes, in contrast to the $MAPbI_3$ experiment (Figure 3.3) which was conducted in air to study degradation. Figure 3.4a shows PLQY (from wide-field PL) and L_D evolution with time over 5 minutes. PL is increasing by an order of magnitude while L_D is decreasing by a factor of 2, which is similar behavior as $MAPbI_3$ degradation in regime III (Figure 3.3a). Figure 3.4b shows confocal PL peak red-shift with time, indicating this film is indeed phase segregating. In this case we also have separated domains forming, not due to irreversible degradation to PbI_2, but rather to formation of local I-rich domains with lower bandgap resulting in carrier accumulation and higher local *np*[65]. Collectively, the PL-L_D results for $MAPbI_3$ degradation and the $MAPb(I,Br)_3$ phase segregation indicate an analogous phenomenon, where a PL increase is coupled with a L_D decrease upon carrier localization in small domains. We conclude that using

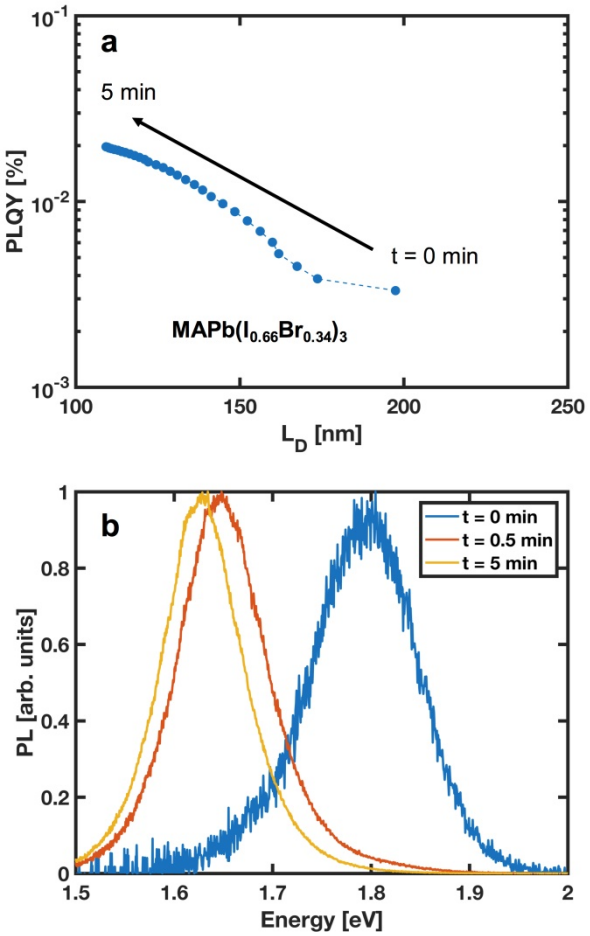

Figure 3.4. **Correlation of PLQY and L_D during phase segregation of $MAPb(I_{0.66}Br_{0.34})_3$ in dry nitrogen**. (a) PLQY (spatially averaged from wide-field PL) and L_D over 5 minutes for the higher bandgap (1.79 eV) $MAPb(I,Br)_3$ with 1 Sun blue LED exposure in N_2. (b) Normalized confocal PL; the peak red-shift from 1.8 to ~1.6eV is characteristic of a mixed-halide material phase segregating into I-rich and Br-rich domains.

PL alone to probe non-radiative recombination is not sufficient when material degradation or phase-segregation occurs, as photobrightening can falsely suggest defect passivation when in fact the material quality for photovoltaic applications is deteriorating. Thus, assessment of defect passivation techniques should include transport measurements in addition to PL.

Having shown the importance of transport measurements in understanding PL results, we use wide-field PL and photoconductivity combined to investigate ligand-assisted crystallization on high-bandgap perovskite films. Surface passivation techniques using Lewis bases such as pyridine

and trioctylphosphine oxide (TOPO) have a beneficial effect on perovskite PL and carrier lifetimes for $MAPbI_3$ by donating electron density to under-coordinated Pb on surfaces[63, 79]. The effect of using surface passivation to reduce the voltage deficit and improve L_D for high bandgap HPs such as $FACsPb(I,Br)_3$ remains unexplored. We focus this study on the $FA_{0.83}Cs_{0.17}Pb(I_{0.66}Br_{0.34})_3$ material, which has an ideal bandgap for the top-cell in a tandem with c-Si or CIGS and has been shown to be phase stable at 1 Sun[16, 36]. Our method builds on the "solvent wash" technique[95], which employs DMSO as a co-solvent to control perovskite crystallization through formation of a perovskite-DMSO complex, then removes DMSO with a perovskite antisolvent such as toluene. We find that employing the solvent wash method to fabricate $FACsPb(I,Br)_3$ yields smooth films (root mean square roughness <5nm) with reproducible phase stability at 1 Sun for 5 min (see Figure 3.11).

Here, we show that incorporation of a Lewis base in the solvent during the solvent wash affects the crystallization process in-situ and results in surface and grain-boundary passivation. For the ligand-assisted crystallization (LAC) experiments, we incorporate Lewis base molecules in a toluene solution to dispense during solvent wash rather than depositing a Lewis base layer in a post-deposition step. We suspect LAC allows Lewis base molecules to accumulate at grain boundaries through the depth of the film and allows higher yield of Pb-Lewis base coordination due to the presence of passivating agent during perovskite crystallization and anneal. Figure 3.5 presents measured PL and L_D with illumination time on films with solvent wash passivation using triethylamine (TEA) and trioctylphosphine oxide (TOPO). PLQY and L_D evolution over 5 minutes of 1 Sun light exposure is shown with arrows. For both TEA and TOPO incorporation, PLQY and L_D increase with increased Lewis base concentration in solvent wash. For untreated films, both L_D and PLQY decrease with time then stabilize, suggesting that light induces bulk

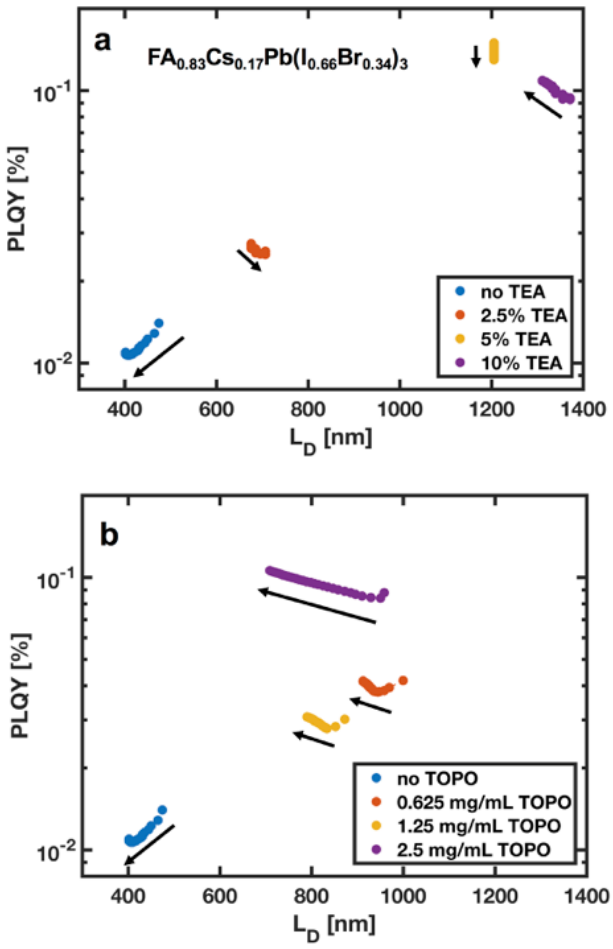

Figure 3.5. **PLQY and calculated L_D with time over 5 minutes of 1 Sun blue LED exposure in N_2 for $FACsPb(I,Br)_3$ films** (bandgap = 1.75 eV) with solvent wash passivation using TEA (a) or TOPO (b). Arrows indicate direction of changing PLQY and L_D from t = 0 min to t = 5 min.

defects in this material that are not directly connected to phase segregation (see Figure 3.11 which shows no red-shift in the PL peak). LAC with TEA enhances PLQY by over an order of magnitude and L_D by a factor of 3.5, as well as reduces the temporal light-induced effects on both PL and L_D. However, the TEA treatment also changed the film morphology and increased the surface roughness. TOPO shows a similar effect on PL and L_D as TEA without changing film morphology, except for the highest TOPO concentration (2.5 mg/mL TOPO case). At this concentration, PL continues to increase with time while L_D decreases rather than stabilizing. The behavior is due to deteriorated morphology (see Figure 3.9) caused by the high TOPO concentration, which results

in carrier localization in small domains with continued light exposure, resulting in loss of transport. This result reemphasizes the importance of transport measurements; without detecting the decrease in transport it could be falsely concluded that 2.5 mg/mL TOPO dosing (or even higher) was optimal for passivating defects despite the adverse effects on morphology and transport. The film with 2.5 vol% TEA LAC exhibits a slight increase in L_D upon illumination, contrasting each other measurement, suggesting TEA and other small amines are excellent molecules for improving diffusion length in HPs if the surface roughness increase can be mitigated. All $FACsPb(I,Br)_3$ (treated and untreated) films are phase-stable as shown by a single, stable PL peak energy with illumination (see Figure 3.11). Photoluminescence and photoconductivity measurements where conducted in N_2 as described in SI.

As discussed previously, L_D as obtained from photoconductivity is a mean carrier diffusion length (and does not provide information about the individual electron and hole diffusions lengths), and thus one needs to measure the short-circuit current to verify its impact on carrier collection. Further, comparing ΔE_F (calculated from PL) with device V_{OC} indicates the origin of voltage loss in $FACsPb(I,Br)_3$ devices. We fabricated devices with TOPO solvent wash only since films with TEA solvent wash had higher surface roughness than untreated films. Figure 3.6 shows device statistics, champion J-V curves, maximum power point stability, and device architecture. TOPO solvent washing gives a modest V_{OC} enhancement, a significant J_{SC} enhancement along with FF reduction, resulting in an overall PCE enhancement. The V_{OC} increase demonstrates that solvent washing with TOPO passivates defects as predicted by higher calculated ΔE_F from PL data. The increased current indicates that an L_D increase from 400nm to 850nm results in better carrier collection in a $FACsPb(I,Br)_3$ device with ~315nm HP layer. The reduction in FF is likely caused

by a voltage dependent photocurrent that results from an interface barrier which might be improved with future optimization.

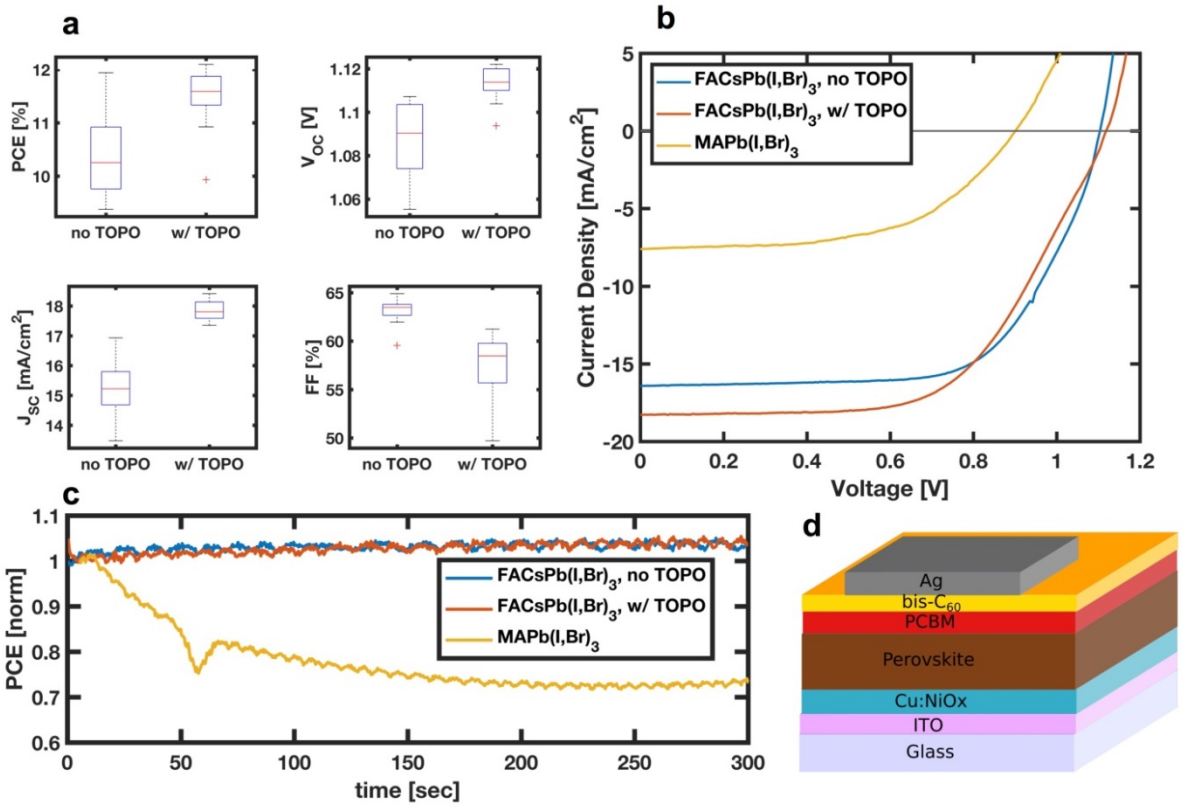

Figure 3.6. **Device data for FACsPb(I,Br)$_3$ devices with and without TOPO solvent wash** with 1.25mg/mL in toluene. (a) Device statistics. (b) Champion J-V curves. (c) Stabilized power output with time under inert atmosphere conditions; FACsPb(I,Br)$_3$ devices give stable output while MAPb(I,Br)$_3$ devices have a decreasing PCE due to phase segregation. (d) Device architecture.

To further confirm that current collection is limited by carrier diffusion length in untreated FACsPb(I,Br)$_3$ devices, we investigated the thickness dependence on device performance (see Figure 3.12). As expected, the J_{SC} decreases by ~16% when increasing the HP layer thickness from ~300nm to ~450nm. These data suggest improving current collection in FACsPb(I,Br)$_3$ devices should address carrier diffusion (not absorption), which we accomplish with TOPO treatment and enhancing L_D. The maximum power point data in Figure 3.6c indicate the FACsPb(I,Br)$_3$ with and

without TOPO solvent wash has stable power output at ~5% above initial value. Interestingly, the power output with time for $FACsPb(I,Br)_3$ devices show a different trend than the L_D data presented in from Figure 3.5; power output increases by ~5% while L_D decreases by 15% for untreated and 10% for TOPO treated case. The slight increase in power output with time is a device effect observed elsewhere for devices with a similar architecture with various HP compostions[23, 96], and it is likely due to trap filling at interfaces or in a transport layer by photoexcited carriers. The small decrease of <15% in L_D in the $FACsPb(I,Br)_3$ layers with time when L_D is already longer than the film thickness has an insignificant effect compared to the time-dependent changes in interfaces present in the devices. In contrast to $FACsPb(I,Br)_3$, $MAPb(I,Br)_3$ devices prepared with a similar procedure do not give stable power output (as expected from L_D decrease from ~200nm to ~100nm in five minutes), emphasizing the importance of addressing phase segregation for stable devices. Power output with time measurements were conducted in an N_2-filled glovebox.

By compiling PL and device data of various films, we reveal the origin of voltage losses in $FACsPb(I,Br)_3$, which is outlined in Figure 3.7. $V_{OC,SQ}$ is the detailed balance limit at 1 Sun, which is 1.46 V for a material with 1.75eV bandgap. It assumes a step function absorption at the bandgap, while real materials exhibit an absorption onset curve much different than a step function. Thus, real materials will have a radiative limit voltage ($V_{OC,rad}$) that is reduced from $V_{OC,SQ}$ due to sub-bandgap absorption. For $FACsPb(I,Br)_3$, we calculated a $V_{OC,rad}$ of 1.43 from electroluminescence (EL) data following the method of Rau[97, 98] (analysis provided in SI). The voltage loss from a real absorption edge is ~30mV in $FACsPb(I,Br)_3$, which is larger than for $MAPbI_3$. In each case, non-radiative recombination plays a significant role, yet in the best case (with TEA treatment), passivation recovers one third of the voltage deficit measured in the untreated film, resulting in attained ΔE_F of 1.29 eV compared to untreated ΔE_F of 1.21 eV.

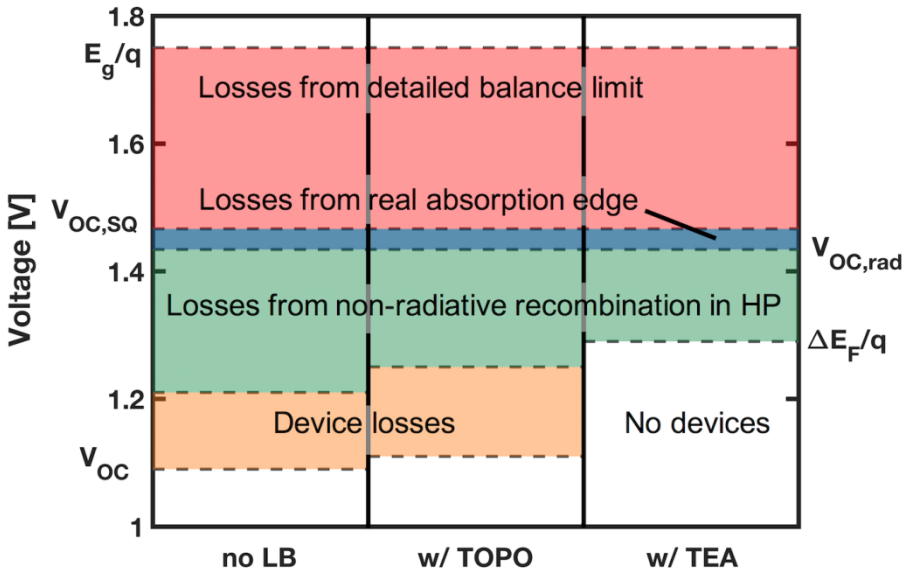

Figure 3.7. **V_{OC} and ΔE_F data for FACsPb(I,Br)$_3$ devices and films with and without Lewis base solvent wash**. $V_{OC,SQ}$ is the detailed balance limit assuming a step function absorption edge for a 1.75 eV bandgap material. $V_{OC,rad}$ is the radiative limit calculated from EL data following the work of Yao et. al (discussed in detail in SI and shown in Figure 3.13). ΔE_F is calculated from wide-field PLQY data using optical bandgap extracted from UV-vis absorbance measurements (Figure 3.10). E_g denotes bandgap.

Since PL spectra for each film are very similar (see Figure 3.13b), we expect $V_{OC,rad}$ differences between these cases to be <5meV. Thus, assumed $V_{OC,rad}$ was equal for each of the three films, since we were unable to fabricate efficient devices and conduct EL experiments with TEA treated film due to surface roughness. Our devices have open-circuit voltages that are reduced from ΔE_F by an additional ~100 mV. The difference between film ΔE_F and device V_{OC} is partly due to interface defects, which is denoted with the yellow region in Figure 3.7. However, ΔE_F data indicate that voltages above 1.2 V are possible for FACsPb(I,Br)$_3$ using surface passivation. Still, it seems there are persistent defects present in FACsPb(I,Br)$_3$ that remain unaffected by surface passivation, in contrast to $MAPbI_3$ where TOPO passivation can enhance PLQY to > 30%[63], indicating ΔE_F much closer to the radiative limit than passivated high bandgap perovskites. Future

efforts to maximize device V_{OC} for tandem-relevant compositions should include both surface passivation as well as efforts to understand and limit formation of bulk defects persistent in the mixed-halide system.

In conclusion, our study of $MAPbI_3$ degradation and $MAPb(I,Br)_3$ phase segregation highlights cases in perovskite films where PL and transport are anti-correlated due to spatial carrier confinement in small domains. These results emphasize the importance of including transport measurements in assessing optoelectronic quality of perovskite films. We also confirm other findings that $FACsPb(I,Br)_3$ materials are phase stable under 1 sun illumination. Further, we show that a simple technique combining absolute intensity photoluminescence to determine PLQY (and quasi-Fermi level splitting) with a photoconductivity measurement to extract the mean carrier diffusion length can be used to assess overall optoelectronic quality. Although the mean carrier diffusion length does not give us direct information about the electron and hole carrier diffusion lengths independently, we show in $FACsPb(I,Br)_3$ that it is correlated with device current. Through simultaneous study of PLQY and mean carrier diffusion length, we optimize a novel Lewis base surface passivation technique to realize quasi-Fermi level splitting improvement from 1.21 to 1.29 eV and mean carrier diffusion length enhancement from 400 to 1400 nm. Devices fabricated with TOPO solvent wash exhibit improved V_{OC} of 20 mV and a remarkable J_{SC} improvement of about 15% to 18.4mA/cm^2, approaching the detailed balance limit current density (for 1.75eV bandgap, $J_{SC,SQ}$ = 20.5 mA/cm^2). The higher mean carrier diffusion length of TOPO treated films will be even more beneficial in semi-transparent devices due to the requirement of thicker films (no benefit from Ag reflection). The quasi-Fermi level splitting results indicate a roadmap for improving the V_{OC} of a phase-stable 1.75eV mixed-halide perovskite beyond 1.2 V, enabling highly efficient cost-competitive two-terminal tandem solar cells.

Methods

Materials Fabrication and Characterization

All films were prepared on pre-cleaned glass substrates which were further cleaned with four 10-minute sonication steps with 5% Alconox in deionized (DI) water, pure DI water, acetone, and 2-propanol, followed with plasma cleaning in Ar plasma for 10 minutes. $MAPbI_3$ films were deposited from a 1.0 M solution in 7/3 vol/vol gamma–butyl lactone (GBL)/dimethylsulfoxide (DMSO). Solution was heated to 70 ˚C then stirred for 90 min then filtered after cooling down with a 0.2 μm PTFE filter. Films were spin coated with a 3-step program: 5 s at 500 rpm, then 60 s at 1000 rpm, then 45 s at 5000 rpm. 700 μL toluene was dispensed on the spinning substrate with 18 s left in the final step. $MAPbI_3$ films were annealed for 10 minutes at 100 ˚C. $FA_{0.83}Cs_{0.17}Pb(I_{0.66}Br_{0.34})_3$ and $MAPb(I_{0.66}Br_{0.34})_3$ films where prepared with a 1.0 M solution in 8/2 vol/vol dimethylformamide (DMF)/DMSO solution, heated/stirred/filtered with the same procedure as $MAPbI_3$ inks. These films were spin coated with a 2-step program: 5 s at 1000 rpm then 20 s at 5000 rpm. 700 μL toluene or toluene + Lewis base solution was dispensed on the spinning substrate with 15 s remaining in the final step. $FA_{0.83}Cs_{0.17}Pb(I_{0.66}Br_{0.34})_3$ films were annealed at 150 ˚C for 50 min and $MAPb(I_{0.66}Br_{0.34})_3$ films were annealed at 100 ˚C for 10 min. All ink mixing, spin coating, and annealing steps were performed in a N_2-filled glovebox.

Absolute intensity confocal PL was conducted in similar procedure as described previously[41]. PL spectra were obtained with a modified Horiba LabRAM HR-800 with 532nm laser excitation and 10x objective. The adjustable confocal hole was set to 800 μm and a 150 gr/mm Czerny-Turner monochromater blazed at 500 nm was used. The photon detection rate was calibrated using a blackbody source (IR-301, Infrared Systems Development) at 850, 950, and 1050 ˚C with 10 μm pinhole (calibration factor was averaged between three temperatures to minimize error). To

calculate 1 Sun excitation flux, an Oriel optical power meter and beam profiler was used to set photon flux equal to above-bandgap photon flux of AM1.5 GT solar spectrum for a 1.75 eV material. All confocal PL experiments were conducted in N_2 filled KF-flange with borosilicate glass window.

Wide-field absolute intensity PL measurements were conducted with a Hamamatsu C11440 camera with Lumencor SpectraX light source and 5x objective. A blue LED was used for excitation, which was filtered with a 29-nm wide bandpass filter centered at 438 nm. The excitation source was passed through a filter cube with dichroic mirror, and emission longpass filter to achieve minimum OD 8 suppression for excitation wavelengths. Excitation photon flux was calibrated with a Newport 91150V Si reference diode to set photon flux equal to above bandgap photon flux for a 1.75eV material under AM1.5 GT spectrum. The Hamamatsu detector was calibrated by preparing a $MAPbI_3$ standard and comparing PL detector counts with PLQY from confocal AIPL setup (which was calibrated using blackbody spectrum at three temperatures). The $MAPbI_3$ standards were measured in N_2 and statistics from >100 measurements were collected for each sample. $MAPbI_3$ calibration measurements were conducted in immediate succession with light exposure reduced to < 1.5 s for both confocal and wide-field measurements.

For photoconductivity measurements, 80nm of Au were evaporated at 2 Å/s in the 4-point geometry shown in Figure 3.2. Current was sourced across pads 1 and 2 while voltage was measured across pads 3 and 4 or 5 and 6 using a Keithley 2400 SourceMeter. For this study, applied current was 1-10 nA and electric field magnitude across the channel was < 10 V/mm. We conducted control experiments to check the impact of this small electric field and did not detect any changes in PL for a sample with this small current applied vs. a sample without any current applied, suggesting the photoconductivity measurement itself does not induce changes in the

perovskite film. Wide-field and photoconductivity measurements were conducted in a closed, N_2-filled stage (Linkam Scientific LTSE420-P) with continuous N_2 purge at 70% of maximum flow, with the stage temperature regulated to 20 ˚C.

Absorbance data were collected with a PerkinElmer Lambda 1050 UV/vis/NIR spectrometer with a 150 mm InGaAs integrating sphere in air. SEM micrographs were collected using an FEI XL830 Dualbeam SEM-FIB on Au-sputtered perovskite films.

Device Fabrication and Testing

ITO glass (15 ohm/sq, Colorado Concept Coatings) was cleaned with sonication and Ar plasma as described previously. Cu:NiOx solution was prepared for the conventional sol-gel method as described elsewhere[99] with 5 mol% Cu to Ni. Cu:NiOx layer was fabricated by spin coating at 3000 rpm for 60 s then annealing at 350 ˚C for 60 min in air. Next, films were transferred into a N_2-filled glovebox for perovskite layer deposition as described previously. PCBM (15 mg/mL in chlorobenzene) was spin coated at 1000 rpm for 60 s then bis-C_{60} (2mg/mL in 2-propanol) was spin coated at 3000 rpm for 30 s. Finally, 150 nm Ag was thermally evaporated at a rate of 2 Å/s.

J-V measurements were conducted in air using a Keithley 2400 SourceMeter Newport Oriel Sol3a Class AAA Solar Simulator calibrated to 1 Sun AM1.5 GT using Newport 91150V Si reference diode. J-V curves and statistics in Figure 3.6 were collected with a reverse voltage sweep at a slow sweep rate of 75 mV/s. Device area was 3.14 mm^2 as defined by Ag contact area (valid due to high resistance in all HP/ETL/HTL layers). Maximum power point data was collected in a N_2-filled glovebox with 450 W Oriel xenon lamp calibrated to AM1.5 GT.

Electroluminescence data was collected with the same set up as confocal PL (Horiba Labram with 150 gr/mm grating blazed at 500nm), but using current injection with Keithley 2400 rather than 532nm photoexcitation. EL experiments were also conducted in N_2-filled Linkam stage with

constant N_2 purge and temperature regulated to 20 ˚C. External quantum efficiency was measured using a chopped monochromatic light beam with calibrated Si photodiode as reference.

ACKNOWLEDGEMENTS. We acknowledge financial support from the U.S. Department of Energy Sunshot Initiative, Next Generation Photovoltaics 3 program, and Award DE-EE0006710. This material is based in part on work supported by the State of Washington through the University of Washington Clean Energy Institute and via funding from the Washington Research Foundation.

SUPPORTING INFORMATION. Photoconductivity measurements of films at various light intensities, SEM images, UV-vis absorbance data, film thickness, Absolute-intensity confocal photoluminescence data, dependence of J_{SC} on thickness, discussion of $V_{OC,rad}$ calculations, and quasi-Fermi level splitting calculations.

3.4 SUPPORTING INFORMATION

Comparison of L_D to published minority carrier diffusion length values

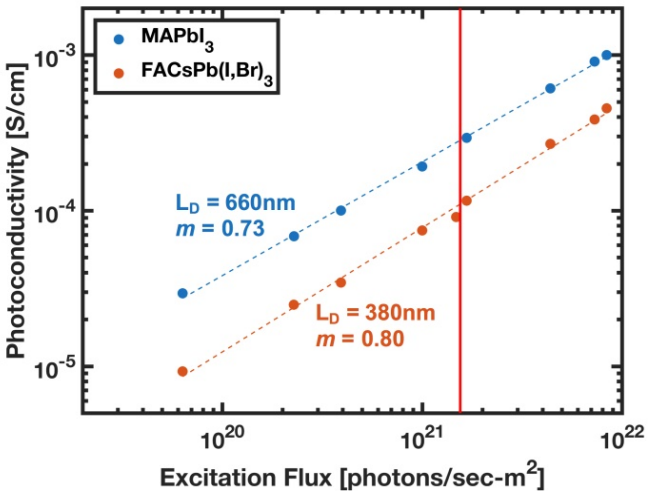

Figure 3.8. **Measured photoconductivity as a function of excitation flux** for $MAPbI_3$ (Eg = 1.6 eV) and $(FA_{0.83}Cs_{0.17})Pb(I_{0.66}Br_{0.34})_3$ (Eg = 1.75 eV, denoted subsequently $FACsPb(IBr)_3$). Vertical line indicates 1 Sun excitation flux for a material with 1.6 eV bandgap. Dashed lines indicate linear fit of log-log plot, with calculate slope m.

Our photoconductivity data on $MAPbI_3$ and $FA_{0.83}Cs_{0.17}Pb(I_{0.66}Br_{0.34})_3$ films are presented in Figure 3.8 with L_D at 1 Sun calculated from equation 3.1 and fitted slope *m* (FACs composition denoted subsequently $FACsPb(I,Br)_3$; this composition has optical bandgap of 1.75eV as shown in Figure 3.10). Our $MAPbI_3$ films have comparable L_D to the films studied in Levine *et. al* as well as $MAPbI_3$ characterized in other studies[88, 89, 92, 93, 100], and *m* is 0.73 rather than 0.5, indicating different recombination dynamics that do not follow the Rose model suggested by Levine *et. al*[89]. This slope does not indicate whether the dominant recombination mechanism is monomolecular or bimolecular as suggested elsewhere[100]. As explained in detail by Levine *et. al*, the interpretation of *m* is not unique[89]. Although $m = 0.5$ could indicate bimolecular recombination as described by Chen *et. al*[100], it could also indicate monomolecular trapping in a recombination center a few kT away from the Fermi level[89].

Material Characterization (SEM, UV-vis)

Scanning electron microscope (SEM) images of films discussed in the main text are presented in Figure 3.9. Trioctylphosphine oxide (TOPO) solvent wash has little effect on morphology until the highest concentration (2.5 mg/mL) where the treatment deteriorates morphology as seen by charging in Figure 3.9f.

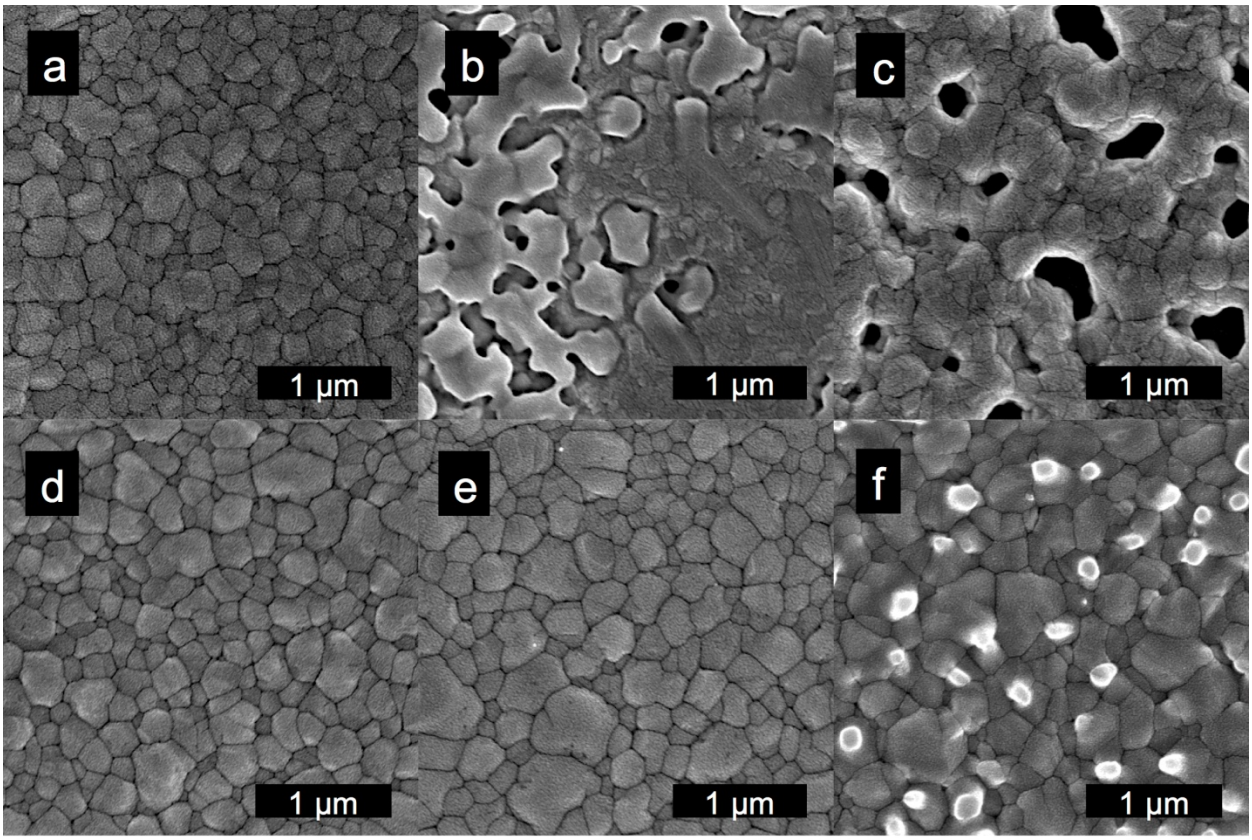

Figure 3.9. **SEM**. (a) FACsPb(I,Br) (b) MAPb(I,Br) (c) FACs w/ 5% TEA (d) FACs w/ 0.625 mg/mL TOPO, (e) FACs w/ 1.25 mg/mL TOPO, and (f) FACs w/ 2.5 mg/mL TOPO

UV-vis absorbance data are presented in Figure 3.10. All compositions have 34% Br/(I + Br) in the ink. Optical bandgap is extracted by fitting the linear region of A^2 vs. energy plot. $FA_{0.83}Cs_{0.17}Pb(I_{0.66}Br_{0.34})$ has a bandgap of 1.75 eV while $MAPb(I_{0.66}Br_{0.34})$ has a bandgap of 1.79 eV. TOPO and TEA treatment have a minimal effect on bandgap, yet TEA treatment reduces the sharpness of absorption edge.

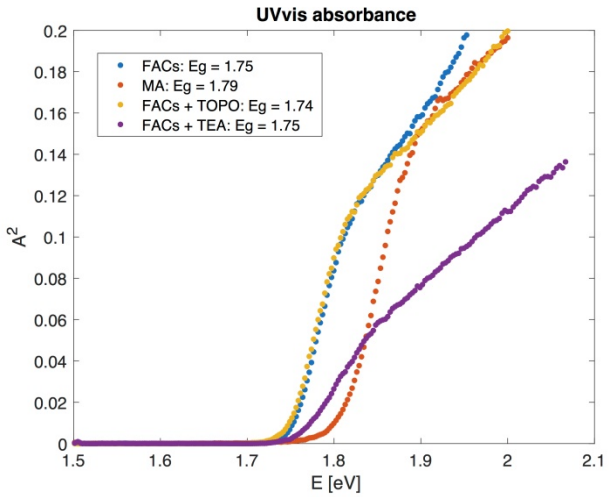

Figure 3.10**. UV-vis absorbance data**; plotted A^2 vs. Energy to extract bandgap for these direct bandgap materials.

Table 3.1 **Film Thicknesses (from Profilometry)**

	Thickness [nm]
$FACsPb(I,Br)_3$	315 ± 10
$FACsPb(I,Br)_3$ + TOPO	317 ± 14
$FACsPb(I,Br)_3$ + TEA	338 ± 14

Confocal photoluminescence results of $FACsPb(I,Br)_3$ films are presented in Figure 3.11. Figure 3.11a-b show example PL peaks for untreated $FACsPb(I,Br)_3$ films, normalized (a) and absolute intensity PL (b). The normalized peaks demonstrate the peak position and peak shape do not change in 5 minutes of 1 Sun laser illumination. The AIPL data demonstrates the PL peak magnitude is decreasing with time. We note the PLQY decrease observed with confocal PL (with 1 Sun laser illumination) is much greater than the PLQY decrease observed with wide-field PL (with 1 Sun LED illumination). We suspect this is due to additional defects created with a small laser illumination diameter of 12 μm, inducing lateral ion migration, and we suggest the PLQY vs.

time data from LED illumination (with large LED illumination area) is more relevant to device implementation. Mean PL energy is a metric that clearly shows peak shifts occur due to phase segregation as shown elsewhere[36]. Figure 3.11b-c show mean PL peak energy for FACs films with TOPO and TEA treatment. In each case, there is no change in mean PL peak energy with 5 minutes 1 Sun illumination, demonstrating these films are phase-stable at 1 Sun. This contrasts with the $MAPb(I,Br)_3$ films, which show a mean PL energy shift from 1.8 to ~1.6 eV (see Figure 3.4 in main text). For the TOPO treated films, increased TOPO concentration in the solvent wash red-shifts the starting PL peak by < 10 meV (as shown in Figure 3.11c), yet the mean PL energy is still stable with time upon illumination.

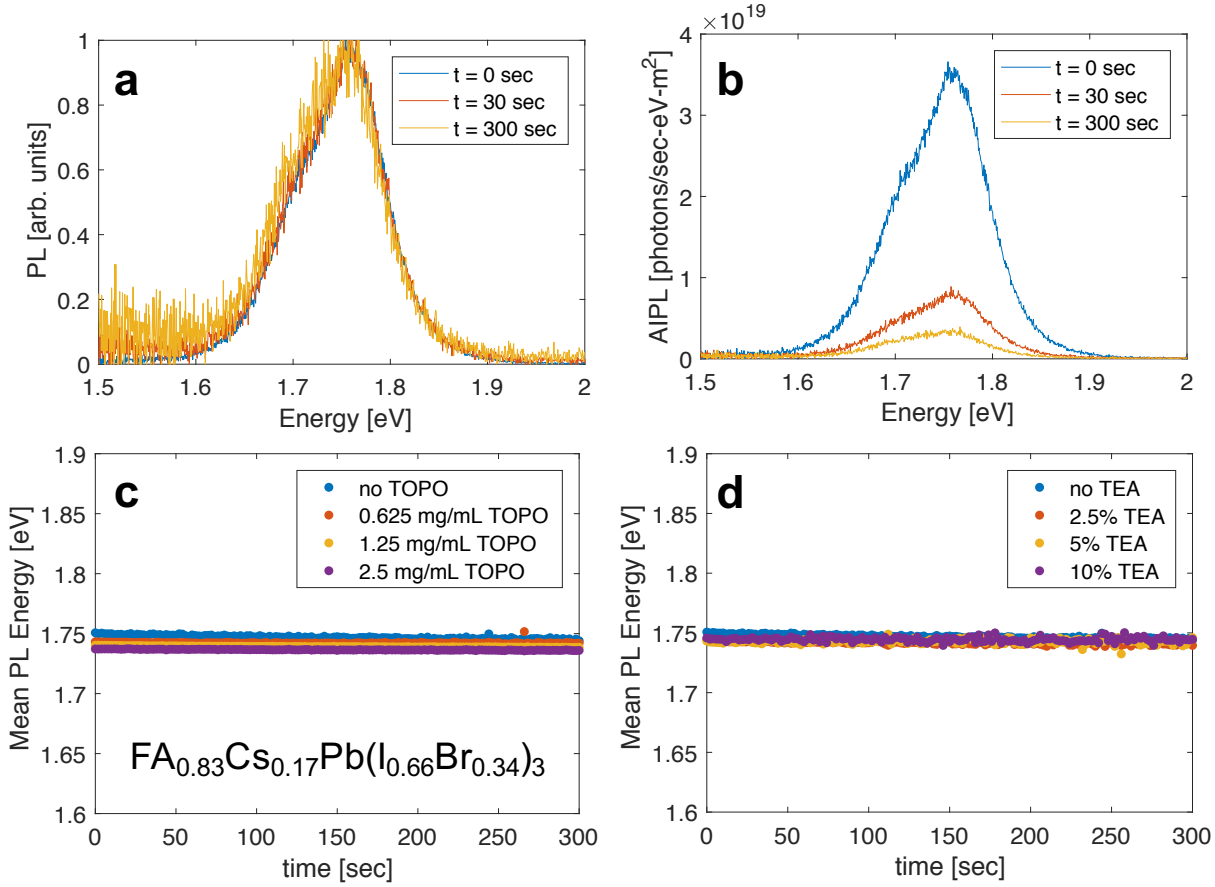

Figure 3.11**. Confocal PL data at 1 Sun photon flux with 532 nm cw laser excitation**. (a-b) PL spectra for $FACsPb(I,Br)_3$ without Lewis base in the solvent wash; normalized PL (a) and AIPL (b). (c-d) mean PL energy with time for TOPO (c) and TEA (d) treated films. In each case, the peak position is stable, indicating these materials are phase stable at 1 Sun excitation.

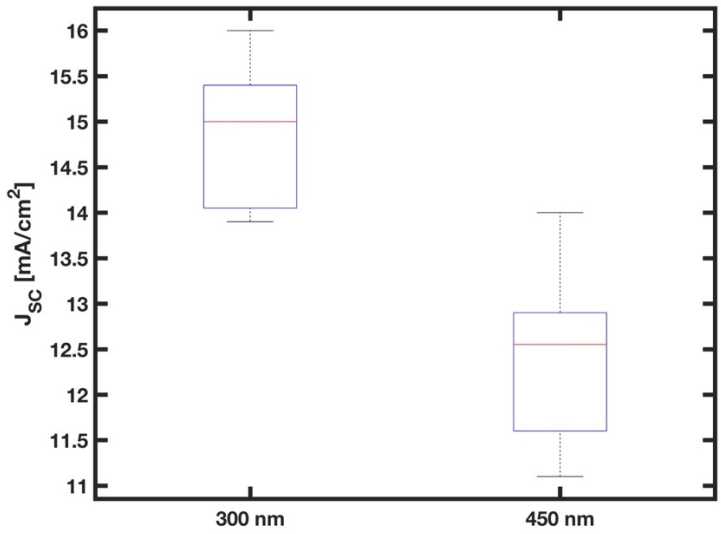

Figure 3.12**. Perovskite layer thickness dependence of J_{SC} for FACsPb(I,Br)$_3$ devices**. Devices with 450 nm thick films were fabricated as described previously, yet from 1.4M precursor ink instead of 1.0M. J_{SC} decreases with increased HP layer thickness, supporting our hypothesis that carrier diffusion length is limiting current collection in untreated FACsPB(I,Br)$_3$ devices. Note this device study also used a different anneal condition than in Figure 3.6 (100 ˚C for 10 min instead of 150 ˚C for 50 min), yet the median J_{SC} for 1.0M ink in this batch (15.0 mA/cm^2) is very similar to the median J_{SC} for the untreated devices shown in Figure 3.6 (15.2 mA/cm^2).

Radiative Limit V_{OC} calculation

We conducted electroluminescence (EL) experiments to calculate $V_{OC,rad}$, the radiative limit open-circuit voltage for $FA_{0.83}Cs_{0.17}Pb(I_{0.66}Br_{0.34})$. We followed the procedure by Yao *et. al* which we will describe briefly here[98]. At open-circuit conditions with only radiative recombination

$$V_{OC,rad} = \frac{kT}{q}\ln\left(\frac{J_{ph}(V_{OC,rad})}{J_{0,rad}} + 1\right). \quad (3.4)$$

where $J_{ph}(V_{OC,rad})$ is the photocurrent density at open-circuit in radiative limit, and $J_{0,rad}$ is the radiative limit of the saturation current density. We assume superposition is valid and replace $J_{ph}(V_{OC,rad})$ by J_{SC}. We must calculate $J_{0,rad}$, which is related to the total emitted photon flux at zero applied bias. Calculation of $J_{0,rad}$ requires a calibrated EL external quantum efficiency (EQE_{EL}). One method to obtain a calibrated EQE_{EL} is to convert EL spectrum into absolute photon flux, which is challenging due to a device area larger than the objective lens field of view. Instead, following Yao *et. al* and other work, we use device EQE (EQE_{Jsc}) to calibrate EQE_{EL} taking advantage of detailed balance arguments[98]. We equate EQE_{Jsc} to EQE_{EL}, which is simply $I_{EL}(E)/\phi_{BB}(E)$ where the spectral blackbody emission can be calculated with $\phi_{BB}(E) = \frac{2\pi E^2}{h^3c^2}\frac{1}{\exp(E/kT)-1}$ with T = 300 K. We use blackbody calibration measurements employed in absolute intensity PL experiments to apply spectral correction to the emitted EL flux, I_{EL}, then use EQE_{Jsc} to convert EQE_{EL} in arbitrary units to absolute EQE. Then we calculate the radiative limit saturation current with

$$J_{0,rad} = \int_0^\infty EQE_{EL}(E)\phi_{BB}(E)dE \quad (3.5)$$

Finally, $V_{OC,rad}$ can be calculated using eq. 3.4 with $J_{0,rad}$ from eq. 3.5 and device J_{SC}, again assuming T = 300 K.

Data employing this calculation in $FA_{0.83}Cs_{0.17}Pb(I_{0.66}Br_{0.34})$ devices (without Lewis base treatment) are shown in Figure 3.12a. EL flux is directly measured with spectral shape correction but arbitrary units; this curve is directly proportional to a photon flux curve. EQE_{EL} is calculated from EL shape and using EQE_{Jsc} to determine magnitude; device EQE_{Jsc} is shown for reference. We note this $V_{OC,rad}$ calculation was only conducted for untreated devices since surface roughness prohibited fabrication of efficient TEA-treated devices. Due to similar PL spectra, we expect films with ligand-assisted crystallization to have similar $V_{OC,rad}$ (see Figure 3.12b). TOPO treated devices may have a slightly lower $V_{OC,rad}$ (~5 mV) due to slightly red-shifted PL peak.

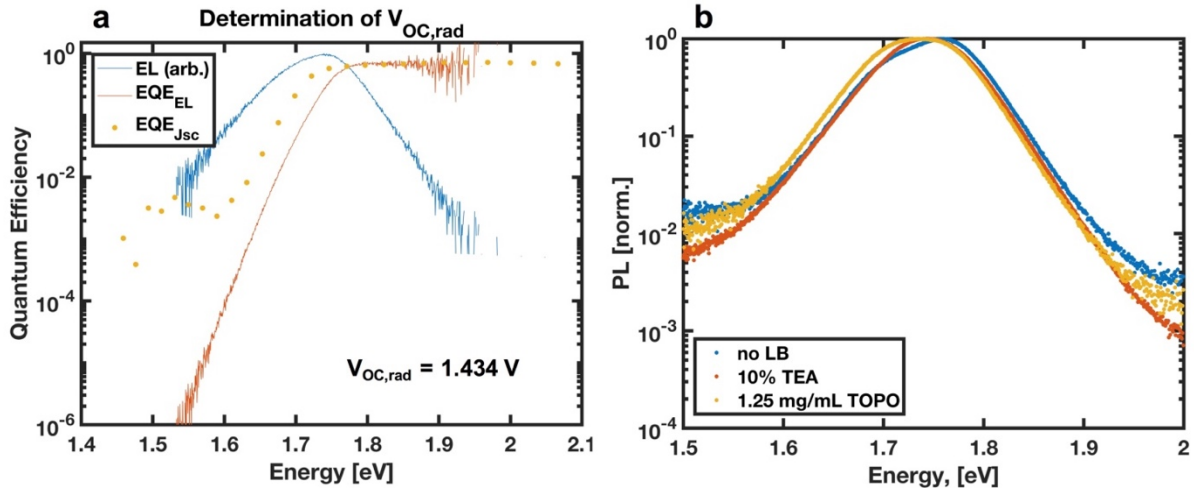

Figure 3.13**.** (a) **Determination of $V_{OC,rad}$ of $FA_{0.83}Cs_{0.17}Pb(I_{0.66}Br_{0.34})_3$** following analysis of Yao et. al. EQE_{EL} is calculated from EL data using, then calibrated using the device EQE_{Jsc} data. $V_{OC,rad}$ is calculated from calibrated EQE_{EL} data using equation 3.4. This value is a representation of the radiative voltage limit for a material with real (non-step function) absorption edge. (b) Photoluminescence peaks for $FA_{0.83}Cs_{0.17}Pb(I_{0.66}Br_{0.34})_3$ with and without ligand-assisted crystallization with TEA and TOPO. The similarity of PL peaks indicates $V_{OC,rad}$ is similar for each material. The TOPO-treated film has a slightly red-shifted PL peak, indicating $V_{OC,rad}$ may be ~5-10 mV lower than the untreated and TEA-treated film.

ΔE_F from PL calculation

Absolute intensity photoluminescence (AIPL) encodes information about radiative recombination, which can be used to determine the quasi-Fermi level splitting (ΔE_F) of a semiconductor. Several methods of calculating ΔE_F for hybrid perovskites have been demonstrated previously[41, 54]. We employ a simple method that is conducive to wide-field PL measurements where we do not obtain spectral emission information. In this method, we calculate ΔE_F directly from external photoluminescence quantum yield[55] ($PLQY_{Ext}$) with the expression

$$\Delta E_F = qV_{OC,rad} + kT \ln(PLQY_{Ext}) \quad (3.6)$$

Some limitations of this method are that precise temperature is unknown, $V_{OC,rad}$ is unknown, and sub-bandgap emission is counted in $PLQY_{Ext}$. If $V_{OC,rad}$ is not measured, it can be replaced with the detailed-balance limit, $V_{OC,SQ}$ as an approximation. Our detailed-balance limit calculation following the method of Shockley and Queisser[101] is described elsewhere[41]. For all ΔE_F results reported in this work, we use eq. 3.5 with $V_{OC,rad}$ calculated from EL as discussed above. We assume a carrier temperature of 350 K (higher than we expect), which will cause equation 3.5 to slightly underestimate the true ΔE_F. For data presented in Figure 3.7, we used stabilized PLQY values (PLQY after 5 minutes of 1 sun blue LED illumination) with eq. 3.5.

Chapter 4. PHASE SEGREGATION IN HIGH-BANDGAP, MIXED HALIDE PEROVSKITES

This chapter shares progress in understanding the halide phase segregation phenomenon, which is observed in mixed-halide perovskites that are candidates for tandem applications. Section 4.1 was conducted in collaboration with Ian Braly (with shared first-authorship on the publication), and was published in ACS Energy Letters[51]. This paper fills a critical gap in understanding the cause of phase segregation and its impact of device performance, and as of March 2020 this paper has received 55 citations. Section 4.2 presents unpublished work describing a photoluminescence model that can be applied to understanding phase segregating HPs.

4.1 Current-Induced Phase Segregation in Hybrid Perovskites and Its Impact on Two-Terminal Tandem Solar Cell Design

Large-bandgap, mixed halide hybrid perovskites are of significant interest since their bandgap can be tuned to be ideal (~1.75 eV) as a top-cell in tandem photovoltaics with silicon, CIGS, or CZTS as the bottom cell. However, previous reports show that many of the mixed-halide perovskites phase segregate when exposed to light, suffer from large voltage deficits, and produce unstable photo-currents due to inhibited carrier collection. In this work, we investigate the origin of phase segregation in commonly employed mixed halide large-bandgap (1.75-1.8 eV) perovskite compositions and elucidate its implication for use in tandem solar cells. Here, we show explicitly for the first time that methylammonium (MA) and MA-cesium (MACs) phase segregate in the dark upon current injection. This is direct experimental evidence that conduction band electrons or valance band holes are the culprit behind phase segregation. However, despite this phase

segregation, MACs devices sustain constant power output at 97% of initial power while the changing absorption profile has an insignificant impact on the current output of a CIGS bottom-cell. In contrast to MA-based cells, formamidinium (FA) containing cells show resilience to phase segregation up to 4 Sun equivalent charge carrier concentrations even when annealed at only 75°C. Collectively, our results indicate that both MACs and FACs cells can sustain constant carrier collection under continuous illumination and are promising candidates for efficient and stable two-terminal tandem devices.

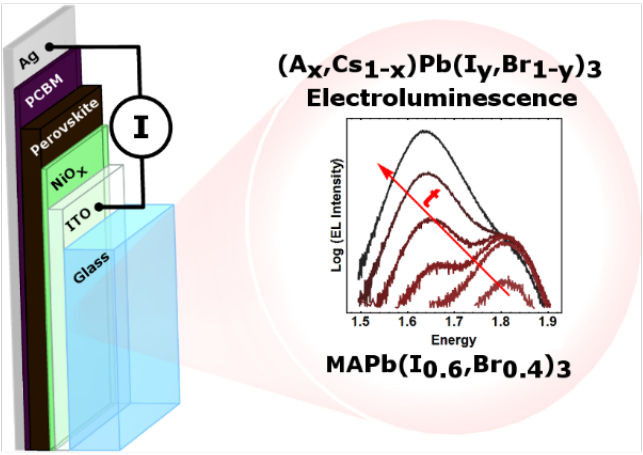

Figure 4.1**. Phase segregation upon current injecting in high bandgap, mixed-halid MA- and MACs-based devices**

For discussion and data showing phase segregation in $MAPb(I,Br)_3$ and $(MA,Cs)Pb(I,Br)_3$ under illumination and upon current injection in the dark, please see original article[51].

We have shown that the $(FA,Cs)Pb(I,Br)_3$ fabricated both with low temperature anneal (FACs-LT) and high temperature anneal (FACs-HT) are phase stable at 1 Sun relevant carrier densities[51], achieved with either photo-excitation or current injection. To probe the boundaries of the phase stability of FACs materials, we investigated phase stability under carrier densities higher than present under 1 Sun illumination. In this experiment, we observed EL and PL emission spectra for both FACs-LT and FACs-HT with time and doubled the photoexcitation flux or current injection

if we did not observe an emission peak low-energy shoulder. We continued this procedure until a low-energy shoulder was finally visible. The results of this experiment are presented in Figure 4.2 a and b for FACs-LT and FACs-HT, respectively. Dashed vertical lines indicate times at which the photoexcitation flux or current injection was doubled. Both FACs-LT and FACs-HT show stable <E> with time at 1 Sun, 2 Suns, and 4 Suns carrier density upon photoexcitation as well as current injection. However, both FACs-LT and FACs-HT display obvious emission spectrum red-shifts at 8 Suns and 32 Suns, respectively. This demonstrates that the FACs materials will ultimately show similar phase segregating behavior as MA materials, however, at several-fold higher excited carrier density.

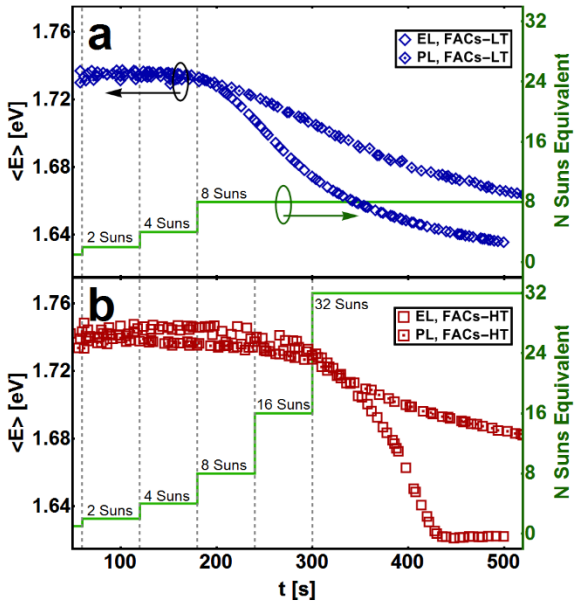

Figure 4.2**. Mean emission spectrum energy with time**. The electroluminescence current density and photoluminescence illumination intensity is doubled every minute. (a) Low temperature annealed $(FA_{0.83},Cs_{0.17})Pb(I_{0.66}Br_{0.34})_3$ under 2, 4, and 8 Suns equivalent current density or illumination intensity. (b) High temperature annealed $(FA_{0.83},Cs_{0.17})Pb(I_{0.66}Br_{0.34})_3$ under 2, 4, 8, 16 and 32 Suns equivalent current density or illumination intensity.

We propose that a combination of larger morphological grains and the presence of size mismatch on the perovskite A^+ site in FACs materials stabilize these materials at 1 Sun excitation. However, as excited carrier induced strain increases with carrier densities at above 1 Sun, nucleation of I-rich clusters to relieve bulk strain will overcome the energy penalty of phase boundaries, and the threshold is higher in FACs than in MA. Further, Figure 4.2 shows that the carrier density required to induce phase segregation in FACs-HT was higher than FACs-LT, indicating that larger grains indeed provide enhanced phase stability within the FACs material class. Interestingly, the threshold carrier density required for phase segregation was equivalent for PL and EL measurements, 8 Suns in the case of FACS-LT and 32 Suns for FACs-HT. These observations confirm that phase segregation behavior is similar for photoexcitation and current injection at comparable excess carrier densities. We note that phase segregation is a function of time as well as carrier density, and one minute may not be sufficient time to observe the slow phase segregation behavior. Indeed, the decreasing <E> slope for FACs-HT at 16 Suns indicates that phase segregation would likely be observed at longer times, suggesting our FACs-HT material is not phase stable at 16 Suns. However, the data unambiguously shows relative trends that the FACs-HT is more stable at higher excitation than FACs-LT and that <E> has similar behavior for EL and PL in both materials.

Collectively, our PL and EL measurements on four different perovskite films (FACs-LT, FACs-HT, MA, and MACs) allow us to investigate impact of carrier density profile on the rate of phase segregation (see EL and PL results for MACs[51]). Recently, Barker *et. al* examined the impact of carrier density profile on rate of phase segregation and discovered that higher excitation photon energies (i.e. blue light) gives faster rate of phase segregation for a comparable absorbed photon flux in $MAPb(I_{0.4},Br_{0.6})_3$.[38] We add to this picture by comparing the rate of phase segregation under

illumination with the rate of phase segregation upon current injection. Under one-sided illumination, both electron and holes have similar profiles with highest concentration close to the illuminated side, while upon current injection the electron and hole concentrations will each be highest closest their selective contacts. Our results confirm that differences in carrier density depth profiles affect the rate of phase segregation, yet we observe different behavior for different compositions. Table 4.1 presents the extreme slope of <E> vs. time data for each of the four films studied, where this slope serves as a quantitative metric to examine phase segregation rate. We find that for MA and MACs, the rate of <E> decay is much faster for photoexcitation than for current injection. Contrarily, the FACs LT and HT films (at the 8 or 32 Suns required to induce phase segregation), show slightly faster <E> decay for current injection than for photoexcitation. Understanding the reasons behind the different relative rates of phase segregation is a complex topic since these experiments were conducted at different excitations (1 Sun, 8 Suns, and 16 Suns), with different excitation mechanisms (EL and PL), and on different materials with distinct mass and electronic transport properties. However, we speculate these observed differences between relative rates of phase segregation in FACs films and the MA/MACs films to be primarily associated with the differences in carrier diffusion lengths of the materials and differences in total absorbed/injected carrier density in the films. We acknowledge that the carrier concentrations (photoexcitation for the PL experiment and injection for the EL experiment) will be about 20-25% different due to non-unity absorptivity of these films at 532 nm. We suspect the fastest phase segregation will occur when the local carrier density of both holes and electrons is the highest (inducing the greatest lattice strain). MA films have shorter carrier diffusion lengths than FACs films,[39] suggesting the highest local carrier densities of both carriers occur at the illuminated side of the substrate during PL measurements resulting in greater lattice strain than with current

injection and faster phase segregation. In contrast, FACs films have longer carrier diffusion lengths which result in lower carrier density gradients within the films, causing faster phase segregation in EL due to slightly higher total carrier injection (due to non-unity absorptivity in PL experiments).

Table 4.1 **Phase Segregation Rates, d<E>/dt [meV/s]**

	MA	MACs	FACs-LT	FACs-HT
PL	-6.27	-6.93	-0.28	-0.27
EL	-1.22	-0.69	-0.58	-1.25

Since the development of monolithic tandem solar cells is one of the key reasons for interest in the large-bandgap hybrid perovskites, we turned our investigation to evaluate the impact of phase segregation on two-terminal monolithic tandem solar cell performance. One potential pitfall is that phase segregation can result in carrier trapping in I-rich domains, which could reduce the current output of the perovskite cell[26-28]. This is especially problematic in a two-terminal tandem which requires current matching. Additionally, a phase segregating top cell could also be detrimental due to changing absorption behavior, which could result in a changed transmitted photon flux and thus altered current output of the bottom cell. We evaluated both criteria (current output of top cell and transmitted photon flux to bottom cell) for MA, MACs, and FACs-HT by measuring current output with time of the perovskite top cell as well as current output with time for a CIGS bottom cell with perovskite a film filter.

Results from these experiments are shown in Figure 4.3. Figure 4.3 a-c show the normalized PL emission spectra of FACs-HT, MA, and MACs films before (dashed line) and after (solid line) five minutes of illumination with Newport AAA Solar Simulator (the exact films used for the experiment with the CIGS device shown in Figure 4.3e). As expected from previous PL results

with 532nm laser excitation (Figure 4.2b), FACs-HT exhibits no PL peak shift while both MA and MACs show red-shifts. The normalized current output at maximum power point for large-bandgap perovskite devices are presented in Figure 4.3d. FACs shows stabilized current output at about 3% above starting value, while MA shows current output decreasing to below 85% the starting value before five minutes. These results are expected and agree with previous findings[21, 26-28]: MA is phase segregating which results in decreased current collection upon carrier confinement in I-rich domains contrasting the phase-stable FACs. Remarkably, the MACs device shows stable current output at ~3% below initial current (as observed in our previous work)[5] despite PL and EL results showing similar phase segregation behavior as MA (see Figure 4.3a-c). For MACs, I-rich domains clearly form as indicated by PL, but this does not have a significant impact on carrier collection.

The J_{SC} as a function of time from a 12.1% efficient solution-processed CIGS cell (see reference for fabrication details, and Figure S11 for JV performance data)[40] with perovskite film filter is shown in Figure 4.3e. This data exemplifies the impact of changing transmitted photon flux to bottom cell on bottom cell current output. In this experiment, the MA and MACs film filters are phase segregating, yet the impact of the changing transmissivity is insignificant. The inset of Figure 4.3e shows a J_{SC} decrease of <0.5% corresponding to phase segregation in both MA and MACs films. This finding is consistent with previous reports showing absorptivity spectra before and after phase segregation,[27, 36] suggesting that either a small fraction of the film is phase segregating, or that the integrated transmissivity is remaining relatively constant (i.e. the above-bandgap transmissivity is increasing as the below-bandgap transmissivity is decreasing). This important result shows MACs as a very interesting case where phase segregation is occurring but only an insignificant impact on current output of either the top cell or bottom cell is detected.

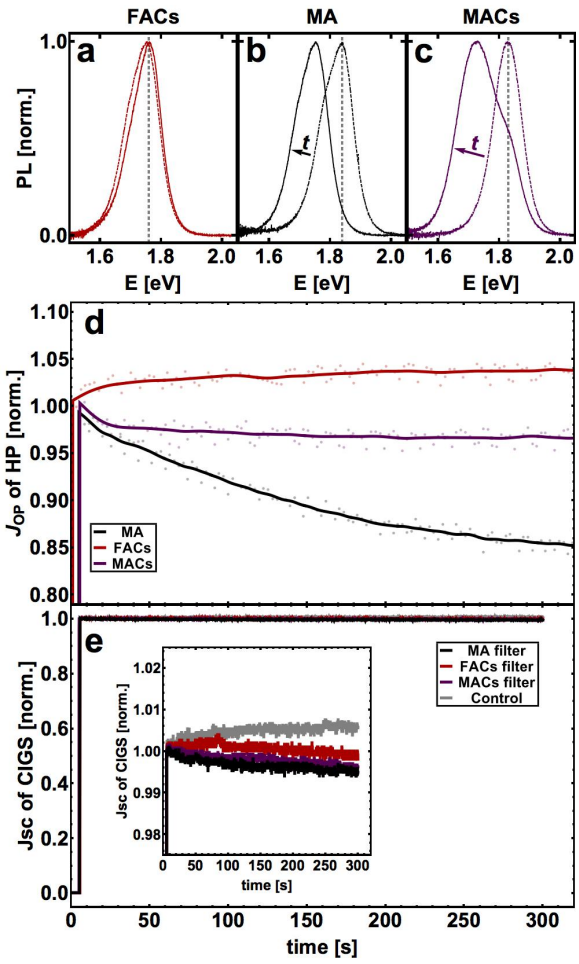

Figure 4.3**. Device current with time during perovskite phase segregation**. Normalized photoluminescence spectra of (a) $(FA_{0.83},Cs_{0.17})Pb(I_{0.66},Br_{0.34})_3$, (b) $MAPb(I_{0.6},Br_{0.4})_3$, and (c) $(MA_{0.9},Cs_{0.1})Pb(I_{0.6},Br_{0.4})_3$ films before (dashed) and after (solid) exposure to AAA solar simulator in an air-free quartz assembly. (d) Normalized maximum power operating current at fixed voltage over five minutes of $MAPb(I_{0.6},Br_{0.4})_3$, high temperature $(FA_{0.83},Cs_{0.17})Pb(I_{0.66},Br_{0.34})_3$, and $(MA_{0.9},Cs_{0.1})Pb(I_{0.6},Br_{0.4})_3$ devices in nitrogen. (e) Normalized CIGS short circuit current over time while filtered by the exact films of (a-c), where the control is with the empty air-free quartz assembly as a filter.

The results presented in Figure 4.3 indicate that either FACs (phase stable) or MACs (phase segregating, but stable currents) are both excellent candidates for the top cell in current-matched tandem applications. More broadly, this result indicates that phase segregation is not necessarily detrimental to realization of efficient, stable tandem solar cells. We also want to point out that the V_{OC}s for cells with MA and MACs films are slightly higher than for cells with phase stable FACs-

HT films. This suggests that phase segregation has only limited impact on the greater voltage deficit observed in large-bandgap perovskites compared to their ~1.6eV bandgap alternatives. We therefore suggest that eliminating phase segregation is not the most important objective in the realization of stable, high efficiency tandems. More important objects are (1) understanding and manipulating bulk defects that seem to cause a relatively large V_{OC} deficit in large-bandgap perovskites and (2) understanding why phase segregation has an insignificant impact on carrier collection for certain large-bandgap perovskites such as MACs films.

Conclusion:

In conclusion, we investigated MA, FACs, and MACs large-bandgap mixed halide perovskite compositions with electroluminescence, photoluminescence, and photocurrent experiments. For the first time, we show phase segregation in the absence of photo-excitation, consistent with excited-state lattice strain sustained by a high carrier density. Additionally, we provide conclusive evidence that FACs perovskites can be prepared to be phase stable at 1 Sun-equivalent carrier densities, even with the smaller grain sizes that result from a 75°C anneal. We further show that larger grains from a high temperature anneal improve the FACs critical room temperature phase segregation excess carrier concentration by a factor of four. We also examine the impact of phase segregation on tandem device operation by measuring current output of phase-segregating perovskite devices as well as a CIGS bottom cell shaded by phase-segregating perovskite filters. Even though the MA device exhibits significant current density decay upon phase segregation as reported previously, we surprisingly reveal stable power output during phase segregation in a MACs device. Finally, we observe the filtered CIGS photocurrent to change less than 0.5% when shaded by severely phase segregating films. Therefore, we conclude that the next generation of low-cost, high efficiency tandem photovoltaics do not need to eliminate excess carrier-induced

phase segregation in the hybrid perovskites top cell, and that the more imposing obstacle in attaining such a photovoltaic technology is the voltage deficit of these large-bandgap perovskite materials.

Acknowledgements

We acknowledge financial support from the U.S. Department of Energy Sunshot Initiative, Next Generation Photovoltaics 3 program, Award DE-EE0006710, and the University of Washington Clean Energy Institute. ARU acknowledges the financial support from the Swiss National Science Foundation (SNSF) under project numbers P2EZP2_152168 and P300P2_164660.

Supporting Information.

Film preparation, device fabrication, non-injecting lateral device fabrication for electric field experiment, experimental details, absorbance spectra, grain-size analysis, XRD detector images, perovskite device current-voltage characterization, additional electroluminescence and photoluminescence data, below-bandgap emission discussion, applied electric field experiment results, and CIGS device current voltage characterization.

4.2 A Two-Phase Photoluminescence Model for Study and Design of Phase Segregating Perovskites

This section presents unpublished data describing a two-phase photoluminescence model for study of phase segregating mixed-halide perovskite heterostructures. The main takeaway from this work is that the ΔE_F of a two-phase perovskite heterostructure will be higher than that of a pure phase HP with similar PLQY and bandgap equal to the lower phase bandgap. This is because a quasi-equilibrium is established between excited carriers in the multiple phases. Although this

work was not completed and published, the insights from this work influenced design and interpretation of experiments in several of our other works[51, 52, 62].

Despite the abundance of work studying and reviewing phase segregation in mixed-halide perovskites[28, 39, 42, 43, 65, 66, 102-104], there are only a few studies that investigate the impact of phase segregation on device performance[39, 40, 62], and a general understanding on how phase segregation impacts V_{OC} and J_{SC} with time has not been fully developed. Indeed, several hypotheses have been recently disproved by published data. One hypothesis is that the ΔE_F (and thus V_{OC}) will decrease upon phase segregation due to carrier transfer into a domains with lower bandgap, leading to a ΔE_F decrease of ~100meV in some cases (see Figure 6c in Braly and Hillhouse[41]). This is not always the case, as recently we demonstrated 2D/3D mixed-halide HPs (with PEA) that exhibit phase segregation but also can sustain constant V_{OC} with time[62]. Another hypothesis is that carrier transfer to the lower bandgap phase impedes current collection, which can be observed by a decaying photocurrent with time[39, 40]. However, we also showed that this is not always true with the interesting case of $(MA,Cs)Pb(I,Br)_3$, which can sustain constant current with time despite phase segregating, as shown in Figure 4.3d[39]. Here, we expand our AIPL model to include two-phase materials, use the updated model to study phase segregation, and ultimately develop a generalized theory for how phase segregation impacts device performance.

Consider the ΔE_F splitting of a two-phase material, with a minority phase that has slightly lower bandgap. Previously, we calculated ΔE_F for this system using the PLQY method with the peak position of the total luminescence, which is typically the lower bandgap phase in a segregated material (e.g. Figure 6a,c in Braly and Hillhouse[41]). This method is inappropriate, as it treats the emission of a minority phase (typically 1-10% of the material) as if it were a pure material. The carrier concentration we obtain from the extracted ΔE_F in this case is an underestimation of up to

two orders of magnitude (suggesting calculated ΔE_F is a significant underestimation). This ΔE_F underestimation can be seen by the offset in the high energy tails in Figure 4.4 (left). However, the information about the mole fraction and ΔE_F of each phase is still encoded in the magnitude and shape of a photoluminescence spectrum although it is not practical to completely expand the model for two direct transitions with two complete parameter sets (yielding 8-9 fit parameters). We can expand our AIPL model by adding only a single term, mole fraction of I-rich phase, if we assume (i) theta and gamma are the same for I-rich and Br-rich phases (theta, gamma for Br-rich phase have little impact on emission), (ii) temperature is the same (has little impact on I-rich emission), (iii) starting Br concentration is known, and bandgap dependence on Br content follows and experimentally measured empirical trend, (iv) the carrier populations in each phase are in equilibrium with each other (ΔE_F constant in I-rich and Br-rich phase). With the updated model, we can fit the full phase segregated peak and determine that there is ~5% I rich phase and ΔE_F of 1.34eV (Figure 4.4 right).

Figure 4.4 demonstrates that the ΔE_F splitting will be higher for the two phase material on the right than for a pure phase material with bandgap 1.698 with the same sub-bandgap absorptivity and a similar PLQY. This gives critical insight on the optoelectronic properties of a two phase material. A mixed-halide perovskite that phase segregates will have some loss in ΔE_F due to carriers moving down in energy to the lower bandgap phase. However, the observed ΔE_F decrease will be a function of the relative mole fraction of the two phases, the difference in bandap, the defect chemistry, and the magnitude of the concentration effect in the smaller E_g phases. Considering these factors, the decrease in ΔE_F as a mixed-halide perovskite phase segregates could be quite small. Collectively, this finding describes why certain phase-instable materials, such as

$(MA,Cs)Pb(I,Br)_3$ or $(PEA,MA)Pb(I,Br)_3$, can give stable device parameters despite demonstrating clear evidence of phase segregation.

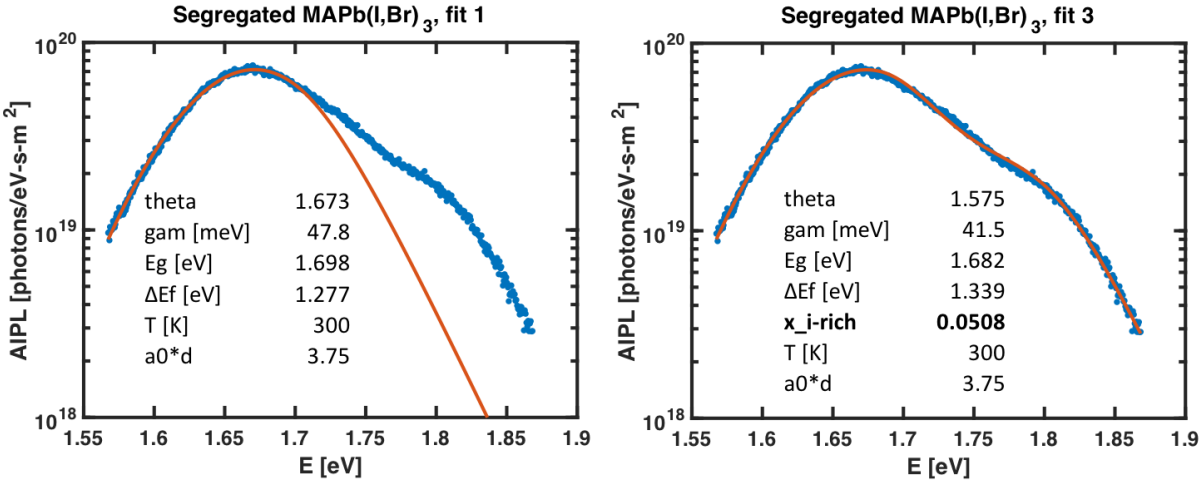

Figure 4.4**. AIPL fits of phase segregated data using AIPL with single (left) and double (right) transition energies**. The left fit omits data > 1.72eV. The ΔE_F on the left matches what the PLQY method would predict (which assumes 100% of a ~1.70eV bandgap material). The mismatch in the high energy tail region indicates that the ΔE_F is not adequately describing the luminescence of this material. Right shows the fit of the updated model, which demonstrates excellent fit through the entire range, with a higher ΔE_F of 1.34 eV.

Chapter 5. ENHANCING DEFECT TOLERANCE AND PHASE STABILITY OF HIGH-BANDGAP PEROVSKITES VIA GUANIDINIUM ALLOYING

The following continues work started in Chapters 3 and 4 to improve the photovoltage and phase stability of high-bandgap, mixed-halide perovskites. Here, we use high-throughput combinatorial screening to study the influence of lattice strain on the band structure and defect chemistry of mixed-halide HPs. This work was published in ACS Energy Letters[52], and received 26 citations (as of March 2020) in the 1.5 years since its publication. Recent work demonstrating high efficiency perovskite-perovskite tandems[105] by the founders of Swift Solar was largely based on technology developed in this paper. In Fall 2019, I received the UW Chemical Engineering Department's "High Impact Publication" award for this paper. Reproduced with permission[52]; copyright Americal Chemical Society 2018.

5.1 ABSTRACT

Although hybrid perovskites (HPs) have tunable bandgap making them amenable to tandem solar cells, the measured V_{OC} does not increase sufficiently with increasing bandgap ($V_{OC}/V_{OC,SQ}$ decreases with increasing bandgap for $E_g > 1.70$eV). We study the impact of A^+ size mismatch induced lattice distortions (in ABX_3 structure) on the optoelectronic quality of high-bandgap HPs and find that the highest quality films have high A-site size-mismatch, where large GA compensates for small Cs to keep the tolerance factor in the range for the perovskite structure. Specifically, we find that 1.84eV bandgap $(FA_{0.33}GA_{0.19}Cs_{0.47})Pb(I_{0.66}Br_{0.34})_3$ and 1.75eV bandgap

$(FA_{0.58}GA_{0.10}Cs_{0.32})Pb(I_{0.73}Br_{0.27})_3$ attain quasi-Fermi level splitting (ΔE_F) of 1.43eV and 1.35eV, respectively using quantitative photoluminescence, which is >91% of the detailed-balance limit for both cases. Films of 1.75eV bandgap $(FA,GA,Cs)Pb(I,Br)_3$ are then used to fabricate p-i-n photovoltaic devices that have a V_{OC} of 1.24 V. This V_{OC} is among the highest V_{OC} reported for any HPs with similar bandgap (1.7 to 1.8 eV) and a substantial improvement for the p-i-n architecture, which is desirable for tandems with Si, CIGS, or a low-bandgap HP. Collectively, our results show that non-radiative recombination rates are reduced in $(FA,GA,Cs)Pb(I,Br)_3$ films and prove that FA-GA-Cs alloying is a viable route to attain high V_{OC} in high-bandgap HP solar cells. This work relieves the limitation of material quality in high-bandgap perovskites and demonstrates that V_{OC} proportionate to bandgap can be achieved with tailored device engineering.

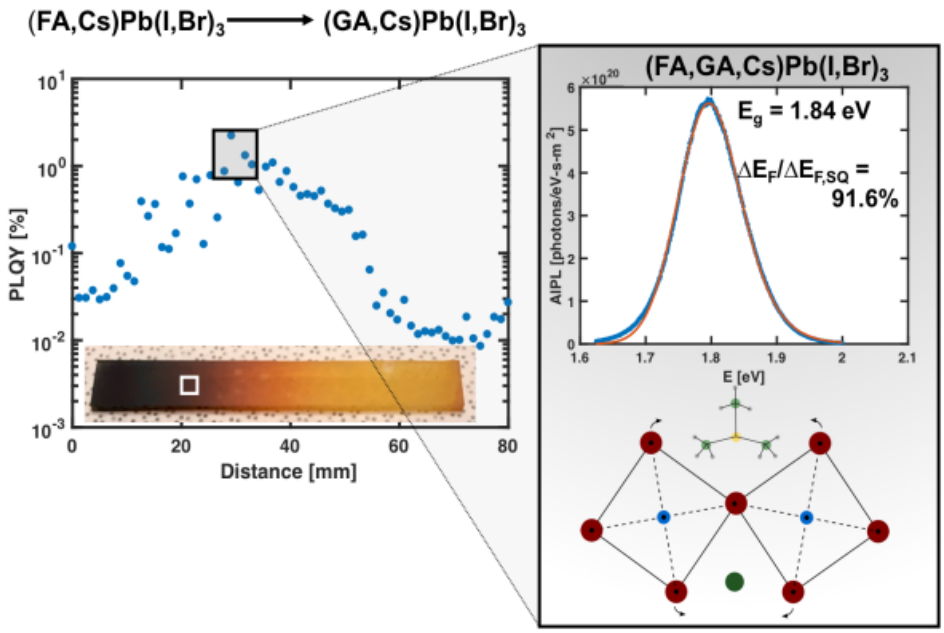

Figure 5.1**. Enhancing Defect Tolerance and Phase Stability of High-Bandgap Perovskites via Guanidinium Alloying**

5.2 INTRODUCTION

In the past five years, the hybrid organic-inorganic perovskites (HPs) have emerged as an exciting material for photovoltaic applications due to unprecedentedly high optoelectronic quality for a material fabricated with a low-temperature solution process. Bandgap tuning in HPs can be easily accomplished by changing halide composition making HPs amendable to tandem applications. For a 1.10 eV bottom cell (such as c-Si or CIGS), the ideal top cell bandgap is 1.75eV[19, 24] (Br/(I+Br)~0.35) while for a 1.22eV bottom cell (the minimum reported HP bandgap) the ideal top cell becomes 1.82eV[19, 24] (Br/(I+Br)~0.40). However, as Br/(I+Br) exceeds 0.20, HPs have been shown to undergo halide redistribution under illumination[38] or current injection[51, 106], resulting in distinct phases with different halide content. The ratio of the measured open circuit voltage to the theoretical Shockley-Queisser (SQ) open-circuit voltage ($V_{OC}/V_{OC,SQ}$) also deteriorates above ~20% Br[35, 41], which has led some investigators to suggest that the voltage deficit in high-bandgap, mixed-halide perovskites is intimately linked to halide phase segregation. Although several reports show compositions that exhibit improved phase stability at 1 Sun conditions[16, 36, 40], the highest $V_{OC}/V_{OC,SQ}$ reported[12] for such compositions is 85% for the 1.75eV bandgap $(FA,Cs)Pb(I,Br)_3$ in an n-i-p architecture (V_{OC} = 1.24 V), which is much lower than the highest reported $V_{OC}/V_{OC,SQ}$ of 92% for a 1.63eV material (V_{OC} = 1.24)[9] and still limited by the absorber material quality. We note that the p-i-n device architecture is preferred for monolithic, two-terminal tandems with either c-Si, CIGS, or a 1.2 HP due to a combination of bottom cell architecture, parasitic absorption, and processing constraints, as evidenced by the state-of-the art efficiencies for all three classes being realized by p-i-n devices[19, 22, 107]. The highest V_{OC}'s obtained for high bandgap HPs with p-i-n architecture is 1.17 V for a 1.75eV absorber ($V_{OC}/V_{OC,SQ}$ =

80%)[108]. Realization of high-bandgap HPs with higher optoelectronic quality is imperative for relieving performance limitation in low-cost multi-junction HP devices.

Here, we employ high throughput combinatorial materials screening with quantitative steady-state photoluminescence analysis within the (MA,FA,GA,Cs)Pb($I_{0.66}$,$Br_{0.34}$)$_3$ composition space, where MA = methylammonium, FA = formamidinium, and GA = guanidinium, and identify high-bandgap HPs that sustain high quasi-Fermi level splitting ($\Delta E_F/\Delta E_{F,SQ}$), exceeding that of previously reported materials. We selected some of the most promising FA-GA-Cs alloys for further investigation, and discover that GA can be incorporated into the perovskite structure in specific cases which induces local lattice distortions. Further, we show that FA-GA-Cs alloys can sustain quasi-Fermi level splitting of >91% of the detailed balance limit maximum for high-bandgap HPs and demonstrate enhanced phase stability. Finally, we implement our 1.75eV (FA,GA,Cs)Pb(I,Br)$_3$ film into devices (with p-i-n architecture desired for tandems) and significantly improve the V_{OC}.

5.3 Results and Discussion

Using combinatorial spray coating, we fabricated composition gradients within the (MA,FA,GA,Cs)Pb($I_{0.66}$,$Br_{0.34}$)$_3$ composition space, using effective tolerance factor and A-site size standard deviation as parameters to choose gradients in an effort to isolate the impact of lattice distortion on optoelectronic quality (detailed in Supporting Information). In this "effective tolerance factor" approach, we choose appropriate ratios of GA and Cs such that the tolerance factor (calculated using mean ionic radii) fall within the perovskite formation range. However,

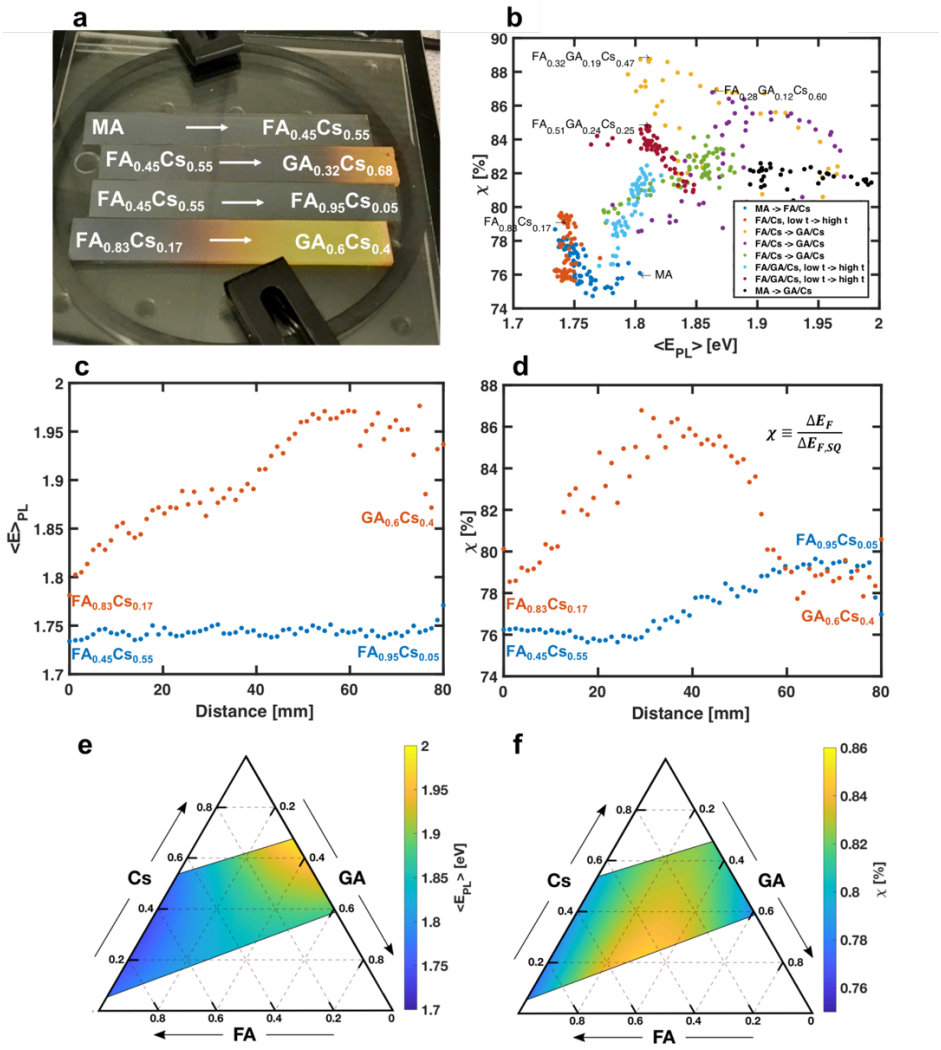

Figure 5.2**. Spray coated A-site composition gradients of HPs** and their optoelectronic quality for a fixed iodide to bromide ratio, or $APb(I_{0.66}Br_{.34})_3$, where A can be an alloy containing FA, MA, GA, or Cs. (a) Photo of four example gradients; composition along the 80 mm substrate is a linear combination of the compositions listed on the ends. Samples are enclosed behind two glass sheets with a quartz top window using an O-ring, vacuum grease, and clamps screwed into an optical stage to ensure AIPL measurements are collected with the samples in a N_2 environment. (b) Compiled AIPL results for eight gradients, showing optoelectronic quality fraction χ vs. mean PL emission energy, with several compositions of interest highlighted ($\chi = \Delta E_F/\Delta E_{F,SQ}$). Note that $\Delta E_{F,SQ}$ is identical to $qV_{oc,SQ}$. (c-d) example results showing (c) mean PL emission energy and (d) optoelectronic quality as the composition changes along the length of the gradient for two example gradients. Note that the absolute intensity PL measurements were collected at 1 Sun photon flux (541 W/m^2 with a 532nm cw laser). (e-f) shows (e) mean PL emission energy and (f) optoelectronic quality, χ, on a ternary plot representing FA-GA-Cs alloys. Interpolation is determined using thousands of PL emission spectra from over five composition gradients in the $(FA,GA,Cs)Pb(I_{0.66}Br_{0.34})_3$ space. White regions are regions where no data was collected**.**

the standard deviation of ionic radii for a GA-Cs alloy will be higher than MA (all A^+ radii are the same size) or even a FA-Cs alloy. This novel method of probing the HP composition space using (i) effective tolerance factor and (ii) distribution of A^+ sizes gives an increased likelihood of finding new compositions that form a perovskite phase while employing larger A^+ ions. Each spray coated composition gradient is prepared using a translating spray nozzle while ramping syringe pump rates with inks containing different A cation compositions, as described previously[41] and discussed in the Methods section. To assess material optoelectronic quality, we measure absolute intensity photoluminescence (AIPL) as a function of position along the composition gradient. The steady-state quasi-Fermi level splitting (ΔE_F), which is the difference between the steady-state non-equilibrium Fermi energy of the conduction band and of the valence band, sets the intensity of the PL and can be determined by fitting the spectral emission profile[54, 55]. A material with 100% PLQY would have precisely the radiative limit quasi-Fermi level splitting ($\Delta E_{F,rad}$), which is typically slightly reduced from the Shockley-Queisser quasi-Fermi level splitting ($\Delta E_{F,SQ}$) due to the presence of a non-abrupt absorption onset because of sub-bandgap absorption. Measuring ΔE_F on a neat film gives the maximum attainable V_{OC} for a device with that film as its active layer ($V_{OC,max} = \Delta E_F/q$). Further, comparing the measured ΔE_F to $\Delta E_{F,SQ}$ gives an easily calculated and fair metric to reveal if increases in ΔE_F are keeping up with increases in bandgap. By studying the quality of the HP layer outside of a completed device stack we directly assess the limitations of the material itself without complicating factors such as defective interfaces or band alignment.

Figure 5.2 presents a photograph of four example spray coated composition gradients (a), along with various methods of representing the gradient AIPL results (b-f). From the visible trends in color shown in Figure 5.2a, one can directly observe that the composition gradient has an impact on optical bandgap. A color change occurs in the two gradients involving GA-Cs, indicating the

optical bandgap increases with GA-Cs incorporation, while the gradients involving only MA and FA-Cs remain dark within the entire composition range, indicating the optical bandgap increases more strongly with GA-Cs incorporation. Figure 5.2d shows optoelectronic quality parameter $\chi \equiv \Delta E_F / \Delta E_{F,SQ}$ as a function of position along the gradient, where the composition is a function of position. The quasi-Fermi level splitting calculations are described in detail in SI, with examples shown in Figure 5.6-5.7. For the ($FA_{0.45}Cs_{0.55}$) -> ($FA_{0.95}Cs_{0.05}$) gradient, results are similar to trends previously reported[36], with the FA-Cs gradient showing an optimum PLQY around 15% Cs (~65mm in Figure 5.2). Considering the exploration of FA-GA-Cs results, we observe several interesting trends. Note that for each of these gradients, as we add GA we also increase the concentration of Cs to keep the effective tolerance factor constant and avoid GA-rich compositions that are unlikely to form a 3D perovskite phase. Most importantly, we notice that there are several FA-GA-Cs compositions that emerge as having much higher χ than MA or FA-Cs compositions, even approaching 90%. Figure 5.2e-f show that there is a sizeable composition region around A = $FA_{0.5}GA_{0.25}Cs_{0.25}$ where mean PL emission energy is less than 1.9eV while χ is greater than 85% . We also notice that the PL emission blue shifts with incorporation of GA and Cs, with many of the highest quality FA-GA-Cs compositions blue shifting from 1.75eV to 1.8-1.9eV. However, the changes in PL emission energy do not seem to precisely match the changes in optical bandgap for certain compositions; the yellow film on the right side of the two GA-containing gradients suggests a bandgap around 2.2 eV, while the PL emission energy increases to only ~1.95eV. One possible explanation is formation of multiple phases at certain locations/compositions (such as at the far right side of (GA,Cs) gradients), where the PL emission is from a minority phase with lower bandgap than the majority phase observed visually. Still, the changes in both optoelectronic quality and PL emission energy indicate that

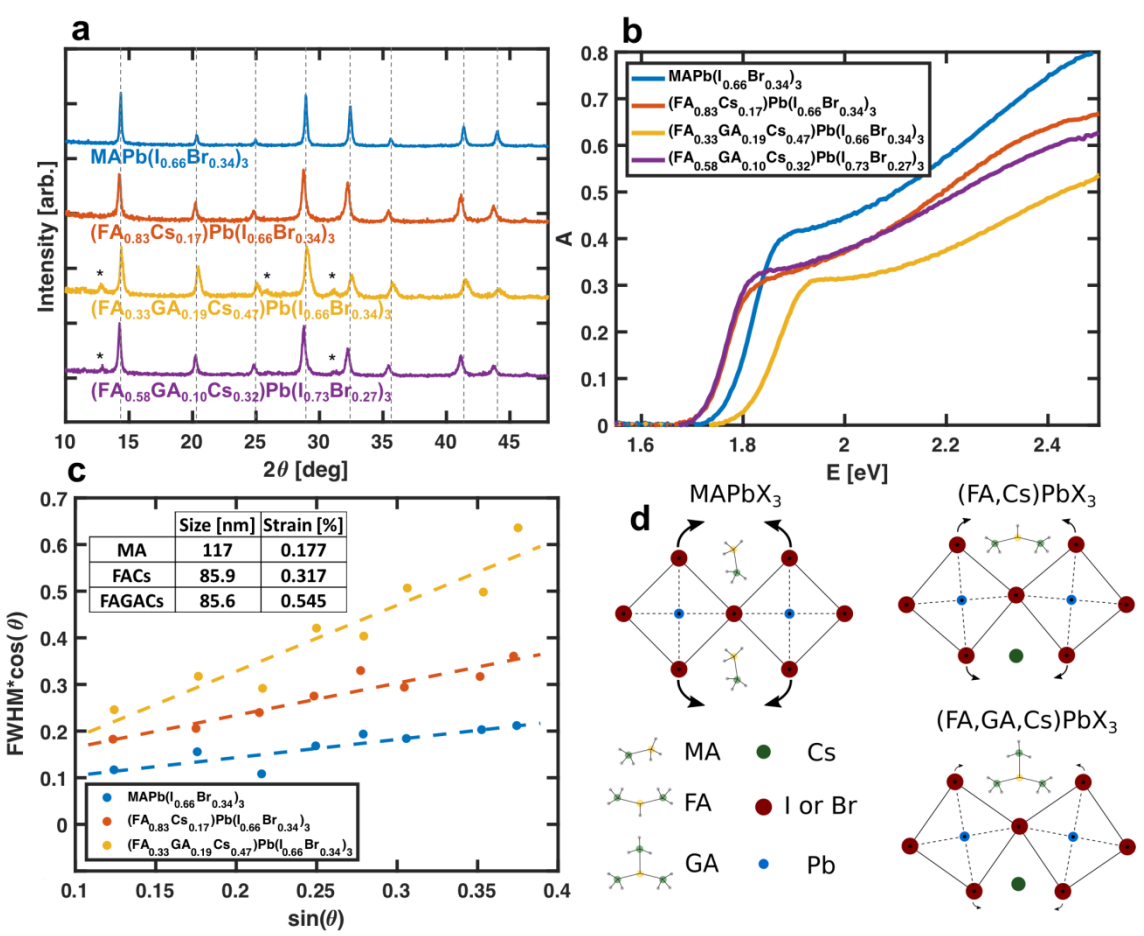

Figure 5.3**. Structural and optical characterization of spin coated films**. (a) XRD of films. (b) UV-Vis-NIR absorbance of select MA, FA-Cs, and FA-GA-Cs HP films. The dashed lines in (a) indicate cubic perovskite phase (P*m*$\underline{3}$*m* with lattice constant a = 6.170 Å), which matches the $MAPb(I_{0.66}Br_{0.34})_3$ pattern precisely. We noted peaks that do not match the cubic perovskite pattern with *, some of which align with PbI_2 2θ positions. (c) Williamson-Hall analysis of three A-site compositions, each with the same bromine content, Br/(I+Br)=0.34. Microstrain increases with increasing size mismatch on A site, while crystalline domain size remains relatively constant. (d) Schematic showing the possible structural impact of incorporating A cations of different sizes into the perovskite structure, which results in reduced dynamic disorder and a narrower distribution of bond angles.

incorporation of additional (GA,Cs) has an impact on both the band structure and defect chemistry in high-bandgap perovskites. To further understand the effect of (GA,Cs) incorporation on optoelectronic and structural properties, we fabricated spin coated films from several compositions

within our spray coated experiment space so we could study carrier transport and phase purity in addition to ΔE_F.

Early reports suggested that GA is not incorporated into the perovskite structure due to its large size and either resides as a passivating agent at surfaces[109-111] or induces formation of a lower dimensional "layered" crystal structure[112-115]. In contrast, more recent reports demonstrate that GA can be incorporated at least up to 25% in $(GA_xMA_{1-x})PbI_3$[116], leading to some improvements in V_{OC} and stability for a ~1.6eV HP. Further, Kubicki *et al.* employ NMR to demonstrate direct evidence of GA incorporation into the $FAPbI_3$ or $MAPbI_3$ lattice forming phase pure materials[117]. This diversity in reported phase purity suggests that GA incorporation into the perovskite structure depends on precise alloy composition and fabrication procedure. This is reflected by trends in changing optoelectronic quality with GA-Cs content observed in our spray coating results, as shown in Figure 5.2.

We measured UV-Vis-NIR and XRD on spin coated films for selected compositions inspired by the spray coated experiment (shown in Figure 5.3a-b) to investigate the phase purity and the discrepancy between optical bandgap and emission energy (Figure 5.2a-b). We also explored some compositions with slightly reduced Br content to precisely target a bandgap of 1.75eV (ideal for the top cell for tandems with c-Si or CIGS bottom cells). We found that formation of secondary phases depends strongly on (i) effective tolerance factor, (ii) standard deviation of A-site ionic radii and (iii) halide content. Figure 5.3a and 5.3b shows several compositions that form cubic perovskite phase and have strong absorption edge. Collectively, we determined that the two compositions $(FA_{0.33}GA_{0.19}Cs_{0.47})Pb(I_{0.66}Br_{0.34})_3$ and $(FA_{0.58}GA_{0.10}Cs_{0.32})Pb(I_{0.73}Br_{0.27})_3$ emerged as the most promising candidates that form majority perovskite phase, have a strong absorption edge, and have improved optoelectronic quality, and the remainder of this work focuses on these

compositions. In the XRD pattern in Figure 5.3a, we noticed differences in peak broadening for the various alloys. Peak broadening can arise due to: (i) the instrument-induced broadening, (ii) size broadening, (iii) strain broadening, or (iv) the presence of impurities with slightly shifted XRD peak positions. We measured all samples on the same instrument (a Bruker D8 Discover with Cu K ✔ source filtered with single crystal diffractive optics), and found the FWHMs to be well above the instrument broadening observed for LaB_6 standard, ruling out (i). These samples have minor phase impurities, where possible secondary phases have distinct peak 2θ positions (see Figure 5.14), ruling out (iv). We thus conclude that the differences in peak broadening observed here are due to size and/or strain, which is discussed subsequently.

A "perfect" crystal is an infinite array of atoms arranged in a repeated pattern with precise lattice spacing *d*. Real crystals have a finite size, and may also have a distribution in *d*, where the root mean square displacement of *d* from the average spacing is the "microstrain". Microstrain can arise from non-uniform lattice distortions (such as from ion size mismatch on a lattice site), dislocations, antiphase domain boundaries, or grain surface relaxation[118]. The best way to distinguish between size and strain from an XRD pattern is to perform Reitveld refinement[119]. However, this may not be practical in cases where there is preferred orientation in films. In these cases, the Williamson-Hall[120] analysis can be used to estimate size and strain effects and compare relative trends. The merits and limitations of the Williamson-Hall analysis have been critically reviewed by Delhez *et al* who identified that the analysis is able to provide an qualitative interpretation of the origins of line broadening effects, but the quantitative results are not generally reliable[121]. To assess the merits and limitations of the Williamson-Hall, we performed the Williamson-Hall analysis on SRM 1979 (a line shape standard provided by NIST) and compared our results (shown in Figure 5.9) to those obtained by the standard developers[122]. We reproduce

similar size and strain trends as published by Cline *et al.*[122] for the two differently sized particles of the SRM 1979 standard. This result gives us confidence that we appropriately utilize the Williamson-Hall analysis in assessing relative trends for the contributions of crystallite size and strain to the XRD peak broadening of samples.

Although perovskite semiconductors commonly have substantial microstrain because of the prevalent use of alloys (which induce non-uniform lattice distortions), the impact of microstrain on optoelectronic properties of perovskites is not well understood or explored. Wang *et al.* find that aluminum ion doping reduces dislocations (and thus reduces total microstrain) which results in a corresponding PLQY increase and reduced Urbach energy[123]. Contrarily, Yang *et al.* find that incorporation of tin in mixed-halide perovskites increases microstrain which results in enhanced device efficiencies and phase stability[40]. We hypothesize that the different origins of microstrain have vastly distinct impacts on optoelectronic properties. Figure 5.3c shows a Williamson-Hall plot to determine microstrain. The microstrain determined by Williamson-Hall analysis of XRD peaks for $(FA_{0.33}GA_{0.19}Cs_{0.47})Pb(I_{0.66}Br_{0.34})_3$ is 1.7 times greater than $(FA_{0.83}Cs_{0.17})Pb(I_{0.66}Br_{0.34})_3$ and 3.1 times greater than $MAPb(I_{0.66}Br_{0.34})_3$, which gives further evidence that the GA and Cs are incorporated into the A site and also confirms that this composition space can be used to probe optoelectronic impact of local lattice distortions. The Williamson-Hall analysis results for $(FA_{0.58}GA_{0.10}Cs_{0.32})Pb(I_{0.73}Br_{0.27})_3$ (with lower Br content) are presented in Figure 5.10; comparison of this with the other compositions here is not straightforward as the X- and A-sites are both expected to affect microstrain. We show the estimated size, strain, and associated errors (esd from fits) in Table 5.3 and the ionic radii statistics (average size and standard deviation in size) in Table 5.4. The trend in standard deviation of A-site ionic radii matches with the measured microstrain, indicating that the A-site ionic radii is a good predictor of the strain in resulting HP

structures. Optical properties were characterized with UV-Vis-NIR absorbance as shown in Figure 5.3b. Figure 5.3b shows that the FA-GA-Cs compositions retain the sharp band edge observed for (FA,Cs)Pb(I,Br)$_3$. We also notice that for Br/(I+Br)=0.34, the bandgap (extracted from linear fit of A^2 vs. E as shown in Figure 5.11) increases from 1.75eV to 1.84eV upon changing the A-site from ($FA_{0.83}Cs_{0.17}$) to ($FA_{0.33}GA_{0.19}Cs_{0.47}$), and that ($FA_{0.58}GA_{0.10}Cs_{0.32}$)Pb($I_{0.73}Br_{0.27}$)$_3$ has 1.75eV bandgap with very similar absorption behavior to ($FA_{0.83}Cs_{0.17}$)Pb($I_{0.66}Br_{0.34}$)$_3$ despite the lower Br content. The bandgap trends extracted from UV-Vis-NIR data match the slight changes in lattice constant observed in the XRD patterns.

We further explore the effect of the composition on optoelectronic properties by measuring AIPL on spin coated films for promising FA-GA-Cs compositions and comparing with MAPb(I,Br)$_3$ and ($FA_{0.83}Cs_{0.17}$)Pb(I,Br)$_3$ as shown in Figure 5.4 (AIPL statistics shown in Figure 5.6). Both of the FA-GA-Cs compositions of interest yield PLQY of ~4.5% and ΔE_F of >91% of the Shockley-Queisser limit, which is a considerable improvement over the MA and FA-Cs films. A detailed explanation of the quasi-Fermi level splitting calculations and results of fitting the AIPL spectra to a unified photoluminescence model[54] are presented in Figure 5.8. We also use the sub-bandgap absorption model extracted from these AIPL spectra[54] to calculate $\Delta E_{F,rad}$ for each composition which is presented in Table 5.2. The ($FA_{0.33}GA_{0.19}Cs_{0.47}$)Pb($I_{0.66}Br_{0.34}$)$_3$ has the greatest sub-bandgap absorption and thus the greatest difference between $\Delta E_{F,rad}$ and $\Delta E_{F,SQ}$ of the films considered, but the defect chemistry is such that the impact from suppressed non-radiative recombination far exceeds the additional losses from increased sub-bandgap absorption. Indeed, the $\Delta E_F/\Delta E_{F,SQ}$ achieved for both ($FA_{0.33}GA_{0.19}Cs_{0.47}$)Pb($I_{0.66}Br_{0.34}$)$_3$ and

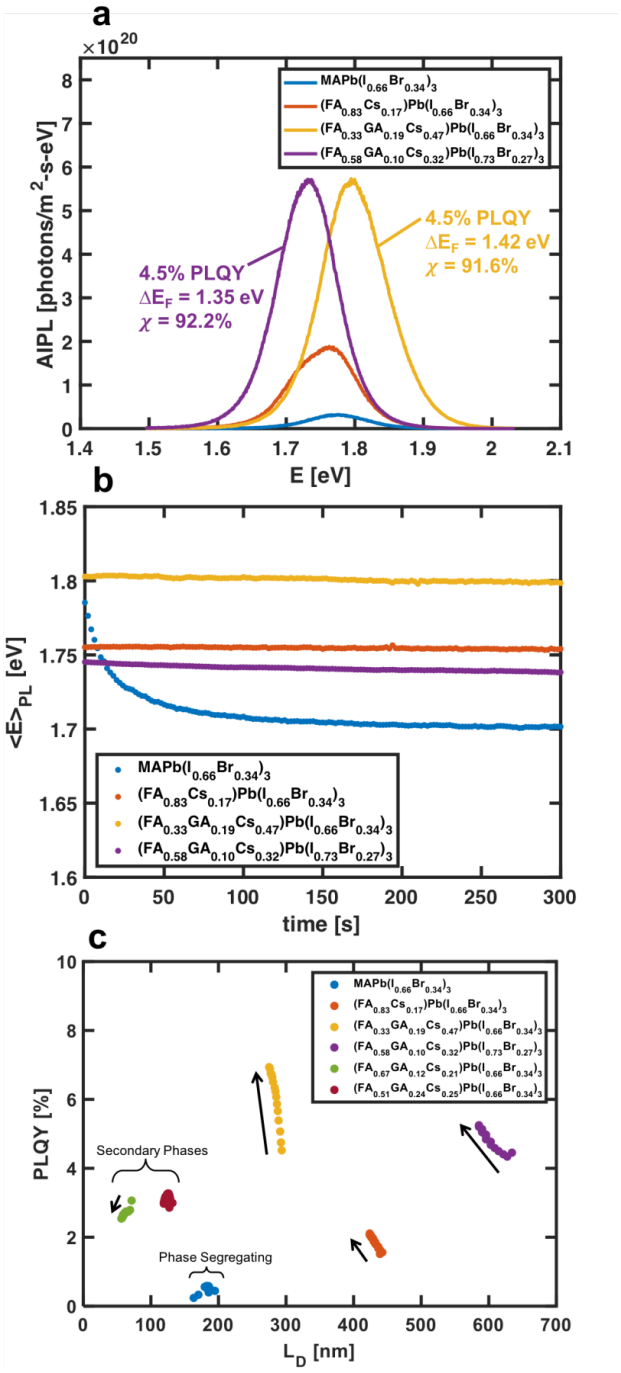

Figure 5.4**. AIPL and PL-L_D results for spin coated mixed-halide films with select A-site compositions**. (a) Characteristic AIPL spectra for each composition (spectrum with median PLQY shown). (b) Mean PL emission energy evolution with time, where PL peak red shift suggests phase segregation. (c) PL and L_D evolution with 2.5 minutes' illumination for various films. Absolute intensity PL measurements were collected at 1 Sun photon flux (541 W/m^2 with a 532nm cw laser for a-b and 657 W/m^2 of ~438nm Blue LED for c).

$(FA_{0.58}GA_{0.10}Cs_{0.32})Pb(I_{0.73}Br_{0.27})_3$ are on par with the $V_{OC}/V_{OC,SQ}$ record for ~1.6eV bandgap HPs[9], indicating that the optoelectronic quality for high-bandgap HPs can be as high as the ~1.6eV variants.

Fabrication of phase stable HPs is important in realization of multi-junction devices with stable power output. Although $(FA,Cs)Pb(I,Br)_3$ has been shown to be relatively phase stable[16, 37], some reports have shown signs of phase instability[36, 42], and thus investigators have concluded that the phase stability of any composition depends strongly on the fabrication scheme and resulting film morphology, thickness, and defect concentration[35, 104, 124]. Other work has shown that although $(FA,Cs)Pb(I,Br)_3$ is phase stable at 1 Sun illumination or current injection, it phase segregates when subject to higher carrier densities[51]. The long term operational stability of the mixed-phase has not yet been determined for any composition. Several mechanisms to describe relative phase stability have been proposed, such as polaron formation at high carrier densities[66] or differences in the dependence of formation free energy between mixed and I-rich domains on carrier density[102]. We studied phase stability of the mixed-halide phase by measuring confocal AIPL with time upon 1 Sun illumination. A PL peak red-shift is indicative of formation of an I-rich phase with locally lower bandgap where carriers accumulate before radiative recombination[38]. The evolution of mean PL emission energy (the first moment of the emission spectrum as a function of photon energy) with time is presented in Figure 5.4b, which shows a PL emission energy decrease from 1.79 eV to 1.70 eV in the first 60 s of illumination for the $MAPb(I,Br)_3$ film. All other films show stable PL emission energies with time, although the $(FA,Cs)Pb(I,Br)_3$ PL spectra have a low energy peak shoulder that could indicate a small amount of phase segregation in this film (see Figure 5.12) . The absence of the low-energy shoulder in $(FA,GA,Cs)Pb(I,Br)_3$ spectra suggests this composition further suppresses phase segregation. To better understand the origin of

the enhanced phase stability in specific alloys, we conducted discharge current measurements to detect ion activation barriers (see Figure 5.13). These measurements reveal a constant ion migration activation barrier for various A-site compositions, suggesting that phase stability is not dependent on the ion mobility in these films, but rather the increased microstrain thermodynamically stabilizes the mixed-halide phase, supporting findings by Draguta *et al.*[102]

In earlier work we discussed the importance of quantifying transport simultaneously with PLQY to determine if improvements in radiative efficiency are accompanied with decreases in diffusion length[37]. Thus, we measured mean carrier diffusion length (L_D) on these films as shown in Figure 5.4c, which plots the PLQY and L_D evolution parametrically with time for several high bandgap HPs throughout a 2.5 min illumination (measurement technique is described in SI). In some cases, the FA-GA-Cs alloys have quite low L_D, even lower than the phase-segregating $MAPbI_3$. XRD measurement (see Figure 5.14) reveals that these cases with low L_D correspond with films with high fraction of secondary phases, indicating that GA is not fully incorporated into the HP lattice. Other cases with relatively phase pure films show that the FA-GA-Cs alloys achieve higher PLQY than FA-Cs films while maintaining similar L_D.

Analysis of these ΔE_F differences for the high-bandgap compositions studied gives insight on the origin of higher non-radiative recombination rates typically observed for the high-bandgap HPs. We consider four possible hypotheses for the lower defect tolerance of high-bandgap HPs, which are discussed in SI. To enhance our understanding of defects in high bandgap HPs, we also studied large-grain films fabricated with SCN^- additive (Figure 5.15 and 5.16). Of our four hypotheses, we conclude there are two possible origins of the higher non-radiative recombination rates in conventional high bandgap HPs: (i) phase segregation is not eliminated even in films that show stable PL emission with time, which facilitates non-radiative recombination at I-rich phase

boundaries or (ii) the higher non-radiative rates observed in high bandgap perovskites arises from changing the position of band edges relative to the bulk defect energy levels (considered quantitatively with Shockley-Reed-Hall non-radiative recombination simulations and shown in Figure 5.17). Whether (i) or (ii) is the primary cause, it is clear that FA-GA-Cs alloys suppress this mechanism to enable lower non-radiative recombination rates.

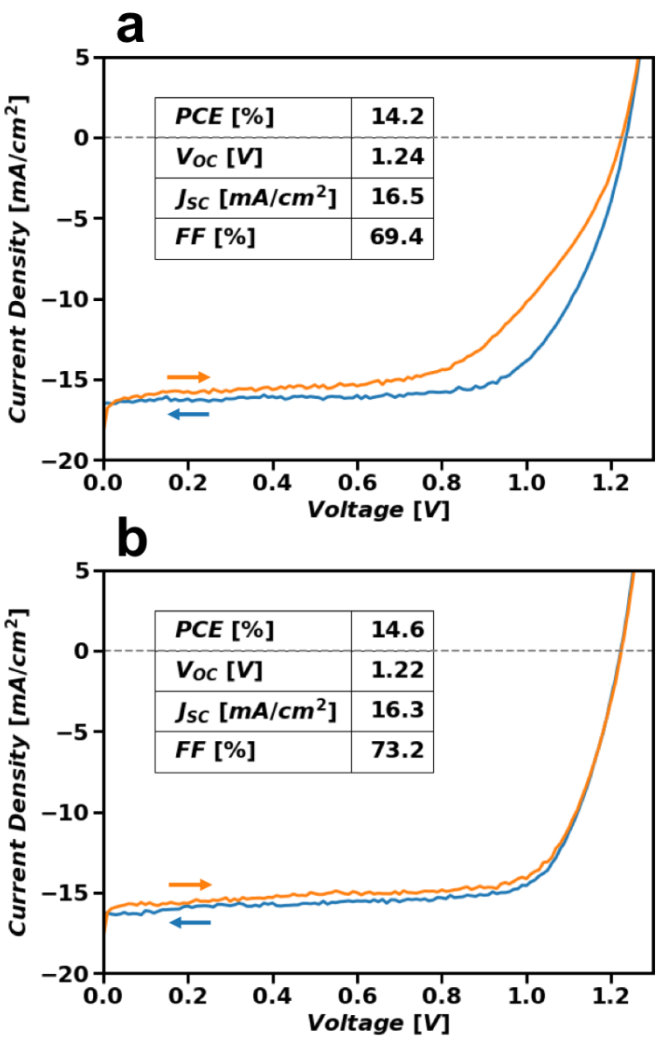

Figure 5.5. **Current-Voltage analysis for completed PV device from $(FA_{0.58}GA_{0.10}Cs_{0.32})Pb(I_{0.73}Br_{0.27})_3$ films** with ITO / PTAA / HP / ICBA / bis-C_{60} / Ag architecture (so called "p-i-n" architecture). (a) J-V for a champion V_{OC} device. (b) J-V for a champion power conversion efficiency device.

The motivation for finding high bandgap absorbers with lower bulk non-radiative recombination rates is ultimately to realize high-bandgap, high V_{OC} devices. Thus, we performed some preliminary studies of the device performance of our FA-GA-Cs alloys. The AIPL, XRD, UV-Vis-NIR, and L_D data suggest that the $(FA_{0.58}GA_{0.10}Cs_{0.32})Pb(I_{0.73}Br_{0.27})_3$ composition has excellent quality with ideal bandgap (1.75eV) for the top cell in a two-terminal tandem with c-Si or CIGS. Realization of two-terminal tandems with c-Si[22], CIGS[23], or HP[19] bottom cells each requires p-i-n top cell architecture to achieve the highest overall efficiency. We implemented our 1.75eV FA-GA-Cs film into a p-i-n device stack with all low temperature processing directly translatable to multi-junction devices. We attained V_{OC} up to 1.24 V (see Figure 5.5) which is a considerable improvement over the previous record of 1.17 V for p-i-n devices with similar bandgap[108]. The difference between the 1.35 eV measured ΔE_F for neat films used for the 1.24 V device V_{OC} indicates that the V_{oc} loss in devices are due to significant interfacial recombination losses or band misalignment rather than the previously observed optoelectronic quality of absorber[19, 37]. Other work demonstrating 1.23-1.24 V with similar bandgap HPs[12, 125, 126] all use the n-i-p architecture and employ passivation strategies such as KI treatment[125], formamide-assisted crystallization[126], or solvent anneal with SCN^- [12]. Our result of high V_{OC} with a simple solvent wash fabrication demonstrates that FA-GA-Cs high bandgap HP is inherently better and a likely route to even higher V_{OC} with proper surface passivation and interface engineering. Further device studies to translate the complete potential of compositional platform developed here will be part of our continued evaluation in future work.

In summary, we used high-throughput combinatorial spray coating to identify two $(FA,GA,Cs)Pb(I,Br)_3$ compositions with bandgaps 1.84 and 1.75 eV with unprecedented optoelectronic quality for this bandgap range. We explored many compositions in the FA-GA-Cs

alloy space and determined that although GA can be incorporated into the perovskite lattice, there are significant compositional constraints and formation of the cubic perovskite phase is dependent on mean tolerance factor and halide ratio. To verify the trends observed with spray coating experiments, we spin coated films of select compositions to confirm excellent morphology and transport for certain $(FA,GA,Cs)Pb(I,Br)_3$ materials. Through photoluminescence modeling we reveal that the increased microstrain in $(FA,GA,Cs)Pb(I,Br)_3$ is detected by an increase in modeled sub-bandgap absorption, yet the impact of additional sub-bandgap absorption on ΔE_F is overshadowed by suppression of non-radiative recombination. By considering multiple hypotheses, we propose the higher non-radiative recombination rates observed in conventional high bandgap HPs arise from either defects at persistent phase boundaries or bulk defects that lie progressively deeper within the bands as the band edges move. With ΔE_F exceeding 91% of the Shockley-Queisser maximum and record device V_{OC} of 1.24 V, we show that $(FA,GA,Cs)Pb(I,Br)_3$ films suppress non-radiative recombination and the material quality of high-bandgap HPs is not an inherent limitation in realization of high efficiency tandem multi-junction devices.

ACKNOWLEDGEMENTS We acknowledge financial support from the U.S. Department of Energy SunShot Initiative, Next Generation Photovoltaics 3 program and Award DE-EE0006710. A. R. and A. K.-Y. J. acknowledge partial support from the Office of Naval Research (under ONR N00014-17-1-2260). This material is based in part upon work supported by the State of Washington through the University of Washington Clean Energy Institute and via funding from the Washington Research Foundation (supporting R.J.S. and A.R. with CEI Fellowship).

SUPPORTING INFORMATION. Experimental methods (Spray coating/spin coating film fabrication, device fabrication, confocal absolute intensity photoluminescence, wide-field PL and

photoconductivity measurements, discharge current measurements, JV-characterization, UV-Vis-NIR, XRD, and SEM), quasi-Fermi level splitting calculations, radiative limit calculations, Williamson-Hall measurements of NIST standard, spray coating supporting results, XRD/UV-Vis-NIR of additional compositions, determination of bandgap from UV-Vis-NIR, discharge current measurements for ion migration studies, and Shockley-Reed-Hall simulations details and results.

5.4 Supporting Information

5.4.1. Experimental Methods

5.4.1.1. Spray Coating Set-up and Film Fabrication

Soda-lime glass substrates (100mm long by 15mm wide) were cleaned with a four-step procedure by sonicating for 10 minutes each in (1) Alconox and DI water, then (2) pure DI water, then (3) acetone, and finally (4) 2-propanol. Shortly before spray coating, the substrates were cleaned for 10 minutes in an Argon plasma. All compositional gradients were deposited in a N_2 atmosphere using an ultrasonic Sono-Tek spray coater contained inside a glovebox with a hot plate maintained at 125°C. Inks were prepared from MAI, FAI, GAI, CsI, PbI_2, and/or $PbBr_2$ as a stoichiometric 0.13M in a 63/37 v/v dimethylformamide (DMF) / 1,4-dioxane (DO) solution mixture. Perovskite ink was deposited via an ultrasonic spray nozzle, which translated above the substrate, delivering ink at a constant rate of 150 μL/min. A gradient of composition was achieved by mixing streams delivered by two pumps of changing flow rates, one ramping up and one ramping down such that a constant overall flow rate was maintained. The nozzle translated at a speed of 1 mm/s along the length of the substrate, oscillating across the width of the substrate for full coverage. Spray coated films were annealed immediately post-deposition at 125°C for 5 min

and then transferred to a sealed container with a quartz glass top for characterization without exposure to air.

5.4.1.2. Spin Coating Film Fabrication

Spin coated films were prepared on 15mm by 15mm glass substrates cleaned with a procedure identical to that of spray coated substrates. All ink preparation, spin coating, and annealing was performed in a N_2-filled glovebox. Inks were prepared in ~1.0M solutions from MAI, FAI, GAI, CsI, PbI_2, $PbBr_2$, and/or $Pb(SCN)_2$, all dissolved in 80/20 v/v mixtures of DMF/DMSO. We used 2% Pb-poor inks, achieved by adding 1.0M total AI + 0.98M total PbX_2. We note that all compositions discussed in this work are "nominal" compositions, or compositions of the precursor ink, as is commonly reported in the perovskite literature. Spin coating was performed in a two-step process: 6 s at 1000 rpm followed by 20 s at 4000 rpm, with 0.7mL of toluene dispensed with 15 s remaining on the second step. The films were then annealed at 125°C for 10 min and transferred to a sealed container with a quartz glass top for characterization.

5.4.1.3. Device Fabrication and Testing

Devices where fabricated with ITO / PTAA / Perovskite / ICBA / bis-C_{60} / Ag architecture. Commercial ITO glass (15 ohm/sq, Colorado Concept Coatings) was cleaned in a sonication bath for 10 minutes' each in 5% Alconox in deionized (DI) water, then acetone, then 2-propanol, then was plasma cleaned for 10 minutes in Ar plasma. The substrates where transferred into a N_2 filled glovebox, where PTAA was spin coated from a 5 mg/mL solution at 4000 rpm for 40 s, then anneal at 60 ˚C for 10 min. The perovskite solvent system was changed slightly to achieve smoother films necessary for efficient planar devices. The $(FA,GA,Cs)Pb(I,Br)_3$ ink was prepared in ~1.0M solutions from FAI, GAI, CsI, PbI_2, and $PbBr_2$, all dissolved in 9/8 v/v mixtures of N-methyl 2-pyrrolidone (NMP)/DMF. We used 2% Pb-poor inks, achieved by adding 1.0M total AI + 0.98M

total PbX_2. The solution was spin coated on top of PTAA at 4000 rpm for 45 sec, with 0.7mL of toluene dispensed with 20 s remaining on the second step, then annealed at 100 ˚C for 10 min. After anneal, the fullerene layers (doped-ICBA and bis-C_{60}) were deposited precisely as described previously[127]. Finally, an 150nm Ag electrode was deposited with thermal evaporation at 2 Å/s.

JV testing was conducted in a N_2-filled glovebox using a 450 W Oriel xenon lamp and Keithley 2400 Source Meter. Photon flux was precisely calibrated to AM1.5GT using a Si-photodiode with KG5 filter. JV curves where collected with a forward sweep immediately followed by reverse sweep with a modest sweep rate of 0.1 V/s. Device area was defined by the Ag evaporated area which was verified to be 3.43 mm^2.

5.4.1.4. Confocal Absolute Intensity Photoluminescence

Confocal absolute intensity PL was performed as reported previously[41]. Samples were excited with a 532nm laser and calibrated to 1 Sun above bandgap photon flux (for a 1.75eV bandgap material based on AM1.5GT spectrum) using an Oriel optical power meter and beam profiler. Photoluminescence spectra were collected with a Horiba LabRAM HR-800 with 10x objective using a monochromator blazed at 500mm with 150 gr/mm with confocal hole set to 800 μm. Calibration of the photon detection rate was performed with a blackbody source (IR-301, Infrared Systems Development) at 1050 ˚C with a pinhole size of 10 μm to determine a calibration factor for photons per count for this system. Statistics for spin coated films were collected by taking 25 measurements spatially distributed across the substrate with illumination times of 1s each. Statistics for spray coated films were collected in a grid of 15 measurements along the width and 115 measurements along the length of the gradient. The statistics of each set of 15 lateral measurements were averaged to create a series of 115 data points describing the characteristics along the length of the gradient.

5.4.1.5. Wide-field PL and Photoconductivity Measurements

Measurements of wide-field absolute intensity PL and photoconductivity were collected concurrently as described previously[37]. To enable four-point photoconductivity measurements, 80nm thick Au contacts were deposited with thermal evaporation at a rate of 2Å/s using a shadow mask to define the four-point geometry described elsewhere[37]. Both wide-field and photoconductivity measurements were collected with the samples enclosed in a temperature controlled stage (Linkam Scientific LTSE420-P) set to 20.0°C and filled with a N_2 atmosphere, with the N_2 purge rate set at 70% of the maximum. Wide-field PL measurements were collected with a Hamamatsu C11440 camera with a 5x objective using blue LED excitation (Lumencor SpectraX, with bandpass filter centered at 438nm) along with a dichroic mirror and emission long-pass filter. The light source was calibrated using Newport 91150 V Si reference diode such that the incident photon flux was equal to the above-bandgap photon flux of the AM1.5 spectrum on a 1.75eV bandgap material. The photoconductivity of films was measured with a four-point geometry with a Keithley 2400 SourceMeter with the electric field induced by the measurement remaining below 10 V/mm.

5.4.1.6. Discharge Current Measurements

Discharge current measurements were conducted following the methods of Game *et. al*[128] to measure the activation barrier to ion migration for various HP films. First, "half-devices" were fabricated with architecture: ITO / NiOx / HP / Au. The NiOx layer was added to prevent shunting for our ~375nm films, although with this asymmetric architecture the discharge current can only be measured in forward bias. ITO glass (15 ohm/sq, Colorado Concept Coatings) was cleaned as described above. The NiOx solution for sol-gel method was prepared as described elsewhere[99], then deposited with spin-coating at 3000 rpm for 60 s, then annealed in air at 350 ˚C for 1 hr. The

NiOx coated substrates where transferred into a N_2 filled glovebox for perovskite layer deposition. Perovskite solution and spin coating were performed precisely as described above. 150 nm of Au was thermally evaporated at a deposition rate of 2 Å/s using a shadow mask with 3.14 mm^2 device area.

Next, the half-devices were transferred into a closed, N_2-filled stage (Linkam Scientific LTSE420-P) with constant N_2 purge. The stage has heating and liquid N_2 elements for temperature control. Thermal grease was used to ensure excellent thermal contact between substrate and temperature stage. The IV measurements and discharge current measurements were conducted with a Keithley 2400 SourceMeter. IV measurements were conducted from 0V to 0.2V at 20 ˚C for all samples which all showed ohmic behavior in this voltage range. Finally, the discharge current measurements were conducted by setting voltage and measuring current in a three step program: set 0V for 20 s, then set +0.2V for 20 s, then set 0V for 20 s. Between the second and third step, the measured current switches to a negative current, which indicates a "discharge current" as ions diffuse back throughout the film. Game *et. al* discuss the origin of the discharge current could be due to either dielectric polarization or capacitive effects due to ion accumulation, yet conclude that characteristic differences in the Q_{dis} dependence on temperature rule out dielectric polarization for temperatures > 160 K[128]. We conducted discharge current measurements in 15 ˚C increments between 50 ˚C and -55 ˚C, although we found Q_{dis} to follow Arrhenius behavior between 50 ˚C and 5 ˚C.

5.4.1.7. UV-Vis, XRD, SEM Characterization

The optical absorbance spectra collected from a PerkinElmer Lambda 1050 UV/vis/NIR spectrometer with an integrating sphere in laboratory atmosphere. Thin film X-ray diffraction

(XRD) measurements (Figure 5.15a) were collected with a Bruker D8 Discover equipped with a Pilatus 100K large-area 2D detector and a Cu anode of wavelength 1.542 Å. The instrument was used with a parallel-beam geometry. For powder XRD measurements (Figure 5.3a,c), the samples were first prepared by scraping off the material deposited on three 1”x1” substrates onto the back (rough) side of a Si wafer, and collecting into a flat, compressed pile with a spatula. Powder XRD was collected with a Bruker D8 Discover equipped with a Lynxeye-XET multi-strip 1D detector. SEM images were collected on Au-coated films with a FEI XL830 Dualbeam SEM-FIB.

5.4.2. Determination of Quasi-Fermi Level Splitting from Photoluminescence

There are three primary methods for calculation of quasi-Fermi level splitting (ΔE_F) from photoluminescence data. Here, we review each and compare the results of each when applied to the hybrid perovskites[41].

5.4.2.1. Quasi-Fermi Level Splitting from PLQY

The simplest method uses an expression proposed by Ross:[56]

$$\Delta E_F = \Delta E_{F,max} + kT \ln PLQY_{Ext} \quad (5.1)$$

where $PLQY_{Ext}$ is the external photoluminescence quantum yield. This method, which we will call the "$PLQY_{Ext}$" method, is simple and can be used to estimate quasi-Fermi level splitting if little is known about the material. One limitation is ambiguity about what is the most appropriate value for $\Delta E_{F,max}$. If little is known about the material, we can do a Shockley-Queisser calculation assuming the bandgap equals the PL peak position and replace $\Delta E_{F,max}$ with $\Delta E_{F,SQ}$. However, this can overestimate the quasi-Fermi level splitting if there is a significant portion of sub-bandgap absorption and emission. More appropriately, if $\Delta E_{F,rad}$ is determined, it can be used as the $\Delta E_{F,max}$ in eq. 5.1.

For the data presented in Figure 5.4 and Figure 5.6, we use the $PLQY_{Ext}$ method (eq. 5.1) with calculated $\Delta E_{F,rad}$ and T= 320 K. This temperature is used as a conservative value in the range of reasonable temperatures. The range of reasonable temperatures is taken to be between room temperature (~295 K) and an elevation of about 60 C (355 K), given than the films are illuminated with 1 Sun intensity and are not very thermally conductive. In addition, full peak fits and high energy tail fits (discussed below yield fitted temperatures close to 320 K). The data in Figure 5.2 is also calculated with the $PLQY_{Ext}$ method, yet $\Delta E_{F,rad}$ is not available for each data point in the gradients, so we alternatively use only the integrated PL above the peak position to determine

$PLQY_{Ext}$ for eq. 5.1, we use $\Delta E_{F,SQ}$ as $\Delta E_{F,max}$, and use temperature = 350K, which likely gives an underestimation of the true ΔE_F.

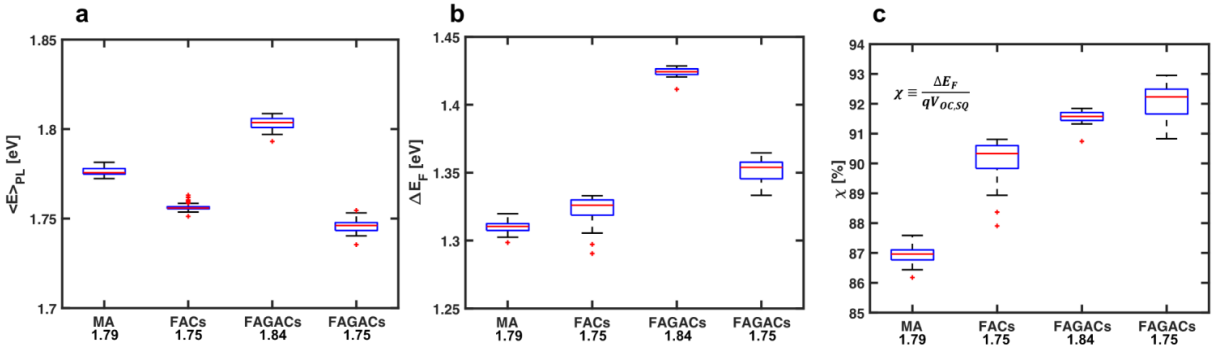

Figure 5.6**. Calculated ΔE_F using $PLQY_{Ext}$ method** with T = 320K. Statistics for 121 spectra are presented (the same films shown in Figure 5.4). (a) mean PL emission energy (b) calculated ΔE_F with $PLQY_{Ext}$ method (c) optoelectronic quality χ (ΔE_F as a % or SQ limit).

5.4.2.2. Quasi-Fermi Level Splitting from Fitting the High-Energy Tail of the PL Peak.

Alternatively, the "high energy tail fit" method, which fits the high energy tail of the PL peak to the generalized plank law. Rearranging the plank law and employing the Wein approximation yields

$$\ln\left[\frac{I_{PL}(E)h^3c^2}{2\pi E^2}\right] = -\frac{1}{kT}E + \frac{\Delta E_F}{kT} \qquad (5.2)$$

which can be fit with a line when the photoluminescence is plot on a log-scale. Although this is a relatively simple method, the fit temperature (and thus ΔE_F) is dependent on precisely which energy window is used for the linear fit suggesting that there is not necessarily a unique T-ΔE_F combination that gives the best fit. Regardless, we calculated ΔE_F for comparison and results are presented in Figure 5.6.

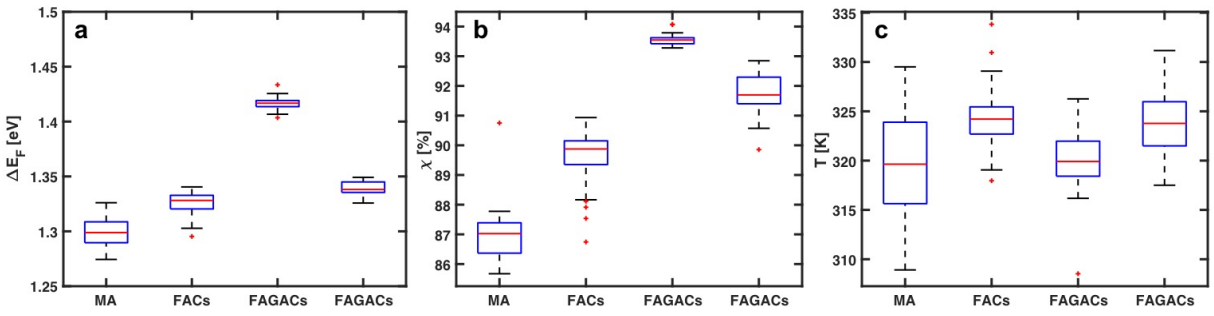

Figure 5.7**. Calculated ΔE_F (a), percent of ΔE_F /$\Delta E_{F,SQ}$ (b), and fit temperature (c) using the high-energy tail fit method**. This shows the same trends and similar ΔE_F as calculated with the $PLQY_{ext}$ or full peak fit methods.

5.4.2.3. Quasi-Fermi Level Splitting from Full-Spectra Fit of PL Peak.

The third method used to calculate ΔE_F is the "full peak fit" method which follows the procedure of Katahara and Hillhouse[54]. We use a modified Lasher-Stern-Würfel equation[57, 58] given by

$$I_{PL}(E) = \frac{2\pi E^2}{h^3 c^2} \cdot \frac{a(E, \Delta E_F, T)}{\exp\left(\frac{E - \Delta E_F}{kT}\right) - 1} \tag{5.3}$$

where the absorption coefficient is modeled by

$$\alpha(E) = \frac{\alpha_0}{\gamma 2\Gamma(1 + 1/\theta)} \int_{-\infty}^{E_g} \left(\exp\left(-\left|\frac{u}{\gamma}\right|^{\theta} \right) \sqrt{(E - E_g) - u} \right) du \tag{5.4}$$

where Γ is the gamma function, γ is an energy broadening parameter for sub-bandgap absorption, θ is an exponent to describe the form of the sub-bandgap tail, and $E_g$is the direct transition energy[54]. The full form of eq. 5.3 used in this study is given as equation 22 in Katahara and Hillhouse[54], which accounts for non-zero band occupation in the absorption model. The modified absorption coefficient, which incorporates occupation effects (assuming symmetric splitting of quasi-Fermi levels from mid gap) is given by

$$\alpha(E, \Delta E_F) = \alpha_{0K}(E)\left(1 - \frac{2}{e^{\frac{E-\Delta E_F}{2kT}} + 1}\right) \quad (5.5)$$

where $\alpha_{0K}(E)$ is the absorption coefficient model at zero band occupation (given by eq. 5.4). The photoluminescence peak data was fit with eq. 5.3 using Levenberg-Marquardt non-linear least squares fit, with fitting parameters E_g, ΔE_F, θ, γ and T and assuming $\alpha_0 d$ is 3.75. We note that the full peak fit requires a single photoluminescence peak (without shoulder features that indicate a secondary transition energy), so we only fit the (FAGACs) films which do not have any peak shoulder features (see low energy shoulder in FACs films shown in Figure 5.13). The full peak fit results are presented in Figure 5.7 and Table 5.1. Interestingly, we see that the full-peak fit deviates from the experimental data at energies far below the bandgap. This suggests that the band tails of these materials have some Urbach like (θ = 1) behavior, but that this is only apparent after the decay of the higher exponent behavior. Thus, we omitted the data in the Urbach region to fit the other parameters. We note that the fit temperature is slightly lower than room temperature (which gives a slight over-estimation of ΔE_F) but is within expected error.

Collectively, analysis of the three methods for calculating ΔE_F all support the findings that (a) the ΔE_F for both (FAGACs) films is an improvement over (FACs) or MA films and (b) the ΔE_F for (FAGACs) is > 91% of the Shockley-Queisser limit.

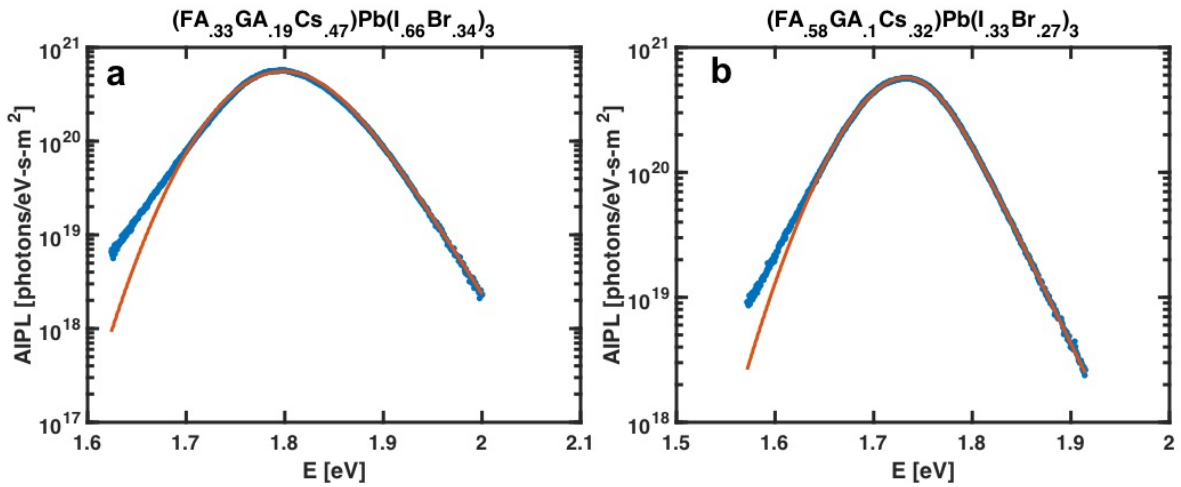

Figure 5.8**. Full peak fit for spin coated FA-GA-Cs films** with composition (a) $(FA_{0.33}GA_{0.19}Cs_{0.47})Pb(I_{0.66}Br_{0.34})_3$ and (b) $(FA_{0.58}GA_{0.10}Cs_{0.32})Pb(I_{0.33}Br_{0.27})_3$. The fit assumes $\alpha_0 d$ is 3.75 (thickness d was measured to be 375nm); fit parameters and calculated χ percent of $\Delta E_{F,SQ}$ are presented in Table 5.1.

Table 5.1 **Full peak fit parameters**

	FAGACs – 1.84 E_g	FAGACs – 1.75 E_g
θ	1.96	1.50
γ [eV]	0.063	0.037
E_g [eV]	1.85	1.75
ΔE_F [eV]	1.48	1.40
T [K]	285	288
χ	94.3%	94.9%

The full peak fit gives us a model for sub-bandgap absorption that describes measured data. Thus, we can us this absorption model to determine the radiative limit quasi-Fermi level splitting, $\Delta E_{F,rad}$, which is typically lower than the Shockley-Queisser limit due to the presence of sub-bandgap absorption and emission. We calculate $\Delta E_{F,rad}$ numerically with an internal balance equation (Generation = Recombination) where the only recombination considered is radiative. This balance can be expressed as

$$G(E_g, \theta, \gamma, \Delta E_F) = \int_0^\infty I_{PL}(E)dE \tag{5.6}$$

where $I_{PL}(E)dE$ is given by equations 5.3-5.5 and the generation flux G is given by

$$G(E_g\theta, \gamma, \Delta E_F) = \int_0^\infty b_{AM1.5GT}(E)\left(1 - \exp\left(-d\alpha\left(E, E_g, \theta, \gamma, \Delta E_F\right)\right)\right)dE \tag{5.7}$$

where d is film thickness and $b_{AM1.5GT}(E)$ is the AM1.5GT spectral photon flux. We use the sub-bandgap absorption model described in eq. 5.4-5.5 in the expression for absorptivity, accounting for occupation effects. The $\Delta E_{F,rad}$ calculations are compiled below in Table 5.2. We note that for the MA, FACs, and FACs + SCN films we used the best full peak fit to estimate θ and γ despite peak shoulders that prevent the model from converging on a perfect fit. The input θ, γ, and E_g and calculated $\Delta E_{F,rad}$ and $\Delta E_{F,SQ}$ are presented in Table 5.2.

Average sub-bandgap absorptivity, $\overline{a_{SB}}$, is a single metric to quantify the amount of sub-bandgap

Table 5.2 $\Delta E_{F,rad}$ **Calculation Results**

	E_g [eV]	θ	γ [meV]	$\Delta E_{F,SQ}$ [eV]	$\Delta E_{F,rad}$ [eV]	$\Delta E_{F,SQ} - \Delta E_{F,rad}$ [meV]	FWHM [eV]	$\overline{a_{SB}}$
MA	1.79	1.51	37	1.502	1.498	4	99	3.14E-03
FACs	1.75	1.51	39	1.465	1.458	7	109	3.49E-03
FAGACs	1.84	1.96	63	1.549	1.527	22	111	5.08E-03
FAGACs	1.75	1.5	37	1.465	1.461	4	102	3.15E-03
FACs + SCN	1.75	1.24	27	1.465	1.465	0	93	2.60E-03

absorptivity for a material and is given by

$$\overline{a_{SB}} = \frac{1}{E_g}\int_0^{E_g}\left(1 - \exp\left(-d\alpha(E, \Delta E_F)\right)\right) dE \tag{5.8}$$

5.4.3. Determination of Domain Size and Strain using the Williamson-Hall Method.

Peak broadening can arise due to: (i) the instrument-induced broadening, (ii) size broadening, (iii) strain broadening, or (iv) the presence of impurities with slightly shifted XRD peak positions. We measured all samples on the same instrument (a Bruker D8 Discover with Cu K✔ source filtered with single crystal diffractive optics), and found the FWHMs to be well above the instrument broadening observed for LaB_6 standard, ruling out (i). These samples have minor phase impurities, where possible secondary phases have distinct peak 2θ positions (see Figure 5.15), ruling out (iv).

The best way to distinguish between size and strain from an XRD pattern is to perform Rietveld refinement . When we performed XRD characterization on the films (and powders obtained from scraping films from the substrate), we observed preferred orientation effects that altered relative peak heights. Further, the A-site cations like FA and GA have rotational motion and cannot be described with fixed atom positions, even with large thermal parameters and fractional occupations. If only one of these complications were present (preferred orientation or rotational motion of asymmetric A-site cations), perhaps refinement could be used with appropriate parameters. However, these factors combine to yield an unstable refinement, with unreasonably high estimated standard deviation values for many refined parameters.

Due to the limitations of Rietveld refinement for this dataset, we determined that a Williamson-Hall analysis is more appropriate for analysis of relative size and strain trends. In order to insure that we have correctly accounted for instrumental broadening, we first measured our instrumental broadening function using a large-domain low-strain LaB_6 XRD calibration sample. Next, we obtained NIST standard SRM 1979 for domain size and strain calibration, measured the samples on our lab instrument, applied the Williamson-Hall analysis to the data, and compared with that

reported by NIST. The W-H plot of the NIST standard samples collected from our diffractometer are shown in Figure 5.9. A W-H plot of an additional HP sample is shown in Figure 5.10.

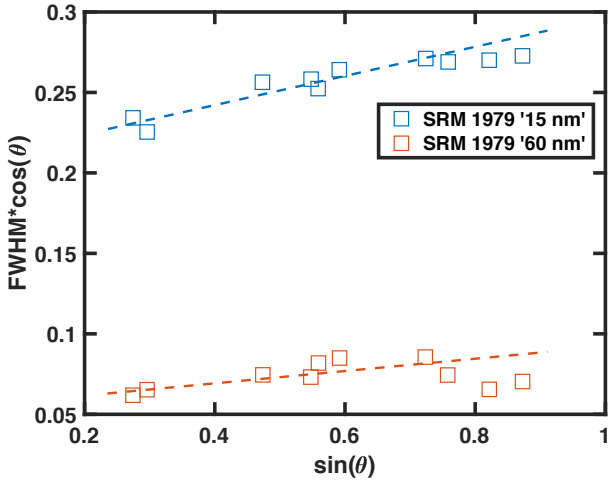

Figure 5.9**. Williamson-Hall plot of NIST line shape standards** SRM 1979, which contains two differently sized ZnO nanoparticles. For clarity, we omit the XRD peaks where growth or deformation faults effect line broadening in the Williamson-Hall fit (following the work of Cline *et. al*[122]). Comparison of this result with the Williamson-Hall plot of Cline *et. al* helps inform the merits and limitations of the Williamson-Hall technique. We extract size of 38.3 and 148 nm for the two differently sized nanoparticles, compared to 25.6 and 92.2 nm reported by Cline *et. al*, showing that our sizes are consistently about 50% greater. For calculated strain, we measure 0.047% and 0.017% for the smaller and larger particles respectively. Cline *et. al* do not report calculated strain directly, but their slopes are very similar to ours, where the larger particle has very little strain and the smaller particle has slightly larger, identical to our observation. Measuring the NIST line shape and comparing our Williamson-Hall plot an identical plot prepared by the standard developers[122] confirms that while the quantitative results are not precise, the measured trends can be appropriately applied to evaluate relative size and strain in our dataset.

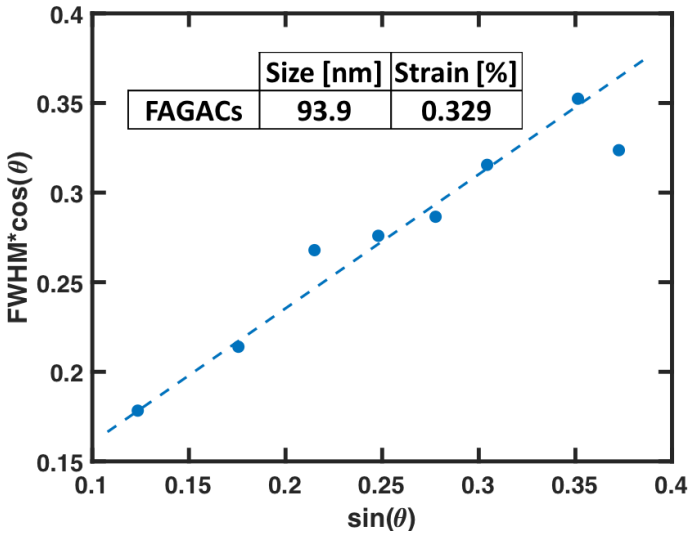

Figure 5.10**. Williamson-Hall plot of a $(FA_{0.58}GA_{0.10}Cs_{0.32})Pb(I_{0.73}Br_{0.27})_3$ powder sample** prepared as described in methods (compare with other compositions presented in main text Figure 5.3c). The strain observed for this composition is higher than $MAPb(I_{0.66}Br_{0.34})_3$ but lower than $(FA_{0.33}GA_{0.19}Cs_{0.47})Pb(I_{0.66}Br_{0.34})_3$ (about equal to $(FA_{0.83}Cs_{0.17})Pb(I_{0.66}Br_{0.34})_3$). This trend suggests both A site and X site contribute to microstrain. This analysis shows the raw output from analysis with JADE software, which uses a LaB_6 pattern for instrument profile function, peak profile fitting to remove contribution of $K\alpha_2$ peak to broadening, and using σ^2 weighing in Williamson-Hall linear fit. Note the error estimates and e.s.d. values of size and strain (in parentheses), which are similar order as the samples in Figure 5.3c (error bars omitted in Figure 5.3c for clarity, but shown below in Figure 5.11).

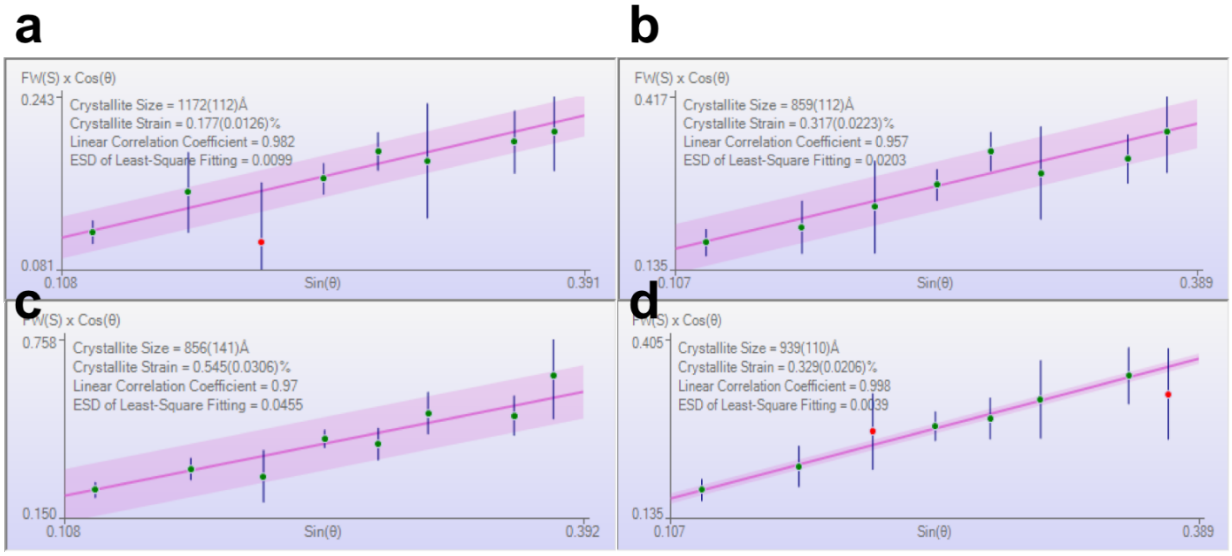

Figure 5.11. **Williamson-Hall plots of (a) $MAPb(I_{0.66}Br_{0.34})_3$, (b) $(FA_{0.83}Cs_{0.17})Pb(I_{0.66}Br_{0.34})_3$, (c) $(FA_{0.33}GA_{0.19}Cs_{0.47})Pb(I_{0.66}Br_{0.34})_3$ and (d) $(FA_{0.58}GA_{0.10}Cs_{0.32})Pb(I_{0.73}Br_{0.27})_3$** demonstrating calculated error from peak FWHM determination and Williamson-Hall fit. Analysis is conducted in JADE.

The compiled Williamson-Hall Results in are shown in Table 5.3. The ESD indicates the estimated standard deviation, compiled using JADE software which accounts for error in the instrument response function, peak full width half max determination, and Williamson-Hall fit. The ESD values for both size and strain are quite low.

Table 5.3 **Williamson-Hall Results**

	Size [nm]	Size ESD [nm]	Strain [%]	Strain ESD [%]
$MAPb(I_{0.66}Br_{0.34})_3$	117	11.2	0.117	0.013
$(FA_{0.83}Cs_{0.17})Pb(I_{0.66}Br_{0.34})_3$	85.9	11.2	0.317	0.022
$(FA_{0.83}Cs_{0.17})Pb(I_{0.73}Br_{0.27})_3$	80.0	8.8	0.193	0.023
$(FA_{0.33}GA_{0.19}Cs_{0.47})Pb(I_{0.66}Br_{0.34})_3$	85.6	14.1	0.545	0.031

$(FA_{0.58}GA_{0.10}Cs_{0.32})Pb(I_{0.73}Br_{0.27})_3$	93.9	11.0	0.329	0.021

Table 5.4 shows statistics for ionic radii along with their standard devications for four HP compositions. The strain determined from W-H analysis follows the same trend as A-site standard deviation.

Table 5.4 **Ionic radii distribution statistics**

	A-site $< r >$ [Å]	A-site $\sigma/< r >$ [%]	X-site $< r >$ [Å]	X-site $\sigma/< r >$ [%]
$MAPb(I_{0.66}Br_{0.34})_3$	2.17	0	2.12	5.39
$(FA_{0.83}Cs_{0.17})Pb(I_{0.66}Br_{0.34})_3$	2.41	10.1	2.12	5.39
$(FA_{0.83}Cs_{0.17})Pb(I_{0.73}Br_{0.27})_3$	2.41	10.1	2.14	5.02
$(FA_{0.33}GA_{0.19}Cs_{0.47})Pb(I_{0.66}Br_{0.34})_3$	2.27	16.9	2.12	5.39
$(FA_{0.58}GA_{0.10}Cs_{0.32})Pb(I_{0.73}Br_{0.27})_3$	2.35	14.1	2.14	5.02

Ionic radii used for Table 5.4 calculation were Cs = 1.88 Å, FA = 2.53 Å, GA = 2.78 Å, I = 2.2 Å, and Br = 1.96 Å.

The microstrain increases from MA to (FA,Cs) then again from (FA,Cs) to (FA,GA,Cs) indicating the tunability of mean displacement of ions away from lattice positions can be achieved through A-site alloying. Recently, Ghosh *et. al* used ab initio molecular dynamics techniques to probe the impact of size mismatch on the A site by replacing a small amount of FA with Cs or

Rb[129]. Both Ghosh *et. al* and Matsui *et. al* report that as smaller A cations are incorporated, the hydrogen bond strength increases[129, 130]. Further, Ghosh *et. al* find that the smaller cation incorporation results in "locking" of the PbI_6 octahedra tilting, which significantly impedes the tumbling of the FA cation in its cage. The locking of octahedra tilting for mixed A cations is attributed to reduction in electronic disorder (due to reduction in bond angle distributions), enhanced carrier mobility and lifetimes[36, 131], and changes in the HP bandgap and band structure[129, 132]. We suggest that increasing microstrain correlates with locking of the PbI_6 octahedra and reduction in bond angle distributions, and that the (FA,GA,Cs) system has more tightly locked PbI_6 octahedra than the (FA,Cs) system. This thermodynamic stabilization suggested from phase stability studies (Figure 5.4b and 5.13) is possibly linked to tighter locking of the PbI_6 octahedra and increased hydrogen bond strength[129, 130] for (FA,Cs)$Pb(I,Br)_3$ and especially for (FA,GA,Cs)$Pb(I,Br)_3$.

5.4.4. Determination of Bandgap from UV-vis-NIR Absorbance

In the main text, we refer to the bandgap of the four HP compositions of primary interest in this study. We extracted bandgap from a plot of UV-Vis absorbance data, by plotting A^2 vs. E and fitting the linear region as shown in Figure 5.12.

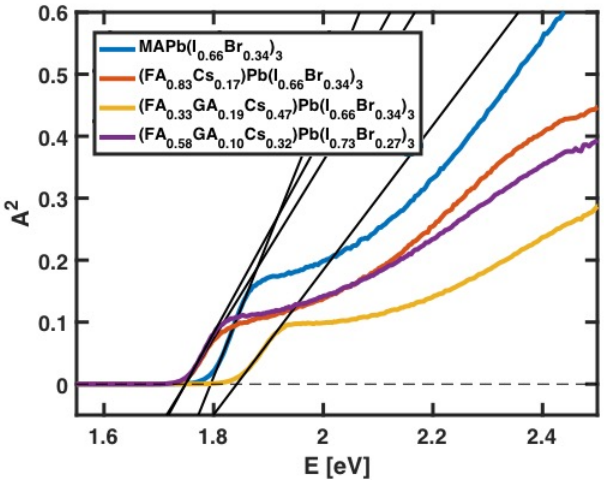

Figure 5.12**. Extracted optical bandgap from fitting linear region in A^2 (Absorbance^2) vs. E plot of spin coated films discussed in main text** (Figures 5.3-5.5).

5.4.5. Phase Segregation Observable from Spectral Fits of PL

The low energy shoulder observied the (FA,Cs)Pb(I,Br)$_3$ PL peak suggests phase segregation persists in this film dispite a stable PL peak energy with time. We plot the residuals of a (FA,Cs)Pb(I,Br)$_3$ peak as well as a (FA,GA,Cs)Pb(I,Br)$_3$ peak (both with 1.75 eV bandgap) to demonstrate this difference, as shown in Figure 5.13.

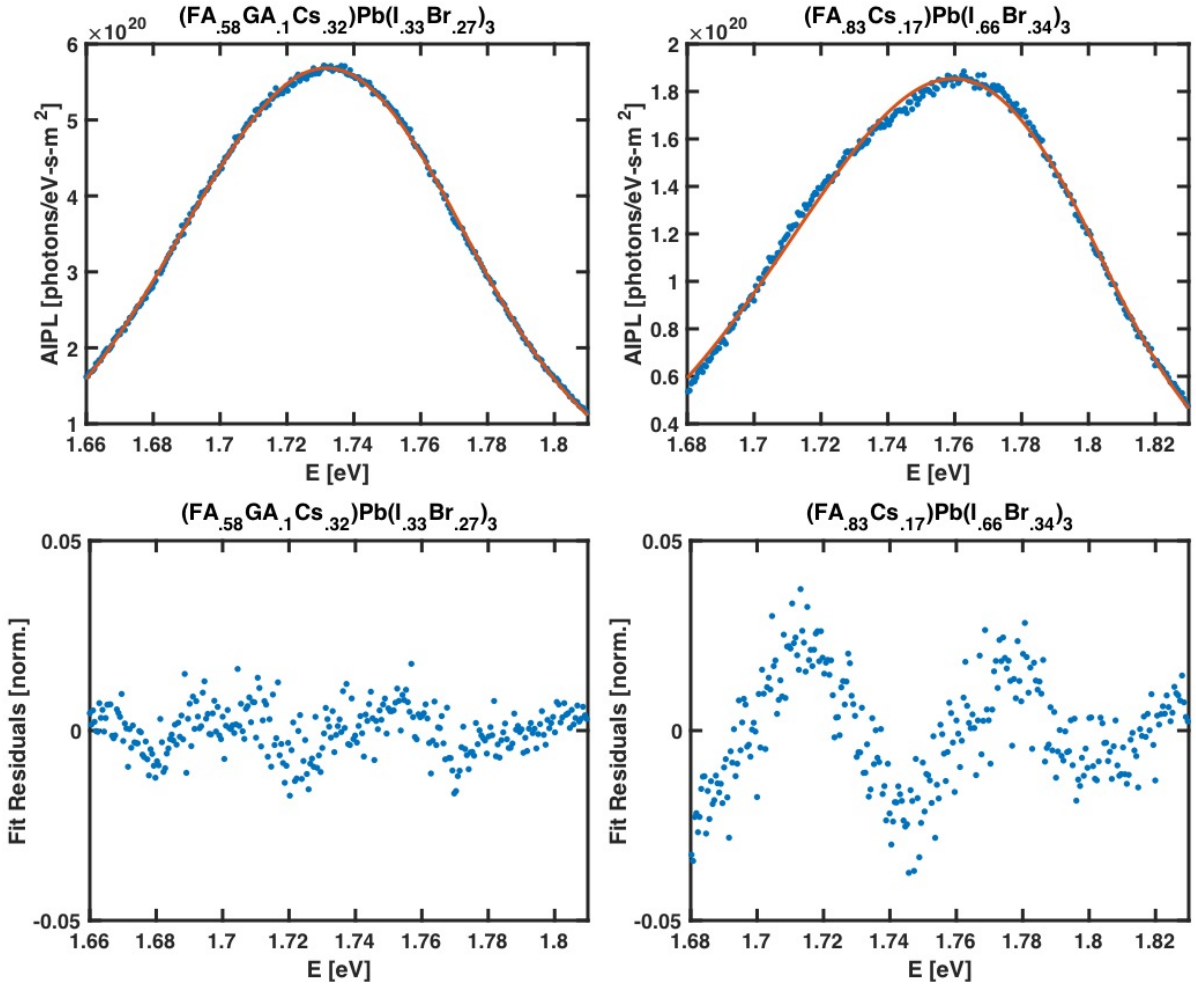

Figure 5.13**. Plot full peak fit result for FACs and FAGACs films**, both with 1.75eV bandgap. The FACs film shows an apparent low energy shoulder in the PL spectrum which causes deviation between the model and experiment data close to the peak maximum. We also show the residuals after full peak fit which makes apparent that this peak shoulder in the FACs film is due to a secondary transition energy centered at 1.73 eV. (FA,GA,Cs)Pb(I,Br)$_3$ alloys further suppress phase segregation and as demonstrated by the absence of the low energy shoulder at 1.73 eV.

5.4.6. Quantification of Ion Migration with Discharge Current Measurements

We also studied ion migration for these various compositions to understand the correlation between ion mobility and phase stability. We followed the methods of Game *et. al*, who measure discharge current as a function of temperature in the dark on a simple $MAPbI_3$ device[128]. We applied 0.2 V across an ITO / NiOx / HP / Au device while measuring dark current through the device in a non-rectifying regime. When the voltage is applied, halide ions move through the film and are blocked at the NiOx – HP interface. We note that A^+ ions are also mobile, yet they have higher activation energies as demonstrated with both experimental[128, 133] and theoretical work[134, 135], so our ionic movement at this low voltage is dominated by I^- and Br^- ions. After the dark current stabilizes, we turn off the 0.2V and observe a "discharge" current of opposite sign (Q_{dis}), which is due to halide ion diffusion back through the HP film. By quantifying the discharge current at multiple temperatures, we can extract an activation barrier, E_a, from an Arrhenius plot. Figure 5.14a shows the discharge current measurement at various temperatures for composition $(FA_{0.33}GA_{0.19}Cs_{0.47})Pb(I_{0.66}Br_{0.34})_3$ and Figure 5.14b shows the Arrhenius plot with linear fit regime and extracted activation barriers. The activation energies have little dependence on the A cation; each A cation for the 34% Br film has an activation energy of 0.24eV. As a control, we measured the discharge current of a $MAPbI_3$ at various temperatures and extracted an ion activation barrier of 0.28 eV (as shown in Figure 5.14c), which is within the range of values determined through both experiment and theory previously[136]. As expected, the activation energy for $MAPb(I_{0.66}Br_{0.34})_3$ is lower than that of $MAPbI_3$ by 40 meV due to contribution of smaller Br^- to the discharge signal. For the mixed-halide films, the bulk ion diffusion is unaffected by A-site composition and has a similar total barrier height to overcome despite an uneven energy landscape present due to A-site mismatch in the (FA,Cs) or (FA,GA,Cs) films. This is an important finding, as it indicates that phase segregation is not correlated with kinetic trapping of ions in the mixed-

halide phase due to the variable ability to deliver ions to I-rich or Br-rich sites, or correlated with large differences in halide vacancy concentrations, but rather the films with A-site size mismatch are thermodynamically stabilized. This finding is consistent with the proposed free energy driving force predicted by Draguta *et. al*[102], while we elucidate that the free energy difference ΔG remains negative at high carrier densities for the (FA,GA,Cs) mixed-halide.

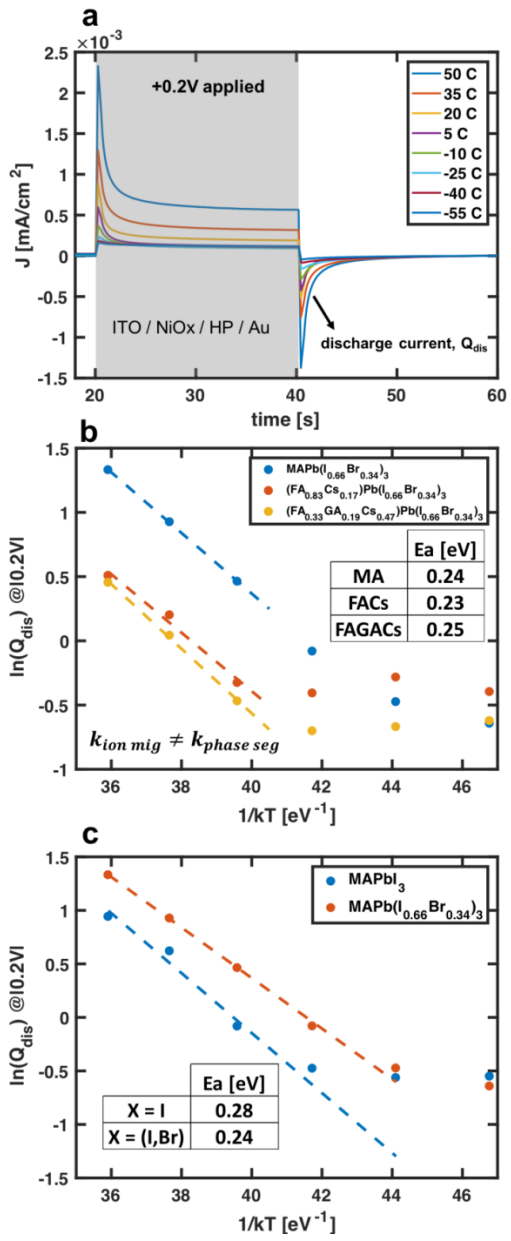

Figure 5.14**. Ion migration results from discharge current measurements**. (a) Example discharge current measurement for (FA,GA,Cs)Pb(I,Br)$_3$ film. A small voltage is applied, then turned off and an observed oppositely-signed current decays as ions diffuse back through the HP film. (b) Arrhenius plot of integrated discharge current changing with temperature for HP films with 34% Br. Fit lines in linear regime give activation barrier for vacancy-assisted halide migration. At lower temperatures, Q_{dis} shows little variation with temperature, suggesting that dielectric polarization (not ion migration) is the primary contributor to Q_{dis} in these regimes as suggested by Game *et. al*[128]. (c) control experiment showing extracted activation energy of MAPb(I,Br)$_3$ vs. MAPbI$_3$. As expected, the mixed-halide has a reduced activation energy due to contribution from smaller Br^- ion.

5.4.7. XRD and UV-Vis for Example FA-GA-Cs Alloys with Phase Impurities

In the main text, we show and discuss several $(FA,GA,Cs)Pb(I,Br)_3$ compositions that are phase pure, as shown in Figure 5.3. However, there are many other compositions that form secondary phases. As is observed in Figure 5.4c, the secondary phases have a negative impact on film quality (especially L_D). Figure 5.15a shows XRD patterns for several examples where secondary phases are formed, with phase pure $(FA,Cs)Pb(I,Br)_3$ included for reference. The $(FA_{0.67}GA_{0.12}Cs_{0.21})Pb(I_{0.66}Br_{0.34})_3$ and $(FA_{0.51}GA_{0.24}Cs_{0.25})Pb(I_{0.66}Br_{0.34})_3$ compositions are the same that are shown to have low L_D in Figure 5.4c. The $(FA_{0.33}GA_{0.19}Cs_{0.47})Pb(I_{0.80}Br_{0.20})_3$ composition has the same A mixture as the 1.84eV composition of interest in main text (see Figures 5.3-5.4), but which much lower Br, demonstrating the cross-correlation in A and X sites in determining structure. We propose that the I-Br alloy gives additional degrees of freedom that enable greater A – site mismatch. The hydrogen bond distance between GA N's and Br can be much shorter than with I before repulsion from nuclear shells begins to dominate. Thus, for the higher Br content, the additional degrees of freedom allow for Br's to coalesce at locations around the GA ion where spatial constrictions suggest a NH—Br bond is more energetically favorable to a NH—I bond. Thus, at Br/I ratios without sufficient Br to allow for this spatial coalescence, the 3D HP phase is thermodynamically restricted and $GAPbI_3$ preferentially forms.

The secondary phases have with peaks consistent with the 1D GAPbI3 phase (discussed in Jodlowski *et. al*[116]), δ-$FAPbI_3$ phase, and PbI_2. Pure $(GA,Cs)Pb(I,Br)_3$ does not form a 3D perovskite phase regardless of the "effective tolerance factor" (tolerance factor calculated using mean ionic radii), indicating that there is additionally a maximum lattice distortion constraint on HP structure formation in addition to a mean ion size constraint. For (FA,GA,Cs) mixtures, $(FA_{0.33}GA_{0.19}Cs_{0.47})Pb(I_{0.66}Br_{0.34})_3$ forms a cubic perovskite phase while

$(FA_{0.51}GA_{0.24}Cs_{0.25})Pb(I_{0.66}Br_{0.34})_3$ forms mostly other phases, indicating that the effective tolerance factor window for formation of cubic HP is narrower than the formation window for compositions with less A-site size mismatch, and the formation window is shifted to tolerance factors below 0.95. We also observe the films with secondary phases have weaker absorption onset with respect to phase pure films, as shown in Figure 5.15b.

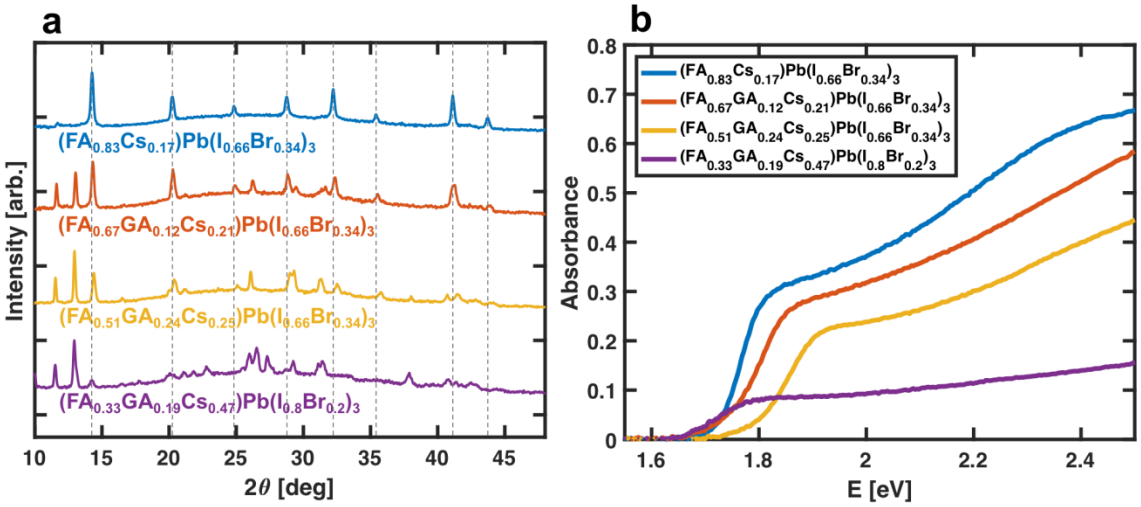

Figure 5.15. **XRD (a) and UVvis (b) characterization of several (FA,GA,Cs)Pb(I,Br)$_3$ compositions that form significant secondary phases**, with guidelines from (FA,Cs)Pb(I,Br)$_3$ pattern shown to guide the eye and highlight peaks that do not fit perovskite pattern . $(FA_{0.83}Cs_{0.17})Pb(I_{0.66}Br_{0.34})_3$ data is presented for reference. The samples are thin films collected on glass, which is why a broad amorphous peak is observed in (a).

5.4.8. Hypotheses for the Origin of Lower Defect Tolerance in High-Bandgap HPs

The limited effect of non-radiative recombination in ~1.6eV HPs despite fabrication via solution processing have shown that energetically favored intrinsic defects do not create effective Shockley-Read-Hall recombination centers[10, 11]. Since there are several reports showing that the defect populations are quite high in hybrid perovskite thin films[10, 11, 13], either the capture cross-section must be low due to a large dielectric constant, or defect energy levels must lie close to or within the band edges to achieve such a high optoelectronic quality . This "defect tolerance" in HPs has been attributed to the orbital character of the band extrema (CB minimum consisting of bonding orbitals with the VB maximum consisting of antibonding orbitals – opposite of typical semiconductors), the low charge carrier effective masses, and the high static dielectric constant[13, 14]. The high bandgap HPs share many of the properties that are predicted to give rise to the exceptional defect-tolerance observed in 1.6eV bandgap HPs. As a result, the cause of higher non-radiative recombination rates in these materials is not currently known. We propose four possible hypotheses to describe the greater voltage losses in high bandgap HPs: **(H1)** greater impact of grain boundary and surface defects (since crystallization is harder to control in the mixed-halides), **(H2)** loss of energy (and quasi-Fermi level splitting) to due to carrier transfer into a low bandgap phase upon phase segregation, **(H3)** enhanced non-radiative recombination upon phase segregation due to defects at phase boundaries, or **(H4)** defect levels at energies that are close to the band edges (or within the bands) in 1.6eV HPs become deeper into the bandgap (towards mid-gap) when the conduction band shifts up and the valence band shifts down in the higher bandgap HPs. We explore and address each of these hypotheses below.

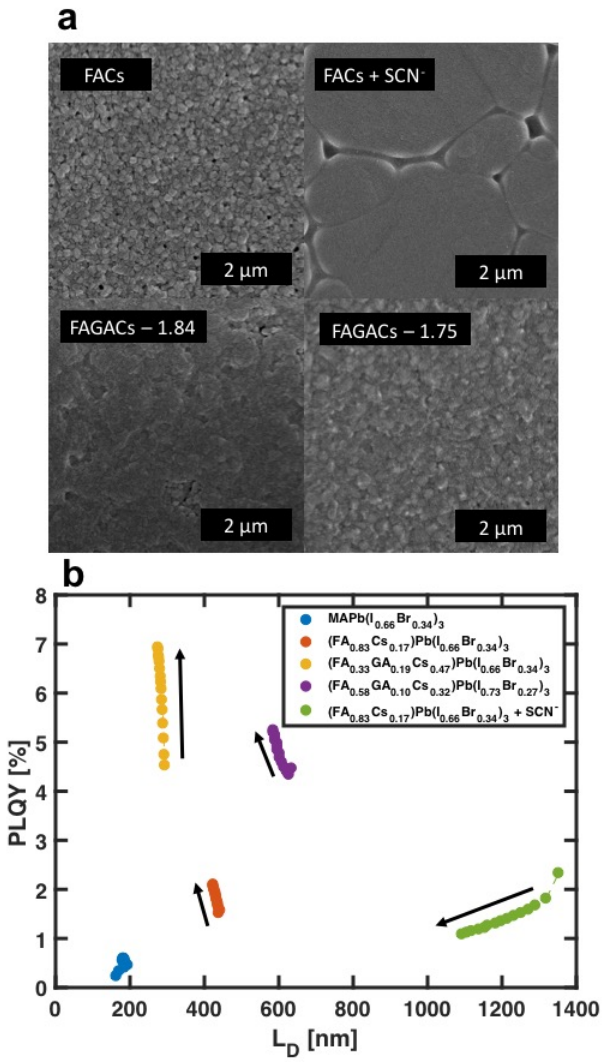

Figure 5.16**. Impact of composition and morphology on optoelectronic properties**. (a) Top down SEM images for various HP films. SCN^- exposure increases grain size to > 2µm. (b) PLQY and L_D evolution over 150 s of continuous 1 Sun exposure with blue LED (657 W/m^2 of ~438nm light). See subsequent discussion.

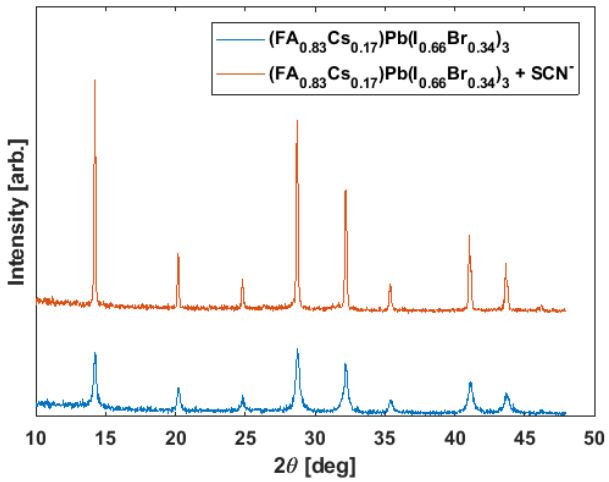

Figure 5.17**. Powder XRD of (FA,Cs)Pb(I,Br)$_3$ spin coated films with and without 5% Pb(SCN)$_2$ in the precursor ink**. We fabricate the large grained films by adding 5% Pb(SCN)$_2$ in place of 5% PbX$_2$ (to keep A/Pb ratio constant). We did not detect formation of PbI$_2$ with 5% Pb(SCN)$_2$ addition into the ink. The FWHM of the (200) peak decreases from 0.287˚ to 0.0896˚ with SCN$^-$ exposure. The narrower FWHM of the (FA,Cs)Pb(I,Br)$_3$ + SCN$^-$ powder pattern confirms that the crystalline domain size is larger for this sample than the other samples. This is consistent with SEM images and observations from other groups[18]. However, the FWHM of the SCN$^-$ sample is approaching the instrument broadening, so analysis with Scherrer or Williamson-Hall method is not practical.

For further insight on the origin of higher non-radiative recombination rates in high-bandgap HPs, we consider the impact of grain boundaries and phase segregation on optoelectronic properties. We explored the impact of grain size on optoelectronic properties by adding Pb(SCN)$_2$ into the HP precursor ink. The presence of thiocyanate anions has been recently shown to dramatically increase grain size leading to improved device performance and environmental stability[12, 110, 137,42], despite recent evidence suggesting the anion is evolved from the film[138]. We incorporate 5% Pb(SCN)$_2$ directly in the HP ink and find a dramatic increase in grain size to over ~2µm without significant formation of PbI$_2$ (see Figure 5.16a and 5.17). Figure 5.16b shows PL and L$_D$ evolution with time, with some of the compositions from Figure 5.4c reproduced here for reference. We observe that the (FA,Cs) film with large grains (with SCN$^-$ in precursor ink) has relatively similar PLQY to the FACs without SCN$^-$ yet an L$_D$ that is around three times higher. For

these two films, the similar PLQY with different L_D indicates that the carrier lifetimes are likely quite similar while the carrier mobilities are much higher for the film with large-grains, even up to an order of magnitude higher (since L_D is proportional to the square root of the mobility-lifetime product).

We conclude that, while the grain boundaries in the (FACs)$Pb(I,Br)_3$ likely contain a high concentration of surface defects, these surface defects are not the dominant recombination centers. Rather, the defect energy levels are likely quite close to the valance or conduction band edges and serve as temporary carrier traps that primarily effect the carrier mobility. This is the expected behavior of defects with energy levels smaller than the demarcation energy (the energy at which thermal emission back into the band is equally as likely as a recombination event). We note that this conclusion assumes the optoelectronic differences between the (FA,Cs) and (FA,Cs) + SCN^- films are primarily due to different grain sizes (not bulk defect chemistry), and further work on alternative large-grain HP fabrication routes would be beneficial to further evaluate the role of surface defects. Although surface defects at grain boundaries do not seem to be the dominant source of higher non-radiative recombination rates in high bandgap HPs, it seems that increasing grain size through SCN^- exposure (or other methods) could be very beneficial due to improved mobility and thus more efficient carrier collection in devices. Environmental stability and phase stability of the mixed-halide phase also have been correlated with grain size[39, 49, 77], which could be additional benefits of SCN^- exposure. We also notice the changes in PL and L_D over time are quite different in the (FA,Cs) films with and without SCN^- exposure. The (FA,Cs) film without SCN^- shows PLQY increase with a slight L_D decrease upon illumination before stabilizing which is consistent with photo-passivation with slight carrier localization observed previously for this composition[37]. In contrast, the large-grained perovskite shows a decrease in both PLQY and L_D

upon illumination, which could be due to light-activated vacancy defects formed with HSCN evolution. The (FA,GA,Cs) compositions shown previously to have low non-radiative recombination rates show similar L_D to the (FA,Cs) film without SCN^- exposure and show the same PL-L_D changes upon illumination. The mixed -halide (FA,GA,Cs) and (FA,Cs) films all have higher L_D than the mixed-halide MA film as expected from previous reports showing low L_D in the MA mixed-halide films[37].

We now consider the impact of thermalization losses (H2, the second of the four possible hypotheses to describe the greater voltage losses in high bandgap HPs) due to phase segregation on ΔE_F. For $MAPb(I,Br)_3$, the mean PL energy decays with time, indicating carrier transfer to a phase with lower energy, which could result in a decline in ΔE_F due to thermalization losses. Calculating the ΔE_F of a two-phase material is beyond the scope of this work. The stabilized ΔE_F of a phase segregating material will depend on the transition energies and mole fractions of each phase, and neither the $PLQY_{Ext}$ method[56] nor the full peak fit method[54] (methods described in SI) allow for a two-phase material in their determination of ΔE_F. However, we note that in Figure 5.2 and Figure 5.4 we compare optoelectronic quality of the films only in the initial (mixed-phase) state. Thus, thermalization losses cannot describe the dependence of ΔE_F on composition observed in these instances. Although we do not explicitly study the differences in initial and stabilized ΔE_F, we note that for the two $(FA,GA,Cs)Pb(I,Br)_3$ films studied, ΔE_F increases with time-under-illumination, as indicated by the combination of a stable PL peak position (Figure 5.5a) along with increasing PLQY with time.

Another mechanism relating phase segregation to a reduction in ΔE_F is formation of defects at phase boundaries (hypothesis H3). For $(FA,Cs)Pb(I,Br)_3$ we notice a PL peak low energy shoulder (Figure 5.13) even in the initial PL measurement, indicating that phase segregation begins

immediately upon illumination. The halide redistribution could create additional surface defects due to formation of phase boundaries that increase the occurrence of dangling bonds within grains. Through this mechanism, phase segregation could be impacting optoelectronic quality even in cases (such as in (FA,Cs)Pb(I,Br)$_3$) where phase segregation is not obvious (there is little carrier transfer into lower bandgap domain). Reducing dangling bonds at phase boundaries within grains is a possible explanation for the ΔE_F enhancement we observe in (FA,GA,Cs)Pb(I,Br)$_3$ films.

Finally, we consider H4, or that defect energy levels with respect to band edges change for higher bandgap HPs. We conducted Shockley-Reed-Hall non-radiative recombination simulations to get a relative picture on how defect energy levels would need to change in the various HP compositions studied to describe the differences in $\Delta E_F/\Delta E_{F,SQ}$ we observe. At a high level, we solve a Generation = Recombination balance for ΔE_F which appears directly in the radiative recombination expression and indirectly in the Shockley-Reed-Hall expression. Ignoring contributions from Auger recombination and assuming monomolecular non-radiative recombination follows the Shockley-Reed-Hall (SRH) model, we can write

$$G = U_{rad}(\Delta E_F) + U_{SRH}(\Delta E_F) \tag{S10}$$

where the radiative recombination rate is expressed as

$$U_{rad}(\Delta E_F, T) = \int_0^\infty \alpha(E) b_e(E, \Delta E_F, T) dE - \int_0^\infty \alpha(E) b_e(E, 0, T) dE \tag{S11}$$

where

$$b_e(E, \Delta E_F, T) = \frac{2\pi}{h^3 c^2} \frac{E^2}{e^{(E-\Delta\mu)/kT} - 1} \tag{S12}$$

and absorption coefficient, $\alpha(E)$, is modeled using eq. 5.5 above with using θ, and γ determined from the full-peak PL fit. SRH recombination is expressed as

$$U_{SRH}(\Delta E_F, T, N_d, E_d) = \frac{np - n_i^2}{N_d \sigma_{cap} \nu_{th}(p + p^*) + N_d \sigma_{cap} \nu_{th}(n + n^*)} \quad \text{(S13)}$$

assuming electrons and holes have equal lifetimes given by defect concentration N_d, capture cross section σ_{cap}, and thermal velocity ν_{th}, and where p^* (n^*) is the hole (electron) concentration when the trap energy is equal to the intrinsic Fermi-level, expressed as

$$p^* = n_i e^{\frac{E_i - E_d}{kT}} \quad \text{(S14)}$$

$$n^* = n_i e^{\frac{E_d - E_i}{kT}} \quad \text{(S15)}$$

where n_i and E_i can be determined from

$$E_i = \frac{1}{2}E_g + \frac{3}{4}kT \ln \frac{m_h}{m_e} \quad \text{(S16)}$$

$$n_i = \sqrt{N_C N_V e^{\frac{-E_g}{kT}}} \quad \text{(S17)}$$

$$N_C = 2\left(\frac{m_e kT}{2\pi\hbar^2}\right)^{\frac{3}{2}} \quad \text{(S18)}$$

$$N_V = 2\left(\frac{m_h kT}{2\pi\hbar^2}\right)^{\frac{3}{2}}. \quad \text{(S19)}$$

Assuming our HP films are intrinsic, we can use simplified non-equilibrium carrier statistics for intrinsic semiconductors, given by

$$n \approx n_i e^{\left(\frac{\Delta E_F}{2kT}\right)} \quad \text{(S20)}$$

$$p \approx n_i e^{\left(\frac{\Delta E_F}{2kT}\right)}. \quad \text{(S21)}$$

Now, we can rewrite balance equation 5.10 where the only unknown is ΔE_F, which we solve for numerically. We use the constants G = 3.51e27 $m^{-3}s^{-1}$, m_e = 0.23 m_o, m_h = 0.29 m_o, α_0=1e7 m^{-1}, ν_{th}= 1e5 m/s, and σ_{cap}= 1e-19 m^2. Note that we set G as a constant for these simulations since we

are comparing with experimental AIPL data where we used a constant excitation flux with 532nm laser, which is well above bandgap for each composition. We calculated ΔE_F for N_d = 1e15 to 1e18 cm^{-3} and for E_d at many possible levels within the bandgap. Results of these simulations are presented below.

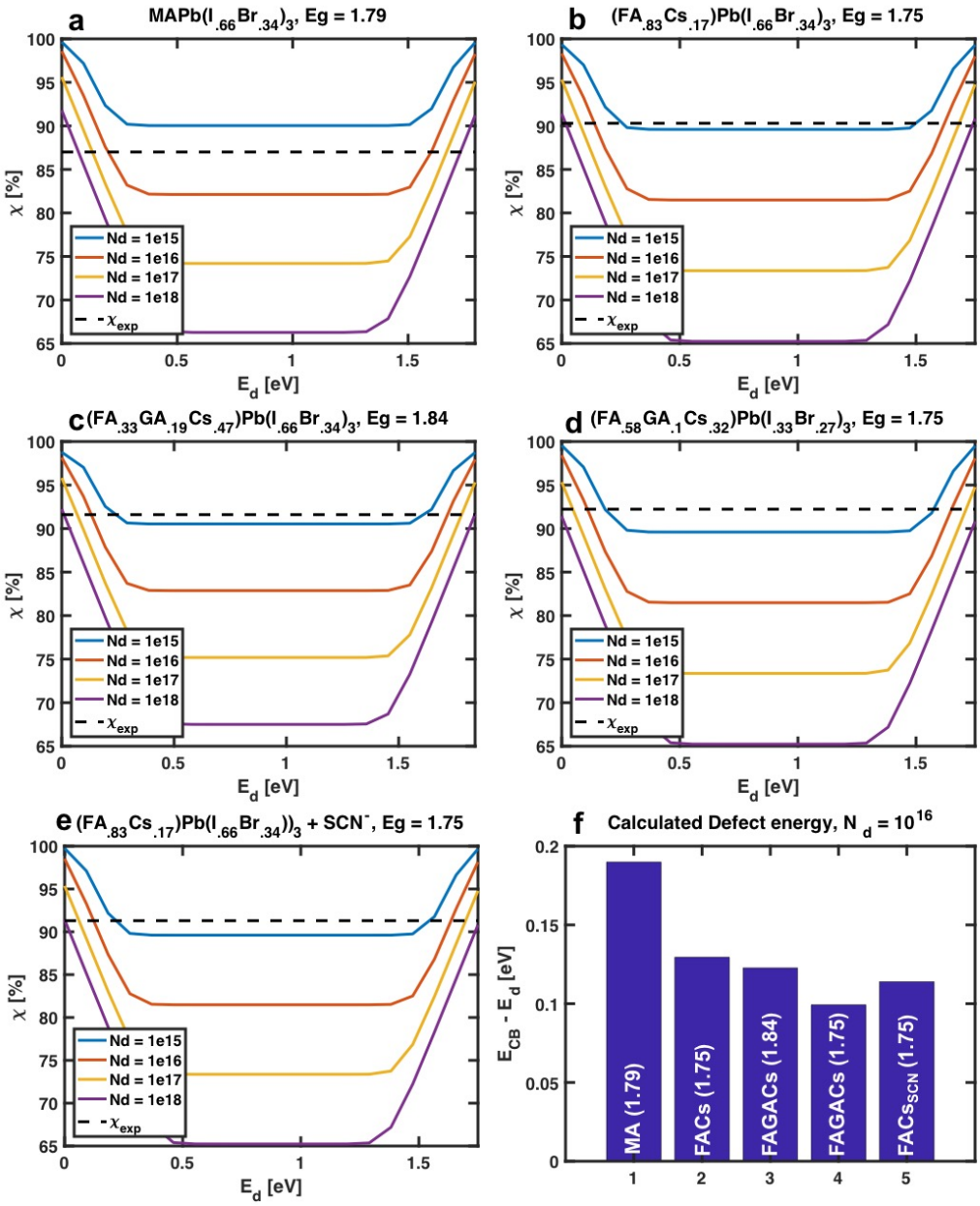

Figure 5.18**. Results of Shockley-Reed-Hall simulations**, where optoelectronic quality fraction χ is calculated as a function of defect density N_d [cm^{-3}] and defect energy level E_d [eV], for five perovskite compositions (a-e). The dashed line in each subfigure represents the measured χ for

each composition from AIPL (Figure 5.4). The intersection of the dashed and solid lines indicate a possible scenario to describe the non-radiative recombination observed in our films. (f) shows the intersection of experimentally observed χ with the $N_d = 10^{16}$ cm^{-3} prediction, with the compositions listed and their bandgaps in parentheses for reference. For example, for $MAPb(I_{0.66}Br_{0.34})_3$, the observed AIPL is consistent with non-radiative recombination from a single defect with concertation 10^{16} cm^{-3} and energy level 0.19 eV below the conduction band minimum.

Assuming the non-radiative recombination present in the spin coated films in Figure 5.4 arise from a single SRH defect with concentration of 10^{16} cm^{-3} (vacancy concentration predicted from discharge current measurements), we calculate the defect energy level consistent with observed results. We see that even for $MAPb(I,Br)_3$, the defect does not need to be far within the bandgap to give the non-radiative recombination rates observed. Changing the difference between the conduction band minimum and defect energy from 0.19 eV to 0.1 eV could completely describe the χ differences observed between $MAPb(I_{0.66}Br_{0.34})_3$ and $(FA_{0.58}GA_{0.10}Cs_{0.32})Pb(I_{0.73}Br_{0.27})_3$. The χ differences between $(FA_{0.83}Cs_{0.17})Pb(I_{0.66}Br_{0.34})_3$ and $(FA_{0.33}GA_{0.19}Cs_{0.47})Pb(I_{0.66}Br_{0.34})_3$ are consistent with a constant defect energy level (with respect to the conduction band edge) with a lowering of the valance band edge by 90 meV (as the bandgap increases from 1.75 to 1.84). We conclude that differences in band energies relative to defect energies likely play a dominant role in the ΔE_F losses of mixed-halide perovskites, and that GA addition could suppress non-radiative recombination through vacancy defects by altering the band structure (lowering conduction band edge compared to other HPs with the same bandgap). Although this hypothesis (H4) is consistent with our dataset, we cannot conclusively determine if this is the origin. Indeed, defects arising at phase boundaries (H3) is another possible description consistent with our dataset. Therefore, we conclude that H3 or H4 are likely the cause of lower defect tolerance in high-bandgap perovskites, and that FA-GA-Cs alloys suppress either (or both) mechanism(s).

5.5 Record Open-Circuit Voltages Enabled via 2D Perovskite Interface Modification

In parallel to the above GA incorporation effort, we developed another strategy for improving the photovoltage of high bandgap HPs, focused on MA- based HPs in the 1.80-1.85eV bandgap range (this higher bandgap is ideal for perovskite-perovskite tandems, where the lower subcell bandgap minimum is ~1.22eV[62]). This work (led by collaborator Adharsh Rajagopal), incorporated the large phenylethylamine (PEA) cation into the film forming a lower dimensional 2D/3D (MA,PEA)Pb(I,Br)$_3$ perovskite structure with E_g = 1.82eV. This material led to V_{OC}s of 1.30 V, which is also 85% of the Shockley-Queisser limit, which surprised and excited the HP community since the 1.80-1.85eV bandgap range has long been considered particularly unstable and low quality. However, one pitfall of this approach is that incorporating the PEA into the bulk of the film has a detrimental impact on the HP L_D and device J_{SC}[62]. Thus, this strategy we outline in the PEA paper is likely not a route toward high efficiency tandems due to mediocre transport and J_{SC}.

We hypothesized that addition of PEA only at surfaces could still lead to V_{OC} enhancement due to passivation of surface defects and reduction in interface recombination without the deleterious impact on L_D and J_{SC}. Since the (FA,GA,Cs) demonstrates the highest quality pure 3D high bandgap HP, we used this as our 3D HP, then added PEA at the top interface with a two step method (spin coat HP, then anneal, then spin coat 0.5-5 mg/mL PEAI in IPA, then anneal again). An example high V_{OC} device results from this (FA,GA,Cs)Pb(I,Br)$_3$ + PEAI 3D + 2D/3D heterostructure are presented in Figure 5.19. With 5mg/mL PEAI in IPA, we experience V_{OC} of 1.29V for a 1.75eV bandgap absorber, which is 88% of the Shockley-Queisser limit voltage. We do however, see a decrease in J_{SC} for the 5mg/mL case. For lower PEAI concentrations (1.25 and

2.5 mg/mL), we observed improvements in V_{OC} and FF with slight decrease in J_{SC}, and overall PCE increase.

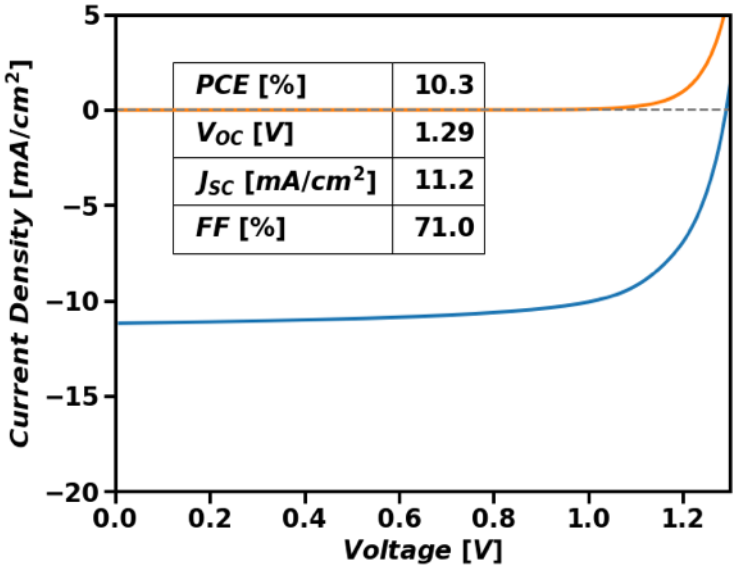

Figure 5.19**. JV curve of (FA,GA,Cs)Pb(I,Br)$_3$ + 5 mg/mL PEAI**.

Initial experiments proved that the PEAI interface modification strategy is promising and a viable route toward high-bandgap HP devices with high PCE and V_{OC}. This work was de-prioritized when I was still working on device optimization when the new DOE grant began (focused on machine learning and stability), and I chose to pivot to other projects. However, we were not the only group with the 3D + 2D/3D heterostructure idea, and several reports using this concept have been reported[139, 140], including work demonstrating the record stabilized HP single junction efficiency[141]. The 2D/3D HPs have also demonstrated enhanced durability to atmospheric stresses[139, 140, 142].

I recommend further exploration of the 3D + 2D/3D HP material space for realization of the most efficient and stable high-bandgap perovskites, where the 3D perovskite employs lattice strain through GA or dimethylamonium (DMA) incorporation.

Chapter 6. MACHINE LEARNING PREDICTION OF HYBRID PEROVSKITE OPTOELECTRONIC PROPERTIES

The guanidinium alloying work presented in Chapter 5 inspired a wider combinatorial search for HPs with ideal optoelectronic properties, not only for the high-bandgap work, but also for the low bandgap and ideal bandgap systems. I employed a machine learning approach, training regression models to predict optoelectronic properties extracted from photoluminescence. I started with "typical perovskites" (see 6.3), or those perovskites which are widely studied, so I could validate my results with the vast literature reports on these compositions. The model predicts that a particular (MA,FA,Cs,Rb)Pb(I,Br)$_3$ composition has the highest $\Delta E_F/\Delta E_{F,SQ}$ of the entire design space, a composition that is indeed quite similar to the (MA,FA,Cs,Rb)Pb(I,Br)$_3$ that has demonstrated the highest unpassivated $V_{OC}/V_{OC,SQ}$ in literature[9]. This finding validates this approach for use in prediction tasks outside of the "typical perovskites" if sufficient data is collected. Although this work was never submitted for publication, these methods and results were shared in a successful proposal aiming to use similar machine learning approaches to predict HP film and device durability.

6.1 ABSTRACT

Hybrid Perovskites (HPs) are an emerging material class that have undergone intensive research recently for possible application in cheap and efficient solar cells. Despite thousands of research papers investigating the unique properties of HPs, a generalized model to connect composition to optoelectronic properties has not been developed. In this work, we utilize high throughput combinatorial material fabrication and analysis along with machine learning to predict HP bandgap and optoelectronic quality fraction (χ). We demonstrate that a random forest regressor with tuned hyperparameters can yield mean test set error of 17 meV for bandgap and 1.4% for χ. Next, we explore replacement of compositional features with a generally extendable feature vector which we accomplish without any increase in test set prediction error. Finally, we consider the generalizability of the model by employing a cross-validation scheme that prohibits training on any materials from the same library. This last study shows the simpler ridge regression model gives better performance on "out-of-class" predictions and provides insight into design of future data collection and modeling efforts.

6.2 INTRODUCTION

Hybrid Perovskites (HPs) are an emerging material that can be used for cheap and efficient solar cells[37, 143, 144]. One aspect that makes HPs attractive for solar cells and other applications is their properties are highly tunable. A "perovskite" is not just one material, but rather a material structure with composition ABX3, where the A, B, and X site can be a wide variety of ions or even an alloy between multiple ions. Thousands of papers have been published in the last five years on the HP materials, many of them studying how ABX_3 composition relates to material properties[36, 40, 108]. Most of these studies consider only a very small compositional or processing change and study the impact on particular material properties relevant to solar cell device efficiency. Because of the narrow scope of individual studies, a broad understanding on how perovskite composition impacts specific device parameters has been elusive to the perovskite research community. Here, we gather an experimental dataset on a wide variety of compositions using high throughput combinatorial spray coating with photoluminescence analysis[41, 52].

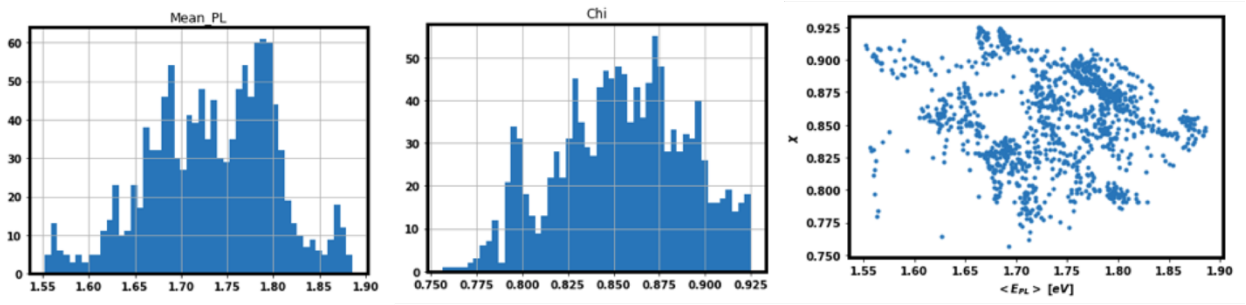

Figure 6.1**. The dataset**; <E_{PL}> and χ are the two responses we are trying to predict.

This provides a large dataset that can be studied with machine learning to understand complex relationships between composition and properties in the HP material space. The goals of this project are to i) develop machine learning models to reliably predict bandgap and χ with composition as input, ii) use an interpretable ML model to understand how

structural/compositional motifs translate to material properties, and iii) replace compositional inputs with engineered features to formulate a model that can suggest out-of-dataset materials with potentially promising properties. This term project is just the beginning using a preliminary dataset that was collected earlier this year, and the hope is to obtain preliminary results as well as inform future data collection efforts.

6.3 DATASET

The initial dataset used in this analysis includes 13,000 photoluminescence (PL) spectra indexed by composition. Each composition has 10 replicate spectra, leaving 1300 unique compositions. These compositions were collected from 26 different gradients (or "libraries", with 50 compositions per library). The responses to predict are mean PL energy ($<E_{PL}>$, an indicator of bandgap) and χ ($\chi = \Delta E_F/\Delta E_{F,SQ}$, or a predictor of device voltage as a fraction of the theoretical limit), and the inputs are compositional features (i.e. A-site composition fractions, B-site fractions, X-site fractions, etc.). In this dataset, A = (MA, FA, GA, Cs, Rb), B = Pb (constant in this work), and X = (I, Br). One constraint is that all component fractions must sum to 1.0. Thus, this dataset has several unique challenges – we do not have an abundance of data, indicating that complex models could fail/overfit. Also, we do not have i.i.d. data, as each composition that comes from the same library is related due to having the same processing, ink, aging time, glovebox atmosphere, etc. We will address these in the following analysis. Figure 6.1c shows the two responses we are trying to predict.

6.4 Results and Discussion

The first objective is to use compositional features to predict $\langle E_{PL} \rangle$ and χ. For all of the experiments conducted here, we saved 20% of the dataset for testing and performed 5-fold cross validation on the training set for model selection and hyperparameter tuning. We conducted initial screening of algorithms using sklearn[145], and identified the random forest regressor (RFR) gave the lowest validation mean squared error (without hyper parameter tuning). We chose to further investigate ridge regression (Ridge) (due to its simplicity) and RFR (since it gave best initial results). We also added polynomial features step, exploring polynomial combinations of features up to degree 3. Due to relatively small dataset, we just tuned hyperparameters using grid search; for Ridge we tuned polynomial degree and lambda, and for RFR we tuned polynomial degree, max features, number of iterators, and maximum depth of a tree. The test set predicted vs. actual values for the tuned models are presented in Figure 6.2. For the interested reader, dependence of RFR validation results on hyperparameters is presented in Figures 6.5-6.7. Figure 6.2 demonstrates we are able to accurately predict both $\langle E_{PL} \rangle$ and χ from composition. Since $\langle E_{PL} \rangle$ is an indicator of bandgap, and χ is an indicator of device voltage, our model can be used to infer bandgap and device voltage merely from composition. This is the first time a model predicted HP bandgap and optoelectronic quality has been developed based on an experimentally measured dataset. Although prior work has demonstrated machine learning prediction of density functional theory (DFT) calculated bandgaps[146], the utility of such models is limited since DFT determined bandgaps can be wildly different from experimental values. As expected, we observe a lower MSE for RFR than Ridge, and we see that $\langle E_{PL} \rangle$ is easier to predict than χ (as indicated by lower R^2 values).

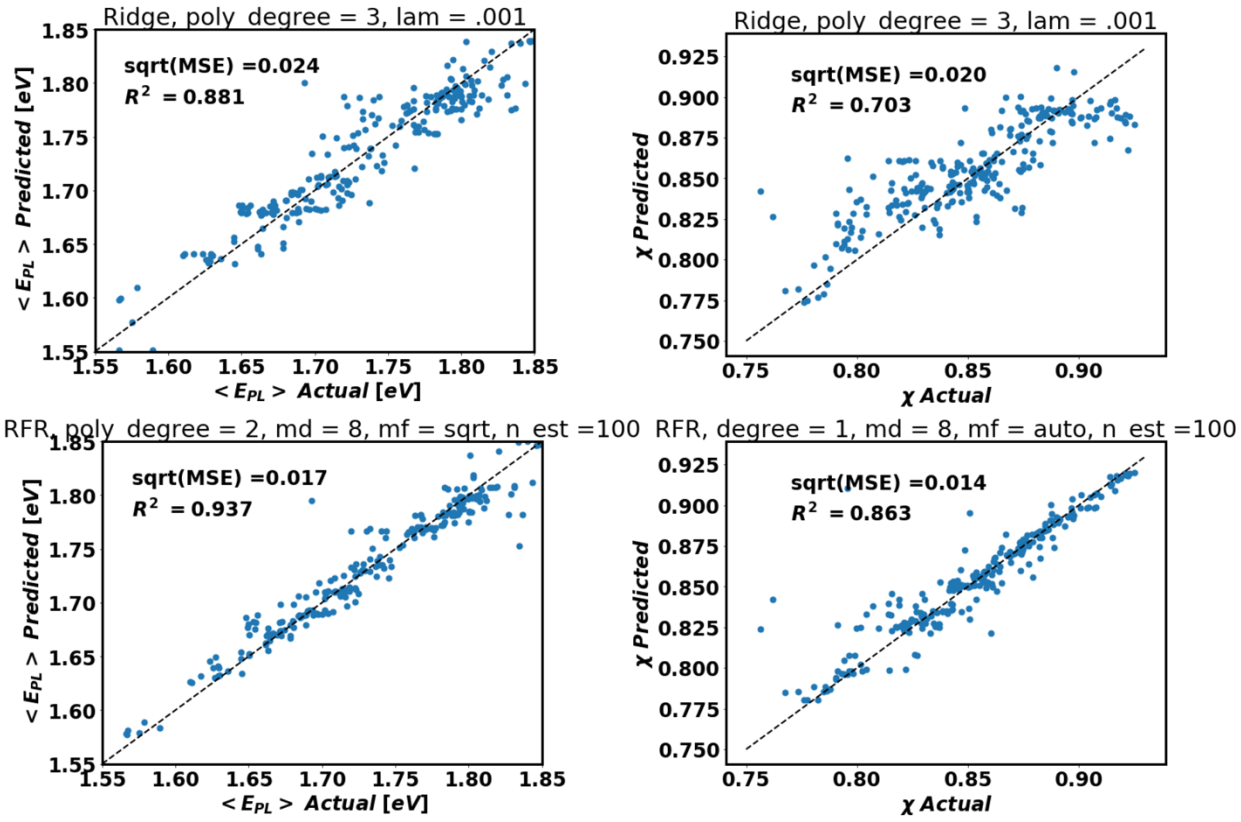

Figure 6.2**. Test set Predicted vs. Actual** <EPL> (left) or χ (right) using Ridge (top) or RFR (bottom).

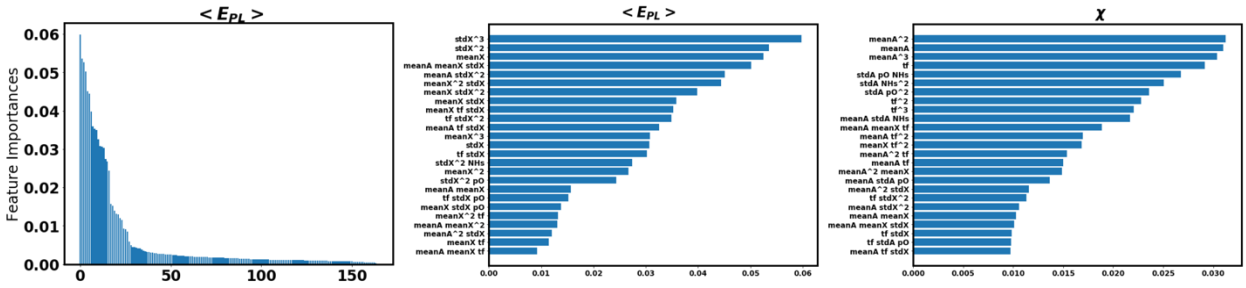

Figure 6.3**. Feature importances for RFR model with generalized feature vector**. Left demonstrates all features for <EPL> prediction. Center shows top 25 features for <EPL> prediction, and right shows top 25 for χ.

The above demonstrates success at predicting optoelectronic properties of HPs that are interpolated within the training set composition space. That is, even though we used a test set (with different compositions than the training set), the compositions all used the same ions and were within the same ranges as used in the training set. Ultimately, we would like to predict properties

of HPs that are not explicitly in our dataset. For example, given sufficient data on $MAPb(I,Br)_3$, $FAPb(I,Br)_3$ and $(FA,Cs)Pb(I,Br)_3$, we would like to predict the properties of $(MA,Cs)Pb(I,Br)_3$. The first step in achieving this objective is generalizing the feature vector. If we use compositional inputs as features, then an out of class composition would give an undefined output. Thus, we use a generalized feature vector, using features such as mean site ionic radii, goldschmidt tolerance factor, site size standard deviation, site mean net dipole moment, site hydrogen bonding potential, etc. We repeated the above analysis with the new feature vector. The actual vs. predicted responses demonstrate we maintain similar performance when switching to generalized feature vector (see Figure 6.8). We were also curious which of these new features are most important for making predictions, so we studied the feature importances for the RFR with hyperparamaters that gave the best validation performance (see Figure 6.3). These results demonstrate the X-site size and standard deviation have the greatest impact on $<E_{PL}>$ while the A-site size and the tolerance factor have the greatest impact on χ. We can interpret these findings to further understand the parameters that impact HP bandgap and device voltage.

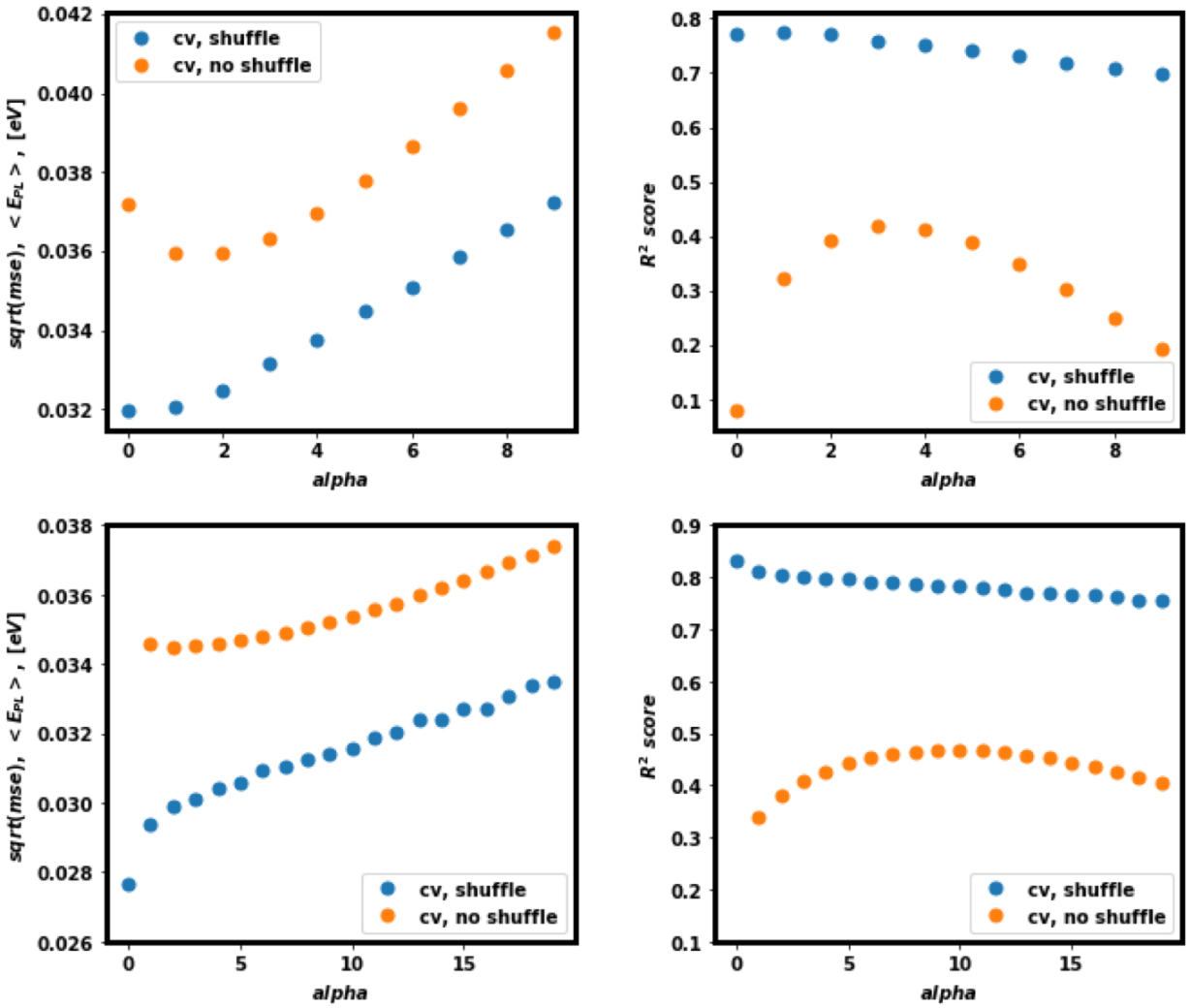

Figure 6.4**. Ridge Regression results** for <E_{PL}>. Alpha is L2 penalty coefficient. Top is original features, Bottom is with polynomial features degree=2.

Figure 6.8 demonstrates success at predicting both <E_{PL}> and χ with the generalized feature vector. However, we are still "interpolating" within our training dataset to check test performance, even though we are now using different features. The next step is to check performance on validation data that is very different from the training data. We do this by enforcing a "no shuffle" cross-validation scheme, where all compositions from the same "family" or library remain together in cross-validation–when a sample is used for validation, no other samples from the same library were included in training. This gives a metric on the generalizability of our model for "out-of-

class" predictions. We find the RFR model gives a negative validation R^2 value for both $\langle E_{PL} \rangle$ and χ, indicating that a simple mean outperforms this model, and the RFR model is not generalizable for out of class predictions. For the Ridge model, we find a negative R^2 value for χ but we are able to get a reasonable model for $\langle E_{PL} \rangle$. The dependence of validation metrics on lambda and polynomial degree are shown in Figure 6.4. We see the mean error increases to 34 meV when predicting out-of-class materials.

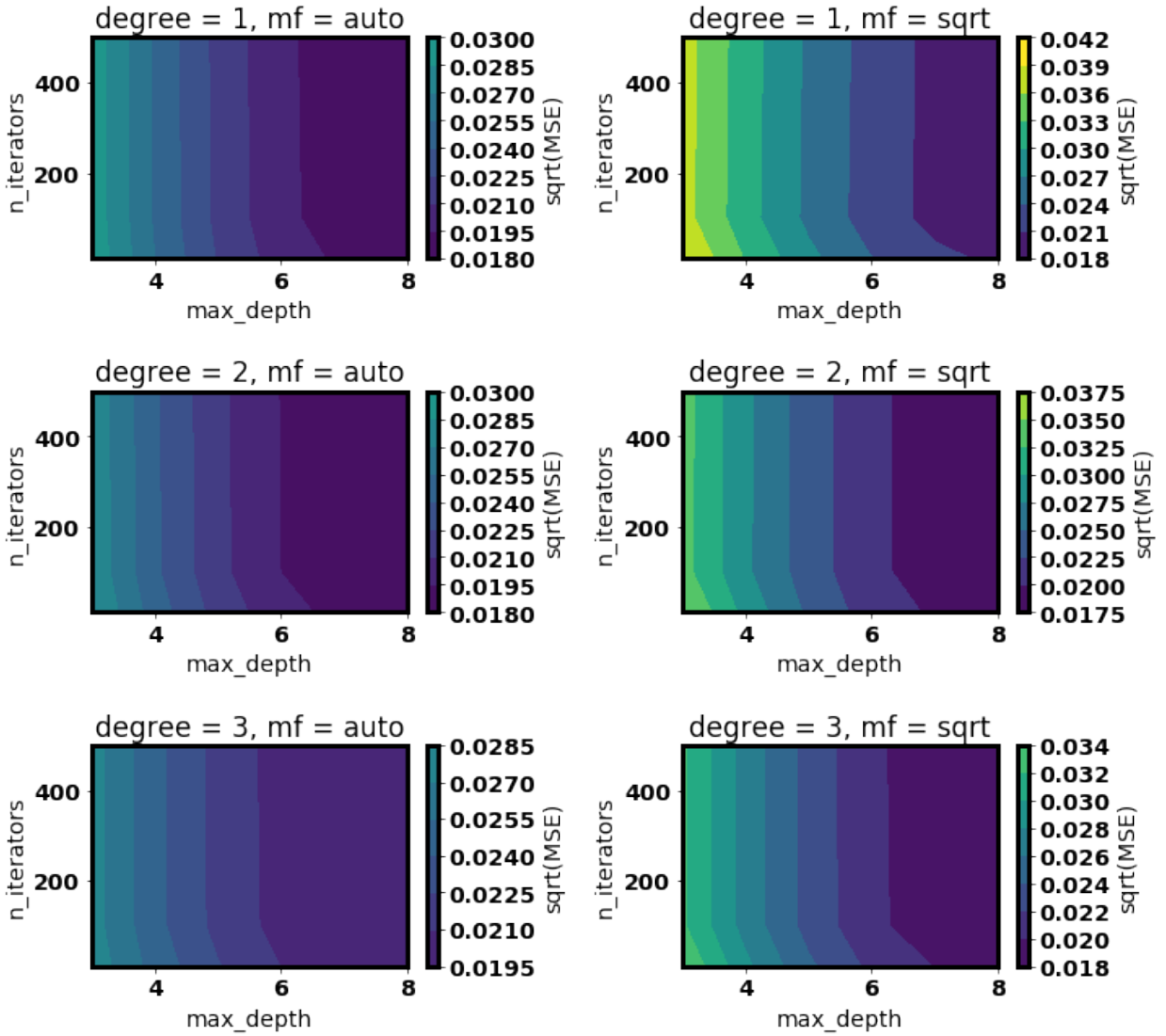

Figure 6.5**. Results of grid search hyperparameter tuning for <EPL>**. degree = polynomial features degree, mf = max feature algorithm, md = max depth of tree, n est = number of estimators used. To see further investigation of max depth, see Figure 6.7.

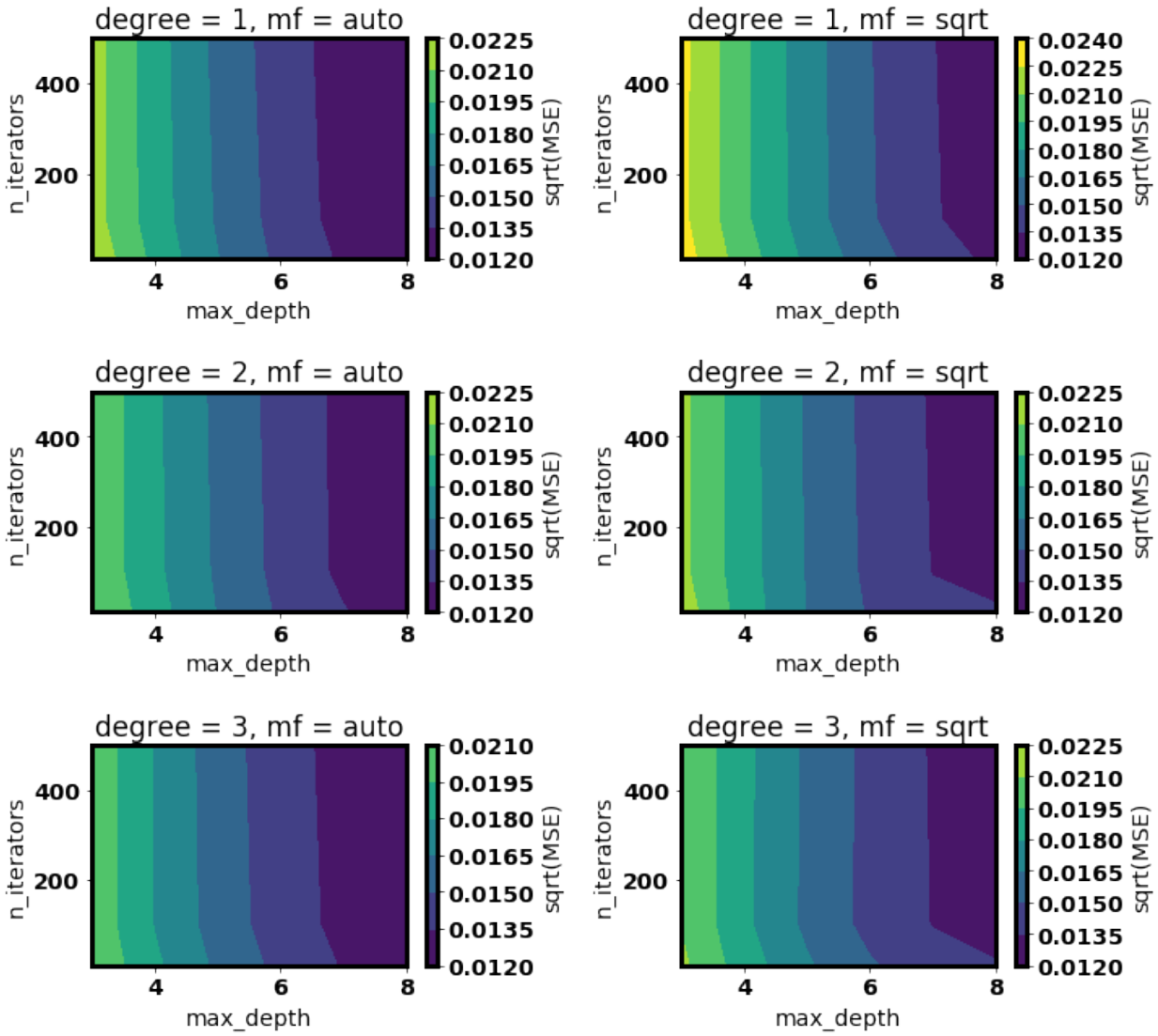

Figure 6.6**. Results of grid search hyperparameter tuning for χ**. degree = polynomial features degree, mf = max feature algorithm, md = max depth of tree, n est = number of estimators used.

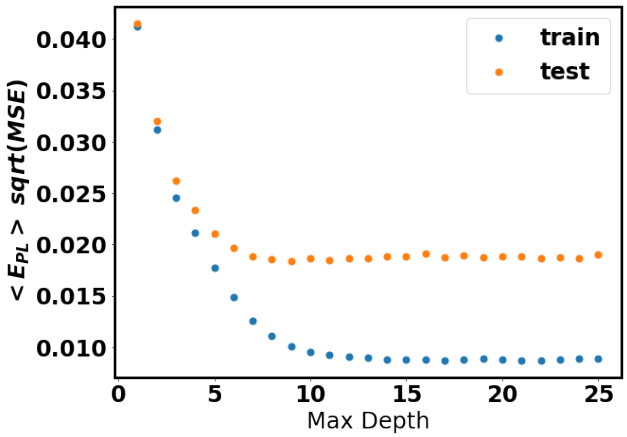

Figure 6.7**. Results further investigation of max depth of tree**. Training error continues to decrease but validation error is at minimum around max depth = 8.

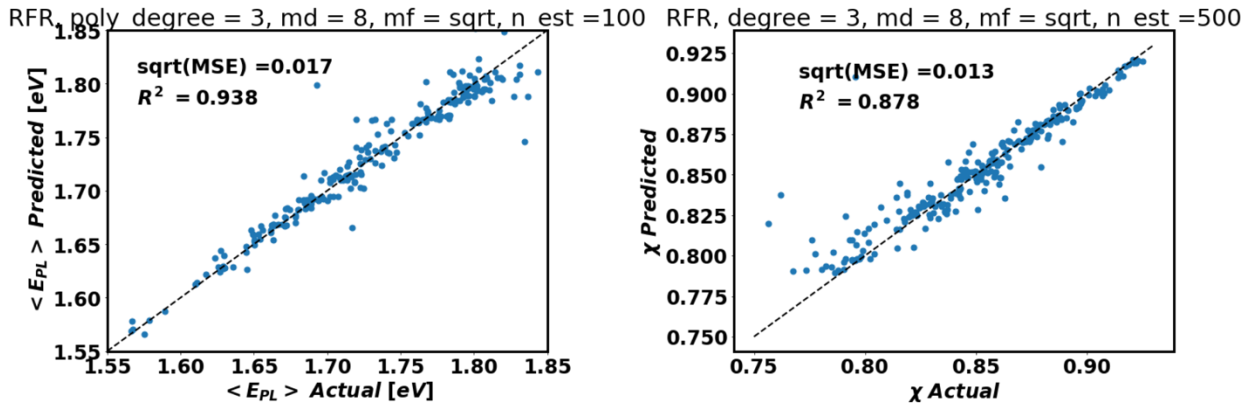

Figure 6.8**. Predicted vs. actual responses for random forest regressor** trained with feature set that does not include compositional features.

In the above analysis, we show for the first time a machine learning model validated to predict perovskite bandgap and perovskite device voltage using an experimentally derived dataset. Our results demonstrate that using a Random Forest Regressor gives quite low test set mean error of 17 meV for $<E_{PL}>$ and 1.4% for χ. We also demonstrate the compositional features can be replaced with generalized features and maintain performance, and we identify which of these new features have the greatest predictive importance. Finally, we challenged the prediction task by using validation scheme that omits all samples from the same library in training, meaning we are trying to predict out-of-class material properties. In this case, we find the simpler Ridge model performs

better, but can only predict $\langle E_{PL} \rangle$ and not χ. Further data collection is necessary to refine the feature list and improve the out of class predictive performance. Other future work could involve predictive modeling of which specific data would be most useful to collect to improve the model performance.

Chapter 7. FORECASTING DECAY OF HYBRID PEROVSKITE OPTOELECTRONIC PERFORMANCE USING TRANSMITTANCE OR DARK FIELD MICROSCOPY

Reliability is becoming the greatest hurdle for commercialization of perovskite solar cells. Due to the wide variety of degradation modes, predicting how long a perovskite device will last in operational deployment is challenging. The following work continues the $MAPbI_3$ degradation case study from Chapter 3 and builds a generalized understanding of $MAPbI_3$ degradation in many different environments. This work also uses a machine learning approach to develop a simple model to forecast time until transport failure from a few early time measurements. The work was published in ACS Energy Letters[53]. Reproduced with permission[53], copyright American Chemical Society 2020.

7.1 ABSTRACT

The practicality and economic viability of hybrid perovskite (HP) solar cells hinges on their operational lifetime, and methods to forecast the performance of perovskites under different operational stresses are greatly needed. Here, we explore the evolution of material-level optoelectronic properties as $MAPbI_3$ degrades and discover universal behaviors where the carrier diffusion length (L_D) decays before quasi-Fermi level splitting (ΔE_F), regardless of specific stress protocol (oxygen, humidity, thermal stress, or combination). We employ a machine learning greedy feature selection model that uses initially measured properties to predict the time it takes L_D to fall to 85% of its initial value with prediction accuracy of 12.8%. This model reveals a strong correlation between the initial rate of transmittance change and the time until loss of transport. We

translate this material-level finding to photovoltaic device-level forecasting by demonstrating that the rate of change of transmittance is equivalent to the rate of change of the spatial standard deviation of dark-field (DF) image intensity (i.e. scattered light intensity) collected in reflection mode (and thus applicable to devices with opaque contacts). This work demonstrates that transmittance and scattering methods are highly effective for accelerated material (and device) stability evaluation and forecasting.

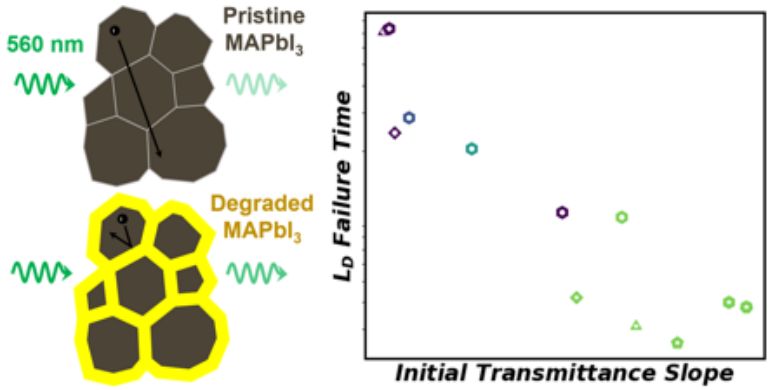

Figure 7.1. **Forecasting Decay of Hybrid Perovskite Optoelectronic Performance using Transmittance or Dark Field Microscopy**

7.2 INTRODUCTION

Hybrid perovskites (HPs) have risen to the forefront of solar cell research due to their exceptional optoelectronic properties[9, 63, 141, 147] and promise of low production costs[148, 149]. Intensive research has enabled certified power conversion efficiencies of single junction HP solar cells to approach parity with silicon[150], and pairing HP with silicon in a tandem configuration has already been shown to increase power conversion efficiency substantially[150]. Recently, research efforts have shifted to understanding the various degradation mechanisms of HPs, which has resulted in longer device lifetimes and even passing some of the stability tests that have been

developed for conventional commercially available solar cells[49, 151-153]. However, perovskites are chemically very different from current commercial PV technologies, and thus degrade differently under various operational and environmental stresses. One important question remains: how long will HP modules last in operational deployment? The ultimate practicality and economics of HP solar cells depend on this answer.

Hybrid perovskites have various possible degradation routes which involve light[46, 154, 155], heat[155, 156], oxygen[46, 47, 154], humidity[157-159], bias[160, 161], metal electrodes[162, 163], hole and electron transport layers[164-166], transparent conducting oxides[167], and mechanical stress[168]. Although encapsulation technology can be developed to prevent humidity from entering and volatile methylamine and hydrogen iodide from leaving the package[151, 152, 169], preventing oxygen ingress on the timescale of decades remains a substantial challenge due to high transmission rates through common encapsulant polymers[170, 171]. Recent progress has shown that encapsulated HP devices have passed PV industry stability standard tests, including the damp heat test (85˚C, 85% RH for 1000 hr in the dark)[22, 151, 152], thermal cycling test (200 cycles of -40˚C to 85˚C in the dark)[151, 152], outdoor (60 kWhr/m^2 in outdoor setting)[153], and UV light (15 kWhr/m^2 under UV light)[153]. However, Duong *et al.* recently showed cells that pass a 85˚C thermal stress test in the dark can fail under the same thermal stress in combination with constant illumination[155]. HPs differ from more mature PV technologies where light is not involved in primary degradation processes. Thus, although passing the industry stability tests is important[172], it is not sufficient to prove that HP devices will survive operational deployment for 30 years. Assessment of HP stability should specifically probe the most relevant and detrimental degradation mechanisms, which involve various combinations of light, heat, oxygen, and moisture[172-175].

Significant prior work investigating the impact of various stresses (light, heat, oxygen, and moisture) on HP stability and optoelectronic properties has been published. Although it is often difficult to compare stability results in the absence of standard testing protocols, extensive progress toward more stable HP devices has been realized by replacing methylammonium (MA) on the A-site[16], using lower dimensional "2D/3D" HP structures[141, 142], employing buffer layers to prevent HP interaction with metal electrodes[48], and encapsulating to prevent ingress of atmospheric species[151]. Although studies of device failure are essential in determining practical device durability, device-level work should be augmented by material-level studies of the evolution of optoelectronic properties to elucidate each relevant degradation mechanism and to design HP materials with fundamentally enhanced stability[174]. Understanding how optoelectronic changes are linked to degradation can give insight on the lifetimes of HP devices subject to operational stresses.

In this work, we examine material level optoelectronic quality changes in $MAPbI_3$ under various combinations of heat, light, oxygen, and humidity stresses using a novel *in-situ* photoluminescence-photoconductivity-transmittance (PL-PC-Tr) measurement technique. This technique simultaneously determines quasi-Fermi level splitting (ΔE_F) and mean carrier diffusion length (L_D), which are material-level metrics for attainable device-level performance metrics of open-circuit voltage and short-circuit current respectively, all while tracking optical transmittance through the HP. The transmittance (at energy above the HP bandgap and below the PbI_2 bandgap) is model-independent and easily measured. We define transmittance as the fraction of light that passes through the sample at normal incidence (light that is diffusely transmitted is not counted). It quantifies the conversion of HP to transparent PbI_2 and is correlated with changes in ΔE_F and L_D. By examining $MAPbI_3$ degradation in various levels of light, humidity, temperature, and oxygen, we find that the L_D deteriorates before ΔE_F in every case. A simple machine learning

algorithm selects features that predict the time it takes for L_D to decrease to 85% of its initial value ($t_{LD,85}$) using only the initial PL, L_D, and Tr timeseries data, yielding a simple model that describes 87% of the variance in our dataset, which contains degradation times spanning over an order of magnitude. The transmittance increase rate is highly correlated with $t_{Ld,85}$, suggesting a simple method to quickly extrapolate material or device lifetime in a very short test. One limitation to employing the transmittance measurement to detect HP degradation in a device configuration is the presence of an opaque metal contact. We overcome this hurdle by demonstrating that reflected dark-field microscope images (specifically the standard deviation of their pixel intensity) are highly correlated to transmittance and can also be used to track and quantify HP degradation. Finally, we study degradation of un-encapsulated $MAPbI_3$ devices and show that spatial changes in dark-field intensity and photoluminescence are early indicators of device failure, which can occur well before L_D failure of similar films under equivalent conditions due to a gradual reduction in shunt resistance as the absorber degrades. Collectively, our work reveals universal changes in optoelectronic properties that occur during $MAPbI_3$ degradation and provides a simple framework for forecasting HP material and device lifetimes.

7.3 Results and Discussion

The experimental setup for the PL-PC-Tr degradation experiments used in this study is shown in Figure 7.2a (Figure 7.6 shows the details of the illumination beam and channel geometry). The perovskite is illuminated with a 560 nm LED with bandpass filter (2.21 eV, above the 1.6 eV bandgap of $MAPbI_3$ and below the 2.34 eV bandgap of PbI_2) through the objective lens of an optical microscope. Calibrated absolute intensity photoluminescence (AIPL) is collected with a filter cube and wide-field camera. Photoconductivity is determined by sourcing a voltage across a narrow channel defined by electrodes on top of the HP film. The transmittance is determined by

measuring the response of a Si photodiode to light passing through the HP film. The film is contained in an environmental chamber with control of temperature, humidity, and oxygen content. Further experimental details are in the SI.

From the photoluminescence and photoconductivity, we calculate the material ΔE_F and L_D and track how these parameters evolve as a function of remaining HP content as determined by the transmittance. The ΔE_F is estimated using the equation $\Delta E_F = \Delta E_{F,max} + kT \ln PLQY_{Ext}$ as described previously[41], where k is Boltzman's constant and T is temperature. The spatial mean external PLQY ($PLQY_{Ext}$) is determined from the wide-field PL data, where $\Delta E_{F,max}$ is the Shockley-Queisser limit ΔE_F determined with initial bandgap extracted from UV-Vis absorbance. For ΔE_F calculations, we assume the spectral shape of the PL emission does not change with degradation (we challenge and discuss this assumption below). The above equation will slightly overestimate ΔE_F due to the presence of sub-bandgap emission. Previously, we found that the overestimation is less than 5 meV,[52] and should not affect the claims here. L_D is determined using the expression $L_D = \sqrt{\sigma_{ph} kT/2q^2G}$, as described previously[37], where σ_{ph} is the photoconductivity, q is the elementary charge, and G is the generation rate. The model assumes that excess carrier concentration at steady-state is uniform over the depth, which is a good approximation for this study since the absorption length is close to the film thickness (300 nm) with diffusion lengths of ~100 nm. For other conditions (thicker films, shorter absorption length, shorter diffusion length), the calculated L_D will not be equivalent to other more sophisticated techniques such as the steady-state photocarrier grating method[89, 176], but it still serves as a relative metric of carrier transport that can quickly be determined. The fraction of undegraded $MAPbI_3$ is estimated using the measured photodiode current due to the transmitted probe beam and comparing it to the transmittance through a $MAPbI_3$ film that is fully degraded to PbI_2. Beer's law is used to

convert change in transmittance to the effective thickness of remaining HP as described in the SI. Since the material-level properties of ΔE_F and L_D are indicators for device V_{OC} and J_{SC} respectively, we directly track device relevant optoelectronic properties in the HP film as degradation proceeds.

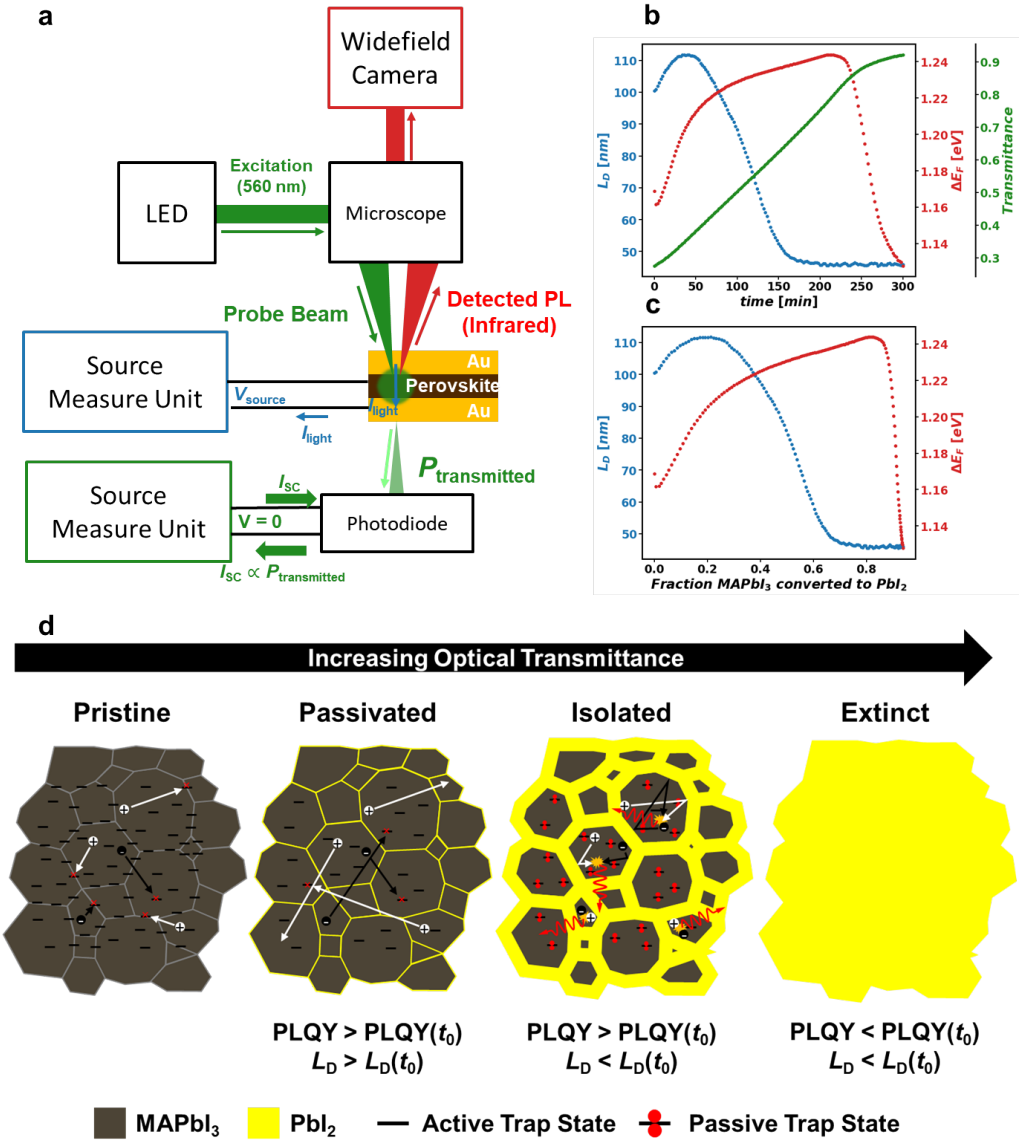

Figure 7.2**. a) Schematic of photoluminescence-photoconductivity-transmittance (PL-PC-Tr) experiment.** Samples are illuminated with 560 nm light (2.21 eV, above the 1.6 eV bandgap of the perovskite and below the 2.34 eV bandgap of lead iodide) via an LED and excitation filter, and absolute intensity PL is detected using a long pass filter and calibrated widefield camera. Photoconductivity is determined by sourcing a voltage across a narrow channel defined by electrodes on top of the HP film and subtracting dark from light current. Transmittance is

determined by placing a Si photodiode below the HP channel to measure changes in the transmitted light over time. (b) Example L_D-ΔE_F-T data for $MAPbI_3$ as it degrades under air, light, and moisture. (c) The same data, with L_D and ΔE_F plotted with fraction HP converted (which is inferred from transmittance data and comparison with a fully degraded film) (d) Schematic indicating optoelectronic evolution during $MAPbI_3$ degradation as transmittance of 560 nm light through the film increases.

Figures 7.2b-c present an example degradation experiment, conducted in air at 60% relative humidity, under 8 Suns illumination at room temperature. Morphological and structural characterization of the $MAPbI_3$ films used in this study are presented in Figures 7.7 and 7.8. We observe similar evolution of optoelectronic properties as reported previously[37], with an initial period of increasing L_D and ΔE_F, followed by a period of increasing ΔE_F with decreasing L_D, and a final period where both ΔE_F and L_D have decayed significantly. Importantly, early transmittance changes demonstrate that beneficial changes in ΔE_F and L_D that occur during the same period are associated with irreversible conversion of $MAPbI_3$ to PbI_2. This finding corroborates recent consensus that the presence of PbI_2 is beneficial to absorber properties, yet also detrimental to long-term stability[177, 178]. Changes in ΔE_F and L_D can occur due to changes in: (i) monomolecular Shockley-Read-Hall lifetimes; (ii) carrier concentration (due to absorption and funneling through PbI_2[179]); and/or (iii) mobility.

To further understand charge carrier recombination dynamics in our degradation experiment, we complemented the PL and PC data with time-resolved photoluminescence (TRPL). We conducted a degradation experiment with identical stress as in Figure 7.2b-c, and removed the film from the stress chamber periodically and measured TRPL. The results are presented in Figure 7.9a-b, Table 7.1 and Figures 7.10-7.11, where the "degraded" film represents a state near the maximum in PLQY where the diffusion length has decreased significantly. Effective monomolecular and bimolecular and lifetimes (and) were evaluated by fitting the TRPL decay traces as described in SI. For both fluences tested, it is found that the monomolecular lifetime increases with

degradation while the effective bimolecular lifetime decreases. Both are commensurate with increasing steady-state PLQY and quasi-Fermi level splitting, as determined in the in-situ PL-PC-Tr experiment. To further understand this effect and corroborate the increase in ΔE_F, we collected steady-state AIPL spectra on pristine and degraded $MAPbI_3$ and fit them with the full-peak fit method described previously[54, 147] and reviewed in the SI (Figure 7.9c, Table 7.2). These data confirm an increasing ΔE_F during degradation, mostly due to suppressed non-radiative recombination but also due to a marginally lower sub-bandgap absorptivity. We therefore infer that effective trap density decreases during the initial stages of degradation simultaneously as the diffusion length is decreasing, as demonstrated by longer monomolecular Shockley-Read-Hall (SRH) lifetimes, higher quasi-Fermi level splitting, and lower sub-bandgap absorptivity. We note that results reported here are obtained with excitation light below the bandgap of PbI_2 (see Figure 7.13). Merdasa *et. al* recently reported differences in optoelectronic properties of partially degraded $MAPbI_3$ when exciting with light above and below the bandgap of PbI_2[179], which we also observe (see Figure 7.10 and SI discussion).

Table 7.1 **PL lifetimes of pristine and degraded $MAPbI_3$ with 640 nm excitation**. τ_1 and τ_2 correspond to the fitting monomolecular and bimolecular lifetimes, respectively.

	Pristine		Degraded	
Fluence [nJ/cm^2]	τ_1 [ns]	τ_2 [ns]	τ_1 [ns]	τ_2 [ns]
214	**87**	35	**155**	17.8
1840	**48**	10	**100**	2.4

Table 7.2 **Extracted full peak AIPL fit parameters for pristine and degraded $MAPbI_3$**, under steady state 10 Suns 532 nm excitation.

	θ	γ [meV]	E_g [eV]	ΔE_F [eV]	T [K]	$\overline{a_{SB}}$
Pristine	1.29	28.0	1.614	1.223	287	2.70e-3
Degraded	1.18	21.3	1.610	1.259	293	2.37e-3

The discussion above gives mechanistic insight into the origin of optoelectronic changes in $MAPbI_3$ during degradation (schematically illustrated in Figure 7.2d). At early times, thin regions of PbI_2 passivate surfaces and reduce SRH recombination without decreasing inter-grain transport (polycrystalline carrier mobility), resulting in increased L_D. Further conversion to PbI_2 isolates the remaining HP domains, forming a disordered energy landscape and rapidly decreasing the mobility, which causes a maximum and then decrease in L_D. Meanwhile, increased PbI_2 content and penetration of atmospheric species further passivate traps on the surface[180, 181] and in the bulk of the HP[182, 183], causing further increases in PLQY. Finally, PLQY disappears as the final domains are converted to PbI_2.

Forecasting Optoelectronic Degradation of HP Films

The foregoing results demonstrate that initial improvements in ΔE_F and L_D are tied intimately to degradation, and we hypothesize that early changes in ΔE_F, L_D, and Tr are strongly predictive of the ability of the HP to withstand a given stress. To test the generalizability of this behavior, we subjected $MAPbI_3$ to 15 different stress conditions with varying degrees of temperature, oxygen, moisture, and light intensity (Figures 7.14-7.16). The "dry N_2" condition is the only case where we observe stable transmittance and thus infer that no degradation occurs during this experiment. However, we do observe light-induced traps that causes an initial decrease in ΔE_F and L_D, followed by stabilization in both. This aligns with many other studies that have identified this behavior[182, 184, 185], which is fully reversible after an appropriate "rest" period in the dark[184, 185].

We observe monotonically increasing transmittance in all other stress environments. By studying these experiments collectively, we identified two universal behaviors: (i) existence of an early-time regime where ΔE_F, L_D, and transmittance are all increasing and (ii) L_D fails (i.e reaches a maximum and then decreases) before ΔE_F fails. This indicates that the optoelectronic evolution we observed above for $MAPbI_3$ in humid air at room temperature is not unique. As $MAPbI_3$ degrades, increases in the SRH lifetimes precedes decreases in the inter-grain carrier mobility, regardless of whether the degradation is initiated by humidity alone, oxygen alone, driven by high thermal stress, or by moderate amounts of these stresses in combination. This finding suggests that the patterns of optoelectronic property evolution are relatively mechanism-agnostic and understanding where a material exists on its degradation trajectory can give clues regarding the time until failure. Observing that L_D fails before ΔE_F in every case aligns with our above description of a degradation mode in which decomposition products impede inter-grain carrier mobility while remaining perovskite domains are being further passivated.

Ultimately, the goal of this work is to predict the effective lifetime of an HP film, based on initial changes in the PL-PC-Tr dataset and the insights into optoelectronic evolution developed above. Given that L_D reaches a maximum and then decreases before ΔE_F reaches a maximum and then decreases, we define the time it takes the L_D to decrease below 85% of its initial value ($t_{Ld,85}$) as the material lifetime metric. We employ machine learning methods to train a model for this prediction task. In a machine learning approach, a test set and validation set are held out from training data to aid model development. The purpose of the validation set is to choose the model and model parameters, while the purpose of the test set is to obtain an unbiased estimate of model error for unseen data[186]. A common validation strategy is to use cross-validation, where we split

the data into k-folds and measure validation error on each fold[186]. Leave-one-out cross-validation is a special case where the number of k splits equals the number of samples.

We have a unique machine learning problem with many possible features but a small number of samples. Our aim is to use features related to the initial five observations of *normalized* PLQY, L_D, and Tr to predict $t_{Ld,85}$. Since we have degradation times that span over an order of magnitude, we use a log transform so that each experiment has relatively equal importance (we predict $\ln(t_{Ld,85})$). We excluded two experiments in our 15-run dataset; degradation was too slow in the dry N_2 experiment ($L_{D,85}$ was not observed) and too fast in the air/80%RH/25°C experiment ($L_{D,85}$ occurs in training region so prediction is trivial). The behavior observed for the air/80%RH/25°C sample differs from the sample with air/80%RH/85°C; the latter does not form a hydrate due to the higher temperature leading to longer time until $L_{D,85}$ (see Figures 7.14, 7.19 and 7.20). In addition to the first five measurements of each variable (diffusion length, photoluminescence quantum yield, and transmittance), we include average slope and curvature for each property over this time range as features. Since we have a small dataset, we limited our model exploration to linear models, including linear regression, Ridge, LASSO, and linear regression with greedy feature selection[187]. Initial cross-validation results suggested that linear regression with greedy feature selection outperformed the other models, so we selected this model to use for testing. The so-called "greedy" feature selection algorithm[187] starts with no features, then adds one at a time based on which will give the lowest validation error using leave-one-out cross validation. We continue to add features until no additional feature reduces the validation error further. One additional advantage of this approach is that it results in a sparse solution, where we obtain a simple model with only the few most important features. The details of the machine learning algorithm are described in detail along with the pseudocode for the greedy selection algorithm in the SI section 1.10. Figure 7.3a shows

the improvements in mean-squared error and R^2 score each iteration, and Figure 7.3b shows the predicted vs. actual $\ln(t_{Ld,85})$. Since the dataset is small, the test set error will strongly depend on the random selection of data to include in testing. To obtain a more accurate measure of testing error we use an outer loop to perform a test-train split and an inner loop to perform feature selection. In the outer loop, we loop over the experimental runs (for different environmental conditions) and held each sample out from feature selection to get an unbiased estimate of error for each sample. We employ an inner loop to perform feature selection using leave-one-out cross validation to determine the feature set. Using this testing scheme, we obtain an average prediction error of 12.8% (all results for each test-train split are shown in Figure 7.17). Figures 7.3a and 7.3b show one characteristic result of an iteration of the outer loop. The experiment labeled "test sample" is completely independent and was not used for training or feature selection. The prediction for all other samples shows the predicted $\ln(t_{Ld,85})$ when each validation sample was held out in the cross-validation step within the inner loop. The inset in Figure 7.3a shows the three features selected and their relative weights, where the magnitude of the bar represents the importance of that feature in the model predictions relative to the variance of that feature in the training dataset.

The results show that the initial slope of the transmittance curve is highly correlated with $t_{Ld,85}$ (shown directly in Figure 7.3c, with the quantitative relationship shown in SI section 10). This is the first feature selected and has the highest magnitude model weight. A greater initial transmittance slope indicates a shorter time to $L_{D,85}$, where the transmittance slope is determined from the first 5 measurements only. Additionally, early behavior in the L_D trajectory adds signal to the prediction. With only three features from the first five time points of our dataset, we can describe 87% of the variance in $t_{Ld,85}$ (with times that span over an order of magnitude). Most of

the variance not described by the model comes in the high temperature, high light intensity cases where there is a sudden, catastrophic failure point (indicated by discontinuity in the derivative of transmittance curve and sudden decrease in L_D as shown in Figure 7.14-7.15). Essentially, our results show that after only 5 measurements of transmittance and L_D, we can predict the time until failure to 12.8% on average, where the timescale to collect 5 measurements is around an order of magnitude less than time until failure, providing a proof of concept of a very simple diagnostic tool to forecast time until critical absorber failure of various materials and devices subject to different stresses.

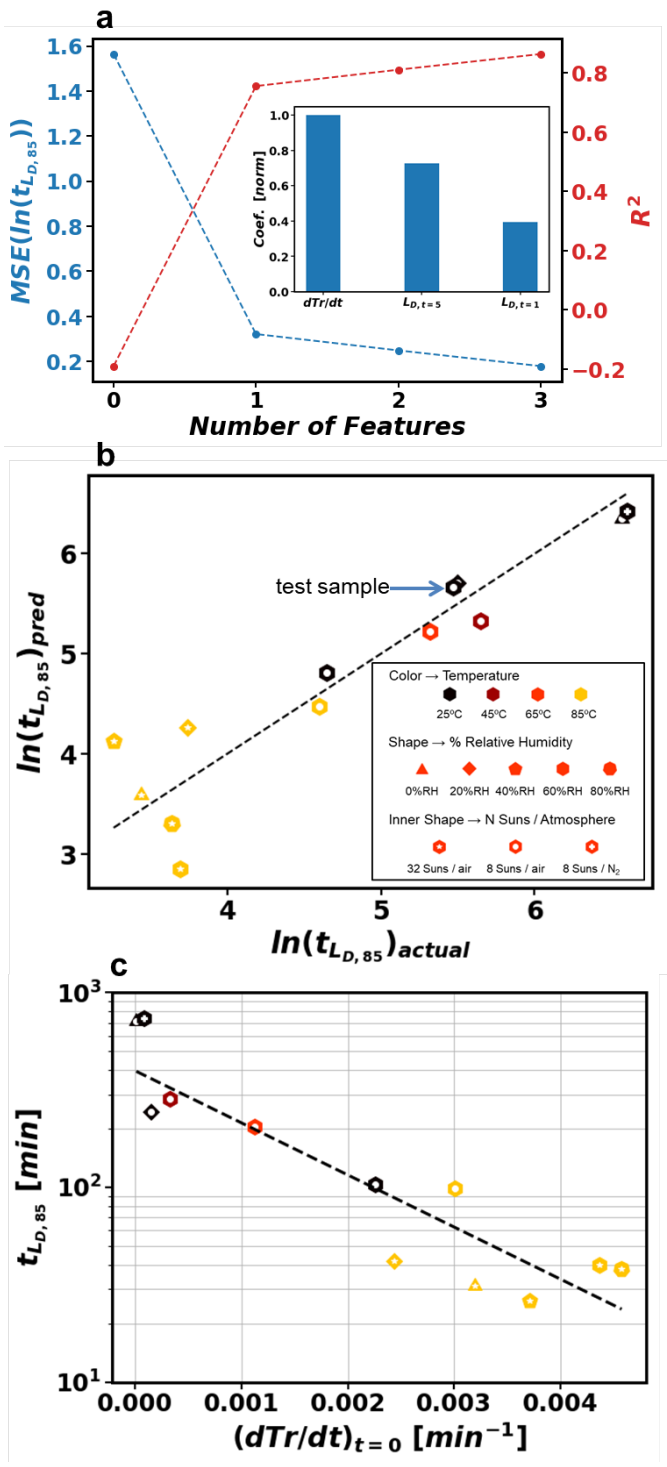

Figure 7.3. **Results of a machine learning to predict the time for L_D to decay to 85% of its original value ($t_{Ld,85}$) using only the first 5 time steps of PL-PC-Tr data.** (a) shows the mean squared error and R^2 for describing the data for each step of the greedy algorithm (step 0 indicates using mean of training Ld,85 and no features). Dashed lines are to guide the eye. Inset shows the relative feature weights for the 3 features selected, normalized to the highest coefficient, where the coefficients are determined using standardized features (not affected by the units used). (b) shows

the predicted vs. actual for the model (note use of log transform due to difference in timescales). Each data point was predicted with cross-validation, meaning that the model was trained excluding that sample. The labeled "test sample" was held out of the entire dataset for greedy feature selection. (c) Demonstrates the relationship between $t_{Ld,85}$ and initial transmittance slope. Dashed-line indicates best fit to all data using only transmittance slope (linear fit with log transform).

Reflected-Mode Dark-Field Microscopy on HP Materials and Devices

Above we demonstrate that L_D deteriorates in HP films before ΔE_F, and that the initial transmittance slope is an excellent predictor of time until L_D failure. Next, we investigate how this insight can be leveraged to predict time until failure in HP devices. However, transmittance measurements are not possible when using an opaque metal back contact in a photovoltaic device. One strategy is measurement of specular reflectivity which is readily measured via bright field microscopy. However, direct correlation of device specular reflectance with absorber transmittance is not straightforward due to the optical properties of the other layers in the device, which may evolve in competing ways as the device degrades (e.g. HP transmittance increases while Ag reflectivity decreases). However, information related to changes in the film morphology, grain boundary structure, or phase distribution can be optically detected by measuring diffuse reflectivity (i.e. scattering) with dark field microscopy, as is shown in Figure 7.18. Further, we noticed in the prior $MAPbI_3$ degradation experiments a substantial change in the diffuse reflectivity with degradation as detected (Figures 7.19-7.20). To test dark field microscopy as an alternative to transmittance to detect and quantify HP degradation, we conducted a $MAPbI_3$ degradation experiment while simultaneously monitoring the evolution of both (Figure 7.4).

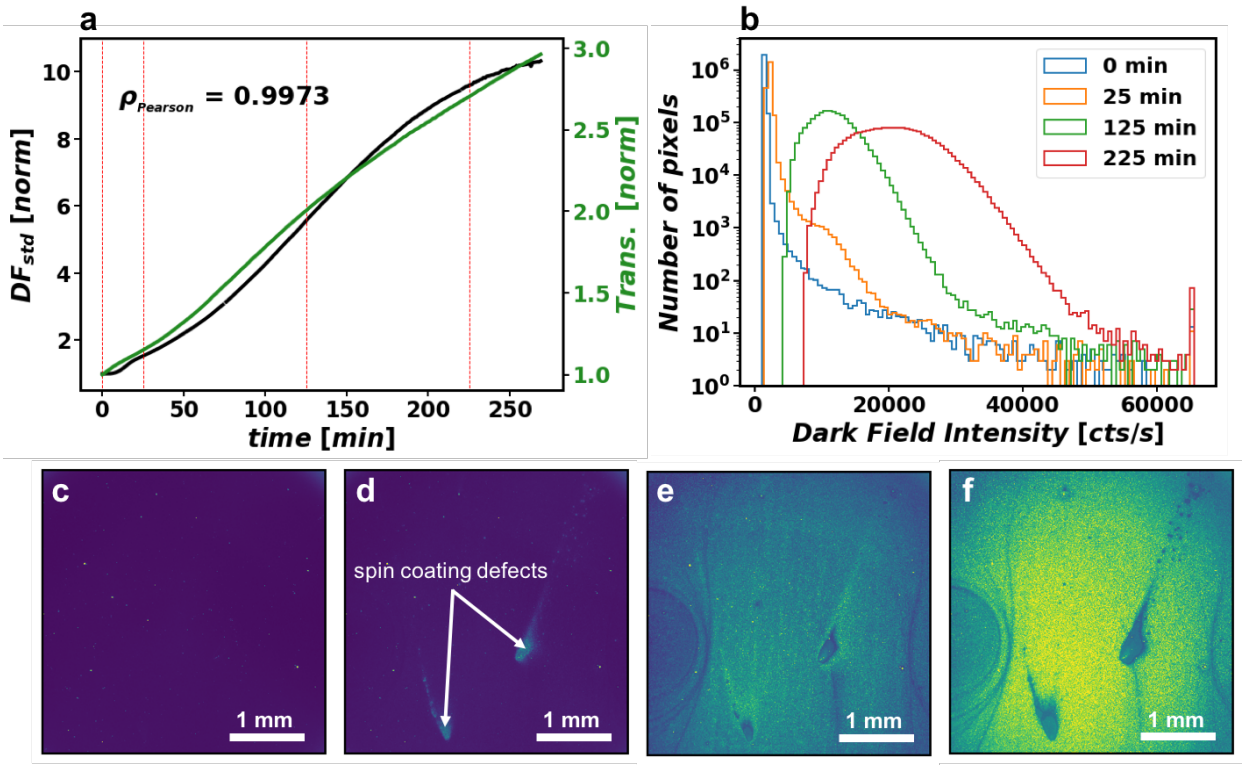

Figure 7.4**. (a) Time evolution of the standard deviation of dark field intensity (DF_{std}) and transmittance as $MAPbI_3$ degrades in air** at 60% RH with steady state illumination with ~8 Suns 560nm LED. Values are normalized to the time = 0 value. Dashed red lines indicate 0 min, 25 min, 125 min, and 225min snapshots used in b-f. The Pearson correlation coefficient between transmittance and DF_{std} is 0.9973. (b) Histogram of dark field intensity at four different times during degradation experiment. Vertical axis represents number of pixels with each intensity, plot on a log scale. (c-f) reflected dark field intensity a 0 min, 25 min, 125 min, and 225 min respectively. Spin coating defects in the film are labeled in (d), which are the first regions to show increased dark field intensity.

The reflected dark field image changes dramatically as $MAPbI_3$ degrades. The image of the pristine film (Figure 7.4c) shows low intensity (as expected for a flat spin-cast film with minimal diffuse light scattering). As degradation advances, the image coarsens and brightens, initially and most dramatically at two spin coating defects but eventually throughout the entire film. These data show that $MAPbI_3$ degradation causes increased light scattering due to formation of additional phase boundaries and small domains with formation of PbI_2 that manifest as increased reflected dark field image intensity and standard deviation. While the mean, median, and standard deviation of dark field intensity show dramatic changes with time, we identified that at early times standard

deviation (DF_{std}) has strongest correlation with the transmittance curve (see Figure 7.21). When considering the entirety of the degradation experiment, DF_{std} is highly correlated with the transmittance (Pearson correlation coefficient = 0.9973), indicating that the dark field can be used as a metric to detect early HP degradation rates and forecast material or device lifetime, even in the presence of an opaque back contact. Further, dark field images map out locations where the degradation is initiated or locally accelerated, which in this case reveals morphological defects related to spin coating. Although we only investigate degradation of $MAPbI_3$ to PbI_2 here, we expect formation of other degradation products in different HP systems to show similar signals in the dark field image, which is a topic for ongoing investigation.

Having identified that dark field microscopy detects material degradation at early times, we conducted degradation experiments on $MAPbI_3$ solar cells in a p-i-n architecture (typical JV curve shown in Figure 7.22). We stressed the un-encapsulated device at open-circuit under 1 Sun, 560 nm LED illumination in air with 60% RH, and we periodically collected dark field images and JV curves to determine how material evolution with time is connected to PV performance parameters and parasitic resistances (Figure 7.5).

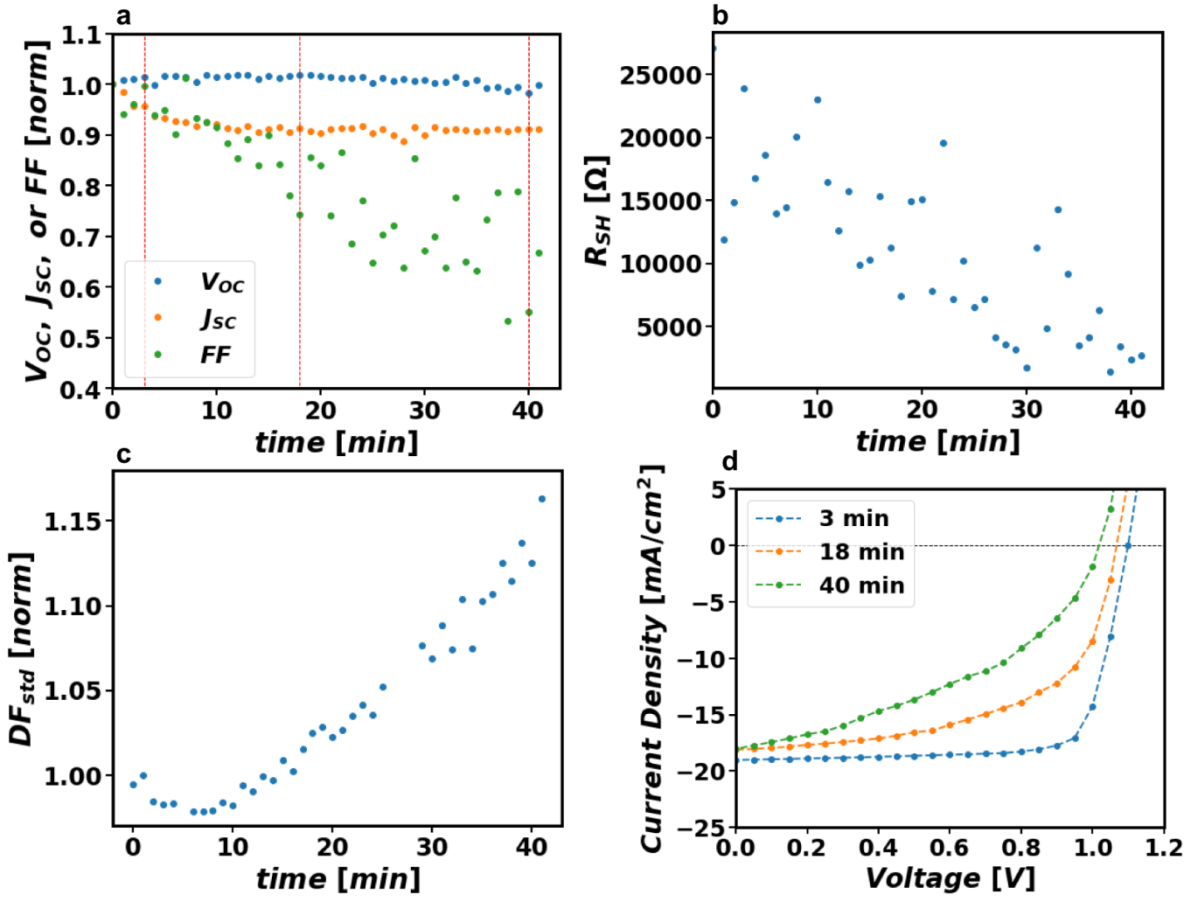

Figure 7.5**. a) Evolution of device parameters with time under open-circuit conditions**, un-encapsulated in air with 60% RH with constant 1 Sun illumination with a 560 nm LED (normalized to the time = 0 value). JV sweeps occur every minute to extract device parameters. (b) Evolution of shunt resistance (R_{SH}) with time, evaluated using a linear fit between 0 and 0.2V. Deteriorating PCE in this experiment is primarily due to decreasing R_{SH}.(c) Evolution of standard deviation of the dark field intensity image with time through degradation (normalized to the time = 0 value). The DF_{std} increase indicates absorber degradation which causes R_{SH} decay. (d) characteristic JV curves through the degradation experiment. The times of these curves correspond to vertical dashed lines in (a).

We observe steady decay in overall PCE, with fill factor changing most dramatically, primarily due to decreasing shunt resistance (Figure 7.5b). Additionally, we have an initial decrease in J_{SC} and increase in V_{OC}. Importantly, the time evolution of the reflected dark field intensity shows an increase in DF_{std} (Figure 7.5c) as also observed in Figure 7.4, indicating absorber degradation in this device over the course of the stress test. The strong anti-correlation between the dark field

standard deviation and the fill factor suggest that the decrease in R_{SH} is induced by absorber degradation (but may be modulated by the quality of other layers in the device). Changes in DF_{std} have an early onset, indicating that initial values of this timeseries could be used to forecast device lifetime. Thus, this parameter facilitates comparison of the extent of degradation across both films and devices. By comparison to studies on films, we note that $L_{D,85}$ in humid air environments typically occurs at a material conversion fraction between 0.3 and 0.6 (Figure 7.16), yet we estimate from Figure 7.4a that the material conversion corresponding to a ~16% increase in DF_{std} is about an order of magnitude lower (<0.05 material fraction, see SI note for estimation details). This indicates that time until degradation to $L_{D,85}$ of a film represents the maximum possible lifetime of a device made with that film (adjusting for differences in HP degradation rates in device vs. film). However, it is likely that the device PCE will decrease below 85% of its initial value before material $L_{D,85}$ is achieved in the device due to a degradation-induced shunt, which requires only local failure of a relatively small region. We suspect that efforts toward reducing the heterogeneity in various device layers will suppress early formation of shunt pathways and enable the device lifetime to move toward or approach the HP $t_{LD,85}$.

In this work, we study signals that can be used to forecast the failure of HP films and devices. We first study the optoelectronic evolution of $MAPbI_3$ with time and show that L_D deteriorates before ΔE_F for a wide variety stress conditions. By employing a simple feature selection machine learning algorithm, we discover that just three features can be used to predict the time for L_D to decrease to 85% of its starting value with a mean error 12.8%, where the initial transmittance slope is the feature with the greatest predictive power. We then show that the standard deviation of intensity of dark field optical microscopy images is highly correlated with transmittance, providing a material degradation proxy applicable to devices with opaque back contacts. Accordingly, we

show that dark field intensity is an early indicator of device failure, where the devices we studied demonstrated gradually decreasing R_{SH} due to $MAPbI_3$ degradation. Collectively, this work provides a framework for accelerated testing of HP devices and demonstrates that transmittance and/or dark field microscopy can be used as forecasting and diagnostic tools.

7.4 SUPPORTING INFORMATION

1. Experimental Methods

1.1 Perovskite Film Fabrication

$MAPbI_3$ precursor ink was prepared by dissolving stoichiometric MAI and PbI_2 at 1M in 9/8 vol/vol N-methyl-2-pyrrolidone (NMP)/dimethylformamide (DMF), then stirred for 1.5 hr at 70 ˚C. Glass substrates (15mm square) were cleaned with a four-step procedure by sonicating for 10 minutes each in (1) Alconox and DI water, then (2) DI water, then (3) acetone, and finally (4) 2-propanol. Shortly before spin coating, the substrates were cleaned for 10 minutes in an Ar plasma. $MAPbI_3$ thin films were fabricated via spin coating in a N_2-filled glovebox. The precursor ink was spin coated at 4000 rpm for 45 sec, then submerged in a diethyl ether (DEE) antisolvent bath for 60 s, then annealed at 100 °C for 10 min. The film thickness was 300 nm as determined by profilometry.

1.2 Perovskite Device Fabrication

$MAPbI_3$ devices were fabricated with the p-i-n architecture ITO / NiO_x / $MAPbI_3$ / PCBM / bis-C_{60} / Ag with a similar fabrication method reported previously[37, 96]. $MAPbI_3$ ink was prepared by dissolving stoichiometric MAI and PbI_2 at 1 M in 7/3 vol/vol γ-butyrolactone (GBL)/dimethyl sulfoxide (DMSO), then stirred at 75 °C for 2 hr, then stirred overnight at room temperature. The NiO_x solution for sol-gel method was prepared as described elsewhere[99]. The PCBM ink was

prepared at 15 mg/mL in chlorobenzene. The bis-C_{60} ink was prepared at 2 mg/mL in 2-propanol and dissolved using a sonicating horn then filtered with a 0.2 μm PTFE filter.

Patterned ITO glass (Thin Film Devices) was cleaned with a four-step procedure by sonicating for 10 minutes each in (1) Alconox and DI water, then (2) DI water, then (3) acetone, and finally (4) 2-propanol. The ITO substrates were cleaned for 10 minutes in an O_2 plasma. The NiO_x solution was spin coated at 3000 rpm for 60 s in air, then annealed at 350 °C for 60 min in air. The substrates were thereafter transferred into a N_2-filled glovebox for spin coating the rest of the layers. $MAPbI_3$ was spin coated at 1000 rpm for 15 s then 4000 rpm for 45s, then 700 μL of toluene was dripped onto the substrate over 3 s with 15 s left in the second step of the spin coating program. The devices were then annealed for 10 min at 100 °C. The PCBM layer was spin coated with a 2-step procedure, first 1500 rpm for 55 s then 5500 rpm for 5 s. The bis-C_{60} layer was spin coated at 3000 rpm for 30. 100 nm of Ag was thermally evaporated at a rate of 2 Å/s.

1.3 Time Resolved Photoluminescence

Time resolved photoluminescence (TRPL) was collected with a Picoquant TRPL instrument equipped with a FluoTime 300 Spectrometer, PDL 820 Laser Driver, and a TimeHarp 260 with PMA Hybrid 50 detector. We used a 2.0 MHz repetition rate with 800 ps time/channel with a 510nm or 640nm excitation source with calibrated fluence.

1.4 Absolute Intensity Confocal Photoluminescence

Absolute Intensity Confocal Photoluminescence was collected as described previously[37, 41]. PL spectra were obtained with a modified Horiba LabRAM HR-800 with 532 nm laser excitation and a 10x objective. The adjustable confocal hole was set to 800 μm, and a 150 gr/mm Czerny− Turner monochromator blazed at 1200 nm was used. The photon detection rate was calibrated using a blackbody source (IR-301, Infrared Systems Development) at 850, 950, and 1050 °C with a 10 μm

pinhole (the calibration factor was averaged between the three temperatures to minimize error). To calculate 1 Sun excitation flux, an Oriel optical power meter and beam profiler were used to set the photon flux equal to above-bandgap photon flux of the AM1.5 GT solar spectrum for a 1.61 eV material.

1.5 Perovskite Film Characterization

Scanning electron microscopy (SEM) micrographs were obtained on Au-coated films using a FEI XL830 Dualbeam SEM-FIB. To avoid charging effects, an Au-Pd coating was sputtered onto the perovskite films prior to imaging. Thin film X-ray diffraction (XRD) measurements were collected with a Bruker D8 Discover instrument equipped with a Pilatus 100K large-area 2D detector and a Cu anode (wavelength 1.542 Å, Kα radiation). The X-ray beam size was defined with a 0.3 mm collimator. Optical absorbance spectra were collected from a PerkinElmer Lambda 1050 UV/vis/NIR spectrometer with an integrating sphere in laboratory atmosphere.

1.6 Perovskite Device Characterization

Current voltage (J-V) curves of $MAPbI_3$ devices were measured under simulated AM1.5 1 Sun illumination using an Oriel VeraSol-2 AAA Solar Simulator and an OSI Optoelectronics UV-100DQ Si photodiode to set the lamp intensity to equal above bandgap AM1.5GT photon flux for a 1.61eV material. Forward and reverse sweeps were conducted with a sweep rate of 0.2 V/s. A device area of ~0.07 cm^2 was used; device area was defined as the intersection of Ag and ITO electrodes and was precisely measured using an optical microscope.

1.7 Photoluminescence – Photoconductivity – Transmittance Degradation Experiments

Simultaneous photoluminescence – photoconductivity – transmittance experiments were conducted with a similar methodology as described previously[37]. Wide-field absolute intensity PL measurements were conducted with a Hamamatsu C11440 camera with a Lumencor SpectraX light

source and Mitutoyo 100x objective. A green LED was used for excitation, which was filtered with a 32 nm wide-band-pass filter centered at 560 nm. The excitation source was passed through a filter cube with a dichroic mirror and an emission long-pass filter to achieve a minimum OD 8 suppression for excitation wavelengths. The excitation photon flux was calibrated with a Newport 91150 V Si reference diode to set the photon flux equal to above-bandgap photon flux for a 1.61 eV material under an AM1.5 GT spectrum. The Hamamatsu detector was calibrated by preparing a $MAPbI_3$ standard and comparing PL detector counts with the PLQY from the confocal AIPL setup (which was calibrated using a blackbody spectrum at three temperatures, as described above).

For photoconductivity measurements, 80 nm-thick Au contacts with a channel spacing of 200 μm were thermally evaporated at 2 Å/s. Photoconductivity was measured by connecting Au contacts to a Keithley 2420 sourcemeter and sourcing + or – 3V while measuring current. The polarity of the applied voltage is switched every measurement to prevent artifacts from ion migration and buildup over the duration of the experiment due to consistent applied voltage. Degradation experiments on films were conducted in a closed stage (Linkam Scientific LTSE420-P) with controlled atmosphere and temperature; those on devices were conducted in a custom-built environmental chamber. Relative humidity (RH) control in the Linkam stage was enabled by bubbling dry gas (air or N_2) through a glycerol/water solution with specific volume ratio to achieve the desired % RH; in the custom chamber, an ultrasonic humidifier was used with a closed-loop controller. Gas flowed through the Linkam stage for the duration of the experiment at a constant flow rate of 2 L/min.

The Linkam stage has a hole in the middle of the heating plate that enables transmittance measurements. An OSI Optoelectronics UV-100DQ Si photodiode was aligned directly under this

hole to detect evolution of transmitted light through the HP film through the duration of the experiment; short-circuit current from the photodiode was detected using a Keithley 2400 sourcemeter.

We used our environmental control chambers to set the temperature, illumination intensity, % relative humidity, and atmosphere composition. The reported temperature denotes the hotplate temperature and is accurate to within 1 C (we do not account for a temperature drop across the glass substrate nor for radiative heating). For humidity, we monitored the % relative humidity throughout the experiment and achieved +/- 5 %RH by employing a humidifier attached with sensor and controller. We measured illumination intensity with a Si photodiode estimate that the intensity fluctuates within less than 2%. For atmosphere composition control, we used a positive pressure of flow from pure N_2 or air cylinder. Based on the above, the variations within each condition are much smaller than the intentional changes in stress condition we performed in our experimental plan and have minimal impact on our overall findings.

1.8 Perovskite Device PL-JV-DF Degradation Experiments

Perovskite device Photoluminescence – Current/Voltage – Dark Field degradation experiments were conducted similarly to the above with certain modifications. An Olympus 5x objective was used with 560 nm LED excitation, and the excitation incident flux was set so that the device J_{SC} under the LED equaled the measured J_{SC} under 1 Sun illumination with a AAA Solar Simulator. The experiment was conducted in an environmental control box with relative humidity maintained at 60%. Widefield PL and reflected dark field images were collected periodically. For Figure 7.5, the device was held at open-circuit while a reverse then forward JV sweep was performed every 1 minute using a sweep rate of 0.24 V/s.

1.9 Data Cleaning and Preparation

For data presented in Figure 7.13-7.15, missing and corrupted data (<1% of all data points) for the ΔE_F, L_D, and transmittance were filled using linear interpolation. L_D data was smoothed by taking the moving average of the moving average with window = 5.

1.10 Machine Learning Model Details

We employed a linear regression model with a greedy feature selection algorithm with leave-one-out (LOO) cross validation for feature selection and a LOO testing scheme. An overview of the method is displayed with pseudocode in Algorithm 1, where N is the number of samples (MAPbI3 degradation at different environmental conditions), D is the number of all possible features, and the stopping criteria for feature selection is when the model error improves less than "error_improvement_threshold," which we set to 0.05 in our experiments. In the "evaluate baseline with 0 features" step, we measure LOO error using the mean of the training set as the predictions (where the training set doesn't contain the left out sample) to get a baseline error to start the algorithm. This is a "greedy" algorithm, because at each step in the **while** loop we add the feature that reduces the LOO validation error the most. Within the **while** loop, there is an inner **for** loop used to perform LOO cross-validation. After the **while** loop we remove the last feature added since this feature did not improve the error greater than "error_improvement_threshold." Since we have a small dataset, we have a testing scheme that loops over the samples to evaluate the test error with N different datasets in the outer **for** loop (see Figure 7.17 for results).

```
Algorithm 1
begin
    for i = 1,2…N
        leave one out train/test split
        define feature_list as an empty array
        evaluate baseline model performance with 0 features
        while error_improvement > error_improvement_threshold
            for d = 1,2…D
                add feature d to "feature_list_temp"
                for j = 1,2…(N-1)
                    leave one out train/validation split
                    define and train linear regression model
                    make validation predictions and evaluate error
                end
                save the mean error using feature d
            end
            add the feature that gave minimum error to feature list
            evaluate "error_improvement" since last step in while loop
        end
        remove the last feature added
        retrain model with entire training set
        evaluate test error
        store model details
    end
end
```

2. Time Resolved Photoluminescence Data Fitting

TRPL data was fit as described previously[188]. Excess carrier density can be described with the differential equation:

$$\frac{dn}{dt} = -k_1 n - k_2 n^2 - k_3 n^3 \tag{7.1}$$

where n is the excess carrier density and k_1, k_2, and k_3 are the monomolecular, bimolecular, and trimolecular recombination rates respectively. Assuming there is little contribution from trimolecular (Auger) recombination, this differential equation has an analytical solution given by

$$\frac{n(t)}{n_0} = \frac{k_1}{(k_1 + \kappa_2)\exp(k_1 t) - \kappa_2} \tag{7.2}$$

where n_0 is the carrier concentration at $t = 0$ and where $\kappa_2 = k_2 n_0$. Thus, the Shockley-Read-Hall (SRH) and radiative effective lifetimes are given by $\tau_1 = 1/k_1$ and $\tau_2 = 1/\kappa_2$.

Raw TRPL data was first preprocessed by (1) removing initial data before excitation, (2) normalizing to the maximum intensity of the TPRL decay, and (3) truncating the end of the TRPL decay when it falls into the noise threshold. Assuming the PL intensity is proportional to $n(t)$, the normalized PL decay can now be fit to equation 7.2 which yields the effective SRH and radiative lifetimes. As shown in Figure 7.8, the fit decays closely match the data.

3. Full Peak Absolute Intensity Photoluminescence (AIPL) Fitting

Full peak fitting to AIPL data was performed as described by Katahara and Hillhouse[54] and applied to perovskite PL spectra in our earlier work[41]. The PL data is fit to a form of the Generalized Planck radiation law, attributable to Lasher, Stern, and Würfel given by:

$$I_{PL}(E) = \frac{2\pi E^2}{h^3 c^2} \cdot \frac{a(E, \Delta E_F, T)}{\exp\left(\frac{E - \Delta E_F}{kT}\right) - 1} \tag{7.3}$$

where the absorption coefficient is modeled by

$$\alpha(E) = \frac{\alpha_0}{\gamma 2\Gamma(1 + 1/\theta)} \int_{-\infty}^{E_g} \left(\exp\left(- \left| \frac{u}{\gamma} \right|^{\theta} \right) \sqrt{(E - E_g) - u} \right) du \tag{7.4}$$

where Γ is the gamma function, γ is an energy broadening parameter for sub-bandgap absorption, θ is an exponent to describe the form of the sub-bandgap tail, and $E_g$is the direct transition energy[54]. The full form of eq. 7.3 used in this study is given as equation 22 in Katahara and Hillhouse[54], which accounts for non-zero band occupation in the absorption model. The photoluminescence peak data was fit with eq. 7.3 using Levenberg-Marquardt non-linear least squares fit, with fitting parameters E_g, ΔE_F, θ, γ and T and setting $\alpha_0 d$ equal to 3.75. A log transform on the data was performed prior to non-linear least squares fitting so that the peak and

tail regions of the AIPL spectra would influence the residuals with relatively equal weight. The average sub-bandgap absorptivity, $\overline{a_{SB}}$, is given by

$$\overline{a_{SB}} = \frac{1}{E_g}\int_0^{E_g}\left(1-\exp\left(-d\alpha(E,\Delta E_F)\right)\right)dE \tag{7.5}$$

which represents a single metric that can describe the quantity of sub-bandgap absorptivity.

4. Converting Si photodiode readings to Transmittance and material conversion X

For Figures 7.2, 7.4, and 7.12-7.13, we report transmittance data and material conversion X based on Si photodiode measurements. We measure the I_{SC} of the Si photodiode, which is proportional to the intensity of light that passes through the perovskite film. As the perovskite film degrades, the transmitted intensity monotonically increases which is detected by an increase in I_{SC} of the Si photodiode (since the 560 nm LED probe beam is below the bandgap of degradation products – see Figure 7.12). We convert I_{SC} to transmittance for films by using measured absorbance of the $MAPbI_3$ and PbI_2 to set a transmittance scale for pristine film and complete conversion (assuming minimal reflectivity), then normalize each experiment to this transmittance scale. This method was employed to exclude small effects the precise photodiode alignment has on absolute measured I_{SC}. We acknowledge that contributions from reflectivity are not negligible, so the reported transmittance scale may deviate slightly from the values reported.

Material conversion fraction is performed using the relation

$$T = 10^{-A(1-X)} \tag{7.6}$$

which is derived from the Beer-Lambert law, where T is transmittance, A is the absorbance of pristine $MAPbI_3$ (from Figure 7.10), and X is the volume fraction of PbI_2. This treatment assumes (i) at all points in degradation, the thickness of $MAPbI_3$ at all locations is proportional to the total volume fraction remaining of $MAPbI_3$ and (ii) there is negligible absorption by PbI_2. Deviations

from assumption (i) could have a small effect on the quantitative X reported, but relative trends will be preserved.

We can further extend this rationale to estimate conversion fraction of $MAPbI_3$ from dark field intensity by using the strong correlation identified between DF_{std} and transmittance observed in Figure 7.5. For a DF_{std} increase of ~16%, the transmittance increases by ~6%, which according to equation 7.6 corresponds to a $MAPbI_3$ conversion fraction of 0.03.

5. Channel and illumination beam geometry for photoconductivity measurements

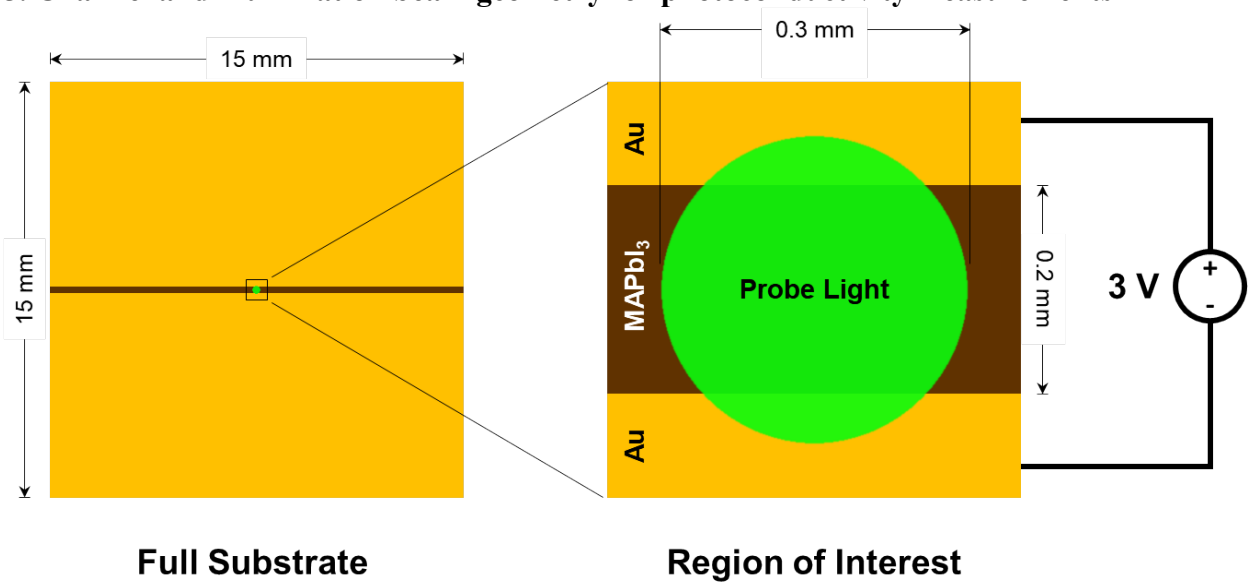

Figure 7.6**. Schematic of probe beam and channel geometry for the samples used in this work**. A circular beam 0.3 mm in diameter is focused in the center of a perovskite channel 0.2 mm wide separating two gold contacts, across which the measurement bias is applied during photoconductivity measurements.

6. Morphological and Structural Characterization of HP Films

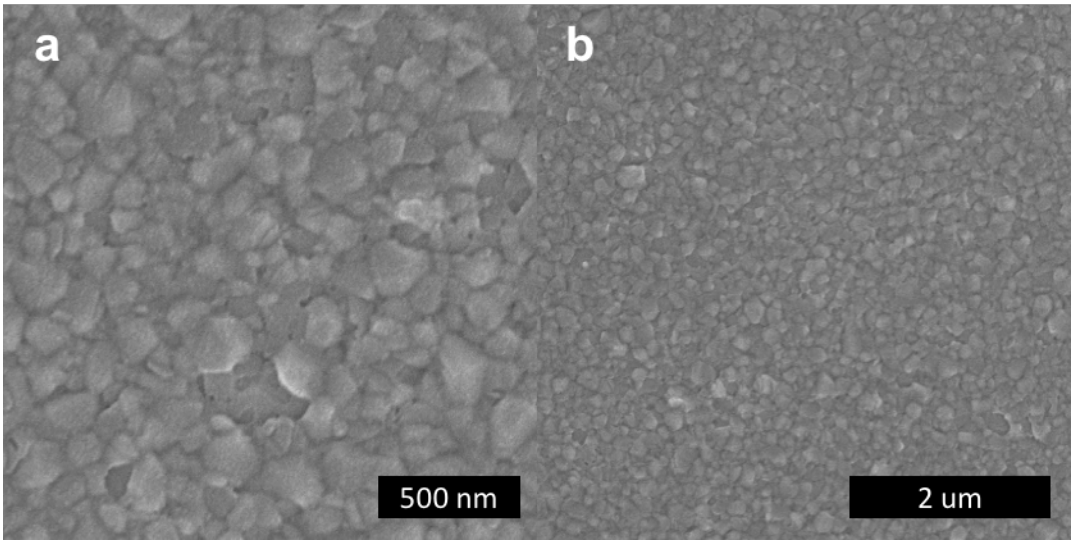

Figure 7.7**. Typical SEM images of $MAPbI_3$ films used in this study.**

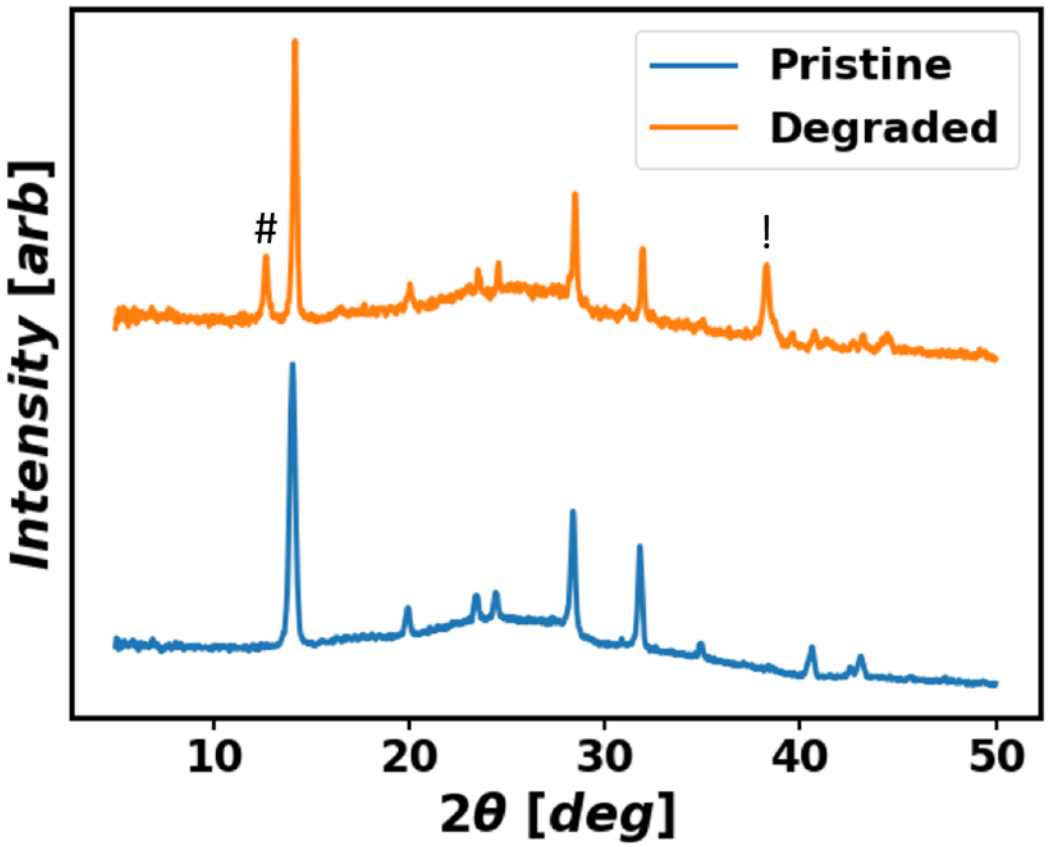

Figure 7.8**. Typical XRD patterns for pristine and degraded $MAPbI_3$ films for stress under light, air, and moderate %RH**. Note that although an XRD beam spot size was selected to fall within the degraded region, perfect alignment of the beam with this region is not possible and thus the "degraded" XRD pattern likely contains contributions from the adjacent, undegraded regions. Peaks distinguishing the primary degradation product PbI_2 and the Au contacts are denoted by the respective symbols # and !.

7. Time Resolved and Steady-State Photoluminescence Results and Discussion

Recently, Merdasa *et al.*[179] have shown that excitation light with energy above the bandgap of PbI_2 (λ_{ex} = 450nm, or 2.76eV; bandgap of PbI_2 = 2.37eV; see Figure 7.12) will cause absorbed carriers in the PbI_2 to recombine in a small "transition phase" between the PbI_2 and $MAPbI_3$, resulting in significantly faster radiative recombination than in pristine $MAPbI_3$. To test if this phenomenon is consistent with our degradation tests, we collected TRPL decays with excitation above and below the bandgap of PbI_2 (Figure 7.9). We observed significantly brighter PL emission and faster radiative decay when exciting with light above the bandgap of PbI_2, corroborating the mechanism suggested by Merdasa *et al.*[179]. Note that the 560nm excitation used in our degradation experiments has minimal absorption by PbI_2 (see Figure 7.12) so this carrier funneling mechanism cannot explain the observed steady-state PLQY enhancements. However, any future work exploring optoelectronic changes in HPs during degradation should acknowledge the substantial differences in PL behavior for excitation energies above and below the bandgap of PbI_2 and other potential degradation products.

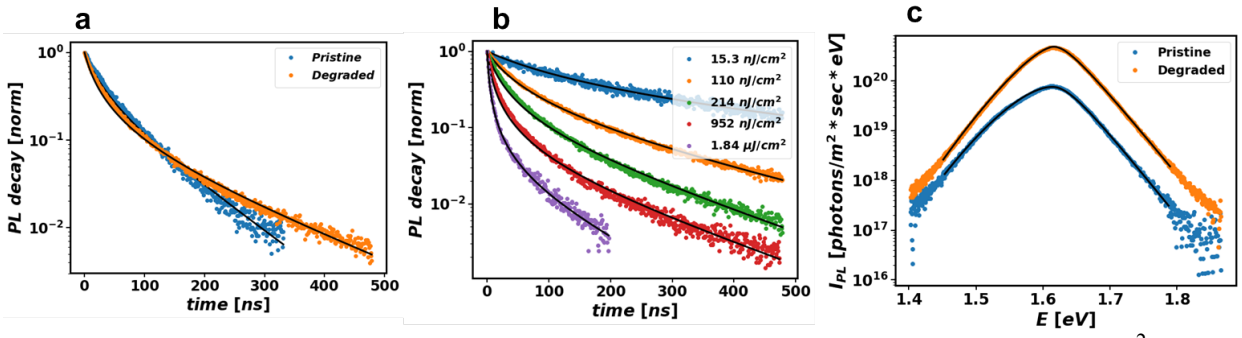

Figure 7.9**. (a) PL decays for pristine and degraded $MAPbI_3$ films** at 214 nJ/cm^2 fluence with 640 nm excitation, where "degraded" indicates an HP film removed from stress chamber in the "isolated" state. Solid line indicates fit model with monomolecular and bimolecular terms to experimental data (see SI). (b) Degraded $MAPbI_3$ film PL decay at various fluences with 640 nm excitation. (c) steady state absolute intensity PL of pristine and degraded $MAPbI_3$ film (excitation 532 nm cw, 10 Suns).

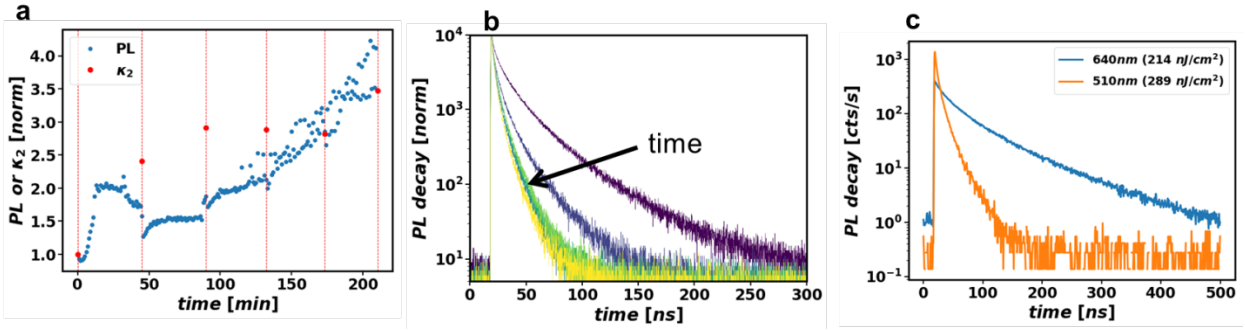

Figure 7.10**. (a) Evolution of steady state PL and effective radiative recombination rate κ_2 during $MAPbI_3$ degradation in air** with 60% RH under 8 Suns illumination with a 560 nm LED. The HP film is removed from stress chamber for ~5 min every 45 min to measure TRPL. TRPL is collected using 510 nm excitation (b) TRPL decay traces for data presented in (a). (c) Comparison of TRPL traces for 510 nm vs. 640 nm excitation at similar fluences.

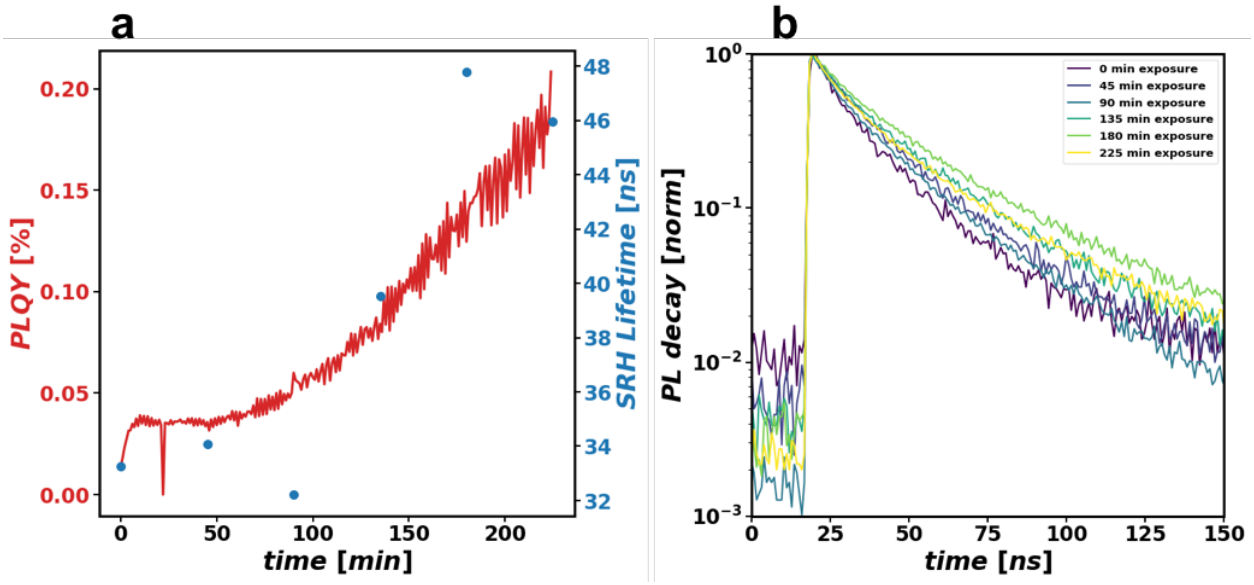

Figure 7.11**. (a) Evolution of steady state PL (from widefield camera measurements) and effective monomolecular (SRH) lifetime during $MAPbI_3$ degradation in air** with 60% RH under 8 Suns illumination with a 560 nm LED. The HP film is removed from the stress chamber for ~5 min every 45 min to measure TRPL. TRPL is collected using 640 nm excitation. (b) TRPL decay traces for data presented in (a).

8. UV-vis Absorbance Characterization of HP Films

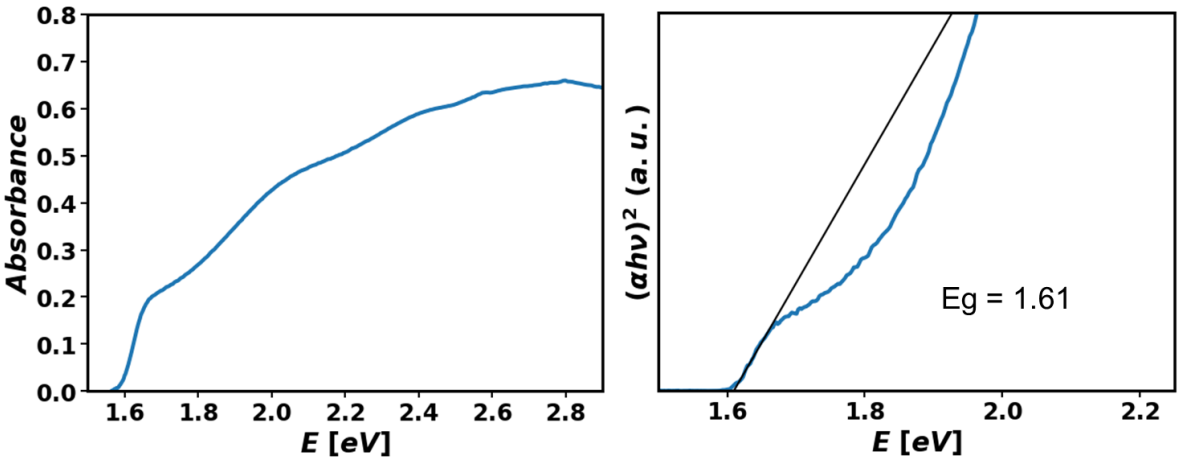

Figure 7.12**. UV-vis absorbance spectrum (a) and Tauc plot (b) of a typical $MAPbI_3$ film used in this study.**

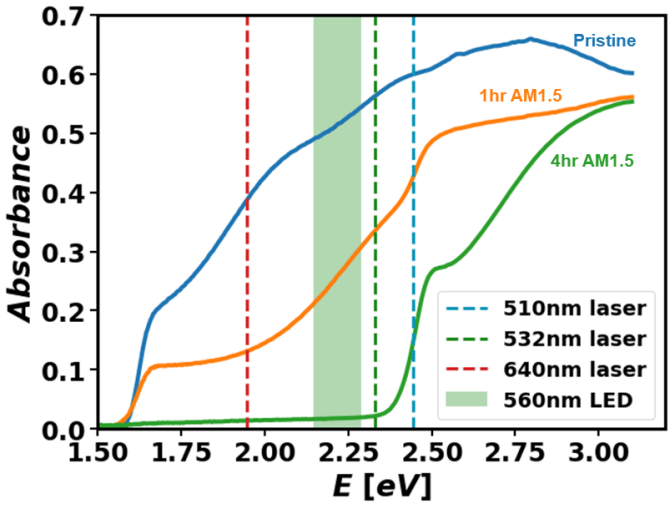

Figure 7.13**. UV-vis absorbance spectra of a $MAPbI_3$ film before and after exposure to a solar simulator for 1 hr and 4 hr in air**. After 1 hr, the film has partially converted to PbI_2, and after 4 hr it has fully converted to PbI_2. The UV-Vis data is overlaid with the excitation sources used in this study. For the 560 nm LED, the boundaries of the region shown denotes where excitation bandpass filter falls below 1.0% transmittance.

9. Photoluminescence – Photoconductivity – Transmittance of $MAPbI_3$ with various Light, Temperature, Atmosphere, and Humidity Stress

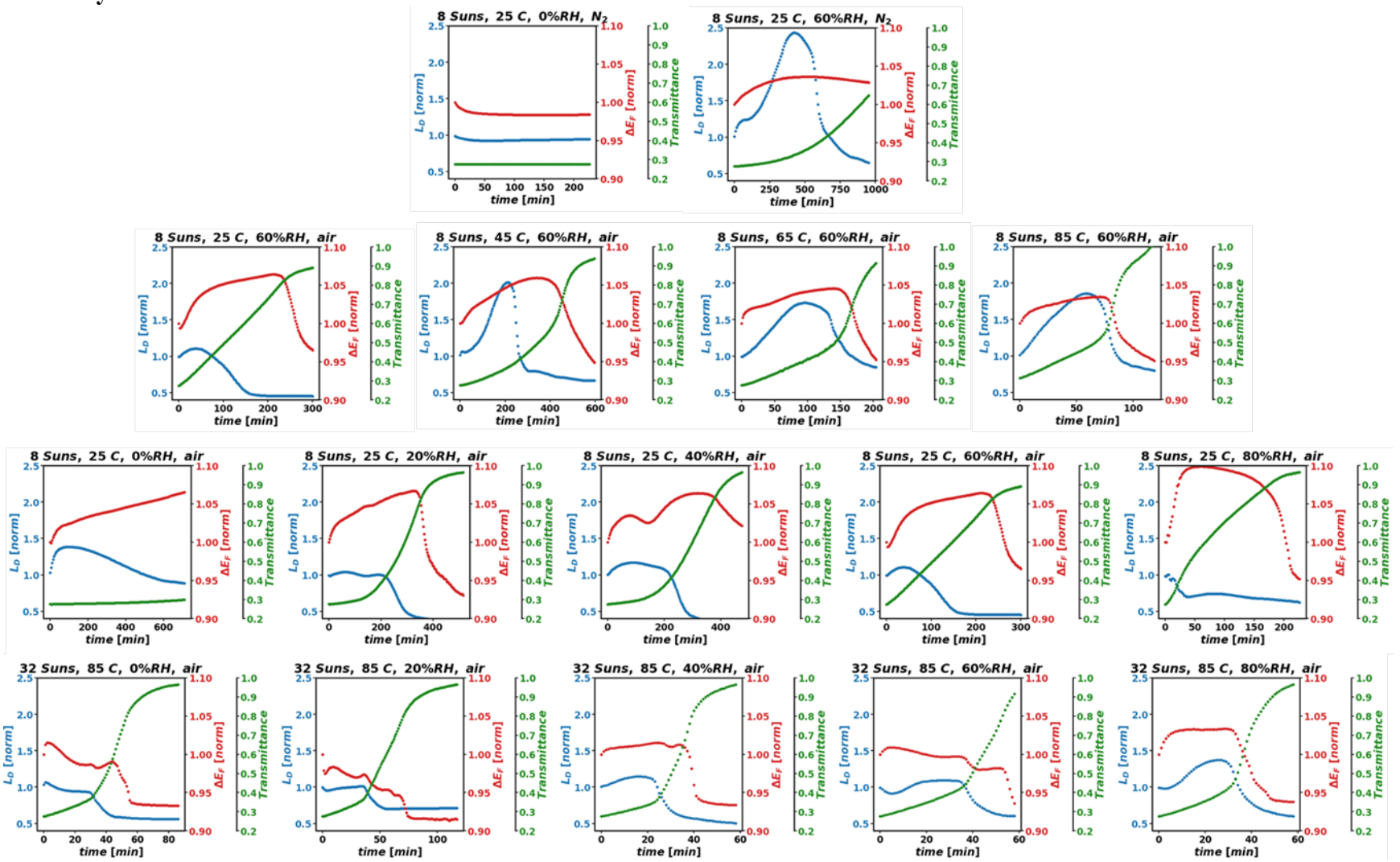

Figure 7.14**. Evolution of ΔE_F and L_D with time for $MAPbI_3$ films under various stresses**. ΔE_F and L_D traces are normalized to the t=0 value, and all data are plot with the same vertical scales. However, note that the horizontal time scales vary.

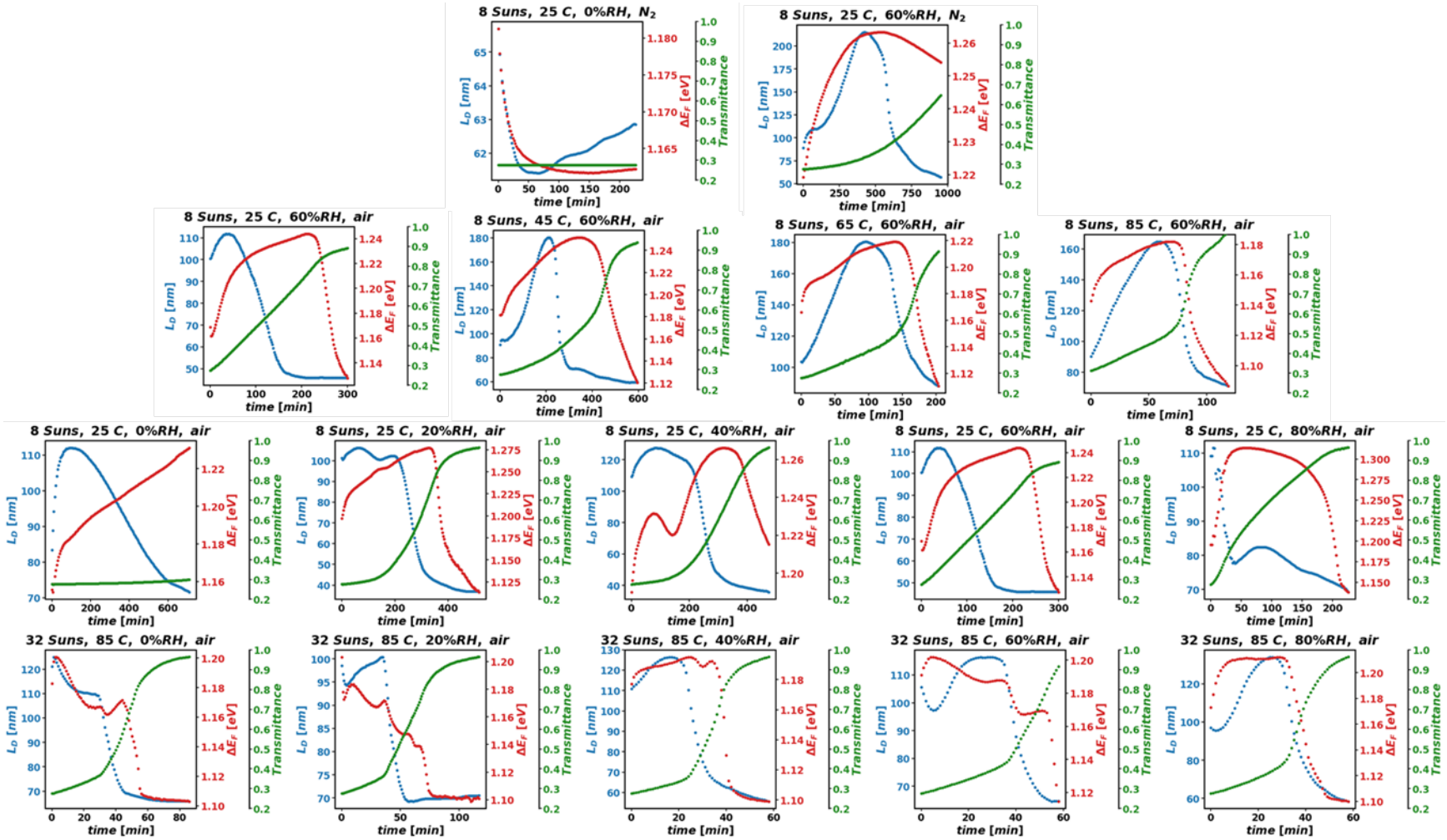

Figure 7.15**. Evolution of ΔE_F and L_D with time for $MAPbI_3$ films under various stresses**. This figure shows the same data as Figure 7.14, but ΔE_F and L_D traces are plot in absolute units and each experiment is auto-scaled. Note that the horizontal time scales vary.

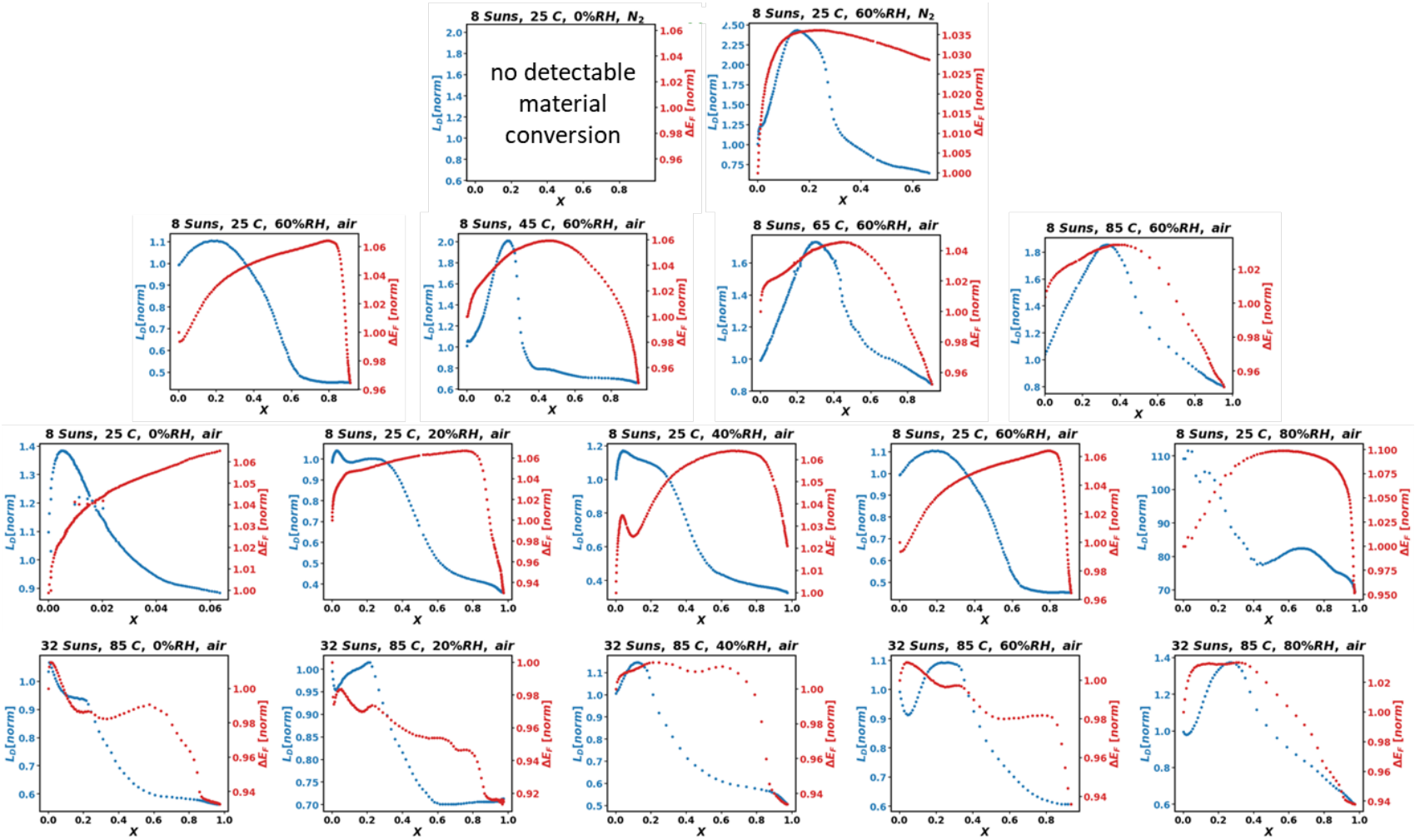

Figure 7.16. **Degradation experiments represented as ΔE_F and L_D evolution with conversion from pure $MAPbI_3$ (X=0) to pure PbI_2 (X=1), assuming Beer's law**. The dry N_2 case is omitted because there is no detectable material conversion.

10. $L_{D,85}$ predictions for all datasets and test samples and transmittance slope fit to all data

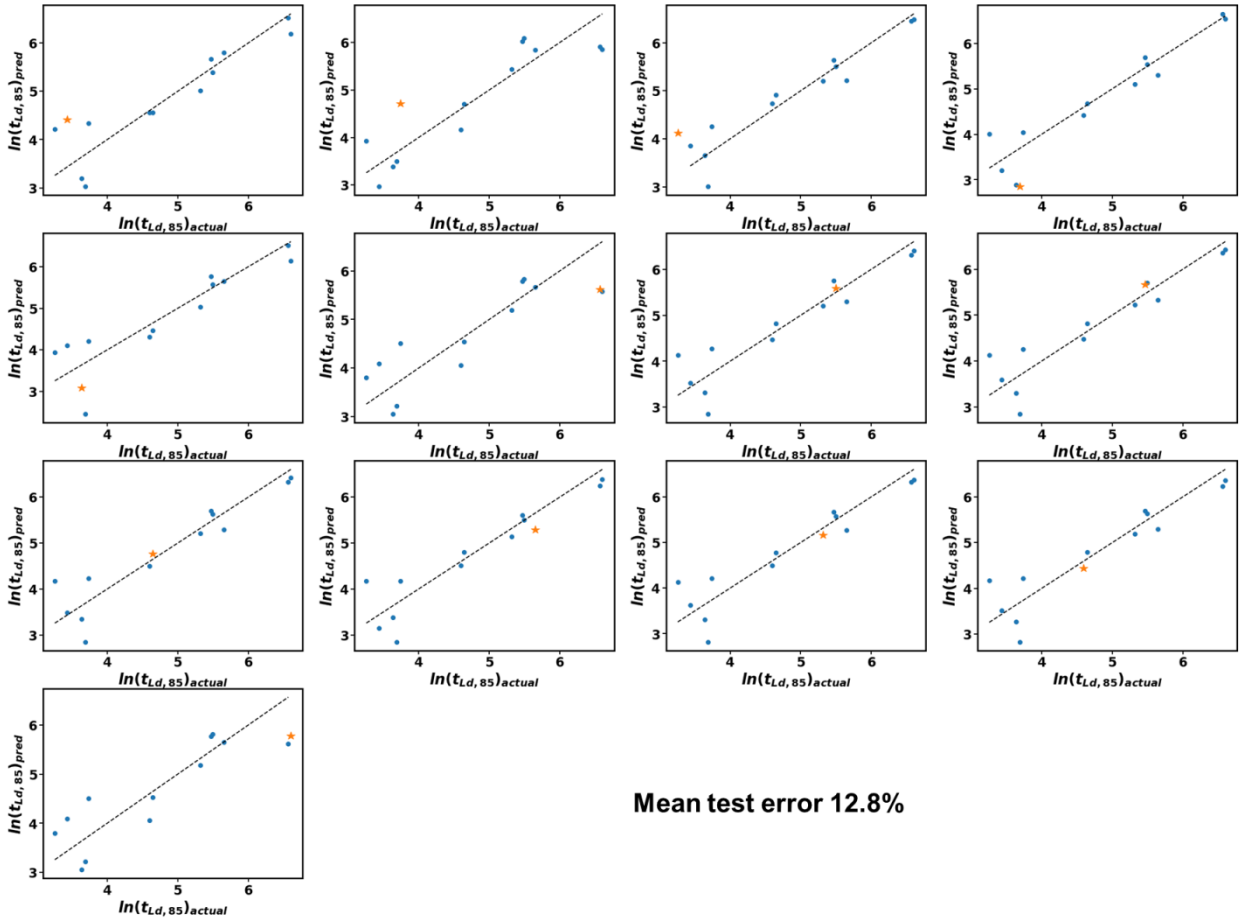

Figure 7.17**. Results of the machine learning feature selection and testing algorithm (Algorithm 1) for each of the 13 different testing folds**. For each case, 1 sample was held out from training and from feature selection, then a model was trained with the remaining data. Each plot shows the predicted vs. actual $ln(t_{L_{D,85}})$, where the star is the sample that was held out of the feature selection process.

Figure 7.3c in the main text shows that there is a strong negative correlation between $t_{L_{D,85}}$ and $\left(\frac{dTr}{dt}\right)_{t=0}$. A rough prediction of $t_{L_{D,85}}$ can be obtained by only measuring the initial transmittance slope. The dashed fit line shown in Figure 7.3c is the best fit to equation 7.7

$$A\left(\frac{dTr}{dt}\right)_{t=0} + B = \ln(t_{L_{D,85}}) \tag{7.7}$$

where A = -615.7 and B = 5.981, with $\left(\frac{dTr}{dt}\right)_{t=0}$ expressed in [min^{-1}] and $t_{L_{D,85}}$ in [min] (valid only within ranges of our dataset shown in Figure 7.3c).

11. Dark field microscopy experimental set-up

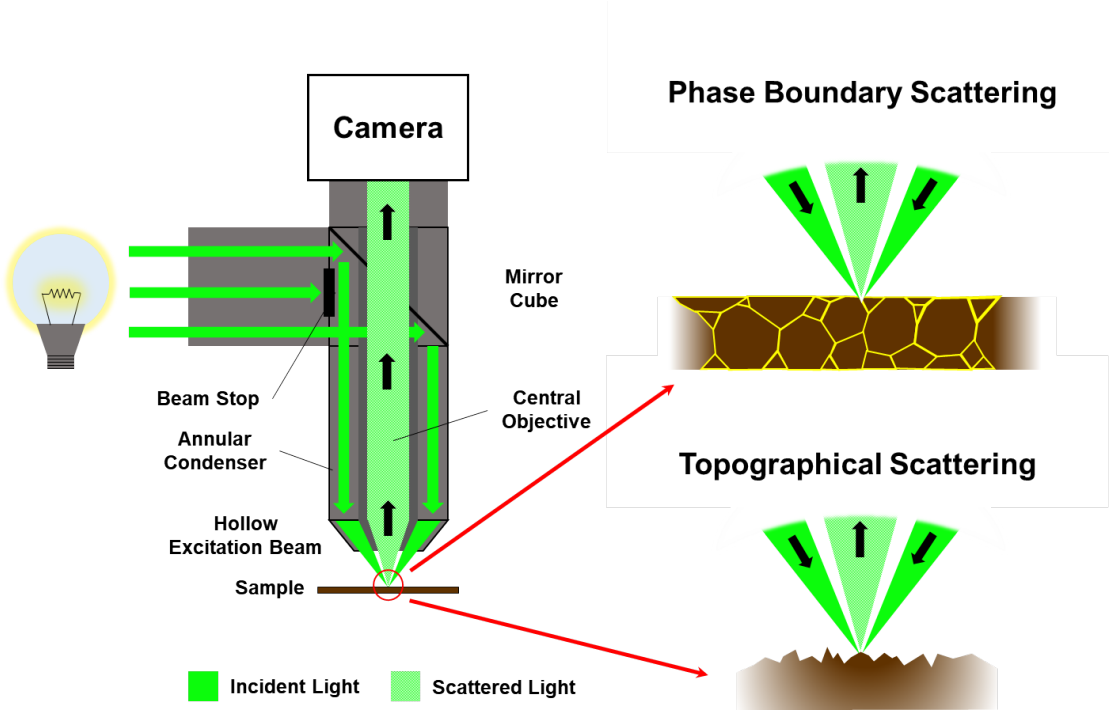

Figure 7.18**. Schematic of reflected light dark-field microscopy**. Probe light is first directed through a mirror cube containing a central beam stop to a ring-shaped condenser (coaxial with the objective lens), forming a hollow cone of light that strikes the sample at an oblique angle. As a result, the central objective collects light that scatters diffusely, but completely rejects the specular component of reflected light, thus providing information on features that specifically result in random scattering such as surface roughness or the presence of secondary phases.

12. Reflected Dark Field Images of Pristine and Degraded $MAPbI_3$ Films

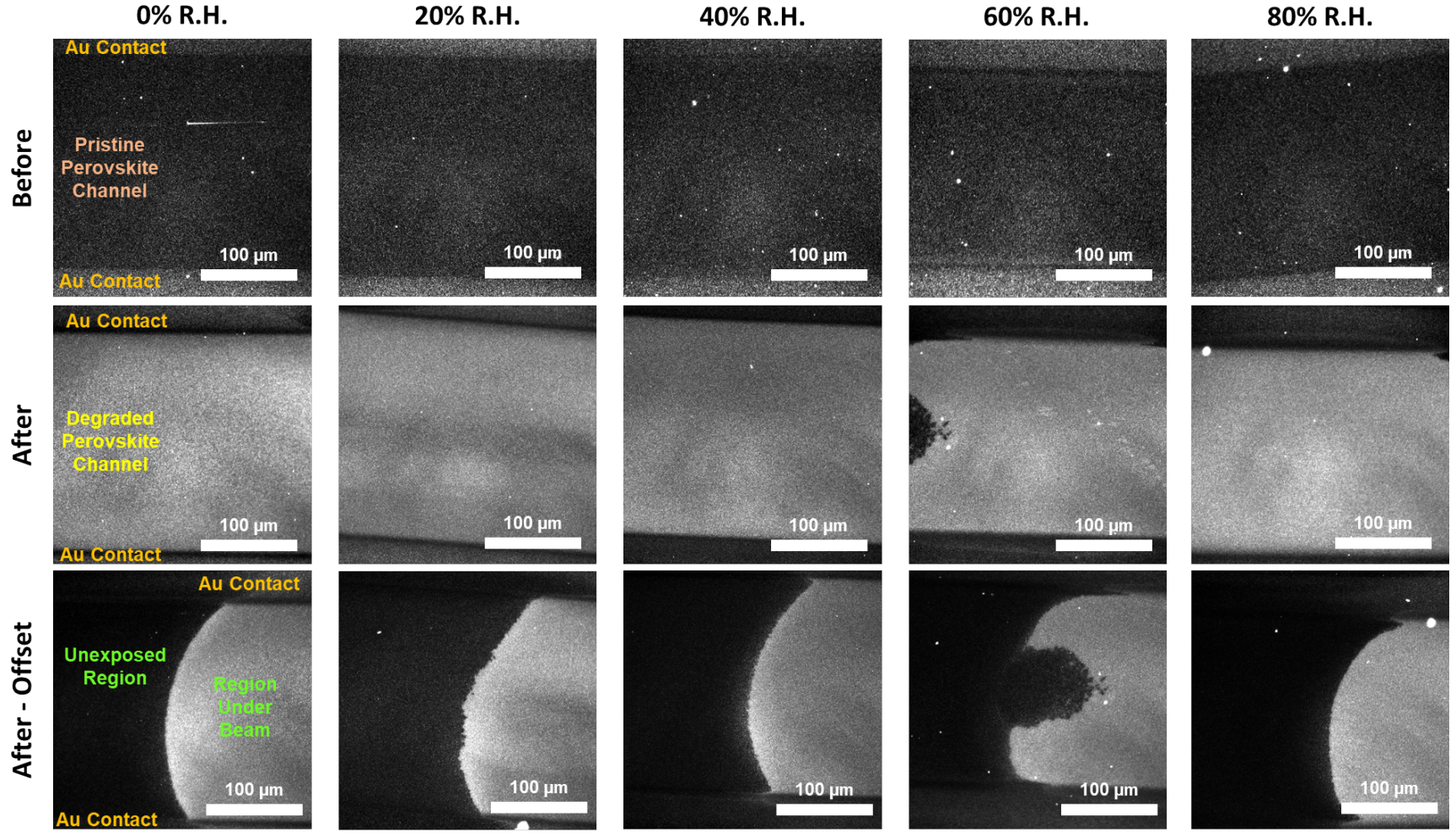

Figure 7.19**. Evolution of dark field intensity during degradation experiments in high stress condition (32 Suns, 85 ˚C) at various %RH**. All images have the same intensity scale. The top row shows before degradation, middle row shows after degradation, and the last row shows after degradation, looking at the light-dark boundary (left side was not directly exposed to the probe beam, and right side was illuminated with 32 Suns). Au contacts are distinguishable by the pattern of roughly horizontal lines at the top and bottom of each image.

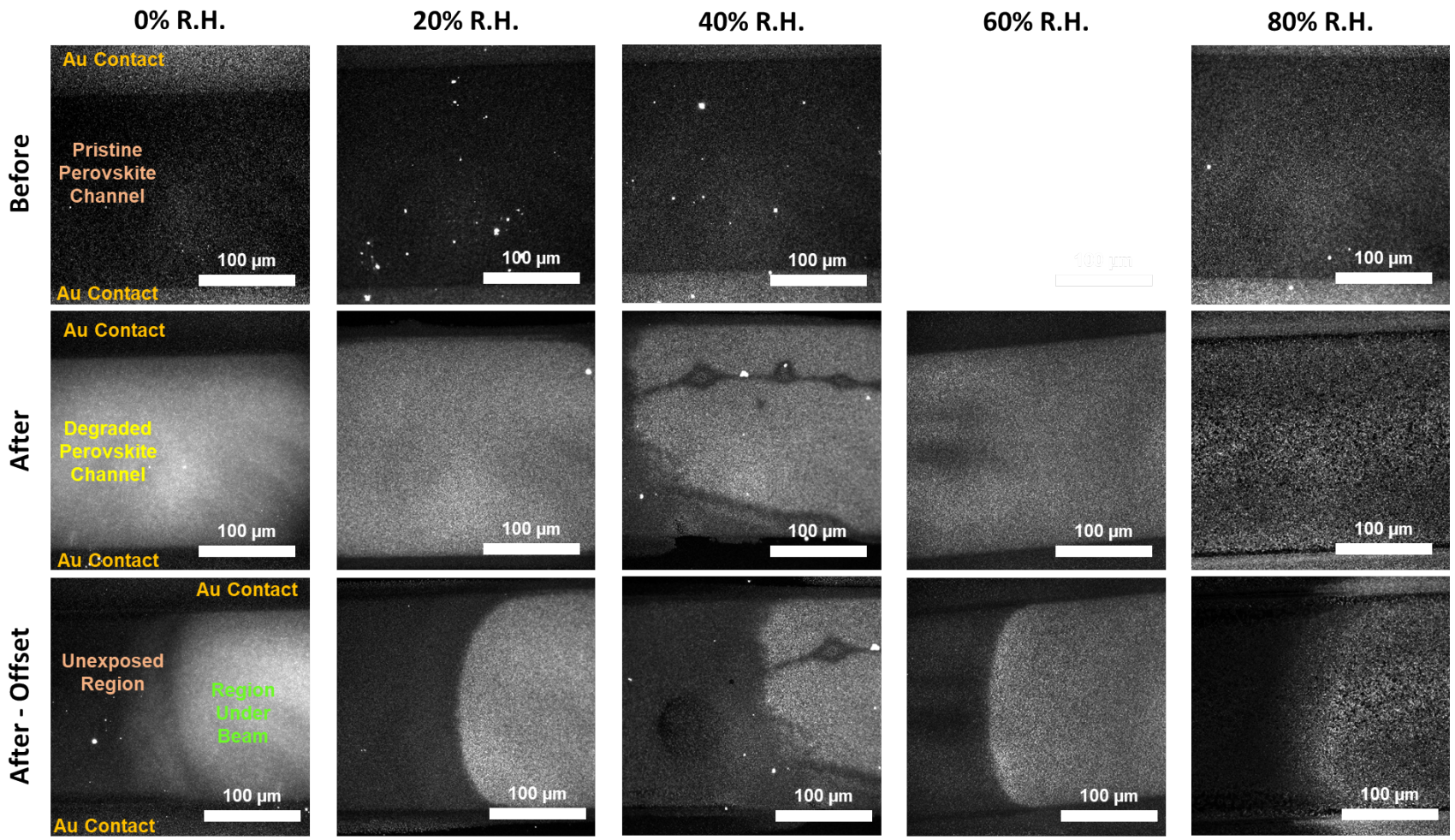

Figure 7.20**. Evolution of dark field intensity during degradation experiments in low stress condition (8 Suns, 25 ˚C) at various %RH**. All images have the same intensity scale. The top row shows before degradation, middle row shows after degradation, and the last row shows after degradations, looking at the light-dark boundary (left side was not directly exposed to the probe beam, and right side was illuminated with 8 Suns). Au contacts are distinguishable by the pattern of roughly horizontal lines at the top and bottom of each image.

13. Correlation between Dark Field Intensity Statistical Features and Transmittance

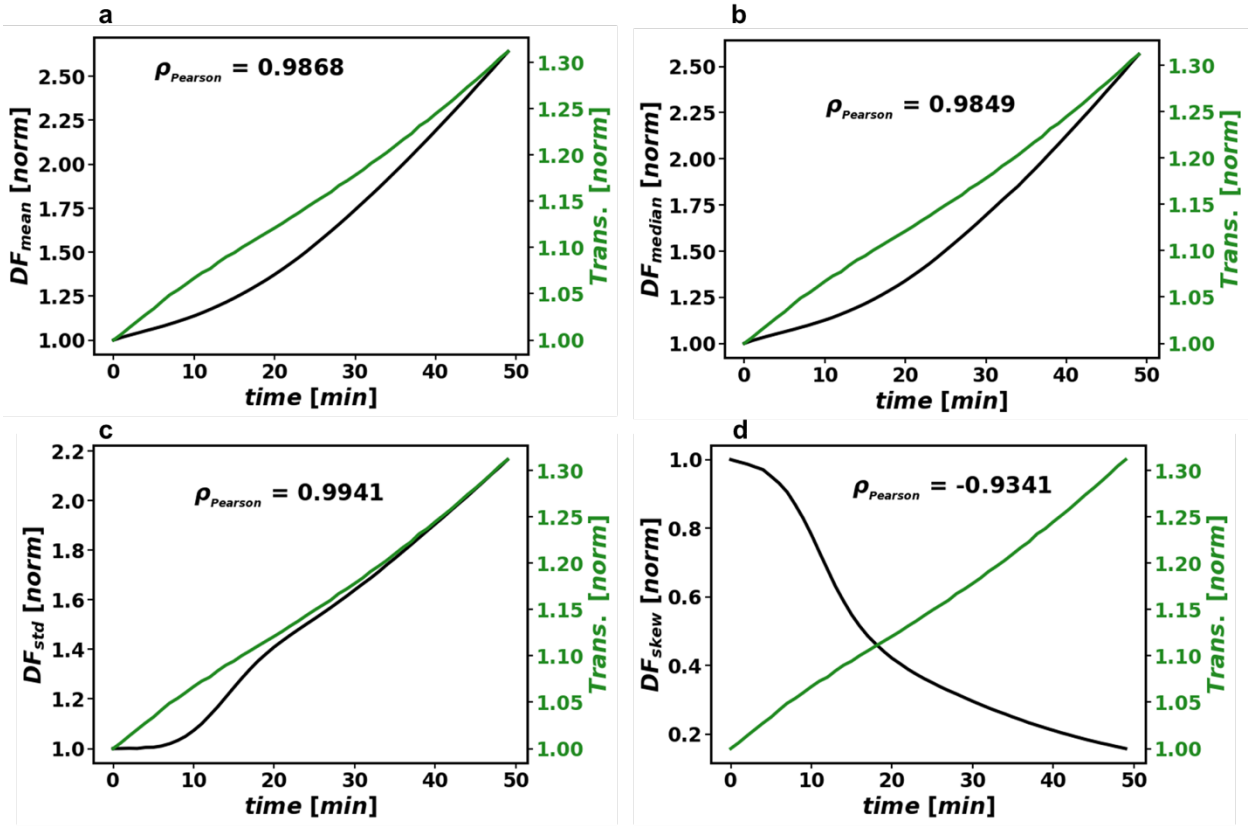

Figure 7.21**. The correlation between the mean (a), median (b), standard deviation (c), and skewness (d) of the dark field image intensity distribution compared to the normalized transmittance** for the first 50 min of degradation in air with 8 Suns illumination and 60% RH (see Figure 7.4 for complete degradation).

14. JV Characterization of $MAPbI_3$ p-i-n device

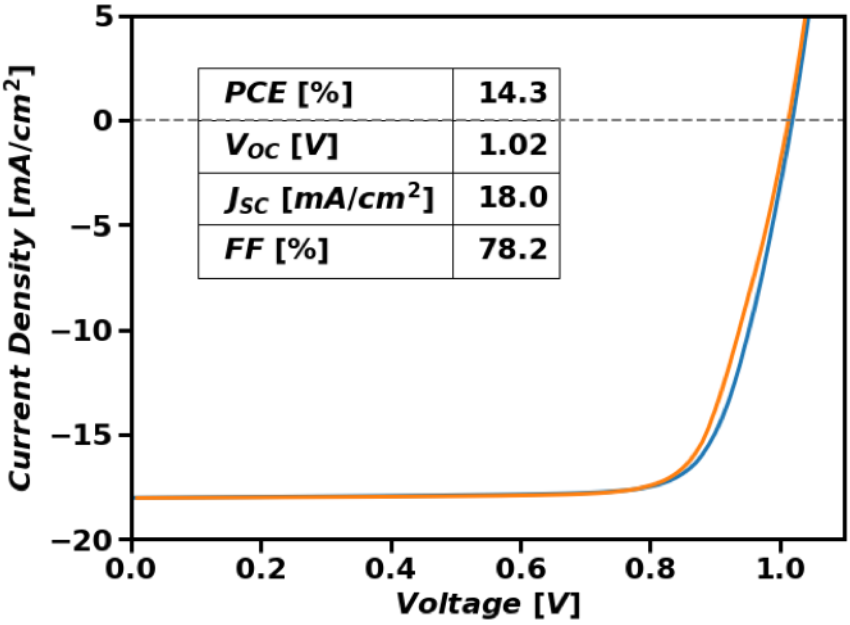

Figure 7.22**. Typical JV curve for $MAPbI_3$ p-i-n devices used in the device degradation studies measured under a calibrated AAA Solar Simulator**.

Chapter 8. CONCLUSIONS AND FUTURE OUTLOOK

The above work focuses on many distinct topics within the perovskites, from simple measurements to assess absorber properties (Chapters 2 and 3), to strategies to improve the quality of high bandgap perovskites (Chapters 4 and 5), to high throughput exploration of the perovskite composition space (Chapters 5 and 6), to methods to forecast durability of perovskite absorbers and devices (Chapter 7). Several important discoveries have been made that have lasting impact on research within the perovskite community and beyond:

- Photoluminescence should be paired with a metric of transport (such as photoconductivity) to appropriately assess a semiconductors' potential as a photovoltaic absorber (Chapter 3)
- The phase segregation phenomenon in mixed-halide perovskites arises due to excited carrier populations, which can occur from photoexcitation or from current injection (Chapter 4)
- Inducing lattice strain by using the size compensating motif (e.g. large guanidinium with small cesium) can alter band structure and enable high optoelectronic quality, high bandgap perovskites (Chapter 5)
- Simple optical measurements such as transmittance and dark field microscopy can be used to forecast the durability of perovskite films and devices (Chapter 7)

During my PhD, perovskite solar cells have gone from an exciting, newly discovered material to a mature technology with promise for commercialization. There are several topics to consider in determining where further scientific work can have the greatest impact.

One main objective in intensive research dedicated toward emerging PV materials is reducing the costs of solar electricity. Perovskite solar cells have many different pathways to commercialization, as single junction, perovskite-perovskite tandems, or perovskite-silicon

tandems. Although it is not yet clear which technology will be most successful, presently it seems the perovskite-silicon tandems have the easiest path to commercialization. Indeed, the certified efficiency of perovskite-silicon tandem solar cells was recently improved to 29.1% (tied with single junction GaAs) and is still rapidly rising. Thus, future scientific work could focus specifically on this technology, focusing on the quality of the high bandgap HP absorber and on device design to minimize optical losses. Strategies to further improve the high bandgap HP absorber using the 2D/3D heterostructure concept are discussed in Chapter 5.5.

Perhaps the most important topic for continued scientific research is understanding the durability of perovskite devices in operational deployment. This effort has several sub-thrusts: (i) encapsulant design and modeling oxygen ingress over the timescale of decades (ii) accelerated stability tests to study how perovskite devices will respond to oxygen, humidity, light, and temperature stress that are expected over lifetime timescales, and (iii) material and device innovations to improve resistance to oxygen, humidity, light, and temperature stresses. If perovskite devices can be shown to survive stress protocols equivalent to a 30+ year encapsulated stack, then this technology will likely make it to market and succeed in reducing overall costs of solar electricity.

PUBLICATION LIST

Below is a list of my publications from my time as a PhD student at University of Washington. I also listed number of citations as of March 2020.

Stoddard, R. J.; Eickemeyer, F. T.; Katahara, J. K.; Hillhouse, H. W., Correlation between Photoluminescence and Carrier Transport and a Simple In Situ Passivation Method for High-Bandgap Hybrid Perovskites. *The Journal of Physical Chemistry Letters* **2017,** *8* (14), 3289-3298. *Paper featured as ACS Editor's Choice.* 28 citations

Stoddard, R. J.; Rajagopal, A.; Palmer, R. L.; Braly, I. L.; Jen, A. K. Y.; Hillhouse, H. W., Enhancing Defect Tolerance and Phase Stability of High-Bandgap Perovskites via Guanidinium Alloying. *ACS Energy Letters* **2018**, *3,* 1261-1268. 26 citations

Stoddard, R. J.*; Dunlap-Shohl, W. A.*; Qiao, H.; Meng, Y.; Kau, W. F., Hillhouse, H. W., Forecasting Decay of Hybrid Perovskite Carrier Transport and Device Performance using Transmittance and Dark Field Microscopy. *ACS Energy Letters* **2020,** *5,* 946-954.

Braly, I. L.*; **Stoddard, R. J.*;** Rajagopal, A.; Uhl, A. R.; Katahara, J. K.; Jen, A. K.-Y.; Hillhouse, H. W., Current-Induced Phase Segregation in Mixed Halide Hybrid Perovskites and its Impact on Two-Terminal Tandem Solar Cell Design. *ACS Energy Letters* **2017,** *2* (8), 1841-1847. 55 citations

Rajagopal, A.; **Stoddard, R. J.;** Jo, S. B.; Hillhouse, H. W.; Jen, A. K. Y., Overcoming the Photovoltage Plateau in Large Bandgap Perovskite Photovoltaics. *Nano Letters* **2018**. 31 citations

Braly, I. L.; **Stoddard, R. J.;** Rajagopal, A.; Jen, A. K.-Y.; and Hillhouse, H. W., Photoluminescence and Photoconductivity to Assess Maximum Open-Circuit Voltage and Carrier Transport in Hybrid Perovskites and Other Photovoltaic Materials. *The Journal of Physical Chemistry Letters.,* **2018,** *9* (13), pp. 3779-3792. 5 citations

Torabi, N.; Behjat., A.; Zhou, Y.; Docampo, P.; **Stoddard, R. J.;** Hillhouse, H. W.; and Ameri, T., "Progress and Challenges in Perovskite Photovoltaics from Single- to Multi- Junction Cells", *Materials Today Energy,* **2019,** *12,* pp. 70-94. 14 citations

Rajagopal, A.; **Stoddard, R. J.;** Hillhouse, H. W.; Jen, A. K. Y., "On Understanding Bandgap Bowing and Optoelectronic Quality in Pb-Sn Alloy Hybrid Perovskites". *Journal of Materials Chemistry A,* **2019,** *7,* pp. 16285-16293. 2 citations

*Equal Author Contribution

VITA

Ryan J. Stoddard earned a dual B.S. / B.M. in Chemical Engineering and Music at Northwestern University near Chicago, Illinois. After Northwestern, Ryan worked at Argonne National Lab in Chicago and SINTEF Energy Research in Norway where he first became interested in using scientific research to develop clean energy technologies. Ryan started his PhD studies at University of Washington in Fall of 2015, where he has focused on developing reliable and inexpensive perovskite solar cells. Ryan currently lives in Seattle with his wife Kristin, and enjoys running, climbing, skiing, peakbagging, dancing, and cooking spicy food.

BIBLIOGRAPHY

1. Fu, R.; Feldman, D.; Margolis, R.; Woodhouse, M.; Ardani, K. *U.S. Solar Photovoltaic System Cost Benchmark: Q1 2017*; National Renewable Energy Laboratory (NREL): 2017.

2. Administration, U. S. E. I., Electric Power Monthly. 2018.

3. Powell, D. M.; Fu, R.; Horowitz, K.; Basore, P. A.; Woodhouse, M.; Buonassisi, T., The capital intensity of photovoltaics manufacturing: barrier to scale and opportunity for innovation. *Energy & Environmental Science* **2015,** *8* (12), 3395-3408.

4. Anaraki, E. H.; Kermanpur, A.; Steier, L.; Domanski, K.; Matsui, T.; Tress, W.; Saliba, M.; Abate, A.; Grätzel, M.; Hagfeldt, A., Highly efficient and stable planar perovskite solar cells by solution-processed tin oxide. *Energy & Environmental Science* **2016,** *9* (10), 3128-3134.

5. Correa-Baena, J. P.; Tress, W.; Domanski, K.; Anaraki, E. H.; Turren-Cruz, S. H.; Roose, B.; Boix, P. P.; Gratzel, M.; Saliba, M.; Abate, A.; Hagfeldt, A., Identifying and suppressing interfacial recombination to achieve high open-circuit voltage in perovskite solar cells. *Energy & Environmental Science* **2017,** *10* (5), 1207-1212.

6. Sofia, S. E.; Mailoa, J. P.; Weiss, D. N.; Stanbery, B. J.; Buonassisi, T.; Peters, I. M., Economic viability of thin-film tandem solar modules in the United States. **2018**.

7. Green, M.; Emery, K.; Hishikawa, Y.; Warta, W.; Dunlop, E. D., Solar cell efficiency talbes (version 48). *Progress in Photovoltaics: Research and Applications* **2016,** *24*, 905-913.

8. Green, M. A.; Ho-Baillie, A.; Snaith, H. J., The emergence of perovskite solar cells. *Nature Photonics* **2014,** *8* (7), 506-514.

9. Saliba, M.; Matsui, T.; Domanski, K.; Seo, J.-Y.; Ummadisingu, A.; Zakeeruddin, S. M.; Correa-Baena, J.-P.; Tress, W. R.; Abate, A.; Hagfeldt, A.; Grätzel, M., Incorporation of rubidium cations into perovskite solar cells improves photovoltaic performance. *Science* **2016**.

10. Yin, W. J.; Shi, T.; Yan, Y., Unique properties of halide perovskites as possible origins of the superior solar cell performance. *Adv Mater* **2014,** *26* (27), 4653-8.

11. Yin, W.-J.; Shi, T.; Yan, Y., Unusual defect physics in CH3NH3PbI3 perovskite solar cell absorber. *Applied Physics Letters* **2014,** *104* (6), 063903.

12. Yu, Y.; Wang, C.; Grice, C. R.; Shrestha, N.; Zhao, D.; Liao, W.; Guan, L.; Awni, R. A.; Meng, W.; Cimaroli, A. J.; Zhu, K.; Ellingson, R. J.; Yan, Y., Synergistic Effects of Lead Thiocyanate Additive and Solvent Annealing on the Performance of Wide-Bandgap Perovskite Solar Cells. *ACS Energy Letters* **2017,** *2*, 1177-1182.

13. Brandt, R. E.; Stevanović, V.; Ginley, D. S.; Buonassisi, T., Identifying defect-tolerant semiconductors with high minority-carrier lifetimes: beyond hybrid lead halide perovskites. *MRS Communications* **2015,** *5* (02), 265-275.

14. Brandt, R. E.; Poindexter, J. R.; Gorai, P.; Kurchin, R. C.; Hoye, R. L.; Nienhaus, L.; Wilson, M. W.; Polizzotti, J. A.; Sereika, R.; Žaltauskas, R., Searching for "defect-tolerant" photovoltaic materials: Combined theoretical and experimental screening. *Chemistry of Materials* **2017**.

15. Forgács, D.; Gil-Escrig, L.; Pérez-Del-Rey, D.; Momblona, C.; Werner, J.; Niesen, B.; Ballif, C.; Sessolo, M.; Bolink, H. J., Efficient monolithic perovskite/perovskite tandem solar cells. *Advanced Energy Materials* **2017,** *7* (8).

16. McMeekin, D. P.; Sadoughi, G.; Rehman, W.; Eperon, G. E.; Saliba, M.; Hörantner, M. T.; Haghighirad, A.; Sakai, N.; Korte, L.; Rech, B.; Johnston, M. B.; Herz, L. M.; Snaith, H. J., A mixed-cation lead mixed-halide perovskite absorber for tandem solar cells. *Science* **2016,** *351* (6269), 151-155.

17. Noh, J. H.; Im, S. H.; Heo, J. H.; Mandal, T. N.; Seok, S. I., Chemical management for colorful, efficient, and stable inorganic-organic hybrid nanostructured solar cells. *Nano Lett* **2013,** *13* (4), 1764-9.

18. Eperon, G. E.; Leijtens, T.; Bush, K. A.; Prasanna, R.; Green, T.; Wang, J. T.-W.; McMeekin, D. P.; Volonakis, G.; Milot, R. L.; May, R.; Palmstrom, A.; Slotcavage, D. J.; Belisle, R. A.; Patel, J. B.; Parrott, E. S.; Sutton, R. J.; Ma, W.; Moghadam, F.; Conings, B.; Babayigit, A.; Boyen, H.-G.; Bent, S.; Giustino, F.; Herz, L. M.; Johnston, M. B.; McGehee, M. D.; Snaith, H. J., Perovskite-perovskite tandem photovoltaics with optimized band gaps. *Science* **2016,** *354* (6314), 861-865.

19. Rajagopal, A.; Yang, Z.; Jo, S. B.; Braly, I. L.; Liang, P. W.; Hillhouse, H. W.; Jen, A. K. Y., Highly Efficient Perovskite–Perovskite Tandem Solar Cells Reaching 80% of the Theoretical Limit in Photovoltage. *Advanced Materials* **2017,** *29* (34).

20. Yang, Z.; Rajagopal, A.; Chueh, C. C.; Jo, S. B.; Liu, B.; Zhao, T.; Jen, A. K. Y., Stable Low-Bandgap Pb–Sn Binary Perovskites for Tandem Solar Cells. *Advanced Materials* **2016,** *28* (40), 8990-8997.

21. Jesper Jacobsson, T.; Correa-Baena, J.-P.; Pazoki, M.; Saliba, M.; Schenk, K.; Grätzel, M.; Hagfeldt, A., Exploration of the compositional space for mixed lead halogen perovskites for high efficiency solar cells. *Energy Environ. Sci.* **2016**.

22. Bush, K. A.; Palmstrom, A. F.; Yu, Z. J.; Boccard, M.; Cheacharoen, R.; Mailoa, J. P.; McMeekin, D. P.; Hoye, R. L. Z.; Bailie, C. D.; Leijtens, T.; Peters, I. M.; Minichetti, M. C.; Rolston, N.; Prasanna, R.; Sofia, S.; Harwood, D.; Ma, W.; Moghadam, F.; Snaith, H. J.; Buonassisi, T.; Holman, Z. C.; Bent, S. F.; McGehee, M. D., 23.6%-efficient monolithic perovskite/silicon tandem solar cells with improved stability. *Nature Energy* **2017,** *2*.

23. Uhl, A. R.; Yang, Z.; Jen, A. K.-Y.; Hillhouse, H. W., Solution-processed chalcopyrite–perovskite tandem solar cells in bandgap-matched two- and four-terminal architectures. *Journal of Materials Chemistry A* **2017,** (7).

24. Hörantner, M. T.; Leijtens, T.; Ziffer, M. E.; Eperon, G. E.; Christoforo, M. G.; McGehee, M. D.; Snaith, H. J., The Potential of Multi-Junction Perovskite Solar Cells. *ACS Energy Letters* **2017**.

25. Yang, W. S.; Noh, J. H.; Jeon, N. J.; Kim, Y. C.; Ryu, S.; Seo, J.; Seok, S. I., High-performance photovoltaic perovskite layers fabricated through intramolecular exchange. *Science* **2015,** *348* (6240), 1234-1237.

26. Yang, W. S.; Park, B.-W.; Jung, E. H.; Jeon, N. J.; Kim, Y. C.; Lee, D. U.; Shin, S. S.; Seo, J.; Kim, E. K.; Noh, J. H., Iodide management in formamidinium-lead-halide–based perovskite layers for efficient solar cells. *Science* **2017,** *356* (6345), 1376-1379.

27. Bi, D.; Tress, W.; Dar, M. I.; Gao, P.; Luo, J.; Renevier, C. m.; Schenk, K.; Abate, A.; Giordano, F.; Baena, J.-P. C.; Decoppet, J.-D.; Zakeeruddin, S. M.; Nazeeruddin, M. K.; Grätzel, M.; Hagfeldt, A., Efficient luminescent solar cells based on tailored mixed-cation perovskites. *Science Advances* **2016**.

28. Stoddard, R. J.; Rajagopal, A.; Palmer, R. L.; Braly, I. L.; Jen, A. K. Y.; Hillhouse, H. W., Enhancing Defect Tolerance and Phase Stability of High-Bandgap Perovskites via Guanidinium Alloying. *ACS Energy Letters* **2018**.

29. Duong, T.; Wu, Y.; Shen, H.; Peng, J.; Fu, X.; Jacobs, D.; Wang, E.-C.; Kho, T. C.; Fong, K. C.; Stocks, M.; Franklin, E.; Blakers, A.; Zin, N.; McIntosh, K.; Li, W.; Cheng, Y.-B.; White, T. P.; Weber, K.; Catchpole, K., Rubidium Multication Perovskite with Optimized Bandgap for Perovskite-Silicon Tandem with over 26% Efficiency. *Advanced Energy Materials* **2017**.

30. Yang, M.; Kim, D. H.; Yu, Y.; Li, Z.; Reid, O. G.; Song, Z.; Zhao, D.; Wang, C.; Li, L.; Meng, Y., Effect of non-stoichiometric solution chemistry on improving the performance of wide-bandgap perovskite solar cells. *Materials Today Energy* **2017**.

31. Zhou, Y.; Wang, F.; Cao, Y.; Wang, J. P.; Fang, H. H.; Loi, M. A.; Zhao, N.; Wong, C. P., Benzylamine-Treated Wide-Bandgap Perovskite with High Thermal-Photostability and Photovoltaic Performance. *Advanced Energy Materials* **2017,** *7* (22).

32. Chen, S.; Hou, Y.; Chen, H.; Tang, X.; Langner, S.; Li, N.; Stubhan, T.; Levchuk, I.; Gu, E.; Osvet, A., Exploring the Stability of Novel Wide Bandgap Perovskites by a Robot Based High Throughput Approach. *Advanced Energy Materials* **2017**.

33. Abdi-Jalebi, M.; Andaji-Garmaroudi, Z.; Cacovich, S.; Stavrakas, C.; Philippe, B.; Richter, J. M.; Alsari, M.; Booker, E. P.; Hutter, E. M.; Pearson, A. J., Maximising and Stabilising Luminescence in Metal Halide Perovskite Device Structures. *arXiv preprint arXiv:1712.04696* **2017**.

34. Bailie, C. D.; McGehee, M. D., High-efficiency tandem perovskite solar cells. *Mrs Bulletin* **2015,** *40* (8), 681-686.

35. Unger, E. L.; Kegelmannc, L.; Suchana, K.; Sörella, D.; Kortec, L.; Albrecht, S., Roadmap and roadblocks for the band gap tunability of metal halide perovskites. *Journal of Materials Chemistry A* **2017**.

36. Rehman, W.; McMeekin, D. P.; Patel, J. B.; Milot, R. L.; Johnston, M. B.; Snaith, H. J.; Herz, L. M., Photovoltaic mixed-cation lead mixed-halide perovskites: links between crystallinity, photo-stability and electronic properties. *Energy and Environmental Science* **2017,** *10*, 361-369.

37. Stoddard, R. J.; Eickemeyer, F. T.; Katahara, J. K.; Hillhouse, H. W., Correlation between Photoluminescence and Carrier Transport and a Simple In Situ Passivation Method for High-Bandgap Hybrid Perovskites. *The Journal of Physical Chemistry Letters* **2017,** *8* (14), 3289-3298.

38. Hoke, E. T.; Slotcavage, D. J.; Dohner, E. R.; Bowring, A. R.; Karunadasa, H. I.; McGehee, M. D., Reversible photo-induced trap formation in mixed-halide hybrid perovskites for photovoltaics. *Chemical Science* **2015,** *6* (1), 613-617.

39. Braly, I. L.; Stoddard, R. J.; Rajagopal, A.; Uhl, A. R.; Katahara, J. K.; Jen, A. K.-Y.; Hillhouse, H. W., Current-Induced Phase Segregation in Mixed Halide Hybrid Perovskites and its Impact on Two-Terminal Tandem Solar Cell Design. **2017**.

40. Yang, Z.; Rajagopal, A.; Jo, S. B.; Chueh, C.-C.; Williams, S.; Huang, C.-C.; Katahara, J. K.; Hillhouse, H. W.; Jen, A. K.-Y., Stabilized Wide Bandgap Perovskite Solar Cells by Tin Substitution. *Nano Letters* **2016,** *16* (12), 7739-7747.

41. Braly, I. L.; Hillhouse, H. W., Optoelectronic Quality and Stability of Hybrid Perovskites from MAPbI3to MAPbI2Br Using Composition Spread Libraries. *The Journal of Physical Chemistry C* **2016,** *120* (2), 893-902.

42. Slotcavage, D. J.; Karunadasa, H. I.; McGehee, M. D., Light-Induced Phase Segregation in Halide-Perovskite Absorbers. *ACS Energy Letters* **2016,** *1* (6), 1199–1205.

43. Brennan, M. C.; Draguta, S.; Kamat, P. V.; Kuno, M., Light-Induced Anion Phase Segregation in Mixed Halide Perovskites. *ACS Energy Letters* **2017**.

44. Tang, X.; Brandl, M.; May, B.; Levchuk, I.; Hou, Y.; Richter, M.; Chen, H.; Chen, S.; Kahmann, S.; Osvet, A.; Maier, F.; Steinrück, H.-P.; Hock, R.; Matt, G. J.; Brabec, C. J., Photoinduced degradation of methylammonium lead triiodide perovskite semiconductors. *Journal of Materials Chemistry A* **2016,** *4*, 15896-15903.

45. Huang, W.; Manser, J. S.; Kamat, P. V.; Ptasinska, S., Evolution of Chemical Composition, Morphology, and Photovoltaic Efficiency of CH3NH3PbI3 Perovskite under Ambient Conditions. *Chemistry of Materials* **2016,** *28* (1), 303-311.

46. Aristidou, N.; Sanchez-Molina, I.; Chotchuangchutchaval, T.; Brown, M.; Martinez, L.; Rath, T.; Haque, S. A., The role of oxygen in the degradation of methylammonium lead trihalide

perovskite photoactive layers. *Angewandte Chemie International Edition* **2015,** *54* (28), 8208-8212.

47. Aristidou, N.; Eames, C.; Sanchez-Molina, I.; Bu, X.; Kosco, J.; Islam, M. S.; Haque, S. A., Fast oxygen diffusion and iodide defects mediate oxygen-induced degradation of perovskite solar cells. *Nature Communications* **2017,** *8*.

48. Bush, K. A.; Bailie, C. D.; Chen, Y.; Bowring, A. R.; Wang, W.; Ma, W.; Leijtens, T.; Moghadam, F.; McGehee, M. D., Thermal and Environmental Stability of Semi-Transparent Perovskite Solar Cells for Tandems Enabled by a Solution-Processed Nanoparticle Buffer Layer and Sputtered ITO Electrode. *Advanced Materials* **2016,** *28* (20), 3937-3943.

49. Leijtens, T.; Bush, K.; Cheacharoen, R.; Beal, R.; Bowring, A.; McGehee, M. D., Towards enabling stable lead halide perovskite solar cells; interplay between structural, environmental, and thermal stability. *Journal of Materials Chemistry A* **2017**.

50. DOE, Solar Energy Technologies Office (SETO FY2018 Funding Opportunity Announcement (FOA) 2018.

51. Braly, I. L.; Stoddard, R. J.; Rajagopal, A.; Uhl, A. R.; Katahara, J. K.; Jen, A. K.-Y.; Hillhouse, H. W., Current-Induced Phase Segregation in Mixed Halide Hybrid Perovskites and its Impact on Two-Terminal Tandem Solar Cell Design. *ACS Energy Letters* **2017,** *2* (8), 1841-1847.

52. Stoddard, R. J.; Rajagopal, A.; Palmer, R. L.; Braly, I. L.; Jen, A. K. Y.; Hillhouse, H. W., Enhancing Defect Tolerance and Phase Stability of High-Bandgap Perovskites via Guanidinium Alloying. *ACS Energy Letters* **2018,** *3*, 1261-1268.

53. Stoddard, R. J.; Dunlap-Shohl, W. A.; Qiao, H.; Meng, Y.; Kau, W. F.; Hillhouse, H. W., Forecasting the Decay of Hybrid Perovskite Performance using Optical Transmittance or Reflected Dark Field Imaging. *ACS Energy Letters* **2020**.

54. Katahara, J. K.; Hillhouse, H. W., Quasi-Fermi level splitting and sub-bandgap absorptivity from semiconductor photoluminescence. *Journal of Applied Physics* **2014,** *116* (17), 173504.

55. Smestad, G.; Ries, H., Luminescence and current-voltage characteristics of solar cells and optoelectronic devices - ScienceDirect. *Solar Energy Materials and Solar Cells* **1992,** *25*, 51-71.

56. Ross, R. T., Some thermodynamics of photochemical systems. *The Journal of Chemical Physics* **1967,** *46* (12), 4590-4593.

57. Lasher, G.; Stern, F., Spontaneous and stimulated recombination radiation in semiconductors. *Physical Review* **1964,** *133* (2A), A553.

58. Wurfel, P., The chemical potential of radiation. *Journal of Physics C: Solid State Physics* **1982,** *15* (18), 3967.

59. Braly, I. Optoelectronic Quality and Stability of Hybrid Perovskites Determined by Steady-State Luminescence Techniques. 2018.

60. Futscher, M. H.; Lee, J. M.; McGovern, L.; Muscarella, L. A.; Wang, T.; Haider, M. I.; Fakharuddin, A.; Schmidt-Mende, L.; Ehrler, B., Quantification of ion migration in CH 3 NH 3 PbI 3 perovskite solar cells by transient capacitance measurements. *Materials Horizons* **2019,** *6* (7), 1497-1503.

61. Bube, R. H., *Photoelectronic Properties of Semiconductors*. Cambridge University Press: 1992.

62. Rajagopal, A.; Stoddard, R. J.; Jo, S. B.; Hillhouse, H. W.; Jen, A. K. Y., Overcoming the Photovoltage Plateau in Large Bandgap Perovskite Photovoltaics. *Nano Letters* **2018**.

63. deQuilettes, D. W.; Koch, S.; Burke, S.; Paranji, R. K.; Shropshire, A. J.; Ziffer, M. E.; Ginger, D. S., Photoluminescence Lifetimes Exceeding 8 μs and Quantum Yields Exceeding 30% in Hybrid Perovskite Thin Films by Ligand Passivation. *ACS Energy Letters* **2016,** *1* (2), 438-444.

64. Zhou, Y.; Wang, F.; Fang, H.-H.; Loi, M. A.; Xie, F.-Y.; Zhao, N.; Wong, C.-P., Distribution of bromine in mixed iodide–bromide organolead perovskites and its impact on photovoltaic performance. *Journal of Materials Chemistry A* **2016,** *4*, 16191-16197.

65. Yoon, S. J.; Draguta, S.; Manser, J. S.; Sharia, O.; Schneider, W. F.; Kuno, M.; Kamat, P. V., Tracking Iodide and Bromide Ion Segregation in Mixed Halide Lead Perovskites during Photoirradiation. *ACS Energy Letters* **2016,** *1* (1), 290-296.

66. Bischak, C. G.; Hetherington, C. L.; Wu, H.; Aloni, S.; Ogletree, D. F.; Limmer, D. T.; Ginsberg, N. S., Origin of reversible photo-induced phase separation in hybrid perovskites. *Nano Letters* **2016**.

67. Yoon, S. J.; Stamplecoskie, K. G.; Kamat, P. V., How Lead Halide Complex Chemistry Dictates the Composition of Mixed Halide Perovskites. *Journal of Physical Chemistry Letters* **2016,** *7* (7), 1368–1373.

68. Werner, J.; Barraud, L.; Walter, A.; Bräuninger, M.; Sahli, F.; Sacchetto, D.; Tétreault, N.; Paviet-Salomon, B.; Moon, S.-J.; Allebé, C.; Despeisse, M.; Nicolay, S.; Wolf, S. D.; Niesen, B.; Ballif, C., Efficient Near-Infrared-Transparent Perovskite Solar Cells Enabling Direct Comparison of 4-Terminal and Monolithic Perovskite/Silicon Tandem Cells. *ACS Energy Letters* **2016,** *1* (2), 474–480.

69. Werner, J.; Weng, C. H.; Walter, A.; Fesquet, L.; Seif, J. P.; De Wolf, S.; Niesen, B.; Ballif, C., Efficient Monolithic Perovskite/Silicon Tandem Solar Cell With Cell Area > 1 cm. *J Phys Chem Lett* **2015**.

70. Futscher, M. H.; Ehrler, B., Efficiency Limit of Perovskite/Si Tandem Solar Cells. *ACS Energy Letters* **2016,** *1* (4), 863–868.

71. Albrecht, S.; Saliba, M.; Correa-Baena, J.-P.; Jäger, K.; Korte, L.; Hagfeldt, A.; Grätzel, M.; Rech, B., Towards optical optimization of planar monolithic perovskite/silicon-heterojunction tandem solar cells. *Journal of Optics* **2016,** *18* (6).

72. Todorov, T.; Gunawan, O.; Guha, S., A road towards 25% efficiency and beyond: perovskite tandem solar cells. *Molecular Systems Design and Engineering* **2016,** *1*, 370-376.

73. Beal, R. E.; Slotcavage, D. J.; Leijtens, T.; Bowring, A. R.; Belisle, R. A.; Nguyen, W. H.; Burkhard, G. F.; Hoke, E. T.; McGehee, M. D., Cesium Lead Halide Perovskites with Improved Stability for Tandem Solar Cells. *J Phys Chem Lett* **2016,** *7* (5), 746-51.

74. Forgacs, D.; Perez-del-Rey, D.; Avila, J.; Momblona, C.; Gil-Escrig, L.; Danekamp, B.; Sessolo, M.; Bolink, a. H. J., Efficient wide band gap double cation – double halide perovskite solar cells. *Journal of Materials Chemistry A* **2017,** *5*, 3203-3207.

75. Ndione, P. F.; Li, Z.; Zhu, K., Effects of alloying on the optical properties of organic–inorganic lead halide perovskite thin films. *Journal of Materials Chemistry C* **2016,** *4*, 7775-7782.

76. Sutton, R. J.; Eperon, G. E.; Miranda, L.; Parrott, E. S.; Kamino, B. A.; Patel, J. B.; Hörantner, M. T.; Johnston, M. B.; Haghighirad, A. A.; Moore, D. T.; Snaith, H. J., Bandgap-Tunable Cesium Lead Halide Perovskites with High Thermal Stability for Efficient Solar Cells. *Advanced Energy Materials* **2016,** *6* (8).

77. Hu, M.; Bi, C.; Yuan, Y.; Bai, Y.; Huang, a. J., Stabilized Wide Bandgap MAPbBrxI3–x Perovskite by Enhanced Grain Size and Improved Crystallinity. *Advanced Science* **2016,** *3* (1500301).

78. Jaysankar, M.; Qiu, W.; Bastos, J.; Tait, J. G.; Debucquoy, M.; Paetzold, U. W.; Cheyns, D.; Poortmans, J., Crystallisation dynamics in wide-bandgap perovskite films. *Journal of Materials Chemistry A* **2016,** *4*, 10524-10531.

79. Noel, N. K.; Abate, A.; Stranks, S. D.; Parrott, E. S.; Burlakov, V. M.; Goriely, A.; Snaith, H. J., Enhanced Photoluminescence and Solar Cell Performance via Lewis Base Passivation of Organic–Inorganic Lead Halide Perovskites. *ACS Nano* **2014,** *8* (10), 9815–9821.

80. Chueh, C.-C.; Liao, C.-Y.; Zuo, F.; Williams, S. T.; Liang, P.-W.; Jen, A. K.-Y., The roles of alkyl halide additives in enhancing perovskite solar cell performance. *Journal of Materials Chemistry A* **2015,** (17).

81. Bi, D.; Gao, P.; Scopelliti, R.; Oveisi, E.; Luo, J.; Grätzel, M.; Hagfeldt, A.; Nazeeruddin, M. K., High-Performance Perovskite Solar Cells with Enhanced Environmental Stability Based on Amphiphile-Modified CH3NH3PbI3. *Advanced Materials* **2016,** *28* (15), 2910-2915.

82. Wuerfel, P., Physics of Solar Cells: From Basic Principles to Advanced Concepts. 3 ed.; Wiley: Somerset, 2016.

83. Tian, Y.; Peter, M.; Unger, E.; Abdellah, M.; Zheng, K.; Pullerits, T.; Yartsev, A.; Sundström, V.; Scheblykin, I. G., Mechanistic insights into perovskite photoluminescence enhancement: light curing with oxygen can boost yield thousandfold. *Physical Chemistry Chemical Physics* **2015**.

84. Fang, H.-H.; Wang, F.; Adjokatse, S.; Zhao, N.; Loi, M. A., Photoluminescence Enhancement in Formamidinium Lead Iodide Thin Films. *Advanced Functional Materials* **2016**.

85. Hillhouse, H. W.; Beard, M. C., Solar cells from colloidal nanocrystals: Fundamentals, materials, devices, and economics. *Current Opinion in Colloid & Interface Science* **2009,** *14*, 245–259.

86. Liu, Y.; Gibbs, M.; Puthussery, J.; Gaik, S.; Ihly, R.; Hillhouse, H. W.; Law, M., Dependence of Carrier Mobility on Nanocrystal Size and Ligand Length in PbSe Nanocrystal Solids. *Nano Letters* **2010,** *10* (5), 1960-1969.

87. Stranks, S. D.; Burlakov, V. M.; Leijtens, T.; Ball, J. M.; Goriely, A.; Snaith, H. J., Recombination Kinetics in Organic-Inorganic Perovskites: Excitons, Free Charge, and Subgap States. *Physical Review Applied* **2014,** *2* (3), 034007.

88. Adhyaksa, G. W. P.; Veldhuizen, L. W.; Kuang, Y.; Brittman, S.; Schropp, R. E. I.; Garnett, E. C., Carrier Diffusion Lengths in Hybrid Perovskites: Processing, Composition, Aging, and Surface Passivation Effects. *Chemistry of Materials* **2016,** *28* (15), 5259–5263.

89. Levine, I.; Gupta, S.; Brenner, T. M.; Azulay, D.; Millo, O.; Hodes, G.; Cahen, D.; Balberg, I., Mobility–Lifetime Products in MAPbI3 Films. *Journal of Physical Chemistry Letters* **2016,** *7* (24), 5219–5226.

90. Elbaz, G. A.; Straus, D. B.; Semonin, O. E.; Hull, T. D.; Paley, D. W.; Kim, P.; Owen, J. S.; Kagan, C. R.; Roy, X., Unbalanced Hole and Electron Diffusion in Lead Bromide Perovskites. *Nano Letters* **2017**.

91. Hoye, R. L. Z.; Schulz, P.; Schelhas, L. T.; Holder, A. M.; Stone, K. H.; Perkins, J. D.; Vigil-Fowler, D.; Siol, S.; Scanlon, D. O.; Zakutayev, A.; Walsh, A.; Smith, I. C.; Melot, B. C.; Kurchin, R. C.; Wang, Y.; Shi, J.; Marques, F. C.; Berry, J. J.; Tumas, W.; Lany, S.; Stevanović, V.; Toney, M. F.; Buonassisi, T., Perovskite-Inspired Photovoltaic Materials: Toward Best Practices in Materials Characterization and Calculations. *Chemistry of Materials* **2017,** *29* (5).

92. Wehrenfennig, C.; Eperon, G. E.; Johnston, M. B.; Snaith, H. J.; Herz, L. M., High Charge Carrier Mobilities and Lifetimes in Organolead Trihalide Perovskites. *Advanced Materials* **2014,** *26* (10), 1584-1589.

93. Stranks, S. D.; Eperon, G. E.; Grancini, G.; Menelaou, C.; Alcocer, M. J. P.; Leijtens, T.; Herz, L. M.; Petrozza, A.; Snaith, H. J., Electron-Hole Diffusion Lengths Exceeding 1 Micrometer in an Organometal Trihalide Perovskite Absorber. *Science* **2013,** *342* (6156), 341-344.

94. Nelson, J., *The Physics of Solar Cells*. 2 ed.; Imperial College Press: 2003.

95. Jeon, N. J.; Noh, J. H.; Kim, Y. C.; Yang, W. S.; Ryu, S.; Seok, S. I., Solvent engineering for high-performance inorganic-organic hybrid perovskite solar cells. *Nature Materials* **2014,** *13* (9), 897-903.

96. Yang, Z.; Chueh, C.-C.; Liang, P.-W.; Crump, M.; Lin, F.; Zhu, Z.; Jen, A. K.-Y., Effects of formamidinium and bromide ion substitution in methylammonium lead triiodide toward high-performance perovskite solar cells. *Nano Energy* **2016,** *22*, 328–337.

97. Rau, U., Reciprocity relation between photovoltaic quantum efficiency and electroluminescent emission of solar cells. *Physical Review B* **2007,** *76* (8), 085303.

98. Yao, J.; Kirchartz, T.; Vezie, M. S.; Faist, M. A.; Gong, W.; He, Z.; Wu, H.; Troughton, J.; Watson, T.; Bryant, D.; Nelson, J., Quantifying Losses in Open-Circuit Voltage in Solution-Processable Solar Cells. *Physical Review Applied* **2015,** *4* (1), 014020.

99. Jung, J. W.; Chueh, C. C.; Jen, A. K. Y., A Low-Temperature, Solution-Processable, Cu-Doped Nickel Oxide Hole-Transporting Layer via the Combustion Method for High-Performance Thin-Film Perovskite Solar Cells. *Advanced Materials* **2017,** *27* (47), 7874-7880.

100. Chen, Y.; Yi, H. T.; Wu, X.; Haroldson, R.; Gartstein, Y. N.; Rodionov, Y. I.; Tikhonov, K. S.; Zakhidov, A.; Zhu, X.-Y.; Podzorov, V., Extended carrier lifetimes and diffusion in hybrid perovskites revealed by Hall effect and photoconductivity measurements. *Nature Communications* **2016,** *7* (12253).

101. Shockley, W.; Queisser, H. J., Detailed Balance Limit of Efficiency of p-n Junction Solar Cells. *Journal of Applied Physics* **1961,** *32* (3), 510.

102. Draguta, S.; Sharia, O.; Yoon, S. J.; Brennan, M. C.; Morozov, Y. V.; Manser, J. M.; Kamat, P. V.; Schneider, W. F.; Kuno, M., Rationalizing the light-induced phase separation of mixed halide organic–inorganic perovskites. *Nature communications* **2017,** *8* (1), 200.

103. Samu, G. F.; Janáky, C.; Kamat, P. V., A Victim of Halide Ion Segregation. How Light Soaking Affects Solar Cell Performance of Mixed Halide Lead Perovskites. *ACS Energy Letters* **2017**.

104. Yoon, S. J.; Kuno, K.; Kamat, P. V., Shift Happens. How Halide Ion Defects Influence Photoinduced Segregation in Mixed Halide Perovskites. *ACS Energy Letters* **2017**.

105. Palmstrom, A. F.; Eperon, G. E.; Leijtens, T.; Prasanna, R.; Habisreutinger, S. N.; Nemeth, W.; Gaulding, E. A.; Dunfield, S. P.; Reese, M.; Nanayakkara, S., Enabling Flexible All-Perovskite Tandem Solar Cells. *Joule* **2019**.

106. Duong, T.; Mulmudi, H. K.; Wu, Y.; Fu, X.; Shen, H.; Peng, J.; Wu, N.; Nguyen, H. T.; Macdonald, D.; Lockrey, M., Light and Electrically Induced Phase Segregation and Its Impact on the Stability of Quadruple Cation High Bandgap Perovskite Solar Cells. *ACS Applied Materials & Interfaces* **2017,** *9* (32), 26859-26866.

107. Todorov, T.; Gershon, T.; Gunawan, O.; Lee, Y. S.; Sturdevant, C.; Chang, L. Y.; Guha, S., Monolithic Perovskite-CIGS Tandem Solar Cells via In Situ Band Gap Engineering. *Advanced Energy Materials* **2015,** *5* (23).

108. Bush, K. A.; Frohna, K.; Prasanna, R.; Beal, R. E.; Leijtens, T.; Swifter, S. A.; McGehee, M. D., Compositional Engineering for Efficient Wide Band Gap Perovskites with Improved Stability to Photoinduced Phase Segregation. *ACS Energy Letters* **2018**.

109. Marco, N. D.; Zhou, H.; Chen, Q.; Sun, P.; Liu, Z.; Meng, L.; Yao, E.-P.; Liu, Y.; Schiffer, A.; Yang, Y., Guanidinium: A Route to Enhanced Carrier Lifetime and Open-Circuit Voltage in Hybrid Perovskite Solar Cells. *Nano Letters* **2016,** *16* (2).

110. Pham, N. D.; Tiong, V. T.; Yao, D.; Martens, W.; Guerrero, A.; Bisquert, J.; Wang, H., Guanidinium thiocyanate selective Ostwald ripening induced large grain for high performance perovskite solar cells. *Nano Energy* **2017,** *41*, 476-487.

111. Hou, X.; Hu, Y.; Liu, H.; Mei, A.; Li, X.; Duan, M.; Zhang, G.; Rong, Y.; Han, H., Effect of guanidinium on mesoscopic perovskite solar cells. *Journal of Materials Chemistry A* **2017,** *5*.

112. Daub, M.; Haber, C.; Hillebrecht, H., Synthesis, Crystal Structures, Optical Properties, and Phase Transitions of the Layered Guanidinium-Based Hybrid Perovskites [C (NH2) 3] 2MI4; M= Sn, Pb. *European Journal of Inorganic Chemistry* **2017,** *2017* (7), 1120-1126.

113. Nazarenko, O.; Kotyrba, M. R.; Wörle, M.; Cuervo-Reyes, E.; Yakunin, S.; Kovalenko, M. V., Luminescent and Photoconductive Layered Lead Halide Perovskite Compounds Comprising Mixtures of Cesium and Guanidinium Cations. *Inorganic chemistry* **2017,** *56* (19), 11552-11564.

114. Soe, C. M. M.; Stoumpos, C. C.; Kepenekian, M. l.; Traoré, B.; Tsai, H.; Nie, W.; Wang, B.; Katan, C.; Seshadri, R.; Mohite, A. D., New Type of 2D Perovskites with Alternating Cations in the Interlayer Space,(C (NH2) 3)(CH3NH3) n Pb n I3 n+ 1: Structure, Properties, and Photovoltaic Performance. *Journal of the American Chemical Society* **2017**.

115. Jodlowski, A. D.; Yépez, A.; Luque, R.; Camacho, L.; de Miguel, G., Benign-by-Design Solventless Mechanochemical Synthesis of Three-, Two-, and One-Dimensional Hybrid Perovskites. *Angewandte Chemie International Edition* **2016,** *55* (48), 14972-14977.

116. Jodlowski, A. D.; Roldán-Carmona, C.; Grancini, G.; Salado, M.; Ralaiarisoa, M.; Ahmad, S.; Koch, N.; Camacho, L.; de Miguel, G.; Nazeeruddin, M. K., Large guanidinium cation mixed with methylammonium in lead iodide perovskites for 19% efficient solar cells. *Nature Energy* **2017,** *2*, 972.

117. Kubicki, D. J.; Prochowicz, D.; Hofstetter, A.; Saski, M.; Yadav, P.; Bi, D.; Pellet, N.; Lewiński, J.; Zakeeruddin, S. M.; Grätzel, M., Formation of Stable Mixed Guanidinium–Methylammonium Phases with Exceptionally Long Carrier Lifetimes for High-Efficiency Lead Iodide-Based Perovskite Photovoltaics. *Journal of the American Chemical Society* **2018**.

118. Warren, B. E., *X-ray Diffraction*. Courier Corporation: 1969.

119. Rietveld, H., A profile refinement method for nuclear and magnetic structures. *Journal of applied Crystallography* **1969,** *2* (2), 65-71.

120. Williamson, G.; Hall, W., X-ray line broadening from filed aluminium and wolfram. *Acta metallurgica* **1953,** *1* (1), 22-31.

121. Scardi, P.; Leoni, M.; Delhez, R., Line broadening analysis using integral breadth methods: a critical review. *Journal of Applied Crystallography* **2004,** *37* (3), 381-390.

122. Cline, J. P.; Leoni, M.; Black, D.; Henins, A.; Bonevich, J.; Whitfield, P.; Scardi, P., Crystalline domain size and faulting in the new NIST SRM 1979 zinc oxide. *Powder Diffraction* **2013,** *28* (S2), S22-S32.

123. Wang, J. T.-W.; Wang, Z.; Pathak, S.; Zhang, W.; deQuilettes, D. W.; Wisnivesky-Rocca-Rivarola, F.; Huang, J.; Nayak, P. K.; Patel, J. B.; Yusof, H. A. M.; Vaynzof, Y.; Zhu, R.; Ramirez, I.; Zhang, J.; Ducati, C.; Grovenor, C.; Johnston, M. B.; Ginger, D. S.; Nicholas, R. J.; Snaith, H. J., Efficient perovskite solar cells by metal ion doping. *Energy & Environmental Science* **2016**.

124. Barker, A. J.; Sadhanala, A.; Deschler, F.; Gandini, M.; Senanayak, S. P.; Pearce, P. M.; Mosconi, E.; Pearson, A.; Wu, Y.; Srimath Kandada, A. R., Defect-Assisted Photoinduced Halide Segregation in Mixed-Halide Perovskite Thin Films. *ACS Energy Letters* **2017**.

125. Abdi-Jalebi, M.; Andaji-Garmaroudi, Z.; Cacovich, S.; Stavrakas, C.; Philippe, B.; Richter, J. M.; Alsari, M.; Booker, E. P.; Hutter, E. M.; Pearson, A. J., Maximizing and stabilizing luminescence from halide perovskites with potassium passivation. *Nature* **2018,** *555* (7697), 497.

126. Kim, J.; Saidaminov, M. I.; Tan, H.; Zhao, Y.; Kim, Y.; Choi, J.; Jo, J. W.; Fan, J.; Quintero-Bermudez, R.; Yang, Z., Amide-Catalyzed Phase-Selective Crystallization Reduces Defect Density in Wide-Bandgap Perovskites. *Advanced Materials* **2018**.

127. Yang, Z.; Rajagopal, A.; Jen, A. K. Y., Ideal Bandgap Organic–Inorganic Hybrid Perovskite Solar Cells. *Advanced Materials* **2017,** *29* (47).

128. Game, O. S.; Buchsbaum, G. J.; Zhou, Y.; Padture, N. P.; Kingon, A. I., Ions Matter: Description of the Anomalous Electronic Behavior in Methylammonium Lead Halide Perovskite Devices. *Advanced Functional Materials* **2017,** *27* (16).

129. Ghosh, D.; Walsh Atkins, P.; Islam, M. S.; Walker, A. B.; Eames, C., Good Vibrations: Locking of Octahedral Tilting in Mixed-Cation Iodide Perovskites for Solar Cells. *ACS Energy Letters* **2017,** *2* (10), 2424-2429.

130. Matsui, T.; Seo, J. Y.; Saliba, M.; Zakeeruddin, S. M.; Grätzel, M., Room-Temperature Formation of Highly Crystalline Multication Perovskites for Efficient, Low-Cost Solar Cells. *Advanced Materials* **2017,** *29* (15).

131. Huang, Y.; Li, L.; Liu, Z.; Jiao, H.; He, Y.; Wang, X.; Zhu, R.; Wang, D.; Sun, J.; Chen, Q., The intrinsic properties of FA (1− x) MA x PbI 3 perovskite single crystals. *Journal of Materials Chemistry A* **2017,** *5* (18), 8537-8544.

132. Whalley, L. D.; Frost, J. M.; Jung, Y.-K.; Walsh, A., Perspective: Theory and simulation of hybrid halide perovskites. *The Journal of Chemical Physics* **2017,** *146* (22), 220901.

133. Yuan, Y.; Chae, J.; Shao, Y.; Wang, Q.; Xiao, Z.; Centrone, A.; Huang, J., Photovoltaic switching mechanism in lateral structure hybrid perovskite solar cells. *Advanced Energy Materials* **2015,** *5* (15).

134. Azpiroz, J. M.; Mosconi, E.; Bisquert, J.; De Angelis, F., Defect migration in methylammonium lead iodide and its role in perovskite solar cell operation. *Energy & Environmental Science* **2015,** *8* (7), 2118-2127.

135. Haruyama, J.; Sodeyama, K.; Han, L.; Tateyama, Y., First-principles study of ion diffusion in perovskite solar cell sensitizers. *Journal of the American Chemical Society* **2015,** *137* (32), 10048-10051.

136. Eames, C.; Frost, J. M.; Barnes, P. R.; O'regan, B. C.; Walsh, A.; Islam, M. S., Ionic transport in hybrid lead iodide perovskite solar cells. *Nature communications* **2015,** *6*, 7497.

137. Tai, Q.; You, P.; Sang, H.; Liu, Z.; Hu, C.; Chan, H. L.; Yan, F., Efficient and stable perovskite solar cells prepared in ambient air irrespective of the humidity. *Nat Commun* **2016,** *7*, 11105.

138. Han, Q.; Bai, Y.; Liu, J.; Du, K.-z.; Li, T.; Ji, D.; Zhou, Y.; Cao, C.; Shin, D.; Ding, J., Additive engineering for high-performance room-temperature-processed perovskite absorbers with micron-size grains and microsecond-range carrier lifetimes. *Energy & Environmental Science* **2017,** *10* (11), 2365-2371.

139. Chen, P.; Bai, Y.; Wang, S.; Lyu, M.; Yun, J. H.; Wang, L., In situ growth of 2D perovskite capping layer for stable and efficient perovskite solar cells. *Advanced Functional Materials* **2018,** *28* (17), 1706923.

140. Cho, Y.; Soufiani, A. M.; Yun, J. S.; Kim, J.; Lee, D. S.; Seidel, J.; Deng, X.; Green, M. A.; Huang, S.; Ho-Baillie, A. W., Mixed 3D–2D Passivation Treatment for Mixed-Cation Lead Mixed-Halide Perovskite Solar Cells for Higher Efficiency and Better Stability. *Advanced Energy Materials* **2018,** *8* (20), 1703392.

141. Yoo, J. J.; Wieghold, S.; Sponseller, M.; Chua, M.; Bertram, S. N.; Hartono, N. T. P.; Tresback, J.; Hansen, E.; Correa-Baena, J.-P.; Bulovic, V., An Interface Stabilized Perovskite Solar Cell with High Stabilized Efficiency and Low Voltage Loss. *Energy & Environmental Science* **2019**.

142. Quan, L. N.; Yuan, M.; Comin, R.; Voznyy, O.; Beauregard, E. M.; Hoogland, S.; Buin, A.; Kirmani, A. R.; Zhao, K.; Amassian, A., Ligand-stabilized reduced-dimensionality perovskites. *Journal of the American Chemical Society* **2016,** *138* (8), 2649-2655.

143. Mei, A.; Li, X.; Liu, L.; Ku, Z.; Liu, T.; Rong, Y.; Xu, M.; Hu, M.; Chen, J.; Yang, Y.; Gratzel, M.; Han, H., A hole-conductor-free, fully printable mesoscopic perovskite solar cell with high stability. *Science* **2014,** *345* (6194), 295-8.

144. Liu, M.; Johnston, M. B.; Snaith, H. J., Efficient planar heterojunction perovskite solar cells by vapour deposition. *Nature* **2013,** *501* (7467), 395.

145. Pedregosa, F.; Varoquaux, G.; Gramfort, A.; Michel, V.; Thirion, B.; Grisel, O.; Blondel, M.; Prettenhofer, P.; Weiss, R.; Dubourg, V., Scikit-learn: Machine learning in Python. *Journal of machine learning research* **2011,** *12* (Oct), 2825-2830.

146. Pilania, G.; Mannodi-Kanakkithodi, A.; Uberuaga, B.; Ramprasad, R.; Gubernatis, J.; Lookman, T., Machine learning bandgaps of double perovskites. *Scientific reports* **2016,** *6*, 19375.

147. Braly, I. L.; deQuilettes, D. W.; Pazos-Outón, L. M.; Burke, S.; Ziffer, M. E.; Ginger, D. S.; Hillhouse, H. W., Hybrid perovskite films approaching the radiative limit with over 90% photoluminescence quantum efficiency. *Nature Photonics* **2018**.

148. Qian, J.; Ernst, M.; Wu, N.; Blakers, A., Impact of perovskite solar cell degradation on the lifetime energy yield and economic viability of perovskite/silicon tandem modules. *Sustainable Energy & Fuels* **2019**.

149. Song, Z.; McElvany, C. L.; Phillips, A. B.; Celik, I.; Krantz, P. W.; Watthage, S. C.; Liyanage, G. K.; Apul, D.; Heben, M. J., A technoeconomic analysis of perovskite solar module manufacturing with low-cost materials and techniques. *Energy & Environmental Science* **2017,** *10* (6), 1297-1305.

150. Green, M. A.; Dunlop, E. D.; Levi, D. H.; Hohl-Ebinger, J.; Yoshita, M.; Ho-Baillie, A. W., Solar cell efficiency tables (version 54). *Progress in Photovoltaics: Research and Applications* **2019,** *27* (7), 565-575.

151. Cheacharoen, R.; Boyd, C. C.; Burkhard, G. F.; Leijtens, T.; Raiford, J. A.; Bush, K. A.; Bent, S. F.; McGehee, M. D., Encapsulating perovskite solar cells to withstand damp heat and thermal cycling. *Sustainable Energy & Fuels* **2018,** *2* (11), 2398-2406.

152. Shi, L.; Young, T. L.; Kim, J.; Sheng, Y.; Wang, L.; Chen, Y.; Feng, Z.; Keevers, M. J.; Hao, X.; Verlinden, P. J., Accelerated lifetime testing of organic–inorganic perovskite solar cells encapsulated by polyisobutylene. *ACS applied materials & interfaces* **2017,** *9* (30), 25073-25081.

153. Bella, F.; Griffini, G.; Correa-Baena, J.-P.; Saracco, G.; Grätzel, M.; Hagfeldt, A.; Turri, S.; Gerbaldi, C., Improving efficiency and stability of perovskite solar cells with photocurable fluoropolymers. *Science* **2016,** *354* (6309), 203-206.

154. Bryant, D.; Aristidou, N.; Pont, S.; Sanchez-Molina, I.; Chotchunangatchaval, T.; Wheeler, S.; Durrant, J. R.; Haque, S. A., Light and oxygen induced degradation limits the operational stability of methylammonium lead triiodide perovskite solar cells. *Energy & Environmental Science* **2016,** *9* (5), 1655-1660.

155. Duong, T.; Wu, Y.; Shen, H.; Peng, J.; Zhao, S.; Wu, N.; Lockrey, M.; White, T.; Weber, K.; Catchpole, K., Light and elevated temperature induced degradation (LeTID) in perovskite solar cells and development of stable semi-transparent cells. *Solar Energy Materials and Solar Cells* **2018,** *188*, 27-36.

156. Dualeh, A.; Gao, P.; Seok, S. I.; Nazeeruddin, M. K.; Grätzel, M., Thermal behavior of methylammonium lead-trihalide perovskite photovoltaic light harvesters. *Chemistry of Materials* **2014,** *26* (21), 6160-6164.

157. Leguy, A. M. A.; Hu, Y.; Campoy-Quiles, M.; Alonso, M. I.; Weber, O. J.; Azarhoosh, P.; van Schilfgaarde, M.; Weller, M. T.; Bein, T.; Nelson, J.; Docampo, P.; Barnes, P. R. F., Reversible Hydration of CH3NH3PbI3in Films, Single Crystals, and Solar Cells. *Chemistry of Materials* **2015,** *27* (9), 3397-3407.

158. Christians, J. A.; Miranda Herrera, P. A.; Kamat, P. V., Transformation of the excited state and photovoltaic efficiency of CH3NH3PbI3 perovskite upon controlled exposure to humidified air. *Journal of the American Chemical Society* **2015,** *137* (4), 1530-1538.

159. Yang, J.; Siempelkamp, B. D.; Liu, D.; Kelly, T. L., Investigation of CH3NH3PbI3 degradation rates and mechanisms in controlled humidity environments using in situ techniques. *ACS nano* **2015,** *9* (2), 1955-1963.

160. Bowring, A. R.; Bertoluzzi, L.; O'Regan, B. C.; McGehee, M. D., Reverse bias behavior of halide perovskite solar cells. *Advanced Energy Materials* **2018,** *8* (8), 1702365.

161. Rajagopal, A.; Williams, S. T.; Chueh, C. C.; Jen, A. K., Abnormal Current-Voltage Hysteresis Induced by Reverse Bias in Organic-Inorganic Hybrid Perovskite Photovoltaics. *J Phys Chem Lett* **2016,** *7* (6), 995-1003.

162. Domanski, K.; Correa-Baena, J.-P.; Mine, N.; Nazeeruddin, M. K.; Abate, A.; Saliba, M.; Tress, W.; Hagfeldt, A.; Grätzel, M., Not all that glitters is gold: metal-migration-induced degradation in perovskite solar cells. *ACS nano* **2016,** *10* (6), 6306-6314.

163. Boyd, C. C.; Cheacharoen, R.; Bush, K. A.; Prasanna, R.; Leijtens, T.; McGehee, M. D., Barrier design to prevent metal-induced degradation and improve thermal stability in perovskite solar cells. *ACS Energy Letters* **2018,** *3* (7), 1772-1778.

164. Yang, J.; Siempelkamp, B. D.; Mosconi, E.; De Angelis, F.; Kelly, T. L., Origin of the thermal instability in CH3NH3PbI3 thin films deposited on ZnO. *Chemistry of Materials* **2015,** *27* (12), 4229-4236.

165. Dunlap-Shohl, W. A.; Li, T.; Mitzi, D. B., Interfacial Effects during Rapid Lamination within MAPbI3 Thin Films and Solar Cells. *ACS Applied Energy Materials* **2019**.

166. Jena, A. K.; Numata, Y.; Ikegami, M.; Miyasaka, T., Role of spiro-OMeTAD in performance deterioration of perovskite solar cells at high temperature and reuse of the perovskite films to avoid Pb-waste. *Journal of Materials Chemistry A* **2018,** *6* (5), 2219-2230.

167. Kerner, R. A.; Rand, B. P., Electrochemical and Thermal Etching of Indium Tin Oxide by Solid-State Hybrid Organic–Inorganic Perovskites. *ACS Applied Energy Materials* **2019,** *2* (8), 6097-6101.

168. Rolston, N.; Watson, B. L.; Bailie, C. D.; McGehee, M. D.; Bastos, J. P.; Gehlhaar, R.; Kim, J.-E.; Vak, D.; Mallajosyula, A. T.; Gupta, G., Mechanical integrity of solution-processed perovskite solar cells. *Extreme Mechanics Letters* **2016,** *9*, 353-358.

169. Kempe, M. D.; Panchagade, D.; Reese, M. O.; Dameron, A. A., Modeling moisture ingress through polyisobutylene-based edge-seals. *Progress in Photovoltaics: Research and Applications* **2015,** *23* (5), 570-581.

170. Uddin, A.; Upama, M. B.; Yi, H.; Duan, L., Encapsulation of organic and perovskite solar cells: a review. *Coatings* **2019,** *9* (2), 65.

171. Hülsmann, P.; Weiß, K. A.; Köhl, M., Temperature-dependent water vapour and oxygen permeation through different polymeric materials used in photovoltaic-modules. *Progress in Photovoltaics: Research and Applications* **2014,** *22* (4), 415-421.

172. Holzhey, P.; Saliba, M., A full overview of international standards assessing the long-term stability of perovskite solar cells. *Journal of Materials Chemistry A* **2018,** *6* (44), 21794-21808.

173. Saliba, M., Perovskite solar cells must come of age. *Science* **2018,** *359* (6374), 388-389.

174. Christians, J. A.; Habisreutinger, S. N.; Berry, J. J.; Luther, J. M., Stability in perovskite photovoltaics: A paradigm for newfangled technologies. *ACS Energy Letters* **2018,** *3* (9), 2136-2143.

175. Snaith, H. J.; Hacke, P., Enabling reliability assessments of pre-commercial perovskite photovoltaics with lessons learned from industrial standards. *Nature Energy* **2018,** *3* (6), 459.

176. Ritter, D.; Weiser, K.; Zeldov, E., Steady-state photocarrier grating technique for diffusion-length measurement in semiconductors: Theory and experimental results for amorphous silicon and semi-insulating GaAs. *Journal of applied physics* **1987,** *62* (11), 4563-4570.

177. Jacobsson, T. J.; Correa-Baena, J.-P.; Halvani Anaraki, E.; Philippe, B.; Stranks, S. D.; Bouduban, M. E.; Tress, W.; Schenk, K.; Teuscher, J. l.; Moser, J.-E., Unreacted PbI2 as a double-edged sword for enhancing the performance of perovskite solar cells. *Journal of the American Chemical Society* **2016,** *138* (32), 10331-10343.

178. Liu, F.; Dong, Q.; Wong, M. K.; Djurišić, A. B.; Ng, A.; Ren, Z.; Shen, Q.; Surya, C.; Chan, W. K.; Wang, J., Is excess PbI2 beneficial for perovskite solar cell performance? *Advanced Energy Materials* **2016,** *6* (7), 1502206.

179. Merdasa, A.; Kiligaridis, A.; Rehermann, C.; Abdi-Jalebi, M.; Stöber, J.; Louis, B.; Gerhard, M.; Stranks, S. D.; Unger, E. L.; Scheblykin, I. G., Impact of Excess Lead Iodide on the Recombination Kinetics in Metal Halide Perovskites. *ACS Energy Letters* **2019,** *4*, 1370-1378.

180. Supasai, T.; Rujisamphan, N.; Ullrich, K.; Chemseddine, A.; Dittrich, T., Formation of a passivating CH3NH3PbI3/PbI2 interface during moderate heating of CH3NH3PbI3 layers. *Applied Physics Letters* **2013,** *103* (18), 183906.

181. Brenes, R.; Guo, D.; Osherov, A.; Noel, N. K.; Eames, C.; Hutter, E. M.; Pathak, S. K.; Niroui, F.; Friend, R. H.; Islam, M. S., Metal halide perovskite polycrystalline films exhibiting properties of single crystals. *Joule* **2017,** *1* (1), 155-167.

182. Brenes, R.; Eames, C.; Bulović, V.; Islam, M. S.; Stranks, S. D., The impact of atmosphere on the local luminescence properties of metal halide perovskite grains. *Advanced Materials* **2018,** *30* (15), 1706208.

183. Euvrard, J.; Gunawan, O.; Mitzi, D. B., Impact of PbI2 Passivation and Grain Size Engineering in CH3NH3PbI3 Solar Absorbers as Revealed by Carrier-Resolved Photo-Hall Technique. *Advanced Energy Materials* **2019**.

184. Tress, W.; Yavari, M.; Domanski, K.; Yadav, P.; Niesen, B.; Baena, J. P. C.; Hagfeldt, A.; Graetzel, M., Interpretation and evolution of open-circuit voltage, recombination, ideality factor and subgap defect states during reversible light-soaking and irreversible degradation of perovskite solar cells. *Energy & Environmental Science* **2018,** *11* (1), 151-165.

185. Khenkin, M. V.; Visoly-Fisher, I.; Kolusheva, S.; Galagan, Y.; Di Giacomo, F.; Vukovic, O.; Patil, B. R.; Sherafatipour, G.; Turkovic, V.; Rubahn, H.-G. n., Dynamics of photoinduced degradation of perovskite photovoltaics: from reversible to irreversible processes. *ACS Applied Energy Materials* **2018,** *1* (2), 799-806.

186. Friedman, J.; Hastie, T.; Tibshirani, R., *The elements of statistical learning*. Springer series in statistics New York: 2001; Vol. 1.

187. Caruana, R.; Freitag, D., Greedy attribute selection. In *Machine Learning Proceedings 1994*, Elsevier: 1994; pp 28-36.

188. Dunlap-Shohl, W. A.; Barraza, E. T.; Barrette, A.; Gundogdu, K.; Stiff-Roberts, A. D.; Mitzi, D. B., MAPbI3 Solar Cells with Absorber Deposited by Resonant Infrared Matrix-Assisted Pulsed Laser Evaporation. *ACS Energy Letters* **2018,** *3* (2), 270-275.